TESIS DE LA UNIVERSIDAD DE ZARAGOZA
2020
59

Carlos Pérez Mejías

The Ejulve cave speleothemic record:from monitoring control to abrupt climate changes during the Pleistocene in the Eastern Iberian Range (Teruel)

Departamento
Ciencias de la Tierra

Director/es
Sancho Marcén, Carlos
Moreno Caballud, Ana

ISSN 2254-7606

Prensas de la Universidad
Universidad Zaragoza

ISSN 2254-7606

Universidad Zaragoza
1542

Tesis Doctoral

THE EJULVE CAVE SPELEOTHEMIC RECORD: FROM MONITORING CONTROL TO ABRUPT CLIMATE CHANGES DURING THE PLEISTOCENE IN THE EASTERN IBERIAN RANGE (TERUEL)

Autor

Carlos Pérez Mejías

Director/es

Sancho Marcén, Carlos
Moreno Caballud, Ana

UNIVERSIDAD DE ZARAGOZA

Ciencias de la Tierra

2019

UNIVERSIDAD DE ZARAGOZA

PhD DISSERTATION

THE EJULVE CAVE SPELEOTHEMIC RECORD: FROM MONITORING CONTROL TO ABRUPT CLIMATE CHANGES DURING THE PLEISTOCENE IN THE EASTERN IBERIAN RANGE (TERUEL).

Author: Carlos Pérez-Mejías

Supervisors: Ana Moreno Caballud (Instituto Pirenaico de Ecología-CSIC)

Carlos Sancho Marcén (Universidad de Zaragoza)

Departamento de Ciencias de la Tierra
Universidad Zaragoza

The Ejulve cave speleothemic record: from monitoring control to abrupt climate changes during the Pleistocene in the Eastern Iberian Range (Teruel)

Tesis doctoral defendida por Carlos Pérez-Mejías dentro del programa de doctorado en Geología, y dirigida por Ana Moreno Caballud (IPE-CSIC) y Carlos Sancho Marcén (Universidad de Zaragoza)

Impreso en España / *Printed in Spain*

First edition, October 2018

A Asunción, Rafael,
Raúl y Elena(s)

Agradecimientos

Soplaba un ligero viento y la temperatura era agradable. Era mediodía, y los compañeros ya se disponían a volver a casa para comer. Tras descender por el Paseo de Cartuja, en pocos minutos llegué a mi destino. Abrí el portal y me dirigí hacia el buzón, y tras recoger una carta, comencé a subir las escaleras. El logo que estaba estampado en el sobre ya me hacía intuir el propósito de la misma. Cerré la puerta tras de mí y fui hasta la cocina. Cogí un refresco y me dirigí al salón. Desde la puerta que da paso al balcón se veía una increíble panorámica de Sierra Nevada. "Aún hay mucha nieve durante esta primavera" –me dije. Escasos minutos después estaría mirando billetes de tren hacia Zaragoza. La carta resultó ser la resolución de las becas de introducción a la investigación del CSIC, estableciendo así el primer paso para conocer al equipo donde años más tarde realizaría la presente tesis.

* * *

Mucho ha llovido desde entonces, durante una gran etapa que se cierra aquí y podría definirse como apasionante y agotadora a partes iguales. Empiezo agradeciendo a mis directores, Ana Moreno y Carlos Sancho, quienes me han acompañado durante todo este camino y sin cuya inestimable ayuda hubiera sido del todo imposible llegar a este punto. Contáis con toda mi admiración y mi respeto. ¡Muchísimas gracias! Este agradecimiento se hace extensible al grupo Paleo-IPE: Blas, Penélope, Graciela...muchas gracias por estar ahí siempre que ha sido necesario y por todo lo aprendido durante este camino. A Miguel Sevilla, siempre dispuesto a echar una mano con GNU/Linux y a motivar para hacer buenos mapas. A Raquel y Matías, por todas las anécdotas, *papiros* y *Tía María* compartidos. A Elena, que más de una vez ha tenido que acompañarme al campo o muestrear alguna estalagmita mía. A María, compañera de aventura en el desafío de máster + tesis. A los que ya han acabado la tesis: Edu y Fernando, que han tomado un nuevo rumbo en su vida; Miguel Bartolomé, que mientras escribo estas líneas seguro que anda metido en alguna cueva en algún lugar del Pirineo; y a Josu, que felizmente volvió a su tierra y sigue al pie del cañón. A los recién llegados: Héctor, Jara y Juan Luis..…sois el futuro del grupo!

Ha sido un enorme placer compartir estos años con el increíble grupo de gente que constituye el IPE: Marina, Natalia, Esteban, Javi, Fernando, Makki, Xavi, Miguel, Antonio 'Chang',

Dani….han sido muchas risas durante los cafés y muchas noches en las que el objetivo era acabar en la López! A José Luis, Manuel y Sophie, por esas escapadas a Andalucía. Al gérmen del comité de fiestas populares, que nunca dudaba en apuntarse a cualquier plan y en el cual estaban Ana y Elena, como no podía ser de otra manera. Mención especial se merece la *conexión Alicante*, Clara y Fergus: sois verdaderamente increíbles. Ha sido todo un placer compartir tantas experiencias junto a vosotros. Gracias también a todos los que habéis hecho posible todas esas partidas de ping pong, y más recientemente de pádel. A los que formaron parte en el inicio: Hugo, Jesús, Gabriel, Iker, Cecilia… También hay un recuerdo para esos compañeros que han pasado de prácticas por el grupo, Ángel con su mente siempre puesta en Marte, y especialmente a Luis, capaz de desplazarse al otro extremo del planeta para luchar por sus sueños. Mis respetos, valiente.

Varias visitas a la Universidad de Oviedo han sido necesarias a lo largo del doctorado, mi infinito agradecimiento a Heather Stoll por facilitarme en todo momento una indispensable ayuda. Muchas gracias a todos los compañeros que siempre han hecho mi estancia allí inmejorable, entre sidras y escapadas a la montaña. Gracias Miguel, Dani, Ana, Bea, Iker, Irene, Pablo, Lorena, Maite, Rosa, Luzma, Fulvio…

Gracias a la Universidad de Barcelona por toda la ayuda recibida por Isa, y mucho ánimo a Mercé, Judit y Albert. ¡Ya os falta poco! Agradecer a Joaquín Perona (UB) la gran cantidad de muestras analizadas, a Josep Elvira los análisis de DRX y a Antonio Delgado (IACT-CSIC) por todas las muestras de lluvia y goteos. Agradecer también de la Universidad de Zaragoza a Cinta Osácar por la ayuda en el análisis de los precipitados en las paredes de la cueva, a Alfonso Meléndez por el reconocimiento de la estratigrafía en campo y a Luis Auqué por toda la ayuda prestada con PHREEQC. Igualmente, a Rebeca Martín (UCM) por el análisis de las láminas delgadas y a Belén Oliva (UAM) por la medición de los planos de falla en el interior de la cueva.

My first contact with an international team in the very beginning of the thesis was with the LSCE-CNRS, in the group leaded by Dominique Genty. Thank you for all your help during that time in Paris. Likewise, I´m indebt to Larry Edwards and Hai Cheng, from the University of Minnesota. Thank you so much for offer me the possibility to work in your laboratory! Thanks to Yanbin and Mathieu for those moments we spent together in *the Library* with a beer, an hamburguer and sharing those great chicken wings. Katee, that Halloween spent with your friends was unforgettable! Natasha, Julia, Akemi, Eline, Valdir…it was great to work with all of you and I wish you the best in the future!

Judit, have you already learned how to use the machine? Don't say 'wait wait wait' again….

Life is what goes between uranium samples

Don't forget it, guys. Best regards from that student that would be running samples until the doomsday. Those visits to Minneapolis were much more special with the help of Phyllis and Laurie. Phyllis, I can't find enough words to acknowledge you for making us the life easier in MN. Thanks for all those cheese curds and beers shared. For that weekend in the cabin in the lakes of the north or the roadtrip through Minnesota and South Dakota, that was so special. I´ve never seen again the stars and the Milkyway so clear during the night such as during that time in the middle of nowhere. Likewise, thanks so much to Christoph Spötl from the University of Innsbruck, for offering me the possibility to use his laboratory of stables isotopes to run part of my samples. Likewise, thanks to Manuela and Paul for helping me there.

Gracias al ayuntamiento de Molinos, en especial a Emilio por tomar pacientemente las muestras de lluvia, y al ayuntamiento de Ejulve, por cederme la llave religiosamente en cada una de mis visitas, que no han sido pocas. Asimismo, gracias a Nicolás por su amabilidad y las facilidades ofrecidas para enseñarnos la cueva en Beteta, y a los espeleólogos Ramón Queraltó y Carles Pons por guiarnos en las cavidades de los macizos de Els Ports y el Garraf. Al grupo vasco, liderado por Arantxa, Martín y Eneko, por la buena acogida que siempre nos han hecho allí. Seguro que el trabajo conjunto en las cuevas del País Vasco y Navarra pronto empezará a dar sus frutos.

El primer año en Zaragoza fue en compañía de los compañeros del máster: Jorge(s), Rafa, Antonio, Julia, Carmen….fueron geniales los momentos compartidos. A los compañeros conocidos durante la carrera, un fuerte abrazo para todos: Vicente, Xabi, Valentin, Toci, Alex, Silvia, Inma, Oli, Jorge, Martínez…un fuerte abrazo a todos.

A Bárbara y Lluna, gracias por todos los momentos vividos juntos. Gracias a los compañeros de piso que han propiciado una convivencia agradable durante la última etapa de la tesis. Fran, Alberto, Isa, Baloo....(recordad cerrarle la ventana para que no se cuele en mi habitación!).

Sin duda han sido fundamentales las escapadas al boulder para desconectar la mente de la tensión asociada a la tesis, muchas gracias a Isaac por estar siempre ahí. Todas esas charlas sobre ciencia siempre permanecerán en mi memoria, a falta de haber puesto una grabadora para inmortalizarlas, claro.

Mientras aún esté por estas tierras, el plan 'boulder + ruso' siempre funcionará. Te dejo con tus movidas *quirales*, pero sabes que siempre serás bien recibido si decides pasarte al lado

oscuro de la geoquímica. Mucha suerte también a Juanvi que está haciendo ya las américas, aunque creo que no la necesitará. Me informan que ya ha caído un *Science*, mi más sincera enhorabuena. Gracias también a Alberto y Raquel por todos los momentos vividos entre presas y magnesio.

Un fuerte abrazo a toda mi familia que siempre se acuerda de mí y a mis amigos de Villena, que me ven bien poco. La verdad es que a medio plazo creo que eso no va a cambiar demasiado. A cambio, podréis ver mundo viniendo a visitarme. Luigi, seguro que contigo coincido en alguna locura en cualquier lugar del planeta. Por tus últimos planes que han llegado ya a mis oídos, veo que apuntas alto, literalmente. A Diego, mucho ánimo con tus planes de futuro, por los cuales ya estás empezando a luchar. Espero tener pronto para leer una versión más avanzada de esa '*cosa*'.

Anschließend habe ich Annika viel zu verdanken, für alles, was wir zusammen erlebt haben. Es gab viele besondere Momente, die bereits unvergesslich sind. Ich freue mich auf unsere spannenden, gemeinsamen Pläne und darauf, viele verlassene Orte zu erkunden. Ich freue mich auf alles. Keine Distanz ist zu groß, um uns zu trennen. Gemeinsam sind wir stark.

…y el ballet cósmico sigue su curso…

Abstract

The present dissertation addresses a complete study of Ejulve cave (Iberian Range, NE Spain) related to the speleogenesis of the cave, the current speleothemic dynamics and the reconstruction of past Pleistocene abrupt climate changes based on its speleothem record. Ejulve cave, located at 1240 m.a.s.l., is a relatively small cave in the southeastern sector of the Iberian Range. The cave is developed in dolomitic limestones and dolostones of the Mosqueruela Fm., Upper Cretaceous in age, affected by the thrust fronts of Portalrubio-Vandellós system, structured during Oligocene and Low Miocene. The landscape is dominated by extensive high-altitude deformed planation surfaces (Main Planation Surface of the Iberian Chain), finally shaped during the Pliocene.

The origin of the cave is expected to have occurred before the final phase of the Main Planation Surface development. The identification of some characteristic cave morphologies such as boxwork, tubes with rising ceiling cupolas, pendants and cups, spongework and micro-corrosion features, suggests a hypogene karst setting during this time. Hence, the hypogene karstification, tentatively occurred during the Mio-Pliocene, could be explained by ascending water flows driven by hydraulic gradients in a confined aquifer, generating a maze network and the characteristic cave morphologies listed above. Additionally, the analysis of the boxwork suggests an earlier stage, probably during the Upper Miocene, of calcite and dolomite infills hosted in discontinuities of the bedrock, formed under phreatic conditions. After the karstification, the cave underwent a transition to epigenic unconfined conditions, driven by the regional uplift and doming mechanisms. After the extensional tectonics during Pliocene-Quaternary, there was the subsequent fluvial incision. Once the exhumation of the karst leads to the vadose phase, it is the starting point for the precipitation of carbonate speleothems, at least from 650 kyr BP.

The study of the cave speleothemic dynamics, including sampling of rainfall, drip waters and farmed calcite, was conducted during four years (2013-2016). The main factor that controls the $\delta^{18}O$ of the rainfall are the temperature effect (r^2 = 0.82, *p-value* > 0.001), showing a seasonal pattern of lower values in winter and higher in summer. Both source effect (together with the rainfall component) and amount effect act as secondary controls. The use of the effective infiltration is crucial to evaluate the recharge of the epikarst, in the semi-arid conditions of the study area. In fact, the use of the effective infiltration reveal that the amount effect exerts a scarce influence on the isotopic variability of the drip waters,

in contrast with the moderate influence that it exerts on the annual $\delta^{18}O$ in rainfall. The sampling of 12 drips throughout the cave indicated that seepage and seasonal drips featured similar $\delta^{18}O$ in dripwaters. The $\delta^{18}O$ seasonality seen in rainfall was also observed in dripwater $\delta^{18}O$, albeit attenuated and lagged, so the homogeneisation process of the waters in the epikarst was not complete. The hydrological response of the cave to the external rainfall is fast, with an increase of drip rates within few weeks in both seasonal and seepage drips during the seasonal rainfall in autumn. However, the lag seen in the $\delta^{18}O$ of autumn-winter rainfall is as long as 21 weeks. These results suggest the existence of a 'piston effect', in which the 'new' water pushed down the 'old' pre-existent water in the epikarst through the fracture network.

The farmed calcite shows a small variation of 0.11 ‰ in $\delta^{18}O$, with similar variability between seasonal and seepage sites. The $\delta^{18}O$ of the calcite showed dependence on the $\delta^{18}O$ of the dripwaters, with a weak influence of drip rate. The variation in $\delta^{13}C$ is of 0.22 ‰, and exhibit seasonality with higher values during summer and autumn, and lower in winter and spring. The $\delta^{13}C$ was more positive in seepage sites, enhanced by degassing kinetics, up to 0.42 ‰ compared to the 0.29 ‰ observed in the seasonal sites. These differences between drip sites are explained by the high correlation of the $\delta^{13}C$ with the drip rate. Therefore, the high $\delta^{13}C$ in the farmed calcite of Ejulve cave was explained by enhanced degassing and low water availability, while low $\delta^{13}C$ values were in concordance with more microbial activity, vegetation productivity, and greater water availability. The ventilation of the cave during late autumn through spring favored the higher calcite deposition rates found during that time. Dripwater chemistry and drip rate exerts as secondary controls on carbonate growth rate.

The reconstruction of past climate changes using stalagmites from Ejulve cave was focused in two main periods: (1) during the transition MIS 8 - MIS 7 using the stalagmite ARTEMISA, and (2) during the periods MIS 5, 4 and 3, using the stalagmite ANDROMEDA. The proxies used were $\delta^{18}O$, $\delta^{13}C$ and Mg/Ca.

The stalagmite 'ARTEMISA' covered the interval 262.7 to 217.9 kyr BP, including the response to the Termination III (T-III), a poorly known glacial-interglacial transition, in contrast to Terminations II and I. The response of the $\delta^{13}C$ and Mg/Ca to the abrupt arid events in the timing of the T-III was clear. Hence, we identify two millennial-scale events (S8.1 and S8.2) that are related to AMOC slowdowns during MIS 8. The sensitivity of the Iberian Peninsula to AMOC changes, due to its latitudinal and geographical location, has been demonstrated previously during Termination I and MIS 3. The variability in $\delta^{18}O$ in the

record also marks the latest event (S8.1) with a change in the $\delta^{18}O$ composition of the sea water in the source of moisture, probably associated with the entrance of freshwater in north Atlantic. After a comparison between T-III, T-II and T-I, the two stadial events we propose have some similarities with Heinrich stadial (HS) 1 and 2. These similarities are supported by intense IRD discharges, the dominance of semidesert taxa in the arid intervals, and the similar phasing of the benthic $\delta^{18}O$. However, the changes in sea level and insolation during S8.1, makes it more similar to the YD than HS-1, precluding the identification of the YD as a unique feature of the most recent termination.

The stalagmite 'ANDROMEDA' covers continuously the interval from 118.9 to 36.9 kyr. During MIS 5, the $\delta^{18}O$ were controlled by orbital pacing, with low precession peaks leading wet conditions. In contrast, during MIS 4 and 3, the $\delta^{18}O$ fluctuations were decoupled from precession, and co-varies with $\delta^{13}C$, suggesting a common control of both isotopes by enhanced degassing of drip waters during dry periods. In general, $\delta^{13}C$ exhibit a clear response to the cold marine events C26 to C23, as well as Dansgaard-Oeschger (D-O) oscillations and Heinrich events.

This record supports previous studies showing a late demise of the Eemian forest stage in southern Europe, and offer new dates from 108.6 ± 0.3 to 108.3 ± 0.3 in this area. The response to Heinrich events were identified by two periods with a marked 'W-shape' pattern in the $\delta^{13}C$. These periods were characterized by the response of the $\delta^{13}C$ to the weak D-O cycles 15 and 18. The variability in the $\delta^{13}C$ is similar between both events, but a different timing is seen, longer in the first event contemporary with HS-6. Two phases were identified within the older W-event (~67-60 kyr), a first one with dry-cold conditions before 63 kyr BP, and a second one with wet-cold conditions afterwards. The younger W-event (~57-53 kyr) is in concordance with the reinforcement of the northeasterly trade winds (NAO+ phase) giving rise to a dry climate in Southern Europe at that time.

On the other hand, the positive correlation seen between $\delta^{13}C$ and Mg/Ca, in both periods (Termination III and MIS 5, 4 and 3), is expected to reflect water availability, vegetation productivity and microbial activity over the cave, such as was suggested by the monitoring results above.

In summary, the present dissertation shows an unusual speleogenesis model in the Iberian Range proposed for Ejulve cave, a complete and careful detailed dataset related to the monitoring of present-day speleothem dynamics, and the

reconstruction of interesting past climate changes. Those features make it the first compilation of such outstanding new brand data in a cave from the Iberian Range. Likewise, it is worth noting the high interest of the paleoclimatic results using speleothems from this cave, especially in the abrupt climate changes. The clear response exhibited during the end of Glacial periods (Terminations), to D-O oscillations and Heinrich events, and the clear link with other key records such as the speleothems from caves in China, makes Ejulve cave an outstanding site for paleoclimatic studies.

Resumen

La presente tesis engloba un completo estudio en la Cueva de El Recuenco (Ejulve, Cordillera Ibérica, NE Península Ibérica) sobre la espeleogénesis de la cueva, la dinámica espeleotémica actual y la reconstrucción de cambios climáticos abruptos durante el Pleistoceno a partir de sus registros espeleotémicos. La cueva de Ejulve, situada a 1240 m.s.n.m., es una cueva relativamente pequeña en el sector suroriental de la Cordillera Ibérica. Se encuentra desarrollada en calizas dolomíticas y dolomías de la formación Mosqueruela, del Cretácico Superior, y está afectada por el arco de cabalgamientos de Portalrubio-Vandellós, estructurado durante el Oligoceno y Mioceno Inferior. El paisaje está dominado por amplias y deformadas superficies de erosión situadas a gran altitud (Superficie de Erosión Fundamental de la Cordillera Ibérica), que terminó de formarse en el Plioceno.

El origen de la cueva debería situarse antes de la fase final de desarrollo de la Superficie de Erosión Fundamental. La identificación de ciertas morfologías de la cueva, muy características, como son el *boxwork*, los tubos con cúpulas ascendentes en el techo, *pendants* y *cups*, *spongework* y rasgos de micro-corrosión, sugieren un origen hipógeno de la misma. Por lo tanto, la karstificación hipógena ocurriría tentativamente durante el Mio-Plioceno, y se explicaría por al ascenso de agua subterránea debido a gradientes hidráulicos en un acuífero confinado, generando así las galerías en forma de laberinto y las morfologías características mencionadas previamente. Adicionalmente, el análisis del *boxwork* sugiere una fase previa, probablemente durante el Mioceno Superior, en la que calcita y dolomita rellenaron las discontinuidades existentes en el epikarst, todo ello bajo condiciones freáticas. Después de la karstificación, la cueva tuvo una transición a condiciones epigénicas sin confinamiento, debido a la reactivación de los procesos regionales de levantamiento y *doming*. Después de la tectónica extensional durante el Plioceno-Cuaternario, se produciría la fase de la incisión fluvial. Así, una vez el karst queda exhumado y se da paso a la fase vadosa, comienza la precipitación de espeleotemas, al menos desde hace 650.000 años antes del presente.

El estudio de la dinámica actual de la cueva, incluyendo el muestreo de lluvia, goteo y carbonato precipitado, fue llevado a cabo durante cuatro años (2013-2016). El principal factor que controla el $\delta^{18}O$ de la lluvia es la temperatura ($r^2 = 0.82$, *p-value* > 0.001), mostrando un patrón estacional con valores más bajos en invierno y más altos en verano. Tanto el área de origen de la precipitación (junto al componente de la lluvia) y la cantidad de lluvia, actúan como controles secundarios. El uso

de la infiltración neta resulta crucial para evaluar la recarga del epikarst en las condiciones semi-áridas propias del área de estudio. De hecho, el uso de la infiltración neta revela que el efecto de cantidad de lluvia ejerce escasa influencia en la variabilidad isotópica del agua de goteo, en contraste con la influencia moderada que ejercía sobre el $\delta^{18}O$ de la lluvia anual. El muestreo de 12 goteos a lo largo de la cueva evidenció que tanto los goteos estacionales como los no estacionales muestran similares valores de $\delta^{18}O$ en el agua de goteo. La estacionalidad vista en el $\delta^{18}O$ del agua de lluvia, es también observada en el agua de goteo, aunque atenuada y con cierto retardo, por lo tanto, no hay un proceso completo de homogeneización de las aguas en el epikarst. La respuesta hidrológica de la cueva a la lluvia externa es rápida, con un incremento en las tasas de goteo en pocas semanas en ambos grupos de goteos durante las lluvias estacionales de otoño. No obstante, el retardo visto en el $\delta^{18}O$ de las lluvias de otoño-invierno asciende hasta un máximo de 21 semanas. Estos resultados sugieren la existencia del 'efecto pistón', según el cual el agua 'nueva' presiona en sentido descendente el agua 'antigua' pre-existente en el epikarst, a través de la red de fracturas existentes.

El carbonato precipitado muestra una escasa variación total de un 0.11 ‰ en el $\delta^{18}O$, con una variabilidad similar entre los goteos estacionales y los no estacionales. El $\delta^{18}O$ del carbonato depende del $\delta^{18}O$ del agua de goteo, con una escasa influencia de la tasa de goteo. La variación del $\delta^{13}C$ es de un 0.22 ‰, y muestra estacionalidad con valores más altos en verano y otoño, y más bajos en invierno y primavera. El $\delta^{13}C$ es más positivo en los goteos no estacionales, los cuales, debido a una mayor desgasificación, registran una variabilidad que asciende hasta el 0.42 ‰, comparado con el 0.29 ‰ de los goteos estacionales. Estas diferencias entre diferentes tipos de goteo están explicadas por la alta correlación entre el $\delta^{13}C$ y la tasa de goteo. Por lo tanto, los valores altos de $\delta^{13}C$ en el carbonato precipitado en la cueva de Ejulve se explican por la mayor desgasificación y menor disponibilidad hídrica, mientras que los valores bajos de $\delta^{13}C$ se registrarían cuando hay más actividad microbiana, mayor productividad vegetal y más disponibilidad hídrica. La ventilación de la cueva desde finales del otoño hasta la primavera, favorece una mayor precipitación de carbonato. De esta manera, tanto la hidroquímica de las aguas de goteo como la tasa de goteo quedan como controles secundarios de la tasa de precipitación de carbonato actual.

La reconstrucción de los cambios climáticos en el pasado utilizado registros espeleotémicos de la cueva de Ejulve se ha centrado en dos períodos: (1) durante la transición de MIS 8 a

MIS 7 a través de la estalagmita ARTEMISA, y (2) durante los períodos MIS 5, 4 y 3 a través de la estalagmita ANDROMEDA. Los indicadores usados han sido $\delta^{18}O$, $\delta^{13}C$ y Mg/Ca.

La estalagmita 'ARTEMISA' creció durante el período 262.7 - 217.9 ka, incluyendo la respuesta climática a la Terminación Glacial III (T-III), una transición glacial-interglacial escasamente conocida, en contraposición a las Terminaciones II y I. La respuesta del $\delta^{13}C$ y Mg/Ca a los eventos abruptos áridos en el desarrollo de la T-III es realmente pronunciada. Por lo tanto, se han identificado dos eventos de escala milenial (S8.1 y S8.2) que estarían explicados por debilitamientos de la AMOC durante MIS 8. La sensibilidad de la Península Ibérica a los cambios en la AMOC, debido a su posición latitudinal y geográfica, ya ha sido demostrada previamente durante la Terminación I y MIS 3. La variabilidad en $\delta^{18}O$ del registro marca el último evento (S8.1) con un cambio en el $\delta^{18}O$ del agua en el área fuente de la precipitación, probablemente asociado a la llegada de agua dulce en el Atlántico norte. Tras una comparación entre la T-III, T-II y T-I, los dos eventos estadiales que han sido propuestos tienen semejanzas con los eventos Heinrich (HS) 1 y 2. Estas similitudes se basan en las intensas descargas de IRD, la dominancia de taxones semidesérticos durante los eventos áridos, y la similar señal del $\delta^{18}O$ de los foraminíferos bentónicos marinos. No obstante, los cambios en el nivel del mar y en la insolación durante S8.1, lo hacen más similar al YD que a HS-1, impidiendo por lo tanto concluir que el YD es un evento único de la última terminación.

La estalagmita 'ANDROMEDA' crece de manera continua durante el intervalo de 118.9 a 36.9 ka. Durante MIS 5, los valores de $\delta^{18}O$ estaban regidos por control orbital, con picos de baja precisión que dan paso a condiciones húmedas. En contraste, durante MIS 4 y 3, los valores de $\delta^{18}O$ se desacoplan de la precesión, y covarían con el $\delta^{13}C$, sugiriendo así un control común en ambos isótopos, debido a una mayor desgasificación del agua de goteo durante los períodos áridos. En general, el $\delta^{13}C$ exhibe una clara respuesta a los eventos fríos marinos desde el C26 hasta el C23, así como a las oscilaciones Dansgaard-Oeschger (D-O) y a los eventos Heinrich.

Este registro apoya los resultados de estudios previos que mostraban un final tardío del Eemiense en el sur de Europa, y ofrece nuevas fechas para dicha finalización, desde 108.6 ± 0.3 a 108.3 ± 0.3 ka para esta área. La respuesta a los eventos Heinrich se establece en dos períodos distintivos en forma de 'W' en el patrón de variabilidad del $\delta^{13}C$. Esos períodos se caracterizan por la respuesta del $\delta^{13}C$ a los débiles eventos D-O 15 y 18. La variabilidad en el $\delta^{13}C$ es similar en ambos eventos, no así su desarrollo, siendo más largo el primer

evento, contemporáneo a HS-6. En el evento W más antiguo (~67-60 ka) han sido identificadas dos fases, la primera caracterizada por un patrón frío-árido antes de 63 ka, y una segunda de patrón húmedo-frío de 63 ka en adelante. El evento W más moderno (~57-53 ka) está en concordancia con un refuerzo de los vientos alisios en el NE (fase NAO+), provocando así unas condiciones de clima árido en el sur de Europa.

Por otro lado, la correlación positiva entre el $\delta^{13}C$ y Mg/Ca en los períodos estudiados (Terminación III y MIS 5, 4 y 3) está en concordancia con mayor disponibilidad hídrica, más productividad vegetal y actividad microbiana sobre la cueva, como sugieren los resultados de la monitorización expuestos anteriormente.

En resumen, la presente tesis muestra un modelo inusual de espeleogénesis en la Cordillera Ibérica propuesto para la cueva de Ejulve, un completo y detallado conjunto de datos procedentes de la monitorización de la dinámica espeleotémica actual, y la reconstrucción de interesantes cambios climáticos pasados. Esas características la convierten en la primera compilación de datos de este tipo en una cueva de la Cordillera Ibérica. Asimismo, conviene recalcar el gran interés de los resultados paleoclimáticos procedentes de estalagmitas de esta cueva, especialmente en cambios climáticos abruptos. La clara respuesta que exhibe durante el final de los períodos glaciares (Terminaciones), durante las oscilaciones D-O o los eventos Heinrich, y la clara vinculación con otros registros clave como las estalagmitas procedentes de cuevas de China, hacen a la cueva de Ejulve un lugar extraordinario para realizar estudios paleoclimáticos.

Contents

1.INTRODUCTION

2. STUDY AREA

3. METHODOLOGY

4. SPELEOGENESIS

5. MONITORING SURVEY

6. PALEOCLIMATE

List of figures

Chapter 2

Chapter 3

Chapter 4

Chapter 5

List of tables

The cure for boredom is curiosity.
There is no cure for curiosity”
-Dorothy Parker

Chapter 1

Introduction

1.1. Motivation

During the first decade of the present century, the speleothem science applied to the interpretation of past climate changes experienced a great revolution. The key relies in the improvement of accuracy and precision of the dating method (U-Th series) with the new generation of MC-ICP-MS and the progress made on determining the different environmental factors that control the isotopic variability (Fairchild and Baker, 2012).

The technical progress reached during that decade could be seen through several outstanding paleoclimate records worldwide. Great examples of such records can be found in Europe, especially with the studies carried out in Alps that covers a great variety of climate changes, such as the onset of an interglacial period (Meyer et al., 2008; Spotl et al., 2008), the Dansgaard-Oeschger (D-O) variability during MIS 3 (Spötl and Mangini, 2002; Spötl et al., 2006), or the Holocene climate fluctuations (Boch et al., 2009). Other important records in Europe spans the D-O oscillations in South France (Genty et al., 2003; 2010), the analysis of the centennial-scale variability in the Holocene in Ireland (McDermott et al., 2001) and finally the records from Italy analyzing the penultimate Termination and last glacial cycle (Drysdale et al., 2007; 2009).

In Near East, it had a great repercussion the pioneers studies in Soreq cave (Bar-Matthews et al., 1999) and the outstanding records from Turkey, Oman and Yemen (Burns, 2002; 2003; Fleitmann et al., 2003; 2007; 2009). Moreover, a major milestone was reached in the study of the paleoclimatology with the records of the Asian Monsoon in China, through the elaboration of long-continuous time series using speleothems, highly resolved chronologically, that allowed carefully analysis and comparison of several glacial terminations (Yuan et al., 2004; Cheng et al., 2006; 2009). Great records were originated also in the islands of the Pacific, such as Borneo (Partin et al., 2007).

Likewise, the studies in America that connects the changes or collapse of ancient civilizations with climate deteriorations were of great interest (Polyak and Asmerom, 2001; Medina-Elizalde et al., 2010). Besides, changes in the polar jet stream (Asmerom et al., 2010) were reported in records from North America, as well as changes in the El Niño/Southern Oscillation in Mesoamerica (Lachniet, 2004) and changes in the American monsoon in Brazil (Cruz et al., 2005a; 2009).

However, few studies are available from the Iberian Peninsula (IP) in that time, a region of great importance due to its location at intermediate latitudes and influenced both by

Atlantic and Mediterranean climates. After some pioneer studies of the karst and the first published chronologies of speleothems (Durán and López, 1989; Durán et al., 1993; Durán, 1996), some studies were starting mainly in the Betic Range (Durán et al., 1999; Jiménez de Cisneros et al., 2003; Hodge et al., 2008), Cantabrian Range (Muñoz-García et al., 2004; Martín-Chivelet et al., 2006; Muñoz-García et al., 2007; Domínguez-Villar et al., 2008, 2009; Moreno et al., 2010), Iberian Range (Muñoz et al., 2009) and Balearic Islands (Vesica et al., 2000; Hodge et al., 2008; Dorale et al., 2010). Pioneer studies were done during that time in the present-day cave dynamics (Martín-Chivelet et al., 2007; Muñoz and Sancho, 2008) and the alteration of textures and geochemical signals (Alonso-Zarza and Martín-Pérez, 2008; Martín-García et al., 2009).

The group of Quaternary paleoenvironments from the Pyrenean Institute of Ecology (IPE-CSIC), together with the University of Zaragoza, have been interested on discerning past climate changes in the IP working at different time scales, from the last century to the last glacial cycles. This group started a research line based on speleothem records around 2009-2010 working in two small touristic caves located in the Iberian Range, 'Ortigosa de Cameros' cave (La Rioja) (Muñoz et al., 2009; Osácar et al., 2014), and 'las Grutas de Cristal', hereafter known as Molinos cave (Teruel) (Moreno et al., 2014; Muñoz et al., 2015; Moreno et al., 2017). The objectives were the understanding of the present-day processes controlling the rainfall isotopic features and the resulting calcite precipitation, and the interpretation of the paleoclimatic signature recorded in the speleothems.

Similarly, in 2011 another cave located in the Pyrenees known as Seso Cave was selected for a PhD thesis focused on the geomorphic approach to the speleogenesis, the study of the present-day precipitates and the reconstruction of the paleoclimate since last 13 kyr (Bartolomé, 2016). Simultaneously, a recognition of speleothem records for paleoclimatic reconstructions and monitoring studies were carried out in different caves located in the South-central Pyrenees ('5 de Agosto' and 'Pot au Feu' caves in Cotiella massif, 'Trucho', 'Osos','Gloces', 'Arnales', 'Manatuero', 'B1' and 'Molino de Aso', among others, in Monte Perdido massif.

Later, in 2012 another cave nearby to Molinos ('El Recuenco' or Ejulve cave) (Teruel) was visited to assess its paleoclimatic potential. That cave was selected as a likely candidate to investigate the past climate variations in an environment more controlled by Mediterranean influences than previously studied caves in the Pyrenees. The first study was centered on analyzing several features of the cave (geomorphology, present-day hydrology and precipitates, cave environmental parameters) and focusing on the potential of its speleothems to reconstruct past

climate conditions. Those preliminary results constituted a master thesis (Pérez-Mejías et al., 2013) that later would lead to the present PhD thesis.

In January of 2013, a wide monitoring survey was started in Ejulve cave, establishing the basis of a longer monitoring program. During 2014 and 2015, several speleothems were sampled and dated in the Department of Earth Sciences, University of Minnesota, under the supervision of Prof. Larry Edwards. The preliminary chronologies of the speleothems from Ejulve cave were very promising. Conversely to Seso or Molinos Cave that mostly exhibited speleothem growth during the Holocene, older periods were recorded in clean and unaltered speleothems from Ejulve cave. Specifically, these new speleothems covered periods such as the climate Termination III (T-III) during the transition from MIS 8 to MIS 7, the end of the interglacial and the Last Glacial inception during MIS 5, and several stadials and interstadials during MIS 4 and MIS 3.

Hence, Ejulve cave offered the possibility to study in depth some abrupt climate changes that are scarcely identified in other sequences in Iberia, and especially in the terrestrial records. The lack of previous studies in caves of the IP covering these periods gave us the possibility to explore for the first time the terrestrial response to those abrupt changes. This is especially important for some periods not described in detail in Europe, as in the case of the T-III or some Heinrich events such as Heinrich 6 making Ejulve records of great originality and interest.

Therefore, the results we present do not have only important implications in the regional scale of the IP, but continental and beyond, due to the significant climate teleconnections (e.g. changes in North Atlantic sea surface condition triggers changes in the precipitation over the IP as well as modifies the Asian Monsoon intensity -*see chapter 6*-). The position of the IP, closer to the Atlantic Ocean than other records in Europe and Asia, and therefore less prone to complex fractionation processes in the $\delta^{18}O$ through the air mass trajectories -*see point 1.5.2, chapter 1*-, has been revealed as a key area to the study of the abrupt changes that took place in the North Atlantic.

In this line, the effort to make high-resolution records with highly-resolved chronologies from Ejulve cave would contribute to a better understanding of the mechanisms behind those climate changes, some of them with a global impact (e.g. Heinrich events). The knowledge of the climate response to the abrupt changes and the proxy data obtained would improve the climatic models that simulates the response of the climate to the changes. The climate models could reproduce the interaction between different climate components (atmosphere, ocean,

cryosphere…), and allow to test whether the output data from the model constitutes a feasible picture of the climate attending to the analysis of the proxies and the variables introduced in the model. The better set the climate model would be the better prediction will be conducted for future climate changes.

1.2. Research goals

The main goal of the present dissertation is to provide accurate and high resolution reconstructions of past abrupt climate changes though the multi-proxy study of speleothems from Ejulve cave. To accomplish that objective, it is needed to assess the current speleothemic dynamics relating to the environmental conditions and features of the carbonate precipitated. Additionally, it results significant to contextualize the stalagmitic deposits in the epigenic speleogenetical evolution of the cave. In this line, several specific goals should be achieved:

1. Speleogenesis:
   - 1.1. Establish the origin and development of Ejulve cave (including the study of special precipitates and morphologies).
   - 1.2. Identify tentative phases of speleothem growth attending to the relative geomorphic position of the fossil speleothems and other clastic deposits.
   - 1.3. Define and characterize the stages of development of the cave.

2. Current speleothemic dynamics (monitoring survey):
   - 2.1. Analyze the factors that control the $\delta^{18}O$ of the rainfall in the area.
   - 2.2. Understand the present-day transference of the $\delta^{18}O$ from the rainfall to the farmed calcite.
   - 2.3. Study of the pattern of isotopic variability in both drip waters and calcite precipitates.
   - 2.4. Evaluate the mechanisms behind the $\delta^{13}C$ variability.
   - 2.5. Test the applicability of the factors that explain the isotopic variability in the present-day precipitates to infer past climate variations.

3. Paleoclimatic reconstruction:
   - 3.1. Establish absolute chronologies using the U-Th method for the tentative phases previously identified of speleothem growth, focusing on samples that would exhibit growth during periods with potential abrupt climate changes.

- 3.2. Understand the processes that explain the $\delta^{18}O$ and $\delta^{13}C$ variability in the samples of this cave.

1.3. Research strategy

Every cave system is unique and the use of different methodologies is necessary to fully comprehend its origin and evolution, its response to environmental variables and its sensitivity to record past climate variations. The speleogenetic study of the cavity is not critical to do paleoclimatic inferences from its records, but represents an important additional information. Understanding the geological setting of Ejulve cave give us more information to understand the origin and development of the cave including the epigenic evolutionary stage responsible of the studied stalagmite records. That was the approach used for the **speleogenetic study** of Ejulve cave, accounting the specific goals 1.1, 1.2, and 1.3 and will be explained in the *Chapter 4*.

The dominant processes controlling the $\delta^{18}O$ and $\delta^{13}C$ frequently cannot be extrapolated to other caves. For this reason, every cave exhibits different sensitivity to climate and the speleothem records may show differences in how they record the climate signal. On that basis, understanding the present-day processes in the cave is a must to carry out confident paleoclimate reconstructions from speleothems (Genty et al., 2014; Riechelmann et al., 2017; Pérez-Mejías et al., 2018). Moreover, the $\delta^{18}O$ in mid-latitudes such as our study area may be affected by several factors, making the interpretation more complex (Scholz et al., 2012; Moreno et al., 2017; Pérez-Mejías et al., 2017). Therefore, the most suitable approach to understand the signal encoded in the speleothem isotopes is through a complete **monitoring survey** of Ejulve cave, accounting the specific goals 2.1, 2.2, 2.3, 2.4 and 2.5. This will be explained in the *Chapter 5* of this dissertation. After all, paleoclimatic interpretation relies ultimately on the use of the present or recent instrumental records as the key to the past (NRC, 2002).

Before any consideration of the speleothems as paleoclimatic archives, the main goal of the present dissertation, other previous analyses are necessary. In a first step, the petrographic analysis of textures and fabrics is very useful to give us information about the conditions of the carbonate

deposition and how the CO_2 degassing was produced during the precipitation process (Frisia et al., 2002). This is important to evaluate whether the equilibrium conditions were reached during the calcite precipitation (see below). Fabrics such as columnar are clear evidence of quasi-equilibrium precipitation (Frisia et al., 2000). In addition, the study of mineralogy and fabrics results indispensable to evaluate whether the original signal contained in the stalagmite has been altered by diagenesis. Any alteration may modify any hypothetical original environmental signal. The diagenetic transformation affecting the primary aragonite in open system conditions can introduce modifications in the timing of the deposition provided by the U-Th dating series (Ortega et al., 2005; Lachniet et al., 2012) but also in the paleoenvironmental signals derived from stable isotopes (Martín-García et al., 2009; Hopley et al., 2009; Zhang et al., 2014; Domínguez-Villar et al., 2017) and trace elements (Martín-García et al., 2009; Hopley et al., 2009; Domínguez-Villar et al., 2017).

Once discarded diagenetic processes, the second step is to obtain a reliable age model for the speleothem growth. In a close system of calcite precipitation, an accurate chronology depends mainly on the initial uranium concentration and the proportion of thorium external to the system (detritical thorium). These conditions will be further explained in the *subpoint 1.5.1*.

The third step is to test whether the carbonate has precipitated in equilibrium. Traditionally, the Hendy test was used for this purpose (Hendy, 1971), although the result of this test does not necessary indicate kinetic fractionation or evaporation (Lauritzen and Lundberg, 1999). In fact, the Hendy test makes the assumption that the covariation between $\delta^{18}O$ and $\delta^{13}C$ responds to kinetic effects, underlying the argumentation that speleothem $\delta^{13}C$ values are not linked to climate and both $\delta^{18}O$ and $\delta^{13}C$ cannot respond with a common signal to climate. Hence, a more confident method is the replication of the isotopic profile from two or more stalagmites (Dorale and Liu, 2009). Unfortunately, it cannot be accounted frequently. In that regard, it is also useful to model the $\delta^{18}O$ through the equations of precipitation in equilibrium, comparing the $\delta^{18}O$ of the dripwaters with the $\delta^{18}O$ of the calcite and the cave temperature (Friedman and O'Neil, 1977; Kim and O'Neil, 1997; Coplen, 2007; Tremaine et al., 2011). However, the existence of disequilibrium effects does not necessary cancel the climatic signal of the isotopes, since in some cases could amplify the climatic signal encoded in the speleothems in seasonal timescales (Pérez-Mejías et al., 2018). Therefore, an adequate understanding of these processes in case-by-case is extremely recommended.

In any case, the comparison with other existent paleorecords, including different proxies is a must. Likewise, working at different scales from a local/regional to a continental/global is more than recommended to evaluate confidently the record we are working on. Whether our record exhibit a signal seen previously in other areas, or conversely exhibit a different behavior, carefully explanation of why such records match (or not) is required. In this regard, the identification of the climate processes behind that signal should be always explored. A multiproxy approach using different paleoarchives (e.g. marine cores, ice, speleothems…) to identify such climate processes is strongly recommended. In this regard, this **paleoclimatic approach** will be successful to account the main goal of the dissertation and the specific goals 3.1, 3.2 and 3.3 (see below), and will be carried out in the *Chapter 6*.

On the basis of the proposed research strategy, the present dissertation is structured as follows. The present *Introduction (Chapter 1)* including the objectives of the research, the method used to reach these objectives (Research strategy), and a brief state-of-the-art of the discipline, in this case focused in the abrupt climate changes and the potential of the speleothem records to perform paleoclimatic inferences. The followings chapters are the presentation of the *Study area (Chapter 2)* and the *Methodology* used during the research *(Chapter 3)*. From this chapter onwards, the main part of the dissertation is dedicated to the results and discussion to achieve the goals explained above, starting with the *Speleogenesis (Chapter 4)*, followed by the *Present-day speleothemic dinamics (Chapter 5)* and ending with the main point of this dissertation, the *Paleoclimatology (Chapter 6)*, subdivided in two points, the first dedicated to the Termination III and the second, for the interval MIS 5 to MIS 3. The dissertation will be closed with the last chapter of the *Epilogue (Chapter 7)*, highlighting the conclusions of the study *(7.1)* and the future perspectives *(7.2)* that appear at the end of the present thesis.

1.4. Abrupt climate changes

1.4.1. Theoretical background

During the 90´s, there was a change on the paradigm to understand the climate changes. The switch from the dominant view of the slow and gradual swings paced by orbital parameters, to the abrupt changes in the Earth climate system in a short interval of time (decadal-centennial scale) was revolutionary. The biggest innovation relies on the concept that the climate (abrupt) change occurs as discrete jumps in the system, once a determinate threshold is exceeded. This new concept has triggered the scientific and social alarm respecting to present-day global warming since the consequences of a hypothetical threshold exceeded are yet unknown.

However, the abrupt changes are not only characteristic of the climate system, in fact they can be seen in other simple physical systems. In order to understand how this paradigm works, a mechanical analogy can be found in Fig. 1.1, extracted from a report of the National Research Council (NRC) of the USA (2002). That system is composed by a balance with two curved cups poised on a fulcrum, and one ball. There are three points of "equilibrium" (a, b, c) in the top of the figure, although the point "b" is rather unstable.

Now suppose we push down the right cup causing a slight tilt (position a1) and we let it go. The ball would roll within the left cup for a while, until the ball stops due to the friction and the system return to its original state. *That is the response of the system to the small perturbations*. Now imagine that we push again the right cup farther down (position a2), the ball will roll over the fulcrum, and would roll through the other side of the balance, reaching a new state of equilibrium. *That is the response of the system when a determinate threshold is exceeded*. The analogy with the climate system is obvious. Furthermore, the report of the NRC was further in explaining the similitudes between both systems, and the difficulties that entail the paleoclimate research.

Following with the analogy, now imagine that you have never seen that balance, and it is hidden in another room. You don't know about the hand that set the things in motion, and you try to figure out the behavior of the system only listening the sounds that the device causes with every movement. Unfortunately, you are listening it from an old gramophone, and some recordings are badly scratched, some parts are lost or garbled. *That is in some way the paleoclimate research*.

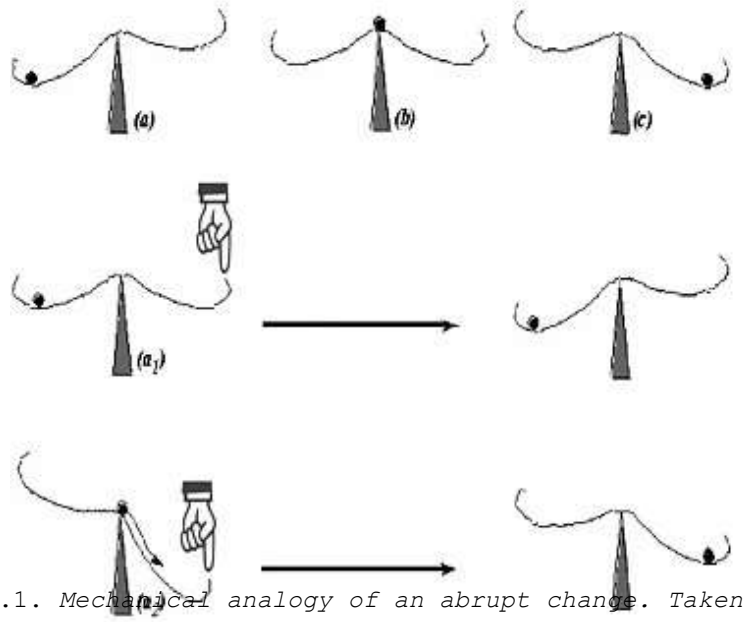

Fig. 1.1. *Mechanical analogy of an abrupt change. Taken from the* NRC (2002).

We could now apply that paradigm directly to an example from the Earth system, such as the proposed by Stocker and Marchal (2000) for the ocean circulation (Fig. 1.2). The oceanic currents cause geographic differences in the supply of heat to the atmosphere, with high mean surface temperatures (SST) in the North Atlantic compared with the Pacific at the same latitude (Macdonald, 1998). In the case of the Atlantic, the Gulf Stream is the responsible of moving warm and saline tropical waters to higher latitudes. Those waters release the heat to the atmosphere, become denser and sink into the deep, conforming a location for deep water formation. The Atlantic Meridional Overturning Circulation (AMOC) is prone to instabilities if the flow of tropical waters to higher latitudes decreases, for example in a climate situation of increased ice melting or increased river runoff, both processes that would decrease salinity. Hence, the density of these waters will be lower, and won't be longer able to sink, stopping, or reducing, the thermohaline circulation.

In a similar way to the previous mechanic example, this ocean-atmosphere system exhibit more than one stable equilibrium as a response to perturbations in the freshwater balance. In fact, the multiple equilibrium points are a feature of the nonlinear systems, such as the Earth climate. If we look into the Fig. 1.2, the system reacts linearly if the freshwater input does

not cross a determinate threshold (situation a). However, an abrupt change occurs in the SST in a scale not seen previously, if the freshwater input is enough to cross the threshold (situation b). Now, if the input ceases, the system could go back to the original state. However, if exists other equilibrium position, the system will reach it (situation c).

A good definition of an *abrupt climate change* can be found in the report from the NRC, (2002) "*An abrupt climate change occurs when the climate system is forced to cross some threshold, triggering a transition to a new state at a rate determined by the climate system itself and faster than the cause. Chaotic processes in the climate system may allow the cause of such an abrupt climate change to be undetectably small*". Therefore, the nonlinear response is a key concept for a better approach to understand the Earth climate system.

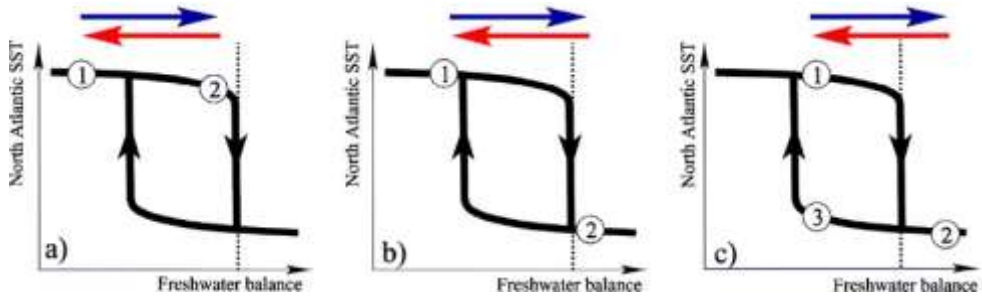

Fig. 1.2. *Ocean-atmosphere nonlinear system. Different responses are possible depending on the input of freshwater: a) linear, reversible; b) nonlinear, reversible, c) nonlinear, irreversible. Taken from Stocker and Marchal (2000).*

The *triggering factors* of an abrupt climate change are numerous, and in the case of the forcings that are external to the system, the timing vary between fast (e.g. outburst flood, volcanic eruption), slow (continental drift, orbital forcing) and somewhere between them (human-produced greenhouse gases). The forcing can be also internal, i.e. the change comes from any part of the climate system itself (e.g. changes in the tropical ocean-atmosphere dynamics could propagate regional changes to global consequences). Sometimes the mechanisms are chaotic and multiple triggers may contribute (Alley et al., 2003). One paradigmatic case of multiple forcing is the ENSO phenomena, combining sea-level pressure, wind intensity, sea surface temperature, surface air temperature and total cloudiness. Therefore, the trigger mechanism that push the system across a threshold, could be a fast mechanism usually

external to the system or just the accumulation of gradual forcings within the system.

Likewise, it is worth noting the concept of *amplifier*, that produce large changes with minimal forcing (Alley et al., 2003). For example, the cooling increases the snow coverage, thus increasing reflection of the incoming solar radiation (albedo) and causes further cooling. In other example, the reduction of the forest cover reduces the evapotranspiration, that is important in many continental regions as a fraction of the moisture that leads to precipitation, thus reinforcing the drought (Kutzbach et al., 1996).

There are also *sources of persistence* in the system, that reinforce the effect of the amplifier (Alley et al., 2003). If there is a long enough period of snowfall on pole lands, an ice sheet may reach enough thickness that the melting is unlikely compared with a weakened ice sheet. In other example, the loss of vegetation reduces the ability of root to capture water and to keep protected the soil, allowing the precipitation and runoff to increase the erosion and soil loss, leading to desertification. Therefore, both amplifiers and sources of persistence are known as *feedbacks*, that sometimes are not easy to identify or could be over/underestimated, making the climate system complex to predict. This complexity arises from the interactions of simple components (atmosphere, biosphere, cryosphere, hydrosphere, lithosphere) that stablish complex feedbacks and interactions between them.

1.4.2. Some examples of abrupt climate changes

Great examples of abrupt climate changes can be found during the *last glacial cycle*, such as a glacial Termination, the D-O cycles or the Heinrich events, and more recently the Younger Dryas (YD). Some paleorecords highlight the fast occurrence of the changes. For example, the annually-resolved resolution of the ice cores in Greenland revealed the timing during the YD, with a cooling during few decades and a warming at the end in one large step of about 8 °C in 10 years, accompanied by a doubling of snow accumulation in 3 years (Alley et al., 1993; Alley et al., 1995; Alley, 2000). Proxies such as δD, deuterium excess, mean particle size or non-sea salt calcium exhibited changes in less than 5 years (Taylor, 1997). In the continental domain, the YD exhibited an abrupt increase in the storminess during the autumn to spring seasons, from one year to the next (Brauer et al., 2008) through a gradual transition of about 350 years to reach a more humid period (M Bartolomé et al., 2015).

A noticeable example of abrupt change and big spatial differences in timing in different systems of the climate, is seen during the D-O oscillations. Those events are characterized by abrupt warmings and gradual coolings, followed finally by a more abrupt cooling. The duration of the interstadials (from Greenland Interstadials -GI- 3 to GI17) is of average 802 ± 79 years in the studies of the surface of the North Atlantic, compared with the 39 ± 4 years in the ice cores from NGRIP (Rasmussen et al., 2016). In the terrestrial record the response to D-O is variable, with records that exhibit sensitivity to those changes (e.g. Genty et al., 2003; 2010) and others without any climatic response (e.g. Arienzo et al., 2015).

A different example of abrupt climate change is the transition from a glaciation to an interglacial period, what is called Termination. Those changes are orbitally-paced, hence linked to the changes in Milankovitch cycles, but with a determinant influence of some internal climate mechanisms, such as the fluxes of heat and carbon that drives the atmospheric CO_2, that are influenced by the meltwater entering in the North Atlantic (Cheng et al., 2009). This is an example of the complex links between the oceanic and atmospheric circulation, that also could trigger abrupt changes during the timing of a orbitally-paced Termination (Cheng et al., 2009; Moseley et al., 2015; Pérez-Mejías et al., 2017).

Likewise, abrupt climate changes occur also during *interglacial* times. Notable examples can be found in the Holocene such as the 8.2 kyr event or the Little Ice Age. In this time, the studied paleorecords also underscore the fast occurrence of the events. The 8.2 event was especially abrupt and coeval between areas, with absolute chronologies between different records at hemispheric scale stablishing a difference

of only ±4 years (LeGrande et al., 2006; Kobashi et al., 2007) and a fast response of the vegetation on central Europe in less than 20 years (Tinner and Lotter, 2001). The precise reconstruction of the timing in Greenland showed that took less than ~20 years to reach the coldest period, with a drop of 3.3 ± 1.1 °C. After ~60 years of maximum cold, the climate recovered the state before the event, only in ~70 years (Kobashi et al., 2007).

Despite the Holocene holds a more stable climate than during last glacial cycle, some abrupt changes have revealed devastating effects over some past human communities. For example, the end of the maya civilization occurred in an interval of ~200 years with several episodes of drought, around 800 to 1000 A.D (Medina-Elizalde and Rohling, 2012). In the same line, a prolonged drought persisting for ~300 years around 4025 ± 150 yr BP, triggered the collapse of the Akkadian empire (Cullen et al., 2000). Despite the sophisticated culture that controlled Mesopotamia had implemented grain-storage and water-regulation technologies (Weiss et al., 1993), the society were vulnerable to such prolonged droughts and finally abandoned that area after four centuries of settlement (Weiss et al., 1993).

It is evident from many past examples that abrupt climate changes had important consequences in human societies. We as society are aware of the negative impact of present-day abrupt climate change – the global warming – but still need to further work on the strategies to mitigate it and/or adapt our life style to future climate.

1.4.3. Abrupt climate records at a regional scale: the Iberian Peninsula

This section presents a regional approach to the state-of-the-art of the abrupt climate changes, first articulated in the Iberian Peninsula and Iberian Margin (maritime) area, and later more specifically focused on the NE Spain, with special interest on the Iberian Range and the Pyrenees. The marine sequences obtained from the Iberian Margin and the Alborán Sea (Cacho et al., 1999; Combourieu Nebout et al., 2002; Goñi et al., 2002; Moreno et al., 2002; de Abreu et al., 2003; Fletcher and Sánchez Goñi, 2008; Sánchez-Goñi et al., 2008; Combourieu Nebout et al., 2009; Naughton et al., 2009; Pena et al., 2010) and Western Mediterranean (Sierro et al., 2005; Frigola et al., 2008) marked the sensitivity of the IP to abrupt climate changes in North Atlantic. Generally, those records do not go beyond 40-50 kyr with accurate chronologies. In the continental realm, the lacustrine sequences exhibited clear response to rapid climate changes during last glacial cycle, such as Fuentillejo maar, Banyoles Lake, Estanya Lake and El Portalet peatbog (Valero-Garcés, 1999; González-Sampériz et al., 2006; Morellón et al., 2009; Vegas et al., 2010). The speleothem records from the IP recorded emblematic abrupt changes, such as those occurring during Termination II (Stoll et al., 2018), the end of the Eemian (Muñoz-García et al., 2007), Heinrich events (Moreno et al., 2010), the Younger Dryas (M Bartolomé et al., 2015; Rossi et al., 2018) and the 8.2 ky event (Domínguez-Villar et al., 2009).

Only three records with evidences of abrupt climate change are located in NE Spain, concretely in the Pyrenees: Seso Cave (M Bartolomé et al., 2015), Estanya Lake (Morellón et al., 2009) and the Portalet sequence (González-Sampériz et al., 2006). No studies of abrupt climate changes have been reported previously from the Iberian Range. The present thesis will improve the knowledge of the response of the terrestrial records from the IP to the abrupt events, through the study of new periods in the past with abrupt changes never reported before in this area. The novelty of this work goes further, presenting sequences unique in Europe such as the Termination III, than in contraposition to T-I and T-II, is poorly known (Pérez-Mejías et al., 2017) or the long time series with a clear response to Dansgaard-Oeschger cycles, including the Heinrich events 4, 5 and 6 (Pérez-Mejías et al., submitted.).

One of the big challenges to evaluate the abrupt climate changes is the lack of independent and highly-resolved chronologies to estimate correctly the timing of the changes and leads and lags between records. The long lacustrine-marine sequences are limited in chronology by the ^{14}C method, while in some cases the existence of tephra layers enable the

construction of independent chronologies beyond the ^{14}C limits (Martin-Puertas et al., 2014; Wolf et al., 2018).

In this regard, the speleothems could be a powerful tool to develop independent chronologies during periods that features high uncertainties with the present age models and the limitations of the dating methods.

1.5. The science behind the speleothems

The use of the speleothems to infer past climate conditions has been proved as a powerful approach. We identify the potential of the speleothem records mainly in two points: firstly, the crucial advantage of the elaboration of independent chronologies with low age uncertainties in comparison with other paleorecords (section 1.5.1), and secondly, the sensitivity of many proxies measured in speleothems directly linked to environmental and climatic changes (section 1.5.2). However, the interpretation of the proxies (mainly the $\delta^{18}O$ and $\delta^{13}C$) is not straightforward, but controlled by site-specific factors, so they need to be carefully explored. The understanding of all the processes that affect the isotopes is essential to carry out paleoclimate inferences.

1.5.1. Absolute datings

The outstanding independent chronologies that are reached in some speleothem records are explained by the great potential of the U-Th method. The ^{14}C use in speleothems is problematic due to the various contribution of the carbon from the bedrock together to that derived from plant roots and soil microbial activity, as well as the organic matter from the soil (Genty et al., 1999; Genty and Massault, 1999; Genty et al., 2001a). Only in limited times can be used, such as in recent speleothems to determine the peak in ^{14}C reached in the atmosphere consequence of the nuclear bomb tests (Genty et al., 1999; Genty and Massault, 1999; Mattey et al., 2008).

The basis of the U-Th method relies on the transport of the uranium (U) to the speleothem via groundwaters, and in a close system, decays radioactively to other daughter isotopes. The ^{238}U decays by alpha emission (half-life (t1⁄2) = 4.47×10^6 kyr) to ^{234}Th (t1⁄2=24 days), which decays by beta emission to ^{234}Pa (t1⁄2=6.7 hours) (Edwards et al., 2003), which decays to ^{234}U, with a much longer half-life (245.3 kyr) (Cheng et al., 2000) which decays by alpha emission to ^{230}Th (t1⁄2=75.7 kyr) (Cheng et al., 2000). Hence, for the carbonate dating, the interesting nuclides are ^{238}U, ^{234}U and ^{230}Th, discarding the others with a too short half-life.

This method can be used, in principle, in samples until 600 kyr (Edwards et al., 1987), although the precision deteriorates beyond 400 kyr. Two are the potential issues: first, the amount of initial ^{238}U in the stalagmite, and second, the addition of thorium external to the decay system (known as 'detrital' Th),

transported with organic matter, colloidal material and sediments. Additionally, a fundamental issue is the ability to quantify the initial amount of the daughter isotope, enabling a determination of the relative fractions of radiogenic and initial daughter. Hence, the age is calculated from the amount of radiogenic daughter. Ideally, there is no need of correction if the initial amount of 'detrital' daughter is negligible. In other cases, the correction can be done estimating the initial ratio of the daughter isotope to a stable isotope of the same element as the daughter (Edwards et al., 2003).

Historically, the precision of the measurements has changed significantly. In earlies 60 and until 80s decades, the alpha-spectrometry needed large sample size and large counting times. The basic problem was the limit of the fraction of atoms that can be detected by decay counting techniques given the large difference between the half-lives of the nuclides (hundreds of thousand years) and the counting times of the laboratory (a reasonable time of weeks). The solution was the development of mass spectrometric methods, that obviate the need to wait for the nuclides to decay, as mass spectrometers detect the atoms of interest directly, in this case the ^{234}U and ^{230}Th (Chen et al., 1986; Edwards et al., 1987). Hence, around the 90s, thermal ionization mass spectrometry (TIMS) improved several issues from the alpha spectrometry, with better analytical precision at the two extremes of the dating range, i.e. young and old ages (Edwards et al., 1987). These developments in the ^{230}Th and ^{234}U measurements were analogous to the accelerator mass spectrometer techniques for ^{14}C analysis. Recently, the multi-collector inductively coupled plasma mass spectrometry (MC-ICP-MS) has decreased again the sample size needed for the analysis and the chemistry preparation has been simplified (Cheng et al., 2013). In some examples, the magnitude of the reduction in analytical uncertainty is really outstanding (Cheng et al., 2009).

Beyond the chronology reached by the U-Th, a recent method is trying to target older periods through the U-Pb. New improvements have been carried out with the use of MC-ICP-MS, being able to do the analysis with samples with low Pb concentrations, however, some problems remain still unsolved (Woodhead and Pickering, 2012). The main issue is the need to apply a correction for initial isotope disequilibrium in the U-series decay chain for relatively young samples (less than 5 Ma). Depending on the stalagmite, especially if the waters exhibit non-equilibrium $^{234}U/^{238}U$, these corrections can shift the U-Pb age by several hundred thousand years (the time required for the U-series daughter products to reach equilibrium), thus increasing the uncertainty. Still, there is no universal strategies for these corrections (Woodhead and Pickering, 2012).

1.5.2. The $\delta^{18}O$ in the hydrological cycle

There are several processes that control the $\delta^{18}O$ on its pathway from the ocean to the speleothem carbonate, through the atmosphere, hydrosphere, soil and epikarst zone. The processes are associated with phase changes (e.g. from liquid to vapour) (Dansgaard, 1964). During these changes, one isotope is favored against the other attending to the differences in the atomic mass, known as *fractionation*, that may be either equilibrium or kinetic (Dansgaard, 1964; Rozanski et al., 1993; Clark and Fritz, 1997; Lachniet, 2009). The kinetics represents disequilibrium conditions that may modify the original climatic signal. Here, the processes affecting the $\delta^{18}O$ are going to be summarized (Fig. 1.3), merged in two different groups: first, atmosphere and hydrosphere, and second, the soil, epikarst and cave environment.

a) Atmosphere and hydrosphere

When the water is evaporated from the ocean, the fractionation favors the isotopes with less atomic mass (light isotopes), hence, less ^{18}O is incorporated into the vapor. The result is a vapor with lower $\delta^{18}O$ than the ocean. The equilibrium fractionation between liquid and vapor was calculated by Clark and Fritz (1997), giving as a result a vapor formed from mean ocean water (hence, $\delta^{18}O$ = 0 ‰ SMOW) with a value of -9.34‰ SMOW with a temperature of 25 °C. In the atmosphere, the condensation of vapor to liquid favor the isotopes of higher atomic mass (heavy isotopes), hence, more ^{18}O is preferentially incorporated to the liquid phase. As a result, the $\delta^{18}O$ of the rain will be higher than the remaining vapor. Moreover, to condense more moisture into the liquid phase, the temperature must decrease. With colder temperatures, more water moisture can be removed from the air mass, due a strong fractionation. The progressive condensation and decrease in the $\delta^{18}O$ of the precipitation is known as *Rayleigh distillation* (Clark and Fritz, 1997; Sharp, 2007; Lachniet, 2009).

As the fractionation is temperature-dependent in a well-known relationship, there is a positive correlation between $\delta^{18}O$ and temperature, known as *temperature effect*, with a slope that may vary in time and space (Dansgaard, 1964; Rozanski et al., 1993). Associated with both temperature effect and Rayleigh distillation, when the air mass is decreasing its temperature and increasing the fractionation vapor-liquid when is lifting over a orographic barrier, is known as *altitude effect* (Clark and Fritz, 1997). Also linked to the Rayleigh distillation, the more distance is crossing the air mass, the lower $\delta^{18}O$ will exhibit. This process is called the *continental effect* (Dansgaard, 1964; Rozanski et al., 1993; Clark and Fritz, 1997).

However, when the air mass is over the continent, this effect could be counteracted by the recycled continental moisture that is going back to the atmosphere, due to the evaporation of waters from soils, lakes and rivers, and exhibit high $\delta^{18}O$ (Koster et al., 1993).

Likewise, it is worth noting the origin of the moisture source, attending to regional differences in $\delta^{18}O$ and temperature in the oceans (LeGrande and Schmidt, 2006), known as *source effect* (Rozanski et al., 1993; Clark and Fritz, 1997). In our study area, the masses from the Atlantic exhibit lower $\delta^{18}O$ than those with Mediterranean origin (Celle-Jeanton et al., 2001; Vandenschrick et al., 2002; Moreno et al., 2014). This effect is not constant in time due to the variations of the $\delta^{18}O$ of the ocean during glacial-interglacial scales. As the evaporation takes preferentially the lighter isotopes, the $\delta^{18}O$ of the ocean is accumulating higher $\delta^{18}O$ as the ice in the continents in increasing (lower $\delta^{18}O$), it is known as *ice volume effect* (Lachniet, 2009). The variation of the $\delta^{18}O$ is around ~1.2 ‰ during the periods of maximum ice volume (Bintanja et al., 2005; Sharp, 2007).

Derived from all the effects presented above, we could argue that the $\delta^{18}O$ values are determined by the season in which the air mass has been originated. Likewise, the temperature in the source area will be determinant, therefore it is expected than the precipitation in winter would exhibit differences in the $\delta^{18}O$ compared with that in summer. Moreover, the precipitation in winter may come from a different source area relative to the precipitation in summer. Those changes are englobed in another effect known as *changes in seasonality* (Denton et al., 2005). During the period of higher temperatures, if the atmosphere has low relative humidity, the drops could be affected by *evaporation* in the cloud base and before reaching the ground in a process out of equilibrium, leading to a precipitation with higher $\delta^{18}O$ (Rozanski et al., 1993). Changes in seasonality also may imply a different *air mass history* that is unique for every air mass (Rozanski et al., 1993), and could be studied through the dominant synoptic patterns of precipitation and/or the air mass trajectories (Krklec and Domínguez-Villar, 2014; Moreno et al., 2014). Finally, during the process of raining there is a decrease in the $\delta^{18}O$ when the rainfall amount is increased, a process dominant in tropical regions, known as *amount effect* (Dansgaard, 1964; Rozanski et al., 1993; Risi et al., 2008). However, this effect has been also documented in extra-tropical areas (Bar-Matthews et al., 2003).

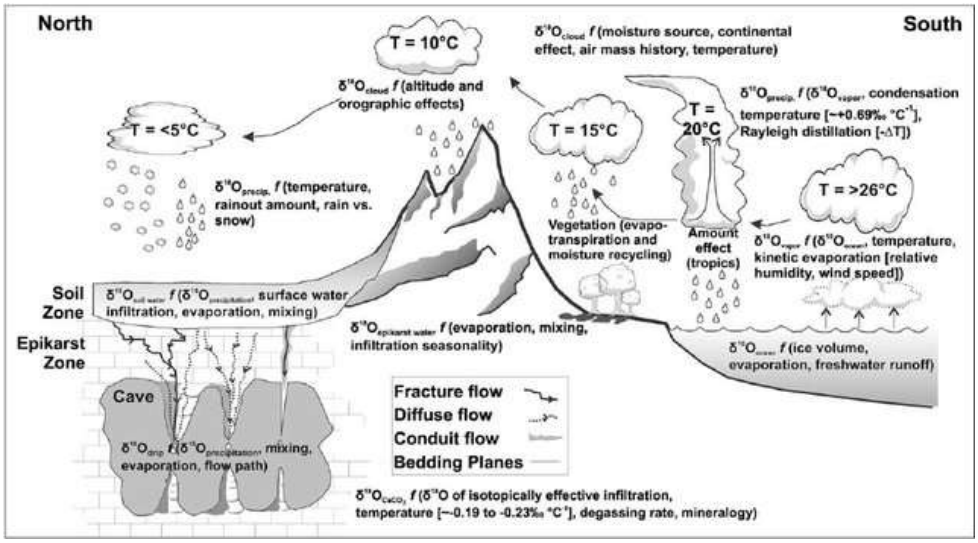

Fig. 1.3. *Primary processes affecting the* $\delta^{18}O$ *in the hydrological cycle. Extracted from* (Lachniet, 2009).

b) Soil, epikarst and cave environment

When the rainfall arrives to the soil, some water can be evaporated, leading to higher $\delta^{18}O$ in the infiltrated waters (Clark and Fritz, 1997). In these cases, typical of dry climates, the mean $\delta^{18}O$ of the drip waters will be higher compared with the weighted mean precipitation, around ~1 ‰ higher in some cases (Ayalon et al., 1998). In contrast, infiltration of lower $\delta^{18}O$ waters may be favored in climates with intense precipitation concentrated in time, or with a *selective infiltration* biased to the winter rainy season, resulting in lower drip water $\delta^{18}O$ than the weighted mean precipitation (Mickler et al., 2006; Wackerbarth et al., 2010). Generally, there is a smoothing of the isotopic signal when a *mixing of different infiltration waters* occurs (Jones and Banner, 2003; Cruz et al., 2005b). When the infiltration waters reach the cave system, the *evaporation* of the drip waters may be important in well ventilated caves. Likewise, some spatial $\delta^{18}O$ variability can be seen within the same cave, attending to the *drip rate discharge* (Baldini et al., 2006).

Calcite precipitation is a cave-temperature dependent process (Friedman and O'Neil, 1977; Kim and O'Neil, 1997; Coplen, 2007; Tremaine et al., 2011) and isotopic equilibrium should be reached between water and the carbonate phases to preserve the original $\delta^{18}O$. That equilibrium is favored when sufficient time is available for the isotope exchange reactions

(Sharp, 2007). In conditions of fast or *enhanced CO_2 degassing*, the equilibrium cannot be reached (Hendy, 1971). The CO_2 degassing depends on the gradient between the drip and the cave atmosphere. Large pCO_2 gradients favor rapid degassing, resulting in higher $\delta^{18}O$ values in the carbonate (Hendy, 1971).

However, the equilibrium fractionation depends also on the *carbonate mineralogy*, with different fractionation factors between aragonite and calcite. Under equilibrium conditions, aragonite should have $\delta^{18}O$ values higher than calcite at 25 °C (Kim et al., 2007). Generally, during the precipitation there is a preferential incorporation of ^{18}O in the carbonate (Sharp, 2007).

1.5.3. The $\delta^{13}C$ and trace metals

The $\delta^{13}C$ is less affected by evaporative effects in the cave, compared with the $\delta^{18}O$ (Fairchild et al., 2006). However, may be affected by other kinetics, as the *enhanced CO_2 degassing*, that changes the $\delta^{13}C$ values in drip waters with an enhancement more than the double (Spötl et al., 2005) explained by the precipitation of isotopically heavy carbonate. In the moment of the precipitation, other kinetic effect would lead to an enrichment in ^{18}O and ^{13}C, as the fluid moved over the surface from the *point of impact* of the drip (Hendy, 1971).

The carbon isotopes usually reflect the balance between isotopically light biogenic carbon derived from the soil CO_2 and heavier carbon dissolved from the limestone bedrock (McDermott et al., 2006), with a clear prevalence of the biogenic carbon against the bedrock-derived in a ratio of 9:1 in most temperate caves (Genty et al., 2001a). In some regions, the carbon variability was interpreted as relative changes in vegetation (*C3 - C4 photosynthetic pathways)* (Dorale et al., 1992; 1998). The $\delta^{13}C$ in the stalagmites ranges typically between −14‰ to −6‰ in carbonates precipitated in equilibrium with CO_2 respired from C3 plants, and −6‰ to +2‰ for that from C4 plants (McDermott et al., 2006). Likewise, the $\delta^{13}C$ variability has also been ascribed to changes in the vegetation cover above the cave, with a variation in the mixing of the soil gas with the atmosphere, notable in such cases that the vegetation cover reaches (or decreases from) a 100% (Hellstrom et al., 1998). In temperate areas of Europe has been demonstrated the link between the production of soil biogenic CO_2 and the $\delta^{13}C$ variability (Genty et al., 2003; 2006; 2010; Pérez-Mejías et al., 2017). In such examples, the low $\delta^{13}C$ is in clear link with higher temperatures and more precipitation, supported by an increase in the soil biogenic CO_2 due to the more vegetation productivity (plant root respiration) and microbial activity. Conversely, the degradation of vegetation and soil will decrease the biogenic CO_2 production and increase the relative proportion of atmospheric CO_2, leading to higher $\delta^{13}C$ values.

There are other proxies that can be used for paleohydrology inferences. When the $\delta^{13}C$ correlates with enhanced ratios of some trace metals such as Mg/Ca or Sr/Ca, it could be a signal of carbonate precipitation upflow, known as Prior Calcite Precipitation (*PCP*) that produce high $\delta^{13}C$ values unrelated to changes in vegetation type or intensity (McDermott et al., 2006). This effect is in relation with the existence of pores and voids in the saturated zone of the epikarst, and therefore occurs when less infiltration is produced, therefore during drier periods. Due to the preferential dissolution of calcite

over dolomite, in general lower Mg/Ca ratios are found that those expected from the rock composition. Therefore, a higher *residence time* of the groundwater during drier conditions, would lead to higher Mg/Ca ratios by enhanced dolomite dissolution (Fairchild et al., 2000; Tooth and Fairchild, 2003; Musgrove and Banner, 2004). However, this mechanism is very slow and is likely to require residence times of months to years (Fairchild et al., 2006). In general, the relevance of this effect is also linked with the changes in the open/close system dissolution (Salomons and Mook, 1986) but has less importance of the $\delta^{13}C$ values, since the percentage of the carbon derived from the rock dissolution is ~10% compared with the ~90% coming from the soil CO_2 in most temperate caves (Genty et al., 2001a). In caves with a strong seasonal variation in temperature, it is expected to see those changes in the calcite Mg, since its partition coefficient is temperature-dependent (Roberts et al., 1998).

The $\delta^{234}U$ content in the drip waters (hence, in the speleothems) has been linked with the soil redox conditions, so an increase in soil organic matter and microbial activity would cause less uranium to be oxidized to the hexavalent state in which is soluble, leading to lower uranium concentration in the groundwaters (Hellstrom and McCulloch, 2000). Hence, an enrichment of the drip waters in ^{234}U due to the increased residence time of the waters, being used together with other proxies (e.g. $\delta^{13}C$, Mg/Ca) supports their use as a water availability and groundwater residence time proxy (Kaufman et al., 1998; Hellstrom and McCulloch, 2000; Polyak et al., 2012; Pérez-Mejías et al., 2017).

Therefore, the understanding of all those factors is crucial to reach the main goal of the present dissertation, aiding to the elaboration of confident climatic inferences using fossil stalagmites -*Chapter 6*- and discerning the climatic control on the isotopes in the rainfall and present-day precipitated carbonate -*Chapter 5*-.

‘The Universe is under no obligation to make sense to you’.

-Neil deGrasse Tyson

Chapter 2

Study area

Ejulve cave is located in the southeastern sector of the Iberian Range, an alpine mountainous structure with orientation NW-SE along NE Spain (Fig. 2.1.A). The Iberian Range delimits the southern border of the Ebro basin (Fig. 2.1.B and 2.2.A). The cave opens into Ejulve mountains, in the eastern side of Sant Just range, where is found the source of Guadalopillo river (Fig. 2.2.B) that constitutes the main drainage of the study area. This sector belongs to the county of Andorra-Sierra de Arcos in Teruel province. The coordinates of Ejulve cave are 40°45'34''N, 0°35'07''W, at 1,240 meters above sea level. The distances of the cave to some relevant locations are 2,3 km eastern of Majalinos peak (summit of Sant Just range in this sector, 1,601 m) and 3,5 km southwestern far from Ejulve village, while the distance to the Mediterranean Sea is 95 km.

2.1. Geological context

Geologically the studied area is framed in the Maestrazgo structural unit that belongs to the Iberian Range in the eastern central Iberian Peninsula (Fig. 2.1.B). The Maestrazgo unit is the easternmost sector of the Iberian Range and constitutes the connection with the Catalonian Coastal Ranges (Simón et al., 2002; Sopeña, 2004). The Iberian Range is a NW-SE trending double verging intraplate orogene (Simón et al., 2002) within the Iberian plate. It shows a moderate degree of deformation and thicker Mesozoic sedimentary record (Sopeña, 2004).

The Iberian Range is limited by the Ebro Basin to the north, the Central System and the Tagus Basin to the west, the Prebetic Range to the south and the Valencia Through to the east (Fig. 2.1.B).

The Iberian Range represents the uplift and compressive inversion of a Mesozoic extensional basin (Álvaro et al., 1979; Simón et al., 2002; Sopeña, A., 2004). The Mesozoic sedimentary sequences are made of shallow marine and continental deposits grouped in two evolutionary cycles, Late Permian-Middle Jurassic and Late Jurassic-Late Cretaceous, both composed of rift and post-rift stages (Simón et al., 2002; Sopeña, 2004).

Subsequent convergence of the Iberian and European plates caused the switch from extensional to compressional tectonic regime in the Iberian Basin producing the inversion of large normal faults active during the Mesozoic (Simón et al., 2002). The deformation resulted in two structural levels, the basement (Variscan basement, Permian and Lower Triassic) and the cover (Jurassic, Cretaceous and Tertiary, separated by a plastic detachment level (Middle-Upper Triassic). Both levels defined

the different compressional architectural styles of the Iberian Range (Simón et al., 2002; Sopeña, 2004).

After the compressional tectonic regime, a Neogene - Quaternary extensional stage composed of two phases at Late Miocene and at Pliocene-Quaternary can be distinguished related to the Valencia trough rifting (Simón et al., 2002). The end of the Late Miocene stage involves the development of extensive planated areas conforming the Main Planation Surface of the Iberian Range (Peña et al., 1984; Gutiérrez et al., 2008). In addition, the Pliocene-Quaternary extensional stage produced some of the most significant morphotectonic features of the Iberian Range (Gutiérrez et al., 2008).

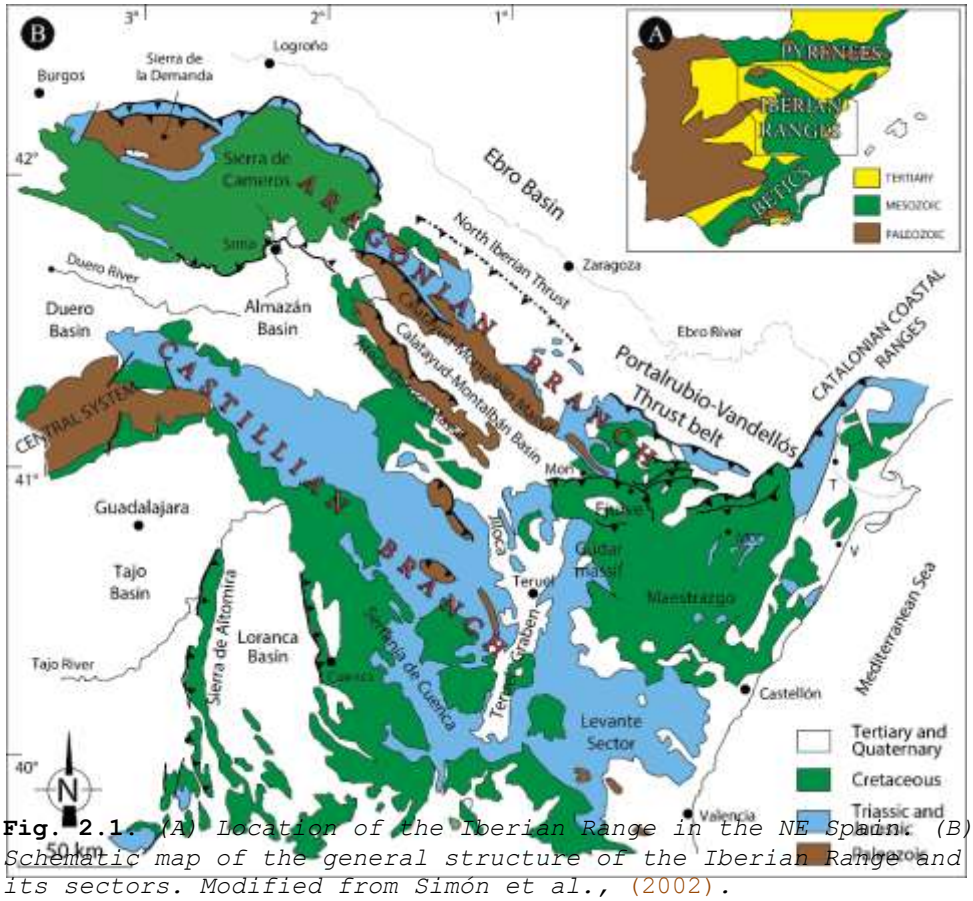

Fig. 2.1. *(A) Location of the Iberian Range in the NE Spain. (B) Schematic map of the general structure of the Iberian Range and its sectors. Modified from Simón et al., (2002).*

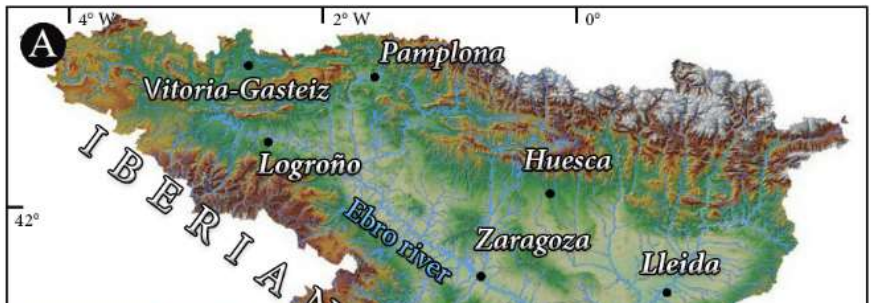

Fig. 2.2. *(A) Hydrographic basin of Ebro river, limited by the Pyrenees in the north and the Iberian Range in the south. The name of some important cities in the Ebro basin has been also added. (B) Detail of the study area, including Ejulve cave and some important mountains, rivers and water reservoirs. Modified from SITEbro (iber.chebro.es).*

2.1.1 Stratigraphy

The cave is developed in the dolomitic limestones and dolostones (Fig. 2.3) of the Mosqueruela Fm (Canérot, 1982) of Cenomanian -Upper Cretaceous- in age. This stratigraphic unit is included in the Late Jurassic-Late Cretaceous rifting sedimentary cycle of the Maestrazgo domain (Simón et al., 2002). Late Jurassic-Late Cretaceous deposits can reach thickness of 4000 m in this basin (Simón et al., 2002).

The Mosqueruela Fm., with a thickness up to 90 meters and 080/65 S orientation, overlaps the clays and sandstones of

Arenas de Utrillas Fm. (Fig. 2.3). The dolomitic limestones and dolostones in the sector of the cave (Fig. 2.4) are followed in southern direction at higher altitudes by Jurassic units such as dolomitic brecchias and carnioles, that overlap limestones and marls (Fig. 2.3).

The sediments of the Mosqueruela Fm. were deposited in transitional estuarine and tidal flat environments (Aurell et al., 2001). These deposits represent the beginning of an important transgressive pulse developing a large carbonate platform and invading extensive domains of the northeast of the Iberian Peninsula (Alonso et al., 1993).

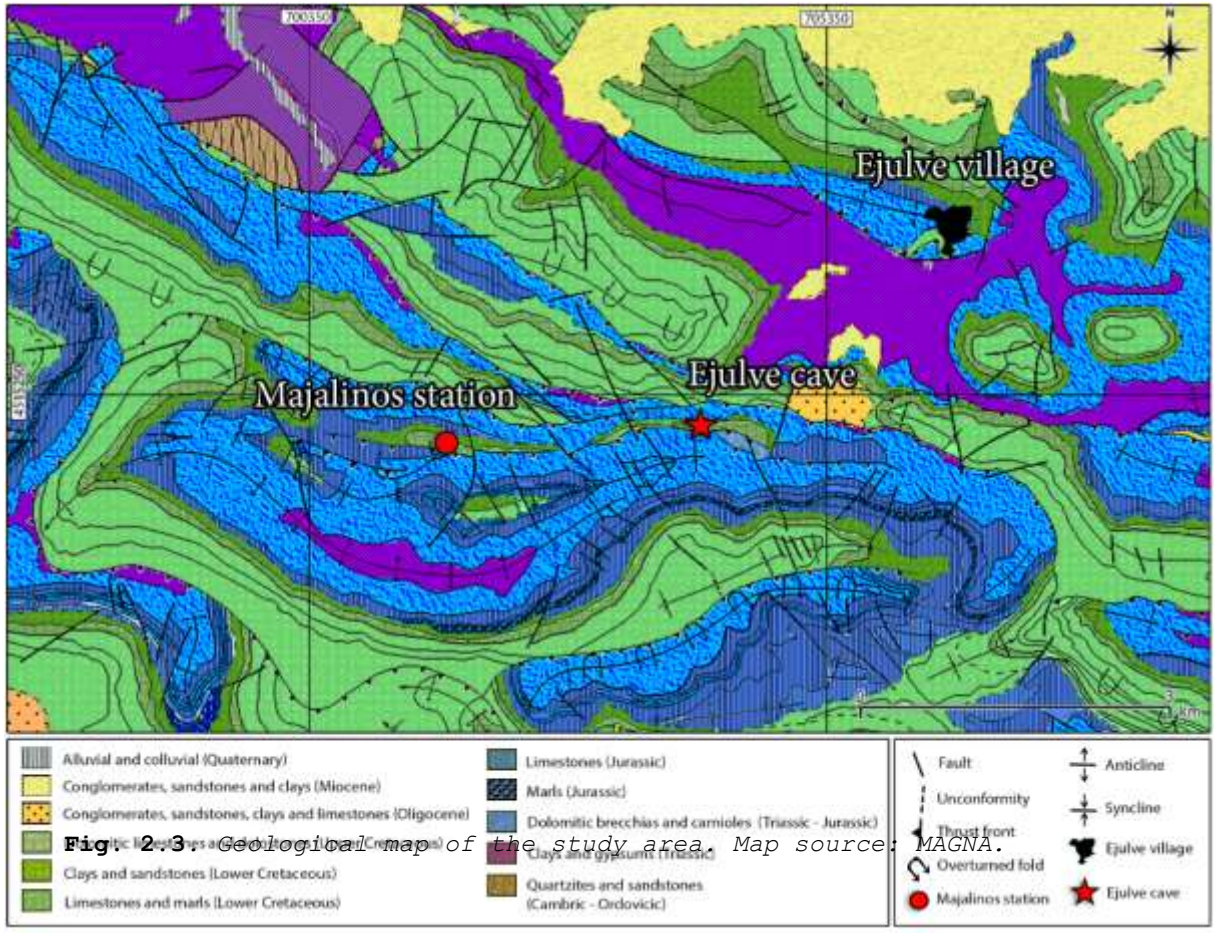

Fig. 2.3 *Geological map of the study area. Map source: MAGNA.*

2.1.2. Structure

In the study area, the Mesozoic coverage is affected by the thrust fronts of Portalrubio-Vandellós system (Canérot, 1974; Guimerà, 1988; Liesa, 1998; Simón et al., 2002) with NW-SE and W-E orientation (Fig. 2.3). This system of several thrust fronts was structured in two stages during Oligocene and Low Miocene (Liesa, 1998), representing the reactivation of large normal faults, active during the Low Cretaceous (Soria, 1997; Liesa, 1998; Simón et al., 2002). As a consequence, there are several faults in this area (Fig. 2.3), merged mainly in two dominant orientations, NNE-SSW and NNW-SSE.

Fig. 2.4. *Dolomitic limestones of the Mosqueruela Fm dipping to the south just above Ejulve cave.*

2.2. Geomorphology

The Iberian Range is a complex mountain chain of ~500 km length, from the Demanda region in the NW to the Mediterranean

coast in the SE, with 200 km maximum width. The highest peaks are San Lorenzo (2270 m a.s.l.) in the NW sector, Moncayo (2313 m a.s.l.) in the central sector and Penyagolosa (1813 m a.s.l.) in the SE sector. The landscape is dominated by extensive high-altitude platforms and planation surfaces (1600–1000 m asl) partitioned by tectonic grabens. The most extensive planation surface is the Main Planation Surface (MPS) of the Iberian Chain (Superficie de Erosión Fundamental de la Cordillera Ibérica) (Peña et al., 1984) shaped during the Pliocene (Gutiérrez and Peña, 1994). This surface was denuding the alpine compressional structures affecting thick and extensive Jurassic and Upper Cretaceous marine carbonate deposits.

The development of the planation surface concluded with an intensive karstic period leading the formation of large fields of dolines and poljes (Peña et al., 1984). The resulting planation surface was partitioned by extensional tectonics during Pliocene-Quaternary (Gutiérrez and Peña, 1994). This morphotopographic framework constitutes the starting point for the subsequent Quaternary fluvial incision (Gutiérrez et al., 2008). Some quaternary staircase terraces and related alluvial cover pediment sequences developed in the main tectonic grabens (Gutiérrez and Peña, 1994). In addition, Middle-Late Pleistocene and Holocene fluvial tufa deposits are very often in non-equilibrium longitudinal stretches of the fluvial network (Sancho et al., 2015). Finally, Pleistocene glacial activity is recognized in the highest areas of central and northwestern sectors. Nevertheless, more significant geomorphic features related to Quaternary periglacial activity are recognized throughout the Iberian Range (Gutiérrez and Peña, 1994).

Specifically, the study area is included geomorphically in the morphostructural unit of San Just-Castellote mountain range defined by Peña et al., (1984). This unit constitutes a mountainous area dominated by remnants of planation surfaces and structural landforms related to the incision of the drainage network guided by the Guadalope River (Fig. 2.2.B).

The reconnaissance of the regional geomorphology suggests a dominance of a planation surface in the landscape, through a gently sloping surface from 1300 to 1100 m, developed from the foothill of Majalinos mountain to the north of Ejulve village (Fig. 2.5). However, the geomorphic interpretation of this planation surface remains complex and two morphogenetic hypotheses have been discussed to explain its origin and development.

In one hand, Pailhé, (1984) interprets this sloping surface as a piedmont planation surface developed during Pliocene. This erosive surface originated at the foothill of the Majalinos mountain that in turn constitutes an isolated remnant of a former planation surface developed during Late Miocene. Consequently, two staircase planation surfaces would be recognized in the area. On the other hand, Peña et al., (1984) integrated the local sloping planation surface in the most extensive deformed planation surface (MPS) shaped between Late Miocene and Pliocene (Simón, 1984; Gutiérrez and Peña, 1994). The deformation of this planation surface reached around 2000 m a.s.l. in the Gúdar massif (Fig. 2.2.B) and was guided by doming processes related to postorogenic regional uplift (Giachetta et al., 2015). The MPS constituted a gently sloping surface from the Gúdar dome until the contact between the Iberian Range and the Ebro Basin.

In addition, the planation surface is affected by faulting and flexures in the Sant Just-Castellote unit that introduced local displacements in the surface. More locally, Sierra (2016) identified a fracture band at the foothill of Majalinos mountain affecting the MPS. In this second hypothesis, Majalinos mountain would constitute a residual relief of the MPS.

In the Sant Just-Castellote unit, some exokarstic landforms are recognized around Las Cuevas de Cañart village (Fig. 2.2.B) (Peña et al., 1984). In addition, some endokarstic features have been identified between Ejulve (e.g El Recuenco Cave) and Molinos (e.g. Las Graderas cave and Baticambras Cave) sectors (Fig. 2.2.B). Up to now, it is not possible to assign the formation of these caves to this regional stage of karstification. Flat topographical features, soluble lithologies and high density of faults and joints favored the water infiltration and development of the karstic landscape. Partionating of the MES related to rifting mechanism (Gutiérrez et al., 2008) triggered the subsequent fluvial downcutting. An approximate rate of regional fluvial incision around 0.6 mm/yr was proposed by Scotti et al., (2014).

The Quaternary fluvial incision led to the development of structural landforms (Fig. 2.5). In the Sant Just-Castellote unit, the incision of the drainage network, guided mainly by the Guadalope River, developed mesas, combes, hog-backs, cuestas and chevrons, according the structural layout of the bedrock. Some deep canyons could be also generated. The prevalence of the fluvial incision in the area did not favor the development of staircase terraces. Only the Guadalope River developed locally a Late Pleistocene terrace at low elevation above the active channel. In addition, Late Pleistocene-Holocene alluvial infilled valleys are recognized when the fluvial network cut across the bedrock composed of softer materials.

Fig. 2.5. *Sloping planation surface at the foot of Majalinos Peak affecting the deformed bedrock around Ejulve cave. Note the incision of the fluvial network related to the Guadalopillo River.*

2.3. Climate

This area is characterized by a climate Mediterranean temperate with strong continentality. The precipitation occurs mainly during both equinoxes, with April, May, June and October as the months with higher amount of precipitation (Fig. 2.6). The summer dryness, feature distinctive of the Mediterranean climates, is also seen in this mountainous area. There is a marked seasonality on temperatures, with mild summers displaying mean temperatures slightly above 20 °C, and cold winters with mean temperatures of 5 °C (Fig. 2.6). During winter, snowfalls may be frequent in this area.

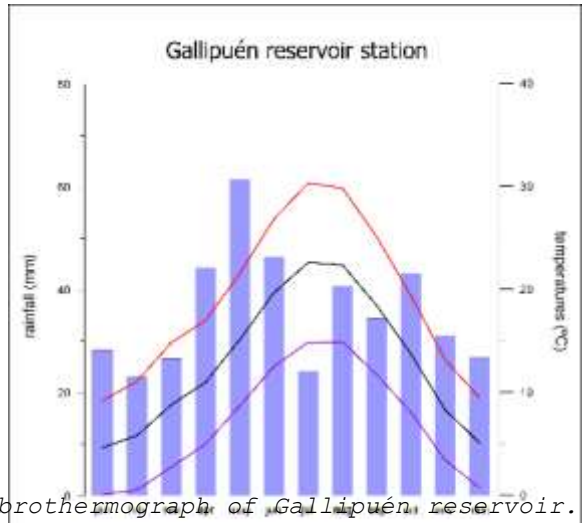

Fig. 2.6. *Ombrothermograph of Gallipuén reservoir. The dataseries spans the period 1981-2010 for rainfall data and 1969-2012 for temperatures. All data were extracted from the Aragonese Institute of Statistics, SAIH Ebro and the State Meteorological Agency (AEMET).*

The ombrothermograph corresponds to Gallipuén reservoir station, located in the course of Guadalopillo river, 19 km far (NE direction) from Ejulve cave (Fig. 2.2.B). Despite the weather station located at Majalinos peak (http://www.saihebro.com) is closer to the cave (Fig. 2.6), the existent dataset is much shorter compared to that of Gallipuén. The same issue of short dataset occurs with the weather station located in Ejulve village, managed by the Government of Aragón (DGA). However, due to the proximity between stations, scarce differences would be expected.

In this way, a close comparison has been carried out between the stations of Ejulve village and Gallipuén during the common

periods 2003-2012 for temperatures, and 1981-2010 for precipitation. It is worth noting the slightly lower temperatures in Ejulve (12.3 °C) compared with Gallipuén (12.6 °C) and the higher rainfall, with 547.3 mm in Ejulve compared with the 431.0 m in Gallipuén. A similar climate conditions to Ejulve village are expected in the area of the cave, perhaps with slight lower temperatures and higher precipitations due to the higher altitude of Ejulve cave.

2.4. Orography and hydrology

The Guadalopillo river is fed by a dendritic network of creeks (Fig. 2.7) and exhibit low annual mean flow rate, less than 0,1 m^3/s (http://www.saihebro.com). The creeks located in the flat areas may show some stagnant water with low flow, such as 'Los Tajos' and 'Las Cercas' creeks, which pass through an area of 1100-1200m of altitude. The highest points in that area are individualized hills that reach 1169m ('Cabezo de Ginebrillo') close to 'Las Cercas' creek, and 1229m ('Puntal de la Sima') close to 'Los Tajos' creek (Fig. 2.7).

Conversely, the creeks coming from the mountains, with higher slopes, may be dry almost the whole year. However, during episodes of high rainfall, the increase in the flow may be important in those creeks. The altitudes in this area ranges between 1200-1300m close to 'Las Quiñonerias' creek (highest point, 'Cabezo de las Quiñonerias', 1339m) and higher altitudes are reached in the creeks coming from Ejulve mountains, in southern direction (Fig. 2.7). The highest point in the study area is Majalinos peak, with 1601m, followed by 'Cabezo Pardo' peak (1594m), in the south of Majalinos (Fig. 2.7). In the area close to the cave, the highest points are 'Cerro de la Pinarota Espesa' with 1534m, located in the SE of Pinarota springs, 'Cerro de las Umbrias' with 1524m, and 'Cabezo Riscal', with 1483m, in the same ridge of Ejulve cave in southern direction (Fig. 2.7). The infiltration would happen during short periods of time due to the high slopes in the area over the cave. It is expected a high recharge of the groundwater microreservoirs in the epikarst during those moments.

Hence, the orography of the area is lower in the north, with 1137m as the highest point of Ejulve village, and between 1100-1200 in the creeks located on the west of the village. The altitude is increasing southern from the 'A-2403' regional road, located at the foothill of Ejulve mountains. In that sector, the altitudes ranges between 1200 to 1600m, and close to 'Cabezo Riscal', the road reaches the highest point in the 'Puerto Majalinos' point, at 1456m.

The source of the Guadalopillo river can be found ultimately in the Canaleta springs, located in the west of Ejulve village (Fig. 2.7). Here, the water from Canaleta springs flows eastwards through 'Las Cercas' creek, and in the south of the village merged with other creeks coming from the east and south, such as 'Las Quiñonerias', 'Los Tajos' and 'Val de Gimeno' creeks, and the other creeks coming from the Ejulve mountains in the south (Fig. 2.7). The Guadalopillo river flows into the Guadalope river, an important tributary of the Ebro river, after Gallipuén and Calanda water reservoirs (Fig. 2.2.B).

In general, the flow rate and the river features in this area are strongly regulated by the anthropic activities, being the high number of water reservoirs a great example of it (Fig. 2.2.B).

Fig. 2.7. *Detail of the dendritic creek network located in the study area. The location of Ejulve cave and other important points such as Majalino weather station, the highest peaks, some springs and the Guadalopillo river are also marked. Map source: PNOA (pnoa.ign.es).*

2.5. Soils and vegetation

Information and data on the soil mapping and soil characterization in the study area are not available. However, soils recognition becomes very significant because its influence in the geochemical signature of the infiltrated water through the vegetation cover developed and the microbial activity. Generally, soils are weakly developed in the study area, favoring a fast infiltration when porous and faulted bedrock outcrops intersect the topographic surface. Two geomorphic units with different soil development can be distinguished. In areas with abrupt topography dominated by structural landforms and planation surfaces, the carbonate bedrock (mainly Jurassic and Cretaceous limestones and dolostones) is frequently exposed, and soil lacks.

In a simple approach and according to the World Reference Base for Soil Resources (2014), some patchy *Leptosols* with an Ah-R sequence developed on flattened areas without unconsolidated detrital cover. *Regosols* with an Ah-C-R sequence developed on flattened and/or with some slope areas covered with unconsolidated detrital materials (Fig. 2.8). Locally, *Calcisols* with an Ah-Bk-C-R sequence have been also recognized in this unit. Finally, in low altitude areas, *Fluvisols*, with an Ah-Bw-C-R sequence, developed on Late Pleistocene-Holocene alluvial infilled valleys.

On these soils a sparse vegetation cover developed. The vegetation of this area belongs to the domain of mid- and upper-Mediterranean bioclimatic schemes. There is a dominance of the scrubland in the surrounding of the cave (Fig. 2.9) characterized by heliophytic shrubs and sparse oaks and pinewoods. This vegetation does not take up so much water, so it is expected high infiltration during the wet season. The domain of the scrubland is common in the north side of the Ejulve mountains. In the SW of the study area, close to Majalinos, there is a higher development of the forest with conifers and higher density of vegetation (Fig. 2.9).

The effects of the devastating wildfire during 2009 can be still observed southern of Ejulve cave, a wildfire that burnt ~3000 hectares only in the municipality of Ejulve. In lower altitudes, grassland and herbaceous crops, dominant in the northern part close to the village (Fig. 2.9) are observed.

Fig. 2.8. *Regosols developed on slopes around Ejulve cave scarps covered with detrital deposits. Note the vegetation cover development and the effect of forest wildfire in 2009.*

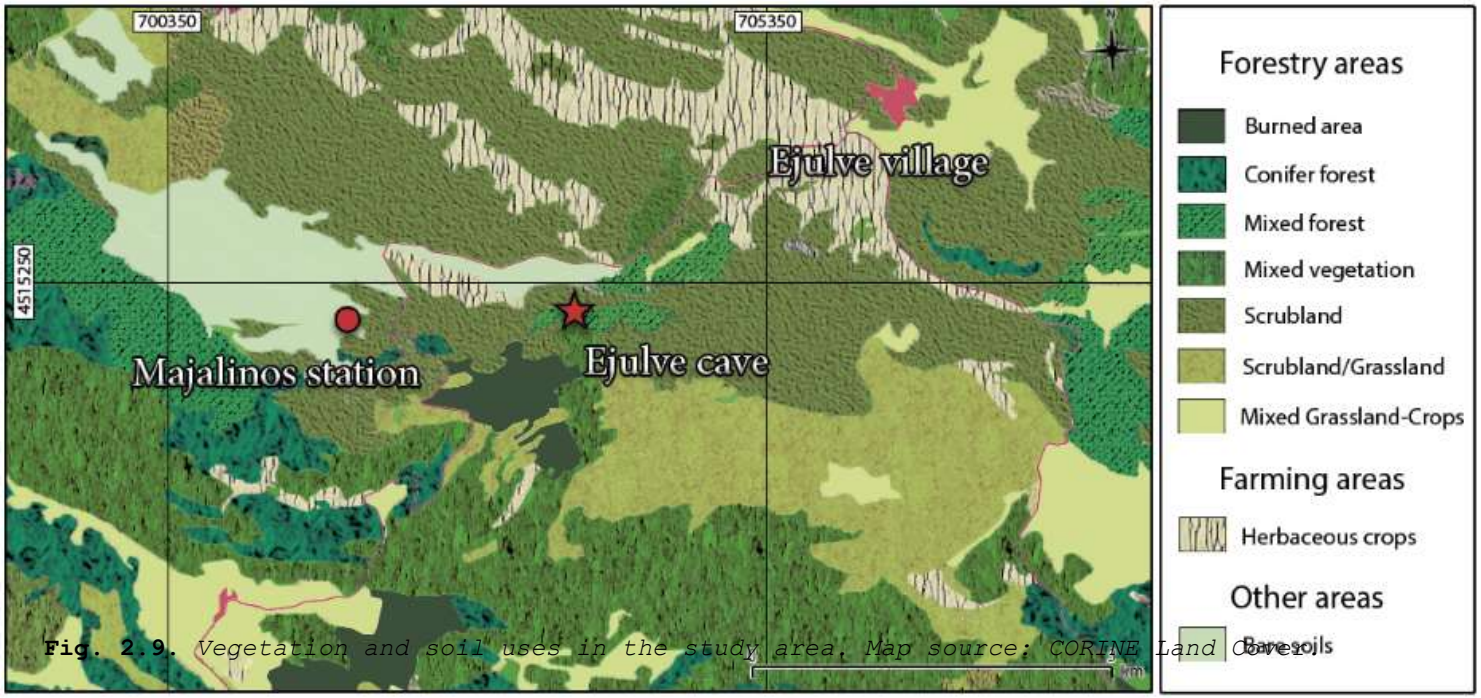

Fig. 2.9. *Vegetation and soil uses in the study area. Map source: CORINE Land Cover.*


CAUTION
RADIOACTIVE MATERIALS
NO EATING, DRINKING, OR FOOD/BEVERAGE STORAGE PERMITTED IN THIS ROOM.
RADIOACTIVE MATERIAL PERMIT HOLDER: Dr. Larry Edwards
PERMIT HOLDER'S EXTENSION: lab: 4-9598/ Larry: 6-0267
IN CASE OF A RADIATION INCIDENT
DO NOT LEAVE.
UNIVERSITY OF MINNESOTA – DEPARTMENT OF ENVIRONMENTAL HEALTH AND SAFETY

"We are all connected: to each other, biologically.
To the earth, chemically. To the rest of the
universe, atomically".
-Neil deGrasse Tyson

Chapter

Methodology

A multidisciplinary approach has been applied to reach the objectives of the present thesis detailed in the Chapter 1. The methodological framework is mainly divided in three strategic lines, as follows: field work, laboratory and desktop work (Fig. 3.1).

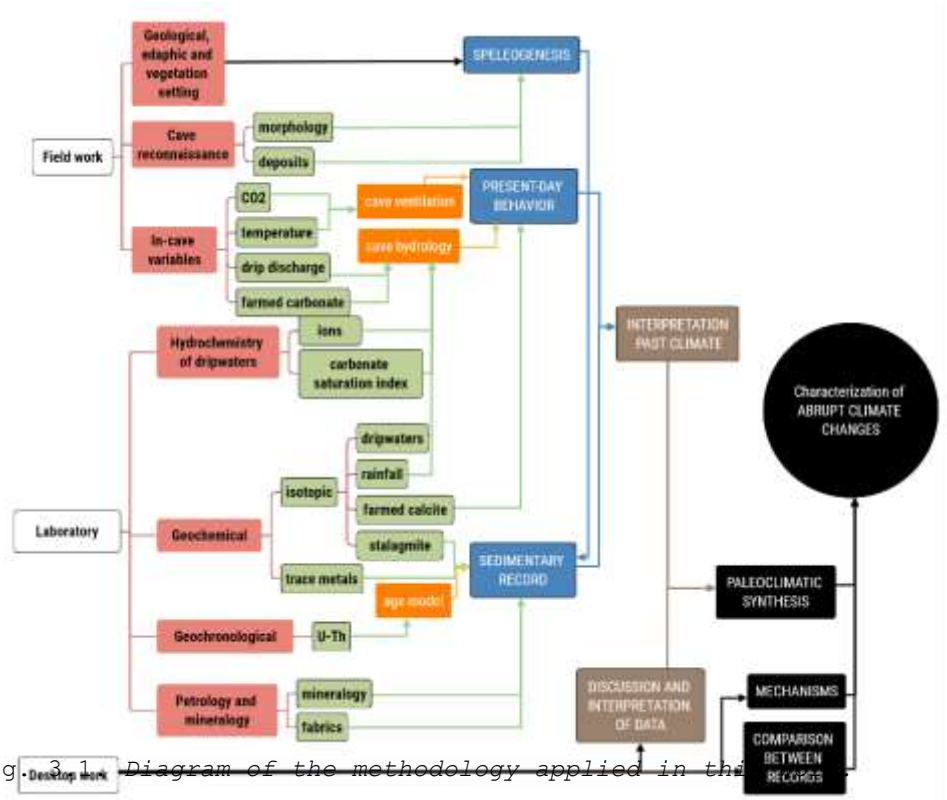

Fig. 3.1 *Diagram of the methodology applied in this*

3.1. Field work

3.1.1. Recognition of geological, edaphic and vegetation cover setting

The first stage of the field work spans: a) Identification of the stratigraphic, structural and geomorphic features of the area surrounding the cave, and b) characterization of the soils and the vegetation cover over the cave (Fig. 3.2). That information gave us relevant insights for a correct interpretation of the cave speleogenesis, the current speleothemic dynamics and the fossil stalagmite record.

Fig. 3.2. *Location of Ejulve cave. Note the basic geological features, general landscape and distribution of vegetation close to the cave. Majalinos weather station, located in the summit of this mountains, is also marked.*

3.1.2. Cave reconnaissance

A morphologic and sedimentary characterization of the cave has been carried out, paying attention to the geometry and morphology of the galleries and chambers, and the identification of the different cave deposits (Fig. 3.3). To do that, major fractures were measured inside the cave and different erosive and accumulative features have been recognized.

Consequently, a variety of morphological features and speleothems were inventoried and described at different scales (cave pattern and cave relief) of Ejulve cave following descriptions by Ford and Williams (2007), Klimchouk (2009) and Dublyansky (2013). The plan view (topography) and the elevation transects (Fig. 3.4) were extracted and modified from Gisbert and Carvajal (1993) and Castellano et al. (2015).

Fig. 3.3. *View of one chamber within Ejulve cave, in which different types of speleothems can be distinguished.*

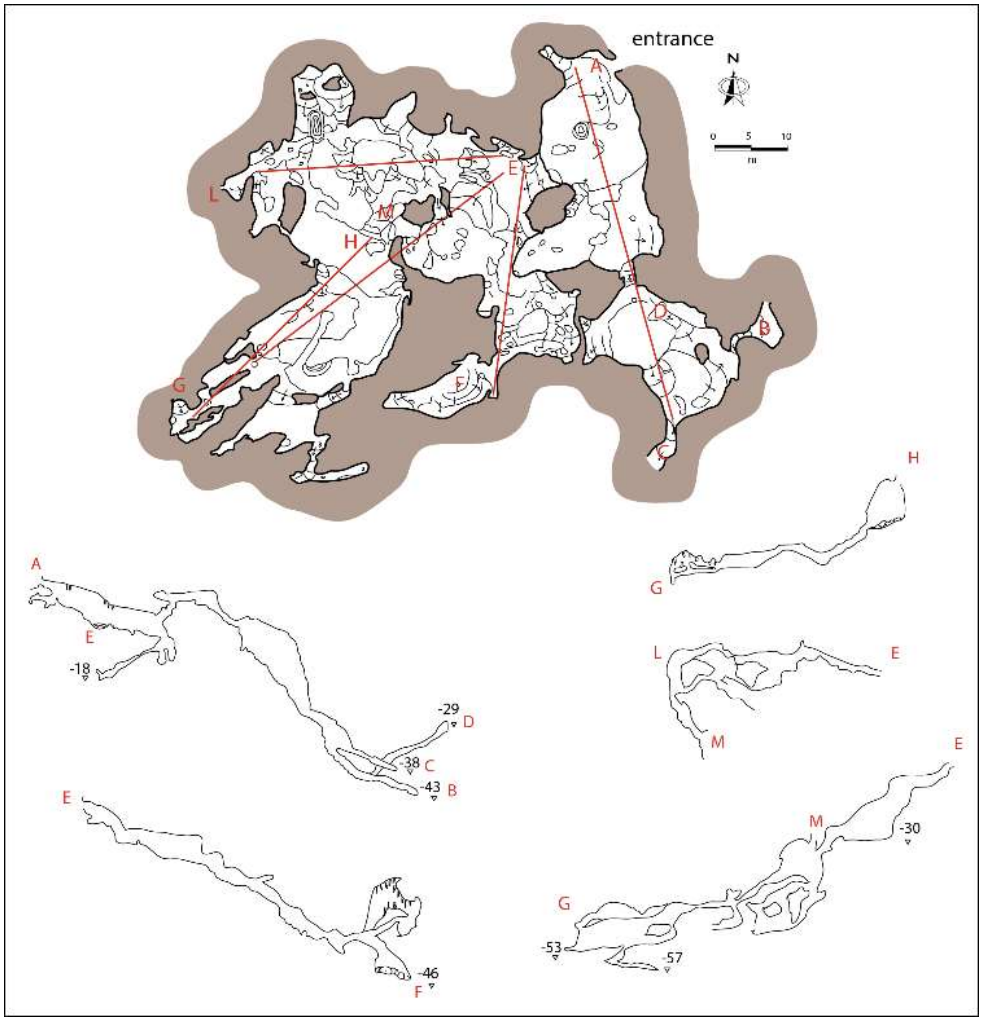

Fig. 3.4. *Plant view and elevation transects from Ejulve cave, modified from Gisbert and Carvajal (1993) and Castellano et al (2015).*

3.1.3. Cave deposits sampling

Several visits to the cave were planned to sampling different types of precipitates, such as stalagmites (Fig. 3.5.A,B), botryoids, aciculars or spar precipitates (Fig. 3.5.C,D,E).

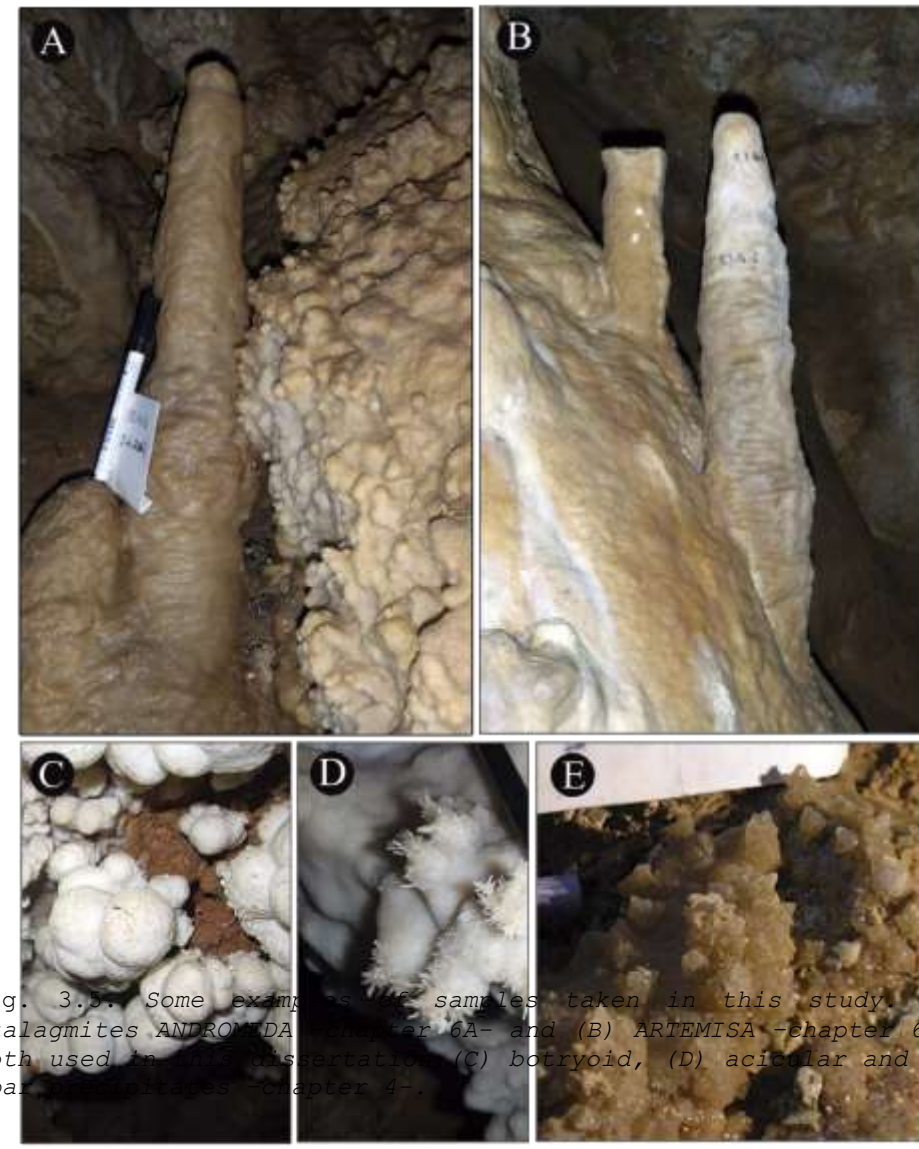

Fig. 3.5. *Some examples of samples taken in this study. (A) Stalagmites ANDROMEDA -chapter 6A- and (B) ARTEMISA -chapter 6B-, both used in this dissertation. (C) botryoid, (D) acicular and (E) spar precipitates -chapter 4-.*

3.1.4. Monitoring and measurement of environmental variables

During the monitoring survey (2013-2016), some environmental parameters were measured and several sampling techniques were carried out, as follows:

- ✓ Measurement of environmental variables inside the cave:
  - Cave-air temperature, using a HOBO® U23 Pro v2 Temperature datalogger.
  - The CO_2 was measured occasionally in different cave chambers close to the dripwater and farmed calcite sampling sites using a portable CO_2 meter (CM-0019 device).
  - Drip discharge was measured in all drip sites (twelve) manually every visit to the cave. Additionally, a pluviometer was installed in one single point to record the changes in discharge in a continuous mode.
- ✓ Sampling for isotopic and hydrochemistry analysis:
  - Isotopic analysis:
    - Daily rainfall samples, collected manually in Molinos village (10 km from Ejulve cave) over a period of six years (2010–2015) by personal of the city hall. δD and $\delta^{18}O$ were analysed.
    - Drip waters in all drip sites, originated in active soda-straw stalactites and sampled from January 2013 to June 2016 (Fig. 3.6.A). δD and $\delta^{18}O$ were analysed.
    - Farmed carbonate in all drip sites, recovered seasonally over glass plates (Fig. 3.6.B,C). $\delta^{18}O$ and $\delta^{13}C$ were analysed.
  - Hydrochemistry measurements in dripwaters extracted from two drip sites, measuring temperature, pH and conductivity.

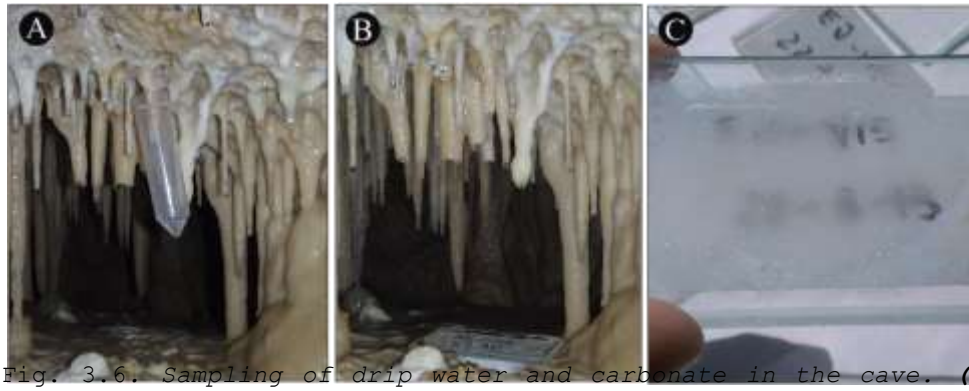

Fig. 3.6. *Sampling of drip water and carbonate in the cave. (A) Sampling of drip waters, (B) glass plates installed below one drip. (C) Farmed calcite recovered in one drip site during spring of 2013.*

3.2. Laboratory work

There are different types of samples in this study, mainly divided in two groups: (1) water samples, from both rainfall and drip water, and (2) carbonate samples, including mainly precipitates such as stalagmites and farmed calcite. Stalagmite samples were cut with a diamond saw along the growth axis in the University of Zaragoza and polished prior to sampling. Those samples were used for several analyses, as follows.

3.2.1. Petrology and mineralogy

Thin-sections from carbonate precipitates were produced and analyzed microscopically at the University of Zaragoza (Servicio General de Apoyo a la Investigación-SAI). The fabrics of carbonate samples were described using observations from a petrographic microscope, according the terminology of (Frisia et al., 2000; Frisia and Borsato, 2010; Frisia, 2015).

Several analysis of mineralogy have been carried out in the stalagmites and cave wall precipitates (standing out the 46 samples of rare precipitates presented in Chapter 4), and were performed at Jaume Almera Institute (ICTJA-CSIC, Barcelona) with a Bruker AXS D5005 set up theta-2theta geometry, with a Cu X-ray tube of up to 2.2 kW and in the University of Zaragoza with a Phillips PW 1729 diffractometer equipped with a graphite monochromator and using CuKα radiation. The mineralogical semiquantitative composition was determined using DIFFRACplus evaluation package.

3.2.2. Geochronology

The strategy during the sampling for U-Th dating was a selective drilling along the different growth intervals focusing on identifying potential hiatus or low-growth periods. A total of 56 samples were used in the data exhibited in the present dissertation: 24 in the chapter 6.1 (ARTEMISA stalagmite), 26 in the chapter 6.2 (ANDROMEDA stalagmite) and 6 in rare carbonates precipitated in cave walls (chapter 4). The U/Th datings were analyzed in a multi-collector mass spectrometry (MC-ICP-MS) (Thermo-Finnigan Neptune) at the University of Minnesota (USA) and the University of Xi'an (China) following the methodology described in Cheng et al. (2013). During the two visits to the University of Minnesota, more than 300 samples has been dated from 57 speleothem records and 7 different caves.

The U-Th method can be separated in two processes: first, the extraction of the U and Th from the carbonate samples through a chemical procedure, and second, the quantification of the isotopes in the MC-ICP-MS. Briefly, the chemical method works as follows: the sample is dissolved with 7N HNO_3 ultrapure, and spiked with a mixed solution of ^{229}Th-^{233}U-^{236}U. Few drops of

perchloric acid ($HClO_4$) had to be added to destroy organic compounds in the sample and to help equilibrating the spike solution. Previously, the beakers were cleaned in a meticulous and long process through several steps, including agua regia (Fig. 3.7.A).

Once the sample is dried down (Fig. 3.7.B) and the Ca was eliminated being dissolved with 2N HCl, a solution of Fe is added. The precipitation of the Fe will be triggered by ammonium hydroxide (NH_4OH), and through several rounds of centrifuge, the atoms of higher mass will be extracted from the sample, containing those of the Th and U. The last step is the separation of both elements using columns filled with an anion exchange resin (Fig. 3.7.C), after filling them several times with 7N HNO_3. The thorium will be extracted of the column using 2N HCl, while the uranium will be extracted using milliQ water.

The samples will be analyzed in the Neptune MC-ICP-MS (Fig. 3.7.D). All isotopes were measured with Faraday cups, except the ^{230}Th and ^{234}U, that will be analyzed by secondary electron multiplier (SEM).

The construction of the age models were done using Bayesian chronological modeling with OxCal (Ramsey, 2008) and the code of StalAge for R (Scholz and Hoffmann, 2011). The age uncertainties were low, around ±2 ky in ARTEMISA, characteristic of the 1% of uncertainty in age, while in ANDROMEDA the uncertainty of the analysis is around 2 to 4‰ of the age.

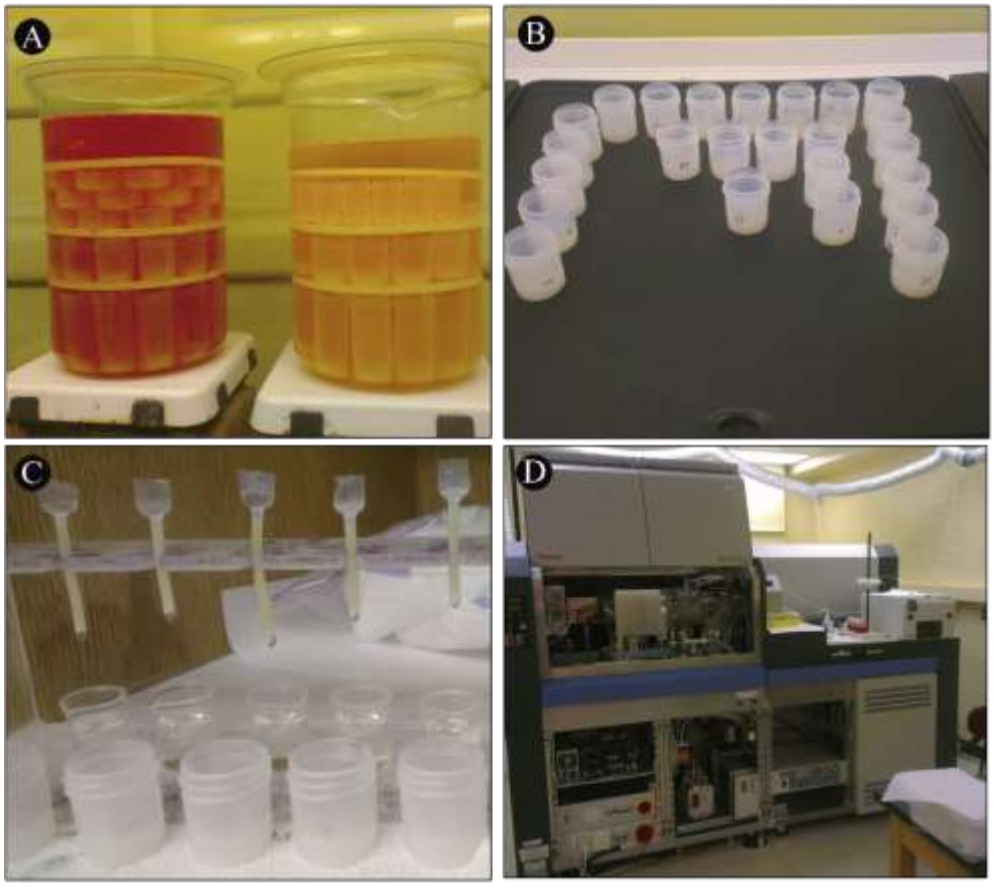

Fig. 3.7. *Procedure used for U-Th datings. (A) One step in the beakers cleaning process, using 'agua regia' -75% HCl, 25% HNO_3-. (B) Drying down the samples in the hot plate. (C) Columns filled with anion exchange resin. (D) Neptune MC-ICP-MS used for the analysis.*

3.2.3. Geochemistry

a) Stable isotopes in water samples ($\delta^{18}O$ and δD)

A total of 406 analyses of isotopes were carried out during the present thesis in the water samples, 125 in rainfall samples and 281 samples in drip waters. The rainfall was sampled every rainy day, following the protocol described in Moreno et al. (2014) based on IAEA-GNIP procedures. The drip waters were sampled twice per season in 5 ml vials—completely filled, capped, and kept refrigerated until further analysis.

All the isotopic analyses of waters were conducted at the Andalusian Earth Sciences Institute in Granada (IACT-CSIC) using a Finnigan Delta Plus XL mass spectrometer. Water samples were equilibrated with CO_2 for the analysis of $\delta^{18}O$ values. Hydrogen was measured as H_2 produced by the reaction of 10 µL of water with metallic zinc at 500 °C following the analytical method of Coleman et al., (1982). The values are reported as $\delta^{18}O$ (‰) and δD (‰) with respect to the Vienna Standard Mean Ocean Water (V-SMOW), with an analytical precision (1σ) of ±0.1‰ for $\delta^{18}O$ and ±1‰ in the case of δD.

b) Stable isotopes in carbonate samples ($\delta^{18}O$ and $\delta^{13}C$)

A total of 1436 isotopic analysis in carbonates were carried out in the present thesis, 90 corresponding to present-day farmed calcite, 43 to rare precipitates in walls and cave ceiling, 9 samples of the bedrock and 1294 in stalagmites. The strategy of sampling was carried out in different stages, generally one first phase of low-resolution analysis and a posterior improvement of the resolution in selected areas of the stalagmite. The first low-resolution analysis aid us to obtain a draft of the isotopic profile of the stalagmite, conforming the first approach to evaluate the response of the isotopes to a changing climate. The improvement of the resolution was applied to those parts of the sample with more interest attending to the age model and the probability to cover some notable abrupt events.

Hence, the first 90 samples in low-resolution were sampled from ARTEMISA, that was improved later with 121 samples in intervals of 0.5 mm and 115 samples every 1 mm. Regarding to ANDROMEDA, a first strategy of sampling every 1 mm was carried out with a total of 410 samples. The improvement of the resolution was applied in the part of abrupt climate changes during with new 558 samples in a continuous-sampling mode using a trench in equal intervals of 0.2 mm (Fig. 3.8.A).

During the monitoring survey of the cave, twelve glass plates were placed below the drip to recover the carbonate that precipitated seasonally from January 2013 to June 2016. 90 samples of precipitated carbonate were sampled from the central part of the glass plates (i.e., the drip impact zone) to conduct further isotopic analyses.

The analysis of the carbonate samples was carried out in three different laboratories, 54,7% of the samples were analyzed at the university of Barcelona, 39% at the University of Innsbruck (the improvement of the resolution of ANDROMEDA) and 6.3% at the University of Oviedo (the first low-resolution profile of ARTEMISA). The analysis in Oviedo and Innsbruck were done during different short research visits to these centres.

The equipment used at the Scientific-Technical Services (CCiT) of the University of Barcelona and at the University of Oviedo were a Finnigan-MAT 252 mass spectrometer fitted with a Kiel Carbonate Device I (Fig. 3.8.B). The standards were run every 6–10 samples with a reproducibility of 0.04‰ for $\delta^{13}C$ and 0.08‰ for $\delta^{18}O$. At the university of Innsbruck, a Thermo Fisher Delta V Plus linked to a Gasbench II was used, following the methodology described in Spötl (2011). All the values are reported as $\delta^{18}O$ (‰) and $\delta^{13}C$ (‰) with respect to the Vienna Pee Dee Belemnite standard (V-PDB).

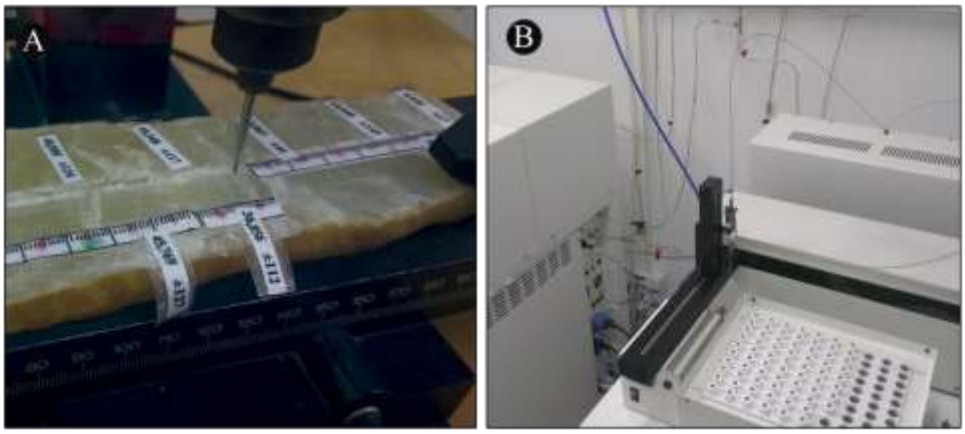

Fig. 3.8. *Procedure used for isotopic composition. (A) High-resolution sampling for isotope analysis, (B) Finnigan-MAT 252, University of Oviedo.*

c) Trace elements

For trace metals analysis, a total of 469 samples were sampled using a 1-mm microdrill tip in equal intervals of 1 mm, 168 samples in ARTEMISA and 301 samples in ANDROMEDA. A similar strategy to the applied in the stable isotopes were carried out, starting with low resolution analysis (5 mm) and improving later with higher resolution (1 mm) (Fig. 3.9.A). The analysis was performed in the University of Oviedo and in the IPE-CSIC labs with a ICP-OES (Thermo Scientific iCAP DUO 6300) (Fig. 3.9.B) using molar ratios of Mg in relation to Ca.

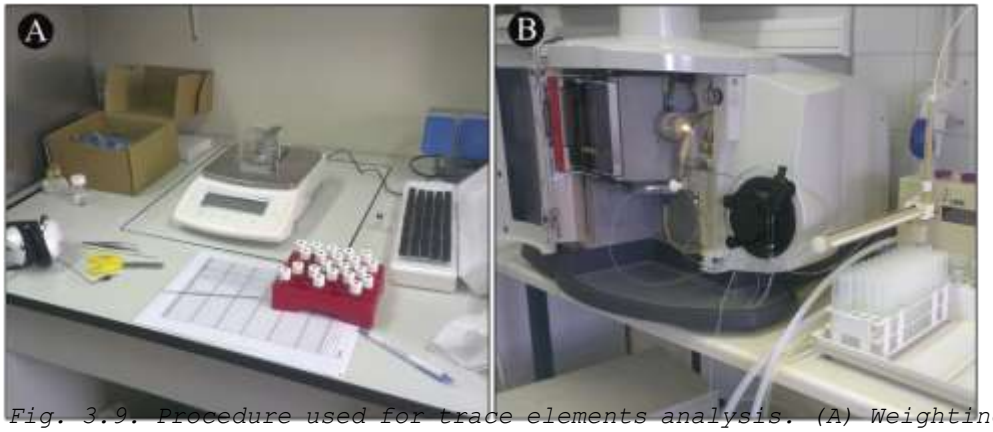

Fig. 3.9. Procedure used for trace elements analysis. (A) Weighting the samples prior to the analysis, (B) ICP-OES, University of Oviedo.

3.2.4. Hydrochemistry

During the monitoring survey, water samples were taken every visit to the cave (1.5 months usually) from two drip sites. The pH was measured in-situ in the cave immediately after water sampling using a pHmeter (Hanna Instruments 410-0902). The electric conductivity was measured using a YSI Professional Plus® handheld multiparameter instrument.

Later, anion-cation concentrations were measured at the Pyrenean Institute of Ecology (IPE-CSIC) lab using a Metrohm 861 ion chromatograph and precautions were adopted to prevent any precipitation of $CaCO_3$ in the vial (e.g., keeping it refrigerated and opening it only before the analysis). The detection limits were 5 ppb for anions and 10 ppb for cations. Alkalinity was calculated by using a strong acid (sulfuric) and two indicators, phenolphthalein for CO_3^{2-} and a mixed indicator of bromocresol green and methyl red for HCO_3^- in 50 ml of sample vials. The hydrochemistry calculations of the saturation indexes

respect to the $CaCO_3$ were estimated using PHREEQC software (Parkhurst and Appello, 2013).

3.3 Desktop work

The starting point is to state a research question that will lead the scientific study. The elaboration of the hypothesis based on our observations through the inductive method is the usual procedure in the experimental sciences. Additionally, the performance of experiments or the measurements of environmental variables will test the proposed hypothesis. In this way, the hypothesis will be refined or discarded attending to the experimental findings.

The discussion and interpretation of the data obtained from the proxies or from the direct measurement of environmental variables, would test our hypothesis. In this way, a comparison with other records is also fundamental in the reconstruction of paleoclimates from a regional point of view. Traditionally, the NOAA has offered a great compilation of published datasets using different proxies to reconstruct past climate changes (http://www.ncdc.noaa.gov/data-access/paleoclimatology-data/datasets). Recently, it is worth noting the global effort to make a main database with data from speleothems (mainly isotopes, but also chronologies, trace metals and more) carried out by the Speleothem Isotopes Synthesis and AnaLysis (SISAL) working group (http://pastglobalchanges.org/ini/wg/sisal/intro). Few months ago, a first version of the database has been released (Atsawawaranunt et al., 2018).

In the future, the use of such databases will make easier the synthesis and analysis of the global response during concrete events, and could be used in climate models that simulate water and carbon isotopes cycles (forward modelling), as well as atmospheric tracers such as dust.

“The most exciting phrase to hear in science,

the one that heralds new discoveries, is not
'Eureka!' but 'That´s funny…'
-Isaac Asimov

Chapter

Speleogenesis

First identification of hypogene subterranean morphologies in the Iberian Range, NE Spain: a case study in Ejulve cave.

Significance

- An innovative hypothesis of the Ejulve cave speleogenesis is presented, based on a hypogene-hydrothermal origin.
- This work involves the study ofcave morphologies and cave deposits.
- Two stages are proposed for the cave development, a former confined hypogenic setting and an unconfined epigenic phase.
- Supported by the existence of a regional low-temperature hydrothermalism.
- First evidences of hypogene speleogenesis in the Eastern Iberian Range.

Abstract

We provide the first insights into the speleogenesis of Ejulve cave (Teruel province, Iberian Range, NE Spain) by studying cave morphologies and speleothems. Calcite and dolomite infills hosted in discontinuities of the bedrock (mean $\delta^{18}O$ of -6.2 ‰ and $\delta^{13}C$ of -6.4 ‰) formed under phreatic conditions during the earliest stages (Upper Miocene post-tectonics) of regional karstic evolution. Later, hypogene karstification occurred during the Mio-Pliocene (3 Ma ago) by ascending water flows driven by hydraulic gradients in a confined aquifer that generated a maze network and characteristic cave morphologies. These forms include boxwork, tubes with rising ceiling cupolas, pendants and cups, spongework and micro-corrosion features, all suggestive of hypogene karst setting.

Current regional low-thermal activity (~22-24 ºC) indicates that karstification may have occurred in a relatively warm confined aquifer. Subsequently, the cave underwent a transition to epigenic unconfined conditions driven by denudation, as a result of regional uplift and doming mechanisms. Once the karst was exhumated, conditions for precipitation of carbonate speleothems prevailed in a vadose environment.

We present mineralogical, petrographic, isotopic and chronological (U-Th dating series) analyses from carbonate speleothems (i.e. stalagmites, farmed carbonate, botryoids, crusts, spars and acicular crystals). Calcite, high-magnesium calcite and aragonite are the most common minerals, whereas columns, dendrites, micrite, mosaics and fans are the main fabrics. Mean $\delta^{18}O$ values of -7.3 ‰ and $\delta^{13}C$ of -9.1 ‰ indicate

relatively low-temperature carbonate precipitation from seepage meteoric waters. Carbonate deposits formed at least from 650 kyr BP.
We propose a two-stage speleogenetic model for Ejulve cave, in which a hypogene phases preceded an epigenic stage, framed in the regional karst exhumation. Our study suggests that the role of hypogene processes should be considered to explain the speleogenesis of other cave systems in the southeastern sector of the Iberian Range.

Keywords
speleogenesis | *cave morphologies* | *carbonate speleothems* | *hypogene caves* | *Iberian Range*

4.1. Introduction

Quaternary karst dynamics in the southeastern sector of the Iberian Range (NE Iberian Peninsula) involve large fields of exokarstic landforms, mainly dolines and poljes, superimposed to a previous extensive Pliocene planation surface (Peña et al., 1984), mostly developed on Mesozoic limestone bedrock (Gutiérrez and Peña, 1994). Also, the external morphosedimentary response to Quaternary karst dynamics, as evidenced by fluvial tufa records, is very well known at regional scale (Sancho et al., 2015). However, this intense exokarstic activity does not keep a parallelism with the development of endokarstic systems and caves, which are very scarce in this region (Castellano et al., 2015).

One remarkable cave in the SE Iberian Range, among others (e.g. Cueva de la Ubriga, Cija de Fortanete, Sima de Val de la Zoma, Cueva de Molinos) is Ejulve cave (also known as El Recuenco Cave, Teruel Province), because of its comparatively large size (~800 m long) and singular morphologies. Ejulve and Molinos caves were initially selected in the region for paleoclimate studies using stalagmites (Moreno et al., 2017; Pérez-Mejías et al., 2017). Nevertheless, the regional speleogenesis of the endokarst in the SE Iberian Range remains uninvestigated.

Speleogenesis deals with the origin and development of cave systems (Ford and Williams, 2007). Two general types of speleogenetic mechanisms, hypogene and epigene, can be distinguished on the basis of the origin (deep or superficial, respectively) of the fluxes of energy and matter (Klimchouk et al., 2000; Ford and Williams, 2007; Palmer, 2011; Klimchouk, 2017). Assessing and developing speleogenetic models (epigene vs hypogene) involve thoughtful cave morphological characterization as well as analysis of secondary cave deposits.

In the Iberian Peninsula, epigene speleogenesis predominates in the main calcareous mountains ranges of the northern (Cantabrian Mountains, Pyrenees, Iberian Range and Catalonian Coastal Range) (e.g. Ortega et al., 2013; Aranburu et al., 2015; Ballesteros et al., 2015; Bartolomé et al., 2015; Dodero et al., 2015) and southern region (Betic Mountain Range) (Durán et al., 1993; Calaforra and Berrocal, 2008). On the other hand, hypogene speleogenesis is not so common and has been only documented in the eastern Betic Mountain Range (southeastern Iberian Peninsula) (Gázquez et al., 2016; 2017) and in Balearic Islands (Ginés et al., 2017).

This study is aimed at providing the first insights into the speleogenesis of Ejulve cave (SE Iberian Range, NE Spain), based on interpretations of cave morphologies and mineralogical, petrographic, isotopic and chronological analyses of carbonate speleothems. We particularly assess the role of hypogene

mechanisms in the development of the cave, in connection with an ancient confined aquifer and regional evolution of the landscape.

4.2. Study area

Ejulve cave (40°45'34''N; 0°35'07''W; 1240 m a.s.l.) is a relatively small cavity located in the southeastern sector (Maestrazgo Unit) of the Iberian Range (Teruel province) (Fig. 4.1), an intraplate alpine mountainous range in northeastern Iberia (Simón et al., 2002). Regional geological bedrock is made of Upper Triassic clays and gypsums, Jurassic carnioles and dolostones, limestones and marls, Lower Cretaceous detrital rocks and Upper Cretaceous limestones and dolostones. It is affected by NW-SE and NE-SW trending folds, thrusts and faults (Simón et al., 2002) (Fig. 4.2.A). Oligocene and Miocene conglomerates, sandstones and claystones topped this Mesozoic sequence. Ejulve cave is developed in highly folded and thrusted Upper Cretaceous dolomitic limestones and dolostones. Jurassic materials including impermeable marls (30 m thick) thrust the dolomitic Upper Cretaceous sequence (Fig. 4.2.B). The cave's bedrock is clearly affected by subsequent intense flattening processes (Fig. 4.2.C).

Previous studies on the Iberian Range geomorphology reveal a general dome-shaped topography, as a response to post-orogenic regional uplift (Scotti et al., 2014; Giachetta et al., 2015). Moreover, the landscape in this region is relatively flat, dominated by extensive high-altitude platforms and planation surfaces (1000-1600 m a.s.l.), multi-storey partitioned by Mio-Plio-Quaternary tectonic grabens related to rifting mechanisms (Gutiérrez et al., 2008). At regional scale, it is remarkable the development of an extensive Pliocene planation surface (Peña et al., 1984; Gutiérrez and Peña, 1994). Regional low-temperature hydrothermal anomalies have been reported by Sánchez et al., (2004) at Virgen de Ariño and Segura de los Baños spa resorts, located 29 km and 38 km far from Ejulve cave, respectively (Fig. 4.1). The water temperatures at the karstic outlets are 22.7 °C at Virgen de Ariño and 24 °C at Segura de los Baños. The groundwaters are calcium-sulfate and calcium-bicarbonate facies, respectively, and the mean $\delta^{18}O$ values are -8.5 ‰ in Ariño and -9.2 ‰ in Segura (Baeza et al., 2000).

Climate in the area is Mediterranean with strong continentality and high seasonal contrast. Mean annual temperature is 8.5 °C and mean annual precipitation is ca. 431 mm, occurring through fall to spring. This temperature, recorded in Majalino weather station located 332 m above the cave, is lower than the mean temperature of the cave (11.3 °C) during the period 2013-2016 (Pérez-Mejías et al., 2018). The soil development is scarce and holds a degraded vegetation cover

dominated by diverse heliophytic shrubs, holm and semi-deciduous oaks (Angosto and Latorre, 2000).

Figure 4.1. *Location of the Ejulve cave. Ariño and Baños de Segura thermal springs are also situated.*

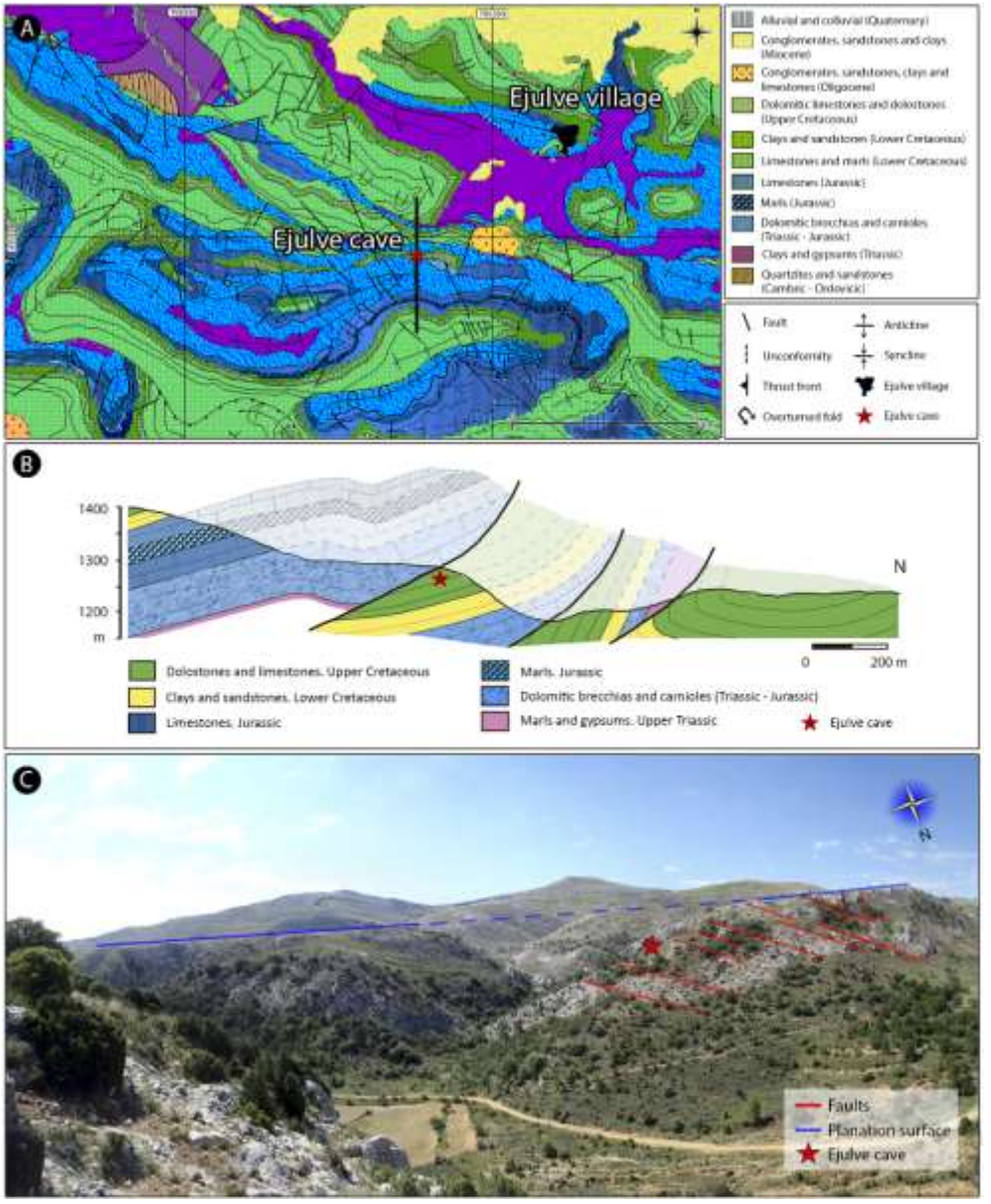

Figure 4.2. *Geological setting of the Ejulve cave. (A) Geological mapping, (B) geological cross section and (C) main geological and geomorphological features around the cave.*

4.3 Material and methods

4.3.1. Survey and sampling

A first detailed cave recognition was carried out using the Ejulve cave topographic maps produced by Gisbert and Carvajal (1993) and Castellano et al., (2015). Some dissolutional features, different types of speleothems, common fault planes and large breakdown deposits are remarkable elements identified in the cave. In order to evaluate the control of the fault net on cave pattern, a total of 31 major fractures were measured and represented in a rose diagram using Stereonet software (Allmendinger et al., 2012; Cardozo and Allmendinger, 2013).

In addition, a variety of morphological features of Ejulve cave were inventoried and described at different scales (cave pattern and cave relief) following descriptions by Ford and Williams (2007), Klimchouk (2009) and Dublyansky (2013). Several samples were collected and identified in Table 4.1. Carbonate blades projected from the cave walls as boxwork formations were also sampled (ID#1-10 in Table 4.1). Additionally, carbonate speleothems including stalagmites (ART and HOR) and farmed carbonate (ID#11-25), botryoidal deposits (ID#26-33), carbonate crust (ID#34-44), carbonate spars (ID#45-50) and acicular crystals (ID#51-57) were collected (Table 4.1). Finally, the dolomitic host rock (ID#58-66) was also sampled. Details of samples and subsamples are reported in Table 4.1. Powder subsamples for X-Ray diffraction (XRD), stable isotope composition and U-Th dating were retrieved using a microdrill. Also, a petrographic study of carbonate samples was carried out using thin sections.

4.3.2. Analytical techniques

Mineralogical semiquantitative composition was determined by powder X-ray diffraction (XRD) using DIFFRACplus evaluation package. The analyses (45 samples) were performed at Jaume Almera Institute (ICTJA-CSIC, Barcelona) with a Bruker AXS D5005 set up theta-2theta geometry, with a Cu X-ray tube of up to 2.2 kW. The fabrics of carbonate samples were described using observations from a petrographic microscope, according the terminology of (Frisia et al., 2000; Frisia and Borsato, 2010; Frisia, 2015). Thin sections were made at University of Zaragoza (Servicio General de Apoyo a la Investigación-SAI). A total of 56 samples were analyzed for stable isotope compositions ($\delta^{18}O$ and $\delta^{13}C$) at University of Barcelona (Scientific-Technical Services) using a Finnigan-MAT 252 mass spectrometer coupled to a Kiel Carbonate Device I. Standards were run every 6 samples with a reproducibility better than 0.03‰ for $\delta^{13}C$ and 0.06‰ for $\delta^{18}O$. Isotope values are reported as ‰ with respect to the V-PDB standard. U-Th analyses (6 samples) were performed using a MC-ICP-MS (Thermo-Finnigan Neptune) at Xian Jiaotong University

(China) following the methodology described in Cheng et al., (2013).

4.4 Results

4.4.1 Cave morphology

4.4.1.1 Cave pattern

Ejulve cave is located very close to the current topographic surface and is overlaid by ~10 m of carbonate rock. The cave is composed of 794 m of galleries, reaching a maximum depth of 55 m. The galleries display a maze network made of irregular chambers interconnected by intricate passages. The three-dimensional pattern shows dominant NW-SE and NE-SW trends forming an angular grid of connected passages (Fig. 4.3.A) controlled by major faults. The dominant fractures run NW-SE while secondary fractures are NE-SW and W-E oriented (Fig. 4.3.A, B). The fracture network is complemented with nearly horizontal faults (Fig. 4.3.B) controlling the shape and size of chambers. Size (height x length x width) of the two largest chambers are 31 m x 16 m x 9 m and 15 m x 23 m x 10 m according to Gisbert and Carvajal (1993). The initial cave size was probably enhanced due to breakdown processes guided by faults as shown by large blocks that detached from the ceiling and accumulated at the bottom of the rooms. Talus deposits related to cataclastic fault breccias have been also identified in chambers of the lower levels of the cave.

4.4.1.2 Cave morphologies

Boxwork formations constitute a network of centimetric-to-decimetric mineral blades projected from cave walls (Fig. 4.4.A) widely distributed throughout Ejulve cave. The blades are composed of calcite-dolomite crystals and kaolinite, with pores lined with calcite and dolomite crystals (Table 4.1). Texturally, a wide-open fabric made of micro-blades and big pores has been identified. The average $\delta^{18}O$ value is -6.4‰, ranging from -5.6‰ to -7.2‰. The average $\delta^{13}C$ value is -5.6‰, ranging from -4.5‰ to -6.1‰ (Table 4.1; Fig. 4.5). The $\delta^{18}O/\delta^{13}C$ diagram (Fig. 4.5) shows that the isotopic values of precipitate blades occupy an intermediate position between the cave deposits (secondary carbonate) and the dolomitic hostrock (see discussion section), displaying a weak correlation using Spearman rank (ρ=0.34) with low statistical significance (p-value=0.34, n=10).

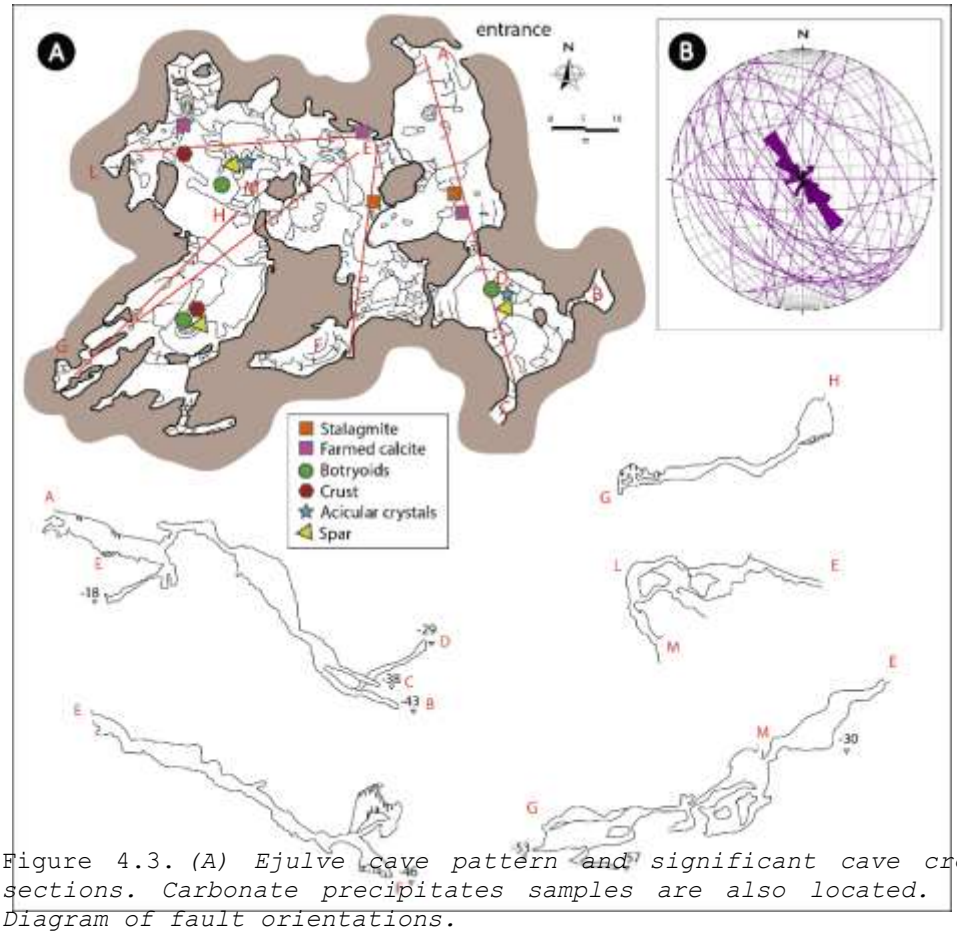

Figure 4.3. *(A) Ejulve cave pattern and significant cave cross sections. Carbonate precipitates samples are also located. (B) Diagram of fault orientations.*

In the central areas of the cave, some ascending tubes of several meters long with decimetric subcircular sections have been identified on cave ceilings, connecting different nearby chambers (Fig. 4.4.B). Occasionally, these tubes display a succession of ascending ceiling cupolas. Other remarkable morphologies of Ejulve cave are pendants and cusps projected downwards from cave ceilings. The shapes of bedrock projections vary between irregular and rounded (pendants) (Fig.4.4.C, D and F) to pointed angular (cusps) (Figure 4.4.E).

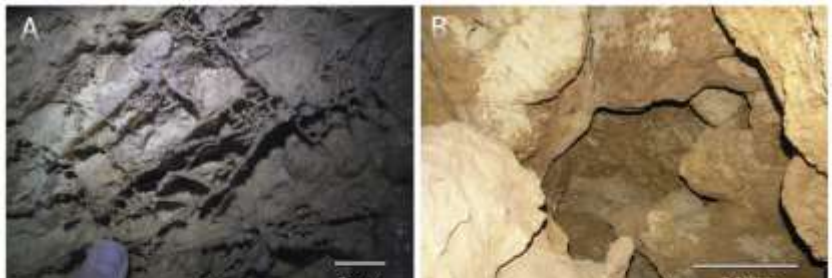

Figure 4.4. *Cave relief morphologies suggestive of hydrothermal origin identified in the Ejulve cave. Boxwork formations (A), tubes with rising ceiling cupolas (B), pendants (C, D, F), cusps coated with botryoidal carbonate deposits (E), spongework (G), and microcorrosion features (karren) affecting dolomitic bedrock lined with botryoidal laminated carbonate (H).*

The surface of the cups, decimetric-to-metric in scale, is normally coated by carbonate speleothems. Among the dissolution morphologies identified in Ejulve cave, the spongeworks stand out. These consist of irregular decimetric frameworks formed in the dolomitic bedrock that are composed by a cluster of irregular interconnected voids (Fig. 4.4.G).

In cases, some bubble trails and pockets scarcely developed are also identified. Finally, some microcorrosion features (karren) affecting the bedrock surfaces are commonly observed

in polished slabs and thick sections, usually covered by carbonate speleothems (Fig.4.4.H). Remarkably, dissolution morphologies related to vadose water flows are absent.

4.4.2 Cave deposits

In general, Ejulve Cave is moderately decorated with speleothems (Fig. 4.6.A). Interestingly, neither allochthonous nor autochthonous fluvial deposits related to running water have been identified in Ejulve cave. Modern calcite precipitation is relevant and shows mean $\delta^{18}O$ value of -8.3 ‰, ranging from -7.3 ‰ to -9.3 ‰, and mean $\delta^{13}C$ value of -9.9 ‰, ranging from -7.2 ‰ to -11.5 ‰ (Pérez-Mejías et al., 2018).

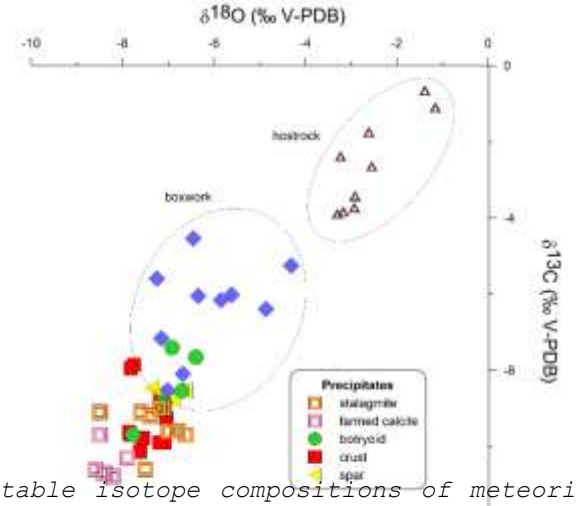

Figure 4.5. *Stable isotope compositions of meteoric speleothems, boxwork blades and dolomite bedrock. Note the correlation of isotope values from boxwork samples and their intermediate position of between dolomite bedrock and the epigenic precipitates.*

Stalagmites and stalactites (Fig. 4.6.A), flowstones and columns are frequent in the upper chambers and galleries of the cave. Several stages of stalagmite growth have been differentiated during MIS 8 to MIS 7e (stalagmite ART) (Pérez-Mejías et al., 2017), the last glacial cycle (MIS 5 - MIS 3) and the Holocene (stalagmite HOR) (Moreno et al., 2017).

Stalagmites are made of calcite and high-magnesium calcite (Table 4.1), displaying a wide variety of columnar (short, elongated columnar, microcrystalline, radiaxial and fascicular types) (Fig. 4.7.B) and dendritic fabrics. The selected samples of stalagmites ART and HOR (Moreno et al., 2017; Pérez-Mejías et al., 2017) exhibit mean $\delta^{18}O$ values of -7.4 ‰ and -7.2 ‰, for

ART and HOR respectively (Table 1; Fig. 4.5). The mean $\delta^{13}C$ values are -9.6 ‰ and -9.2 ‰, for ART and HOR respectively.

The presence of other cave precipitates is also significant in Ejulve cave. Botryoidal deposits, carbonate crust, acicular crystals and carbonate spars are very common and distributed throughout the cave (Fig. 4.3). Botryoidal deposits (coralloid or popcorn) are commonly centimetric in size, globular precipitates on the bedrock and sometimes on pendants, that appear in chambers and passages in the mid-to-upper sections of the cave (Fig. 4.4.E and 4.6.B,C,D). Botryoids are principally made of calcite and high-magnesium calcite (Table 1), with minor dolomite and show nucleus of columnar feathered fabric (Fig. 4.7.C) surrounded by laminae of alternate micrite and columnar elongated fabrics (Fig. 4.7.D).

The botryoidal deposits of Ejulve cave exhibit mean $\delta^{18}O$ values of -7.0 ‰, ranging from -6.4 ‰ to -7.8 ‰ (Table 4.1; Fig. 4.5). The average $\delta^{13}C$ value is -8.5‰, ranging from -7.4 ‰ to -9.7 ‰. The ages of three botryoidal speleothems are 449±17.5 kyr, 238.2±1.9 kyr and 155.9±2.2 kyr (Tables 4.1 and 4.2).

Carbonate crusts are centimetric coatings (up to 6 cm thick) covering cave walls and irregular bedrock morphologies with mammillary shape in surface (Fig. 4.6.E). The internal laminae are occasionally merged in microstratigraphic units separated by unconformities. Coatings are made of calcite and high-magnesium calcite, displaying columnar (short, elongated and microcrystalline) and mosaic fabrics. Sparse dolomite has been also identified. The mean $\delta^{18}O$ value is -7.5 ‰, ranging from -7.1 ‰ to -7.9 ‰ (Table 4.1; Figure 4.5). The mean $\delta^{13}C$ value is -9.2 ‰, ranging from -7.9 ‰ to -10.1 ‰. The age of one carbonate crust sample is 639.1±160.7 kyr (Tables 4.1 and 4.2).

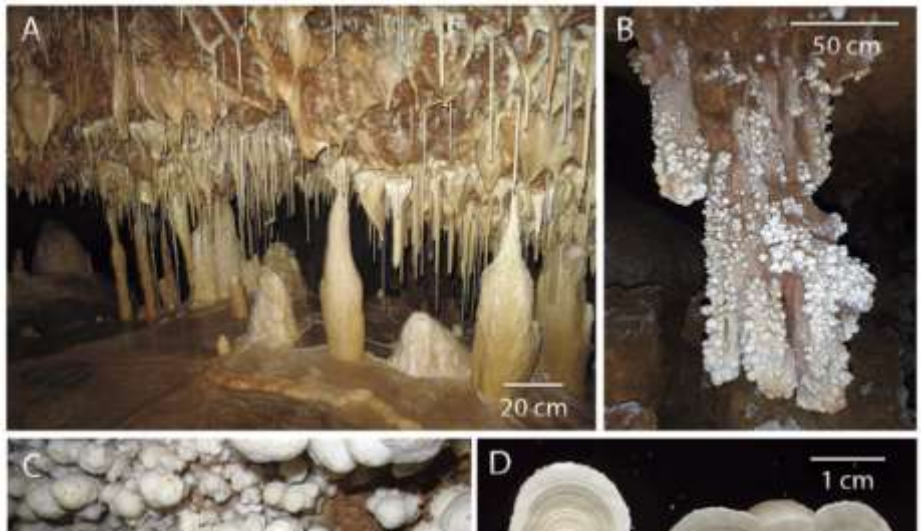

Figure 4.6. *Subaerial cave deposits identified in Ejulve cave. Stalagmites, stalactites, soda-straws and gours (A), botryoidal deposits (B, C, D), carbonate crusts (E), crystalline acicules (F, G) and carbonate spars (H).*

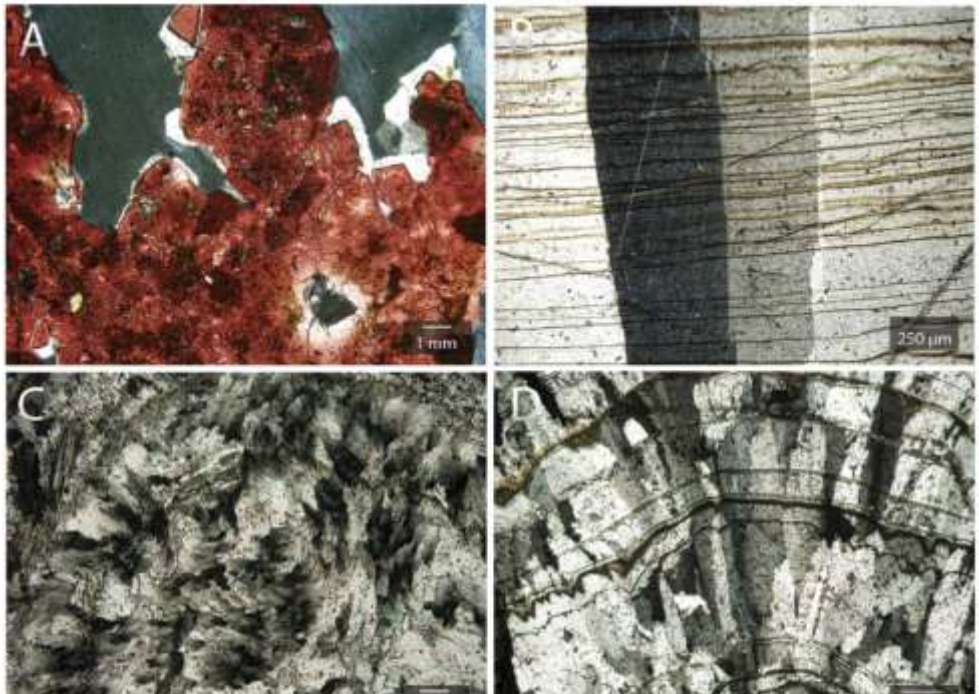

Figure 4.7. (A) Microscopic open framework of crossed precipitate boxwork blades. Pores are lined by calcite (red dyed) and dolomite (crossed polars). Carbonate speleothem fabrics. (B) Calcite columnar elongated (crossed polars) (ID#16, Table 1). (C) Calcite columnar feathered from the nucleus of a spherulitic growth (botryoid) (crossed polars) (ID#26, Table 1). (D) Calcite columnar elongated from the laminated coating of a spherulitic growth (botryoid) (crossed polars) (ID#30, Table 1). (E) Fan ray fabric made of aragonite crystalline needles parallel polars) (ID#57, Table 1). (F) Rhombohedral faces from a calcite spar (parallel polars) (ID#45, Table 1).

ID	Sample	Sub	Type	Fabric	Mineralogy (%)					$\delta^{18}O$ ‰ VPDB	$\delta^{13}C$ ‰ VPDB	Age (kyr)
					calcite	calcite -Mg	aragonite	dolomite	kaolinite			
1	EJ-RA	a	boxwork		80			20		-6.4	-6.1	
2	"	b	"							-5.6	-6.0	
3	"	c	"							-7.2	-5.6	
4	"	d	"							-6.5	-4.5	
5	GOT-1		"		46			54		-4.3	-5.3	
6	GOT-2		"		48			52		-5.9	-6.2	
7	HOJ	a	"		81			13	6	-6.7	-8.1	
8	"	b	"		88			12		-7.0	-8.5	
9	HUE-2		"		61			34	5	-4.9	-6.4	
10	HUE-3		"		59			37	4	-7.2	-7.2	
11	ART	a	stalagm.	columnar (microcrystalline)	100					-8.5	-9.1	239.3 ±2.2
12	"	b	"	columnar (elongated)	100					-7.0	-9.6	233.9 ±2.5
13	"	c	"	"		100				-7.5	-10.6	236.7 ±2.7
14	"	d	"							-7.1	-9.0	262.7 ±3.2
15	"	e	"							-6.8	-9.6	218.2 ±2.0
16	HOR	a	"	columnar (elongated, microcrystalline)		100				-7.2	-9.0	6.1 ±0.2
17	"	b	"	"		100				-6.6	-9.7	6.1 ±0.1
18	"	c	"	columnar (elongated, microcrystalline), dentritic	100					-7.4	-9.2	2.9 ±0.1
19	"	d	"							-7.6	-9.1	3.9 ±0.1
20	"	e	"							-7.4	-9.2	5.0 ±0.1

Table 4.1 *(continue on next pages). Characteristics of boxwork carbonate blades and epigenic carbonate precipitates. Samples of the stalagmites ART and HOR belongs to previous paleoclimate studies (Moreno et al., 2017; Pérez-Mejías et al., 2017) while the samples of farmed-calcite pertain to a wide monitoring survey carried out in Ejulve cave (Pérez-Mejías et al., 2018).*

ID	Sample	Sub	Type	Fabric	Mineralogy (%)					$\delta^{18}O$ ‰ VPDB	$\delta^{13}C$ ‰ VPDB	Age (kyr)
					calcite	calcite -Mg	aragonite	dolomite	kaolinite			
21	EJ-1		farmed calcite		100					-8.5	-9.7	
22	EJ-17		‘’		100					-7.9	-10.3	
23	EJ-20		‘’		100					-8.4	-10.7	
24	EJ-60		‘’		100					-8.6	-10.6	
25	EJ-67b		‘’		100					-8.2	-10.8	
26	H8	a	botryoid	columnar (feathered, elongated), micrite	100							
27	‘’	b	‘’		100					-7.1	-8.8	
28	HR		‘’	columnar (elongated), micrite		100				-6.7	-8.5	
29	Rossetta		‘’	columnar (feathered, elongated), micrite		100				-7.1	-8.9	
30	EJM-1		‘’	‘’		100				-6.9	-7.4	
31	EJM-15		‘’	‘’								238.2 ±2
32	EJM-9		‘’	‘’	96			4		-6.4	-7.7	
33	EJM-19		‘’	‘’	100					-7.8	-9.7	
34	H1	a	crust	columnar (elongated, microcrystalline), mosaic		100				-7.1	-8.7	
35	H1	b	crust			100				-7.8	-7.9	
36	‘’	c	‘’		100					-7.8	-7.9	
37	H4	a	‘’	columnar (feathered, elongated), micrite, mosaic	100					-7.9	-9.6	639.1 ±161
38	‘’	b	‘’							-7.8	-9.7	
39	‘’	c	‘’							-7.6	-10.1	
40	H6	a	‘’	columnar (feathered, elongated), micrite	100					-7.1	-9.9	
41	‘’	b	‘’		100					-7.2	-9.9	

ID	Sample	Sub	Type	Fabric	Mineralogy (‰)					$\delta^{18}O$ ‰ VPDB	$\delta^{13}C$ ‰ VPDB	Age (kyr)
					calcite	calcite -Mg	aragonite	dolomite	kaolinite			
42	H9	a	‘’	columnar (elongated, microcrystalline), mosaic		100				-7.1	-9.2	449 ±17
43	‘’	b	‘’		100					-7.2	-8.8	
44	‘’	c	‘’		100					-7.6	-9.8	
45	H2		spar	columnar (elongated, microcrystalline)	100					-7.2	-8.8	169.8 ±2.3
46	H3		‘’	‘’		96		4		-6.6	-8.5	
47	H5	a	‘’	‘’		96		4		-6.9	-8.7	551.1 ±77
48	‘’	b	‘’	‘’						-7.4	-8.5	
49	‘’	c	‘’	‘’						-7.2	-8.5	
50	EJM-18		‘’	‘’		100						155.9 ±2.2
51	EJMa-1		acicular	fans (rays, circular)	19		78	35				
52	EJMa-3		‘’			62	26	12				
53	EJMa-4		‘’	fans (rays, circular)		65	35					
54	EJMa-5		‘’			80	16	4				
55	EJMa-15		‘’		30		70					
56	EJMa-16		‘’			40	60					
57	EJMa-19		‘’	fans (rays, circular)	100							
58	dol-1		host rock							-3.2	-3.9	
59	dol-2		‘’							-3.3	-3.9	
60	dol-3		‘’							-2.9	-3.5	
61	dol-4		‘’							-2.9	-3.8	
62	dol-H2	a	‘’							-1.2	-1.1	
63	‘’	b	‘’							-1.4	-0.7	
64	dol-H3		‘’							-2.6	-2.7	
65	dol-H9	a	‘’							-3.2	-2.4	
66	**‘’**	b	**‘’**							**-2.6**	**-1.8**	

Acicular crystals (crystalline needles) are millimetric in size and grow on the bedrock or on botryoidal deposits (Fig. 4.6.F,G). They are mostly made of aragonite, although calcite, high-magnesium calcite and dolomite have been identified as minor components (Table 4.1). Microfabric of grouped needles is made of fans (rays and acicular) (Fig. 4.7.E).

Carbonate spars are present as crystals millimetric-to-centimetric in size with rombohedral or nailhead developments that mainly grow on the bedrock, breakdown blocks or in places are linked to botryoids (Fig. 4.6.H). They are common in the floors of the mid-to-lower sectors of the cave. Although the spars are mostly composed of calcite, small amounts of dolomite have been also identified (Table 4.1). Spar crystals are made of columnar elongated and columnar microcrystalline fabrics (Fig. 4.7.F). The mean $\delta^{18}O$ value is -7.1 ‰, ranging from -6.6 ‰ to -7.4 ‰ (Table 1; Fig. 4.5). The mean $\delta^{13}C$ value is -8.7 ‰, with -8.5 ‰ maximum and -8.9 ‰ minimum values. The age of two carbonate spar samples are 551.1±76.6 kyr and 169.8±2.3 kyr (Tables 4.1 and 4.2).

Sample Number	^{238}U (ppb)	^{232}Th (ppt)	^{230}Th / ^{232}Th (atomic x10^{-6})	$\delta^{234}U$* (measured)	^{230}Th / ^{238}U (activity)	$\delta^{234}U_{Initial}$** (corrected)	^{230}Th Age (yr BP)*** (corrected)
H2	63.8 ±0.0	6745 ±135	135 ±3	74.1 ±1.4	0.8659 ±0.0020	120 ±2	169761 ±2258
H4	56.8 ±0.0	294 ±6	3278 ±70	22.8 ±1.4	1.0295 ±0.0029	138 ±81	639084 ±160696
H5	38.1 ±0.0	3037 ±61	211 ±4	18.4 ±1.6	1.0195 ±0.0038	87 ±22	551089 ±76602
H9	70.8 ±0.1	18983 ±380	64 ±1	37.2 ±1.2	1.0356 ±0.0023	132 ±8	448985 ±17453
EJM-15	92.0 ±0.1	140 ±3	10151 ±228	45.8 ±1.1	0.9391 ±0.0018	90 ±2	238181 ±1948
EJM-18	47.9 ±0.0	5740 ±115	131 ±3	206.4 ±1.4	0.9558 ±0.0032	320 ±3	155904 ±2236

^{230}Th dating results. The error is 2□□□Sample number are refered to mm from base
*□^{234}U = ([^{234}U/^{238}U]$_{activity}$ – 1)x1000.
** □$^{234}U_{initial}$ was calculated based on ^{230}Th age (T), i.e., □$^{234}U_{initial}$ = □$^{234}U_{measured}$ x e$^{□234xT}$.
Corrected ^{230}Th ages assume the initial ^{230}Th/^{232}Th atomic ratio of 4.4 ±2.2 x10^{-6}.
Those are the values for a material at secular equilibrium, with the bulk earth ^{232}Th/^{238}U value of 3.8.
The errors are arbitrarily assumed to be 50%.
***B.P. stands for "Before Present" where the "Present" is defined as the year 1950 A.D.

Table 4.2. *^{230}Th dating results of some epigenic carbonate precipitates. Sample names are indicated in Table 4.1.*

4.5. Discussion

4.5.1 Evidences of Ejulve cave speleogenesis

4.5.1.1 Cave morphologies

Regional geological features (stratigraphy, tectonic structure, geomorphology and hydrogeology) must be considered to discern between hypogenic and epigenic speleogenesis (Klimchouk, 2017). In the case of Ejulve cave, the permeability of the stratigraphic sequence shows heterogeneity with depth. Triassic-Jurassic dolomite breccias and carnioles are the most permeable unit, whereas Jurassic marls are the most impermeable strata. Regarding the structure, it is remarkable that Jurassic marls thrusts the Upper Cretaceous dolomitic limestones and dolostone sequence where the cave was formed. Hence, both local stratigraphy and regional structure allow confined conditions that would facilitate the formation of Ejulve cave in a high-pressure hypogene karst setting related to ascending water (Ford and Williams, 2007; Klimchouk, 2009; Palmer, 2011; Klimchouk, 2013).

Careful recognition of morphological cave features is determinant to assess the origin of cavities (Palmer, 2011). Importantly, dissolutional morphologies related to vadose/epigene running water processes are absent in Ejulve Cave. In contrast, cave morphologies commonly identified in hypogenic karstic environments are relatively abundant.

The carbonate blades, today forming part of boxwork formations, were precipitated formerly in discontinuities and joints of the dolomitic bedrock before cave formation. These carbonates precipitated probably during Upper Miocene, after the orogenic alpine phase occurred during Oligocene and Lower Miocene (Simón et al., 2002). The isotopic composition shows higher mean values of $\delta^{18}O$ (-6.2 ‰) and $\delta^{13}C$ (-6.4 ‰) than other cave deposits in Ejulve, but lower than dolomite hostrock (Fig. 4.5). Thus, the distribution of values in the $\delta^{18}O$-$\delta^{13}C$ diagram between cave deposits and hostrock may indicate the contribution of relatively low temperature water and the significant input of CO_2 from the dolomitic bedrock (mean value $\delta^{13}C$ of -2.6 ‰). High-temperature carbonate formed from freshwater-type aquifer water generally shows lower $\delta^{18}O$ values (e.g. <-10 ‰), because of the effect of temperature on the oxygen isotopes fractionation during carbonate precipitation, and higher $\delta^{13}C$ (0 ‰) due to CO_2 contributions from the bedrock or deep processes (Bakalowicz et al., 1987; Orvošová et al., 2004; Spötl et al., 2009; Gradziński et al., 2011; Gázquez et al., 2018). The comparison between isotopic composition of blades and hydrotermal carbonates allows discarding the role of hydrothermalism in the precipitation of carbonate blades. The petrography of boxwork formations shows the presence of detrital

crystals of dolomite suggesting the incorporation of dolomite hostrock components to the final precipitated carbonate blades. Likewise, the moderate correlation coefficient between $\delta^{18}O$ and $\delta^{13}C$, in spite of the low statistical significance in a small number of analyses (n=10), could also be interpreted in terms of kinetic fractionation during carbonate deposition (e.g. (McDermott et al., 2006)) related probably to enhanced degassing processes (Day and Henderson, 2011).

On the other hand, the arrangement of the cave passages in Ejulve Cave exhibits a maze network developing an angular grid (Fig. 4.3), rather common of hypogene cave systems, related to ascending flow through major fractures (e.g. Bakalowicz et al., 1987; Palmer, 1991; Klimchouk, 2009; Dublyansky, 2013). Chambers connected by passages formed by convection processes in the phreatic zone (Dublyansky, 2013). Besides, increased size of chambers by condensation-corrosion processes in subaerial conditions would occur during more recent phases (Audra et al., 2002; 2009).

Other cave morphologies (Fig. 4.4) suggesting a hypogene origin under subaqueous high-pressure conditions have been identified in Ejulve cave. Ascending phreatic flows were responsible for the development of ceiling rising channels with associated chains of cupolas (Klimchouk, 2009; Dublyansky, 2013). These features are included in the transitional wall and ceiling features component of the morphologic suite of rising flow (MSRF), described in other hypogene cave systems elsewhere (Klimchouk, 2009). Bedrock partitions including ceiling pendants and cusps, develop basically by enlargement of adjacent cavities under both subaqueous and subaerial conditions (Dublyansky, 2013). Regarding the smaller scale morphological features identified, spongeworks (Palmer, 2011; Dublyansky, 2013) and bubble trails (Audra et al., 2002; Forti et al., 2002; Gázquez et al., 2015) occur in a subaqueous setting whereas boxwork formations and corrosion features (Palmer, 1991; Audra et al., 2002; Audra et al., 2009; Dublyansky, 2012; Dublyansky, 2013) form under subaerial conditions.

In regard to the isotopic composition of hydrothermal processes, it is accepted that the stable isotope values of the carbonate hostrock may be altered by circulation of hot water (Dublyansky, 2012; 2013). The surface of the dolomite bedrock in Ejulve cave does not show significant weathering features. Besides, microscopic recognition of the samples does not evidence hostrock alteration. This may indicate that hypogene processes in Ejulve cave did not occur at high temperature. Nevertheless, the absence of isotope alteration of the bedrock does not necessarily point out to a non-thermal cave origin as has been evidenced in other caves (Dublyansky, 2012; Spötl et al., 2016).

Some cave morphologies in ceilings may have not been preserved due to the gravitational processes producing breakdown deposits guided by nearly horizontal faults. This circumstance is common when hypogene speleogenesis and tectonic uplift occur simultaneously (Dublyansky, 2013), probably related to the transition from confined to unconfined hydrogeological conditions. Overprinting of former hypogenic morphologies by subsequent epigenic processes can be common in this type of karstic environments (Klimchouk, 2017).

Both cave pattern and cave morphologies in Ejulve cave are, thus, suggestive of a hypogene origin that formed under high pressure in a low-temperature hydrothermal karst setting. This is a feasible hypothesis attending to the regional thermal springs observed, an indirect evidence of hydrothermal cave speleogenesis (Dublyansky, 2013). Current geothermal flow in the southeastern sector of Iberian Range derives from infiltrated meteoric water and emerges driven by hydraulic gradients, where fast water circulation occurs through favorable vertical structures that affect mainly to hydrostratigraphic favorable units (Triassic-Jurassic dolomite breccias and carnioles) (Sánchez et al., 2004). Here, we hypothesize that the formation of Ejulve cave could have happened under low-temperature hydrothermal karstic conditions. Meteoric infiltrated waters would increase the temperature according to the crustal geothermal gradient (Sánchez et al., 2004). According to the water source and flow, a meteoric regime (Klimchouk, 2017) is suggested to govern the regional hydrogeological pattern. This flow regime is very common in post-orogenic areas where infiltrated waters reach deep zones, when heterogeneous stratigraphic permeability and convection flow is related to the topography (Klimchouk, 2017). However, thermal crust anomalies derived from crustal extension and volcanism in northeaster Spain during Mio-Pliocene (Lewis et al., 2000) cannot be ruled out.

4.5.1.2 Cave deposits

Ejulve cave hosts a wide variety of carbonate speleothems, most of which are clearly related to infiltration of meteoric water under epigenic karst conditions. Remarkably, neither autochthonous nor allochthonous fluvial deposits are present. In contrast, breakdown deposits are frequent as it is indicated above.

The growth of some stalagmites from MIS 8 to the present has been previously studied (Moreno et al., 2017; Pérez-Mejías et al., 2017). Other precipitates such as botryoidal calcite deposits (or coralloids) are very common in Ejulve cave (Fig. 4.6). Besides, calcite crusts, aragonite acicules and calcite spars have been also identified (Fig. 4.6). These precipitates

are common in shallow hydrothermal karst environments (e.g. Dublyansky, 2012) formed from saturated water vapor in subaerial environments and from saturated ascending warm water in low hydrodinamic subaqueous conditions (Bakalowicz et al., 1987; Audra et al., 2002; Gradziński et al., 2011; Leél-Őssy et al., 2011; Dublyansky, 2012). Nevertheless, these carbonate precipitates also appear frequently in unconfined epigenic karst environments (e.g. (Ford and Williams, 2007)). Caddeo et al. (2015) explains the formation of coralloids as the result of the effect of degassing, evaporation and diffusion mechanisms, and Vanghi et al. (2017) propose the role of hydroaerosol produced by dripping water and the evaporation regulated by cave ventilation. On the other hand, formation of aragonite acicules requires active degassing and evaporation processes (Frisia et al., 2002).

The stable isotope composition of botryoidal deposits, carbonate crusts and spars (Fig. 4.5) is a very useful proxy to elucidate the hydrothermal/low-temperature origin of these calcite precipitates. Mean $\delta^{18}O$ values are -7.0 ‰ (botryoids), -7.5 ‰ (crusts coatings) and -7.1 ‰ (spars) and mean $\delta^{13}C$ values are -8.5 ‰ (botryoids), -9.2 ‰ (crusts coatings) and -8.7 ‰ (spars). These values, are very close to those expected for calcite formed at relatively cold temperature and stalagmites growing during MIS 8 to MIS 7e (mean values of $\delta^{18}O$ = 7.4 ‰ and $\delta^{13}C$ = -9.6 ‰) (Pérez-Mejías et al., 2017) and Holocene (mean values of $\delta^{18}O$ = -7.2 ‰ and $\delta^{13}C$ = -9.2 ‰) (Moreno et al., 2017) (Fig. 4.5). The differences in $\delta^{18}O$ from the different precipitates can be explained by carbonate precipitation in non-equilibrium conditions because of evaporation and/or enhanced CO_2 degassing processes. Therefore, stable isotopic data suggest a meteoric origin rather than thermal water contributions for the formation of these speleothems. Comparison with isotopic data from hydrothermal carbonates in other systems worldwide (normally $\delta^{18}O<10‰$) also points to a non-hydrothermal origin of Ejulve precipitates (Bakalowicz et al., 1987; Orvošová et al., 2004; Spötl et al., 2009; Gradziński et al., 2011; Gazquez et al., 2018). Precipitation of botryoids, carbonate crusts and carbonate spar aggregates occurred from 639.1±160.7 kyr to 155.9±2.2 kyr (Table 4.2), simultaneously to the growth of some vadose speleothems from MIS 8 to the present (Moreno et al., 2017; Pérez-Mejías et al., 2017) (Table 4.1).

Concerning hydrochemistry, both basic mineralogy (Table 4.1) and fabrics (Fig. 4.7) of cave precipitates in Ejulve cave suggest waters enriched in Mg derived from the dolomite bedrock. Thus, feathered columnar and elongated columnar may be formed because of the presence of Mg (Frisia and Borsato, 2010; Frisia, 2015). High Mg content also favors the formation of aragonite acicules. Aragonite precipitates in caves from Mg-rich waters exhibiting low saturation with respect to calcite (Spötl et al.,

2016), and can last over time (10^5-10^6 years) despite the tendency to transform into calcite under superficial conditions (Alonso-Zarza et al., 2011). Dolomite has been identified in acicular, botryoid and spar precipitates but is not quantitatively relevant. Although, dolomite formation in karstic environments remains unclear and can be influenced by microbial activity (Alonso-Zarza and Martín-Pérez, 2008; Jones, 2010), its occurrence as detrital component in Ejulve cave precipitates derived from the host rock cannot be totally discarded.

4.5.2 Geomorphic evolution of Ejulve cave

Successive stages in the speleogenesis of Ejulve cave can be differentiated attending to the geomorphic arrangement of cave morphologies and cave deposits discussed above. Furthermore, evolutionary stages can be contextualized in the regional landscape framework (Fig. 4.8). The earliest phase involved the rising flow favored by the hydraulic gradient in a confined aquifer, and the precipitation of carbonate in stratigraphic discontinuities and joints of the bedrock. These processes occurred tentatively during the Upper Miocene after alpine tectonic deformation.

During the second stage (Fig. 4.8) the passages and cave chambers developed, as well as the network maze and cave morphologies (boxwork formations, tubes with rising ceiling cupolas, pendants and cups, spongeworks and microcorrosion features). Ascending water-flows in hypogene karst conditions (subaqueous and subaerial) were involved in this stage. The cave formation occurred probably during Mio-Pliocene, coinciding with the development of the regional planation surface (Peña et al., 1984; Gutiérrez and Peña, 1994).

The third stage coincides with the final stage of development of the planation surface (Upper Pliocene) (Peña et al., 1984; Gutiérrez and Peña, 1994). Lowering of the topographic surface by denudation led to the beginning of cave exhumation. Subsequent landscape partition leaded by tectonics (Gutiérrez et al., 2008) occurred and the incision of the fluvial network related to regional uplifting started at 3 Ma (Scotti et al., 2014; Giachetta et al., 2015), causing the beginning of the lowering of the local water table level.

During the final stage the increasing of fluvial incision and the lowering the base level continued. A Quaternary rate of fluvial incision of ~0.6 mm/yr related to uplift is proposed by Scotti et al. (2014). Under epigenic conditions a wide variety

of subaerial and subaqueous vadose speleothems precipitated in the cave. Common breakdown processes masked some cave morphologies. According to the age of the speleothems, this stage started after than 650 ka and lasts until today (Moreno et al., 2017; Pérez-Mejías et al., 2017).

In summary, the morphologies of Ejulve cave developed under hypogene confined conditions (a low thermal karst setting is not discarded) and cave deposits precipitated under epigenic subaerial conditions in later stages. Then, a switch from hypogene to epigenic hydrogeological setting took place. This speleogenetic change is common in hypogene caves and is controlled by the synchronous uplift and denudation mechanisms (Klimchouk, 2013). Regional Pliocene-Quaternary denudation, causing an extensive planation surface (Peña et al., 1984; Gutiérrez and Peña, 1994), was driven by crustal doming and uplift (Simón, 1989; Lewis et al., 2000; Giachetta et al., 2015) and led to exhumation of the karst.

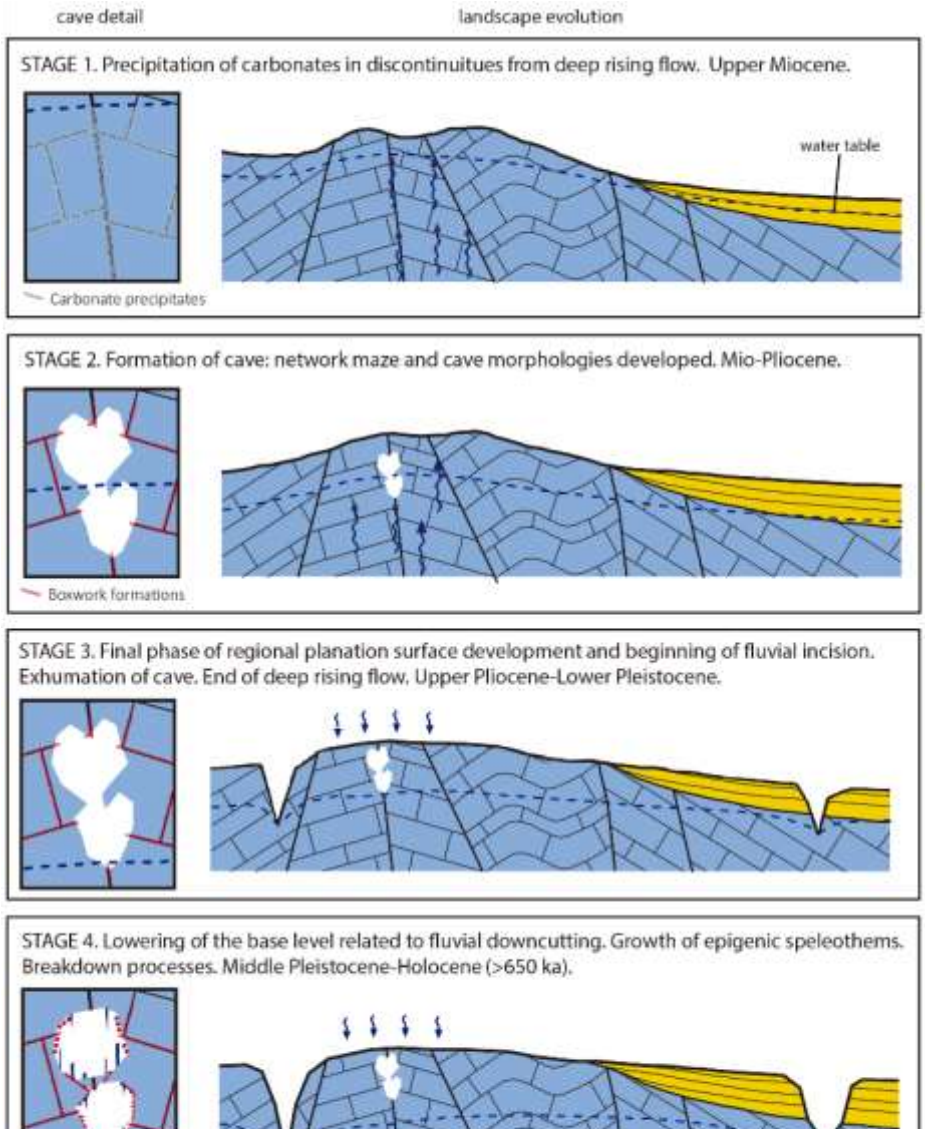

Figure 4.8. Geomorphic schematic evolution of Ejulve cave. Successive stages from confined hypogene to unconfined epigenic conditions are differentiated and related to regional landscape evolution. Scale is not adjusted.

4.6. Conclusions

We provide the first evidence for hypogene speleogenesis in the SE Iberian Range based on morphologies of Ejulve cave and regional signs of an ancient confined aquifer. We propose a two-stage speleogenetic model composed of a former confined hypogenic setting that probably prevailed during Upper Miocene and Pliocene, and a subsequent unconfined epigenic phase. The switch from hypogene to epigene conditions occurred before 650 kyr BP and was driven by regional geodynamic and geomorphic factors (e.g tectonic uplift and fluvial network incision).

The main signs of hypogene speleogenesis are the arrangement of cave passages in a maze network and cave morphologies, including boxwork formations, tubes with rising ceiling cupolas, pendants and cups, spongeworks and microcorrosion features, most of them formed in phreatic conditions in a confined aquifer. During the more recent epigene stage and once the regional groundwater level abandoned the cave, subaerial carbonate speleothems formed in Ejulve cave, including stalagmites, botryoids, crusts and spars, made of columnar calcite and high-magnesium calcite.

The stable isotope composition of carbonates suggests relative cold temperature formation, similar to the modern cave temperature. This rules out any significant geothermal influence on the cave level during the past 650 kyr, although low-temperature hydrothermal conditions during earlier stages of the Ejulve cave speleogenesis cannot be discarded, as evidenced by modern low-grade hydrothermal springs are present close to Ejulve cave. We conclude that hypogene speleogenesis should be considered as main speleogenetic mechanism that may have generated other caves in this sector of the Iberian Range.

“The cosmos is within us. We are made of star-stuff.

We are a way for the universe to know itself”
-Carl Sagan

Chapter 5

Present-day speleothemic dynamics

Transference of isotopic signal from rainfall to dripwaters and farmed calcite in Mediterranean semi-arid karst

Significance

- *Complete analysis of the* $\delta^{18}O$ *during the full pathway from the rainfall to the farmed calcite.*

- The spatial differences between drip sites within the same cave are also explored, showing small variability among seasonal and seepage drips.

- The seasonality seen in the $\delta^{18}O$ of the rainfall is kept in the $\delta^{18}O$ of the drip waters, but not in the $\delta^{18}O$ of the farmed calcite in a seasonal scale.
- Both $\delta^{18}O$ and $\delta^{13}C$ values are amplified by enhanced degassing kinetics during dry periods.
- The $\delta^{13}C$ values show seasonality with lower values recorded when the soil microbial activity is higher, with increased vegetation activity and water availability.

Abstract
This study was conducted in Ejulve cave (Spain, southwestern Europe) over a period of four years (2013–2016) to identify the factors affecting the isotopic composition of rainfall, dripwaters, and farmed calcite. The results indicate that $\delta^{18}O$ of rainfall in the study area was mainly controlled by the *temperature effect* (r^2 = 0.82, p-value < 0.001) with *source effect* and *amount effect* being secondary controls. Additionally, it exhibited a seasonal pattern with lower values indicated during winter and higher in summer.
The use of effective infiltration to evaluate the recharge of the epikarst is extremely important in semi-arid karst climate conditions. This analysis revealed that while the *amount effect* exerted a moderate control on the annual $\delta^{18}O$ in rainfall, it had a lower influence on the isotopic variability of the rainfall potentially infiltrating the karst aquifer.
The sampling of 12 drip locations in Ejulve cave indicated that seepage and seasonal drips featured similar $\delta^{18}O$ values in dripwaters. The homogenisation process during the infiltration in the epikarst was not complete, therefore, the $\delta^{18}O$ seasonality seen in rainfall was also observed in dripwater $\delta^{18}O$, albeit attenuated and lagged. With the seasonal increase in rainfall in autumn, drip rates of seasonal and seepage groups increased within a few weeks. However, the lower $\delta^{18}O$ of autumn-winter rain was observed in dripwaters with a lag as long as 21 weeks.
The $\delta^{18}O$ in farmed calcite showed a small variation of 0.11‰ while the $\delta^{13}C$ varied seasonally with a variation of about 0.22 ‰ and indicated higher values during summer and autumn and lower values in winter and spring. Seasonal and seepage sites exhibited similar $\delta^{18}O$ variability. However, $\delta^{13}C$ was more positive in seepage sites and was enhanced by degassing kinetics to produce a variability of up to 0.42‰ in contrast to the 0.29‰ observed in the seasonal sites.
The $\delta^{18}O$ of calcite showed dependence on the $\delta^{18}O$ of dripwater with a weak influence of the drip rate. However, $\delta^{13}C$ exhibited a higher correlation with the drip rate and high $\delta^{13}C$ was explained by enhanced degassing and low water availability while

low $\delta^{13}C$ values were in concordance with higher microbial activity, vegetation productivity, and greater water availability. The ventilation of the cave during late autumn through spring favoured the higher calcite deposition rates found during that time.

Keywords
stable isotopes | *precipitation* | *dripwater* | *farmed calcite* | *semi-arid karst*

5.1. Introduction

The study of speleothems as a paleoclimate proxy has increased markedly in the last two decades. Stable isotopes are the most widely used proxy in speleothem studies, however, studies in recent decades have indicated that the interpretation of stable isotopes in speleothems is complex because the climate information encoded in isotopes depends on the setting of the speleothem record (latitude, altitude, temperature, continentality). In addition, the local cave settings and hydrology (thickness of bedrock, infiltration mode, ventilation, prior calcite precipitation) also condition the isotopic signal of speleothems.

Monitoring studies across a range of speleothem-producing geographical areas are fundamental to elucidate these processes. Studies which monitor $\delta^{18}O$ in precipitation ($\delta^{18}O_p$), dripwater ($\delta^{18}O_d$), and the resulting speleothem calcite (as well as its growth rate) provide an understanding of the complete transfer of the signal and yield the most confident interpretations of past climate from speleothem records (Fairchild and Baker, 2012; Genty et al., 2014; Duan et al., 2016; Riechelmann et al., 2017).

The general climatic and environmental factors influencing $\delta^{18}O_p$ are well-known and have been examined in recent reviews (McDermott, 2004; Lachniet, 2009; Pape et al., 2010; Genty et al., 2014). However, the relative importance of these factors varies significantly at regional and local scales. Detailed analyses of processes driving isotopic variation in rainfall in recent years have been conducted at the regional scale in tropical/equatorial climates (Cobb et al., 2007; Lachniet and Patterson, 2009; Wirmvem et al., 2014), climates controlled by the monsoon regime (Breitenbach et al., 2010; Jeelani et al., 2013; Luo et al., 2013; Rai et al., 2014; Guo et al., 2015; Meiliang et al., 2015; Resmi et al., 2016; Zhan et al., 2016), in arid domains (Ma et al., 2012; Feng et al., 2013; Michelsen et al., 2015; Wang et al., 2015; Ren et al., 2017), semi-arid climates (Kebede and Travi, 2012) and in the temperate domain with oceanic climates (Genty et al., 2014; Krklec and Domínguez-Villar, 2014; Stumpp et al., 2014; Affolter et al., 2015; Stoll et al., 2015a; Tyler et al., 2016; Riechelmann et al., 2017), subtropical climates (van Beynen and Febbroriello, 2006; Onac et al., 2008; Lambert and Aharon, 2010; Pape et al., 2010; Feng et al., 2014), and continental (Vodila et al., 2011) and Mediterranean end members (Friedman et al., 1992; Dotsika et al., 2010; Oster et al., 2012; Moreno et al., 2014; Dumitru et al., 2017).

The Spanish Network of Isotopes in Precipitation, part of the IAEA-GNIP (Global Network of Isotopes in Precipitation),

has assessed the contributions of latitude and altitude to spatial variations of rainfall isotopes in Spain (Diaz et al., 2007). The Iberian Peninsula (IP) is characterised by significant diversity of geographic and climatologic features as well as by two different moisture sources (Moreno et al., 2014); therefore, a systematic sampling of precipitation is needed to understand the transfer of variability in $\delta^{18}O_p$ to the cave dripwaters.

While $\delta^{18}O_d$ is expected to be ultimately controlled by $\delta^{18}O_p$, it may also be affected by evaporation in soil and the epikarst, variable transfer of rain to different dripwater sites due to karst hydrology, and the variable homogenisation of precipitation in the karst/epikarst aquifer. In terms of discharge, many caves indicate a strong link between dripwater discharge and rainfall, often indicated by a fast response in drip rates (Baker et al., 1997; Perrin et al., 2003; Cruz et al., 2005b; Lambert and Aharon, 2010; Moreno et al., 2014; Guo et al., 2015).

Additionally, dripwaters show a delay in the isotopic signal by a few months (Jones and Banner, 2003; Onac et al., 2008; Moerman et al., 2014; Van Rampelbergh et al., 2014; Affolter et al., 2015; Comas-Bru and McDermott, 2015) to several years (Genty et al., 2014; Riechelmann et al., 2017). In some cases, dripwaters do not reflect the isotopic variability seen in the rainfall (Chapman et al., 1992; Caballero et al., 1996; Williams and Fowler, 2002; Schwarz et al., 2008; Kluge et al., 2010; Pape et al., 2010; Moquet et al., 2016) or indicate variability induced by evaporation in the soil and the epikarst (Bar-Matthews et al., 1996; Denniston et al., 1999).

The transference of the isotopic signal between precipitation and dripwaters can be affected by processes in the soil and the epikarst (Genty et al., 2014; Duan et al., 2016). In previous studies, seasonal $\delta^{18}O_d$ cycles have been modelled by allowing the value of infiltrating $\delta^{18}O_p$ to be modified by evapotranspiration, calcite dissolution, the residence time of infiltrating water, and mixing of water parcels of different ages (Wackerbarth et al., 2012). Within the cave, different drip points may show different $\delta^{18}O_d$ values due to different patterns of infiltration or the existence of numerous epikarstic microreservoirs (Fuller et al., 2008; Treble et al., 2013; Cuthbert et al., 2014; Duan et al., 2016). The different flow pathways and mixing can produce different $\delta^{18}O_d$ even if fed by the same $\delta^{18}O_p$ (Moerman et al., 2014).

Hence, the characterisation of dripwaters is crucial to identify the drips that have a clear relationship with the climatic signal. Establishing the hydrological response of the cave by coupled measurements of $\delta^{18}O_p$ and $\delta^{18}O_d$ elucidates the

influence of the flow regime in the host rock above the cave and the extent to which $\delta^{18}O_d$ is sensitive to the external rainfall (Baker et al., 2012).

Under equilibrium conditions, the $\delta^{18}O$ of speleothem carbonate ($\delta^{18}O_{ct}$), formed from a given $\delta^{18}O_d$, should depend only on the cave temperature which controls the fractionation between dripwater and calcite. However, previous studies on the $\delta^{18}O$ of farmed calcite have revealed additional kinetic fractionation effects correlated with the calcite deposition rate (Mickler et al., 2006; Feng et al., 2012). In addition, the temperature-dependent fractionation factor observed in some farmed calcites suggests a higher water calcite fractionation factor (potentially due to kinetic fractionation effects) than that observed in laboratory experiments (Tremaine et al., 2011).

Therefore, the study of natural cave calcite precipitation is fundamental to elucidate the processes controlling oxygen isotopic fractionation in speleothems. Moreover, farmed calcite elucidates the controls of carbon isotopic composition of stalagmites and their relationship with drip rate, ventilation, and seasonal temperature cycles outside the cave (Tremaine et al., 2011; Meyer et al., 2014).

In this paper, the results from a four-year monitoring study of isotopes in precipitation, dripwater, and farmed calcite in a cave in northeast Spain are presented. This region is characterised by a strong seasonal Mediterranean climate and the aim of this study was to elucidate the processes by which climate signals may be transferred from the $\delta^{18}O$ of atmospheric precipitation to the $\delta^{18}O$ of modern actively forming speleothem calcite. Additionally, the different factors controlling the $\delta^{18}O$ of rainfall (temperature, amount of rainfall, altitude, and source of moisture), dripwater (drip discharge, degassing, hydrochemistry, and infiltration biased to the wet season), and farmed calcite (growth rate and disequilibrium effects) were addressed. Finally, a detailed study of spatial differences between the isotopic signals of drips and farmed calcite was conducted within a single cave to evaluate the effect of different hydrological pathways through the host rock.

5.2. Site description

Ejulve cave (40°45´34´´N, 0°35´07´´W, 1269 m.a.s.l.) is located in the southwest of Ejulve village, Teruel (Aragón, NE Spain) (Fig. 5.1A). This mountainous region belongs to the Iberian Range and shows a high gradient of altitudes (e.g., 695 m.a.s.l. for Gallipuén, 1601 m.a.s.l. for the Majalinos station) (Fig. 5.1A). Ejulve cave developed from limestones and dolomitic limestones of the Upper Cretaceous age.

The maze passages were 794 m in length and 55 m in depth. The entrance represented the highest point of the cave. The host rock thickness above the cave is reduced, around 10 m. The soils were weakly developed in the study area. The carbonate bedrock was usually exposed above the cave, and two types of patchy aridisols could be recognised (Soil Science Division Staff, 2017): a) shallow (≤ 25 cm) and stony soils developed on the bedrock in high altitude areas, and b) shallow soils developed on the alluvial sediment in low altitude areas. Additionally, there were some abandoned anthropic terraces above the cave.

The scarce soils supported vegetation, such as heliophytic shrubs (*Genista scorpius*, *Thymus vulgaris*, *Rosmarinus officinalis*), sparse evergreen oaks *(Quercus ilex*), and *Pinus halepensis*, that belonged to the mid-Mediterranean and the upper-Mediterranean bioclimatic schemes.

The climate in this area is Mediterranean temperate with strong continentality. The long-term data (Fig. 5.1.B and Table 5.1) at the Gallipuén station indicate an annual temperature of 13 °C with mean values of 22 °C in summer and 5 °C during winter. The mean maximum temperatures reach 9 °C in winter and 30 °C in summer, while the mean minimum reach 0 °C in winter and 15 °C during summer (Table 5.1).

The mean rainfall is 431 mm indicating a climate characterisation close to semi-arid conditions. A few snow storms are known to occur during winter and it is postulated that the soil over the cave could be covered by snow for a few weeks in winter. The potential evapotranspiration (PET) is high throughout the year and higher than the monthly rainfall from March to October (brown area, Fig. 5.1.B).

The climate data from 2010 to 2015 (the period covered in this study) showed some peculiarities that differed from the average long-term climate for the area (Fig. 5.1.C). The minimum temperatures were slightly higher in both winter and summer and the maximum temperatures were also found to be higher in winter (Table 5.1). Consequently, the mean monthly temperatures were slightly higher during the study period (mean = 14.6 ± 0.3 °C, s = 0.8 °C) compared to the long-term data (mean = 13.3 ± 0.1 °C, s = 0.7 °C).

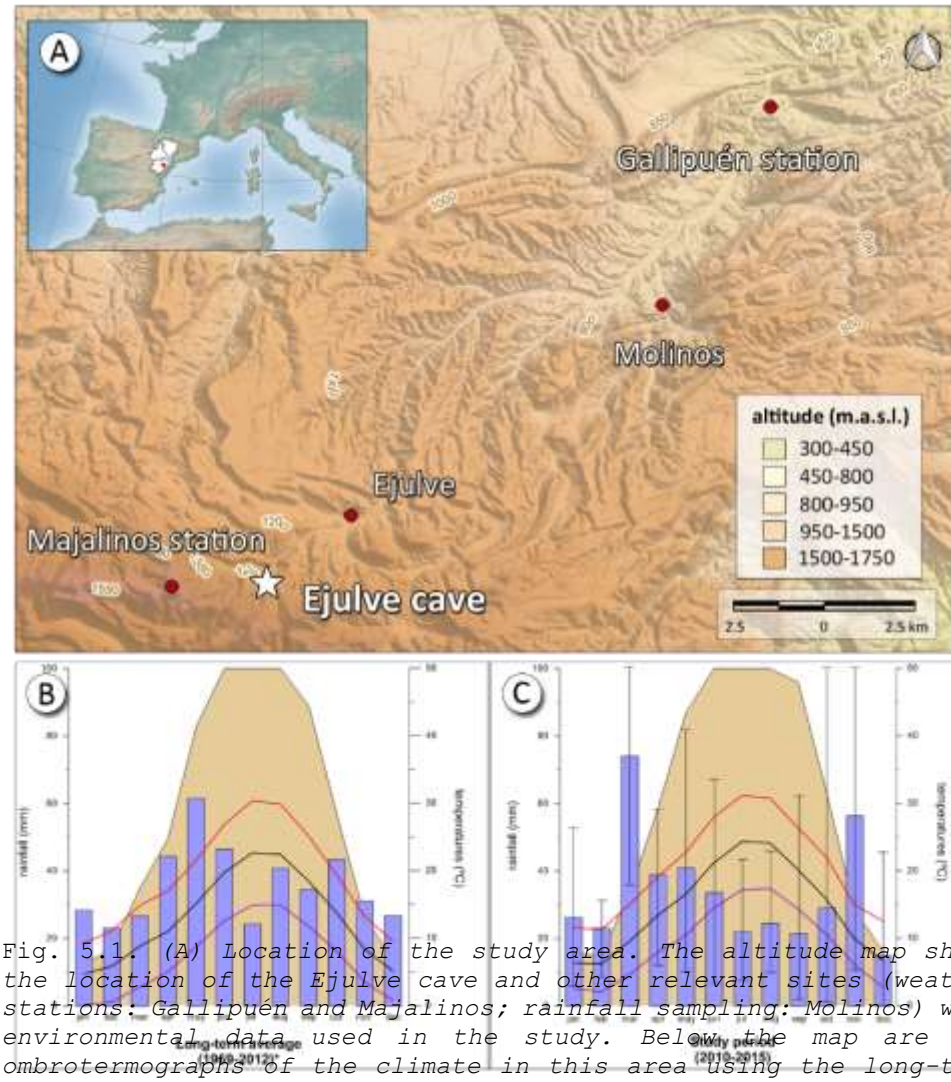

Fig. 5.1. (A) Location of the study area. The altitude map shows the location of the Ejulve cave and other relevant sites (weather stations: Gallipuén and Majalinos; rainfall sampling: Molinos) with environmental data used in the study. Below the map are the ombrotermographs of the climate in this area using the long-term period results (B) and the five-year of the period of study (C) The brown area remarks the potential evapotranspiration, and the lines are the mean values of high, mid and low temperatures –red, black and violet, respectively-). The vertical bars mark the maximum rainfall in the study period during each month.

It is noteworthy that high precipitation seasonality was recorded during the study period indicating drier summers in comparison to the long-time series. Additionally, the inter-annual differences in precipitation should be remarked; the year 2012 was exceptionally dry with only 283 mm precipitation,

representing 65% of the mean rainfall per year. Moreover, October and December were particularly dry during the years 2011, 2013, and 2015 and among the rainiest months in 2012 and 2014 (Table 5.1).

Changes in seasonality between the study period and the long-term data were indicated by the increase in rainfall during November and the dominance of March as the rainy month instead of May (Table 5.1). This recent increase in precipitation during March led to difficulties in characterising it as winter or spring rainfall because the "traditional" rainfall during spring was occurring earlier than usual during the winter period.

Therefore, although the weather in this area is characterised by equinoctial precipitations (i.e., spring and autumn), in this study, autumn to spring was characterised as the wet season, and summer as the dry season. Similar changes in the seasonal precipitation pattern have been observed in the IP during the past decades, notably the reduction of spring as the dominant precipitation season and the increase of rainfall during fall (de Luis et al., 2010).

A few months during the wet season (October, April, and May) indicated mean precipitation values lower than the PET. In these cases, whilst the mean precipitation values were less than the PET, the precipitation overcame the PET in some of the studied years (black bars, Fig. 5.1). Although April and May exhibited more uncertainties with regard to the possibility of infiltration through the epikarst since the maximum rainfall and PET displayed similar values, some infiltration during intense/prolonged rainfall events cannot be overlooked. Therefore, October to May were established as the months with effective infiltration (precipitation minus PET greater than zero). This behaviour could have determined the present-day infiltration pattern of the water to the cave.

Long-term data

	Jan	Feb	Mar	Apr	May	Jun	Jul	Aug	Sep	Oct	Nov	Dec	TOTAL
Rainfall (mm) during 1981-2010													
mean	28.3	23.1	26.6	44.3	61.5	46.5	24.2	40.8	34.5	43.3	31.1	26.8	431.0
Temperatures (°C) during 1969-2012													
min	0.1	0.5	2.7	5.0	8.7	12.5	14.9	14.9	11.7	8.1	3.4	0.7	6.9
max	9.2	11.1	14.8	17.0	21.5	26.8	30.3	29.8	25.1	19.4	13.1	9.5	19.0
mean	4.6	5.8	8.8	11.0	15.1	19.7	22.6	22.4	18.4	13.7	8.3	5.1	13.0

Study period data

	Jan	Feb	Mar	Apr	May	Jun	Jul	Aug	Sep	Oct	Nov	Dec	TOTAL
Rainfall (mm) during 2010-2015													
2010	53.8	32.7	37.1	45.2	61.8	**	**	**	17.1	47.6	11.8	12.4	282.4*
2011	4.7	8.4	112.5	49.5	82.9	21.1	15.5	10.0	3.4	1.9	115.2	14.2	439.3
2012	13.7	9.6	21.9	17.6	10.5	7.6	15.9	19.9	12.3	109.2	38.6	6.5	283.3
2013	31.7	31.3	75.3	58.7	57.4	47.6	8.2	21.8	16.6	2.6	58.4	9.7	419.3
2014	25.9	23.5	36.1	51.5	18.7	24.6	26.8	24.4	61.8	4.2	69.7	45.9	418.4
2015	27.4	32.6	161.5	11.2	14.3	67.0	43.5	46.3	17.8	8.8	44.6	0	475.0
mean	26.2	23.0	74.1	39.0	40.9	33.6	22.0	24.5	21.5	29.1	56.4	14.8	407.1
	Jan	**Feb**	**Mar**	**Apr**	**May**	**Jun**	**Jul**	**Aug**	**Sep**	**Oct**	**Nov**	**Dec**	**mean**
Temperatures (°C) during 2010-2015													
min	2.5	2.1	4.6	7.9	10.4	14.5	17.2	17.4	14.3	10.6	6.1	2.8	9.2

max	11.6	11.2	15.0	19.1	22.7	27.9	31.2	30.7	26.3	22.0	14.9	12.6	20.4
mean	6.3	6.2	9.5	13.4	16.5	21.2	24.3	24.1	20.1	15.8	9.9	6.7	14.5

* year not complete

** data not available

Table 5.1. *Meteorological data of the study site.*

5.3. Methods

5.3.1. Monitoring and sampling

A detailed monitoring survey was conducted in Ejulve cave over a period of four years (2013–2016) and rainfall was sampled since 2010 (Table 5.2). Environmental parameters were measured both inside the cave (cave air temperature and CO_2) and outside (surface air temperature (SAT)). The temperature inside the cave was measured every hour in continuous-mode using a HOBO® U23 Pro v2 Temperature/RH datalogger. However, the relative humidity measurements could not be obtained due to equipment malfunction. The CO_2 was measured occasionally in different places close to the dripwater and farmed calcite sample points using a portable CO_2 meter (CM-0019 device). The temperature outside the cave was measured (as mean day values) at the Majalino meteorological station (Ebro river basin, www.saihebro.com) (Fig. 5.1). Daily rainfall samples were collected manually in Molinos village (10 km from Ejulve cave, Fig. 5.1) over a period of six years (2010–2015) following the protocol described in Moreno et al. (2014) based on IAEA-GNIP procedures.

Dripwaters were studied through inspection and tracing of drips in different sections of the cave (Fig. 5.2) that showed water discharge in the present-day. Twelve drip sites with different discharge rates in diverse areas of the cave were sampled from January 2013 to June 2016 (Table 5.2). All dripwaters selected originated in active soda-straw stalactites. The discharge rate (drips/min) was measured during each visit to the cave (twice per season). However, one additional sampling point was measured continuously throughout the year using an installed pluviometer (model 7852M of Davis Instruments) connected to a HOBO® Pendant Event UA-003-64 datalogger. However, the record was not completely continuous as the unit malfunctioned during some months (Table 5.2).

The dripwater was sampled twice per season in 5 ml vials—completely filled, capped, and kept refrigerated until further analysis. The average pH was measured in-situ in the cave immediately after water sampling at drips EJ-2 and EJ-7 (Fig. 5.2) using a pH meter (Hanna Instruments 410-0902). The electric conductivity was measured using a YSI Professional Plus® handheld multiparameter instrument.

Glass plates were placed below the drip (Fig. 5.2) to recover the carbonate that precipitated seasonally from January 2013 to June 2016 (Table 5.2). The precipitated carbonate was sampled from the central part of the glass plates (i.e., the drip impact zone) to conduct further isotopic analyses. The growth rates have been expressed as weight per unit surface area unit (mg/cm^2) per season corrected by the days that the glass plates were in the cave.

5.3.2. Analytical techniques

The isotopic analyses of water (rainfall and dripwater) were conducted at the Andalusian Earth Sciences Institute in Granada (IACT-CSIC) using a Finnigan Delta Plus XL mass spectrometer. Water samples were equilibrated with CO_2 for the analysis of $\delta^{18}O$ values. Hydrogen was measured as H_2 produced by the reaction of 10 µL of water with metallic zinc at 500 °C following the analytical method of Coleman et al. (1982). The values are reported as $\delta^{18}O$ (‰) and δD (‰) with respect to the Vienna Standard Mean Ocean Water (V-SMOW), with an analytical precision (1σ) of ±0.1‰ for $\delta^{18}O$ and ±1‰ in the case of δD.

The monthly weight-averaged precipitation was calculated using Eq. (1):

$$\delta^{18}O = \frac{\sum_{i=1}^{n} R_i \, \delta^{18}O_i}{\sum_{i=1}^{n} R_i} \quad (1)$$

where, $\delta^{18}O_i$ is the isotopic composition of the rainfall in Molinos (‰), R_i is the amount of rainfall (mm) at the Gallipuén meteorological station near Molinos (Fig. 1), and 1 and n represent the first and last days of the month, respectively.

Stable isotope analyses of farmed carbonate on glass plates were performed at the University of Barcelona (Scientific and Technologica centers, CCiT) using a Finnigan-MAT 252 mass spectrometer fitted with a Kiel Carbonate Device III. Standards were run every 6 to 10 samples with an analytical precision (1σ) of 0.04‰ for $\delta^{13}C$ and 0.08‰ for $\delta^{18}O$. Values are reported as $\delta^{18}O$ (‰) and $\delta^{13}C$ (‰) with respect to the Vienna Pee Dee Belemnite (V-PDB) standard.

Anion-cation concentrations were measured in the Pyrenean Institute of Ecology (IPE-CSIC) lab using a Metrohm 861 ion chromatograph and precautions were adopted to prevent any precipitation of $CaCO_3$ in the vial (e.g. keeping it refrigerated and opening it only before the analysis). The detection limits were 5 ppb for anions and 10 ppb for cations. Alkalinity was calculated by using a strong acid (sulfuric) and two indicators, phenolphthalein for CO_3^{2-} and a mixed indicator of bromocresol green and methyl red for HCO_3^- in 50 ml sample vials.

The hydrochemistry calculations were estimated using PHREEQC software (Parkhurst and Appello, 2013). The PET was calculated using the Thornthwaite equation (Thornthwaite, 1948). The correlations indicated in this manuscript were calculated using the Spearman rank correlation coefficient (ρ). All regressions were lineal and estimated using one dependent and one independent variable, however, in case of multiple lineal regressions, one dependent and two independent variables were used. Modelling of the extent of prior calcite precipitation

(PCP) and carbonate growth rate using variables measured in Ejulve cave was conducted using the I-STAL model (Stoll et al., 2012).

Monitoring timeline

	2010	2011	2012	2013	2014	2015	2016
rainfall sampling	✓	✓	✓	✓	*Jan-May	*Jan-Jun	-
drip waters	-	-	-	✓	✓	✓	*Jan-Jun
pluviometer	-	-	-	*Jan-Mar May-Dec	*Jan-May	*Apr-Dec	*Jan-Apr
farmed carbonate	-	-	-	✓	✓	✓	*Jan-Jun
cave temp. and CO_2	-	-	-	✓	✓	✓	*Jan-Oct
hydrochemistry	-	-	-	✓	✓	✓	*Jan-Apr

Tick mark (✓) covers the full year.
Asterisk (*) remarks the period with data.
Dash (-) is used in years with no data

Table 5.2. *Monitoring timeline of this study. Note the gaps in the pluviometer measurements due to a malfunction.*

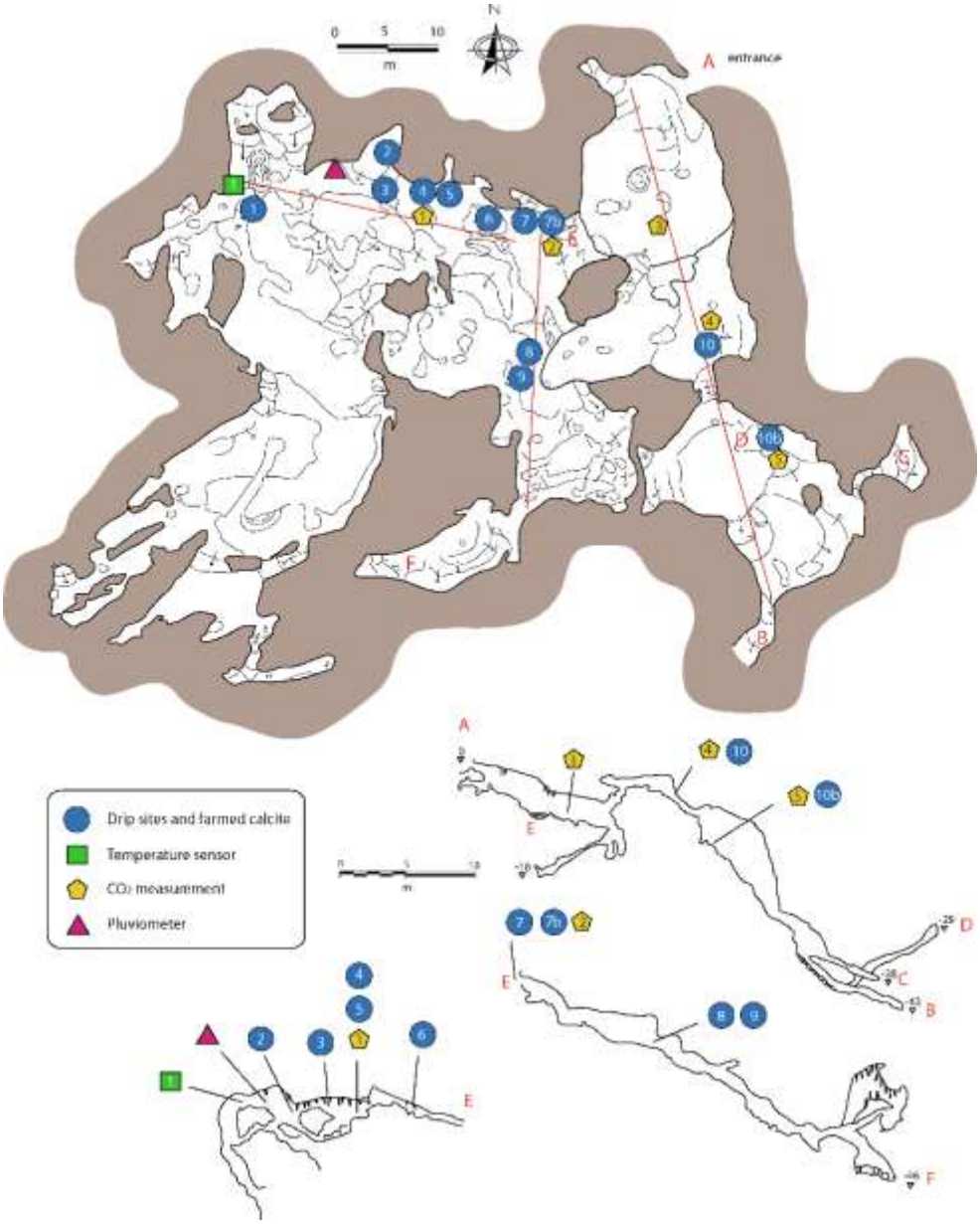

Figure 5.2. *Topography of Ejulve cave with plane view and elevation, including sampling sites.*

5.4. Results and interpretation

5.4.1. Environmental parameters

The daily mean SAT at Majalinos station (332 m above the cave) ranged between −9.4 °C and 26.1 °C with a mean value of 8.5 °C during the monitoring period. On the other hand, the cave air temperature values remained quite stable, spanning from 11.1 °C to 11.5 °C (s = 0.06 °C) (Fig. 5.3). The differences in altitude between both sites (cave and station, Fig. 5.1) were consistent with the difference in mean temperatures.

The cave air pCO_2 measurements showed the highest values from late summer to early fall (2160 ppm) and lower values in winter (461 ppm) (Fig. 5.3). Therefore, pCO_2 began to rise with the onset of July to reach the highest values from August to October. Subsequently, pCO_2 decreased and stabilised during January and recorded low values until next July (Fig. 5.3). This trend was common for the five measurement points.

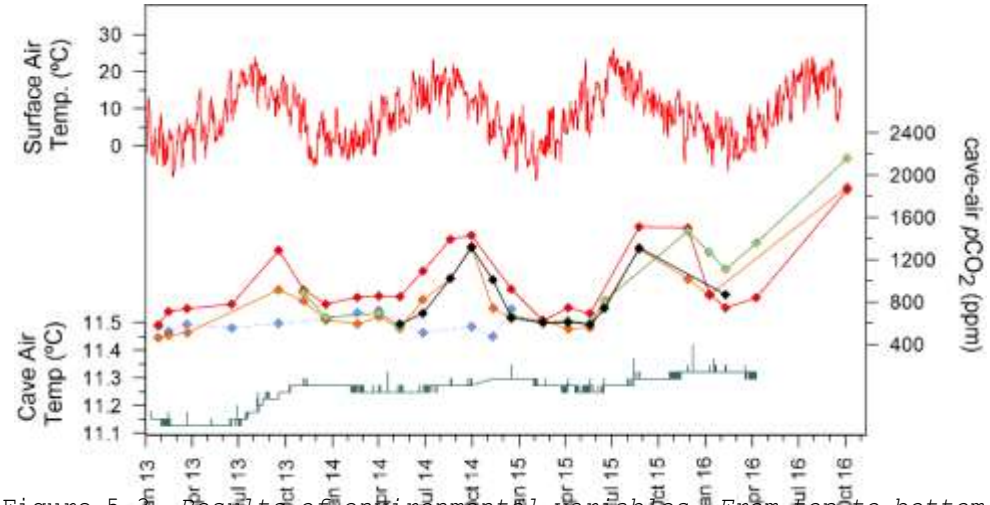

Figure 5.3. *Results of environmental variables. From top to bottom, surface air temperature (SAT) in Majalinos station (red), cave-air pCO_2 measurements inside the cave in five different points: #1 (red), #2 (orange), #3 (blue), #4 (avocado green) and #5 (black) (see Fig. 5.2 for the location of each measurement point), and temperature inside the cave.*

Points #1 (red) and #4 (green) recorded higher summer values due to deeper location in the cave with limited ventilation (Fig. 5.3) and, consequently, indicated the largest fluctuations. In contrast, points #2 (orange) and #5 (black) showed similar lower maximum summer values. While point #2 was close to the entrance, the data from point #5 suggest a connection to the exterior, probably though open fractures (Fig.

5.2). The lowest values were recorded at point #3 (blue) which was located in the same chamber as the entrance and exhibited higher ventilation.

The pCO_2 results suggest an effective ventilation of the cave from late fall to spring when the cold and dense surface air sank into the cave through the cave entrance as well as the joints and fractures of the bedrock. This ventilation continued during spring despite the increase in the SAT. During the onset of summer, the ventilation was weak and overtook the threshold of average temperature of the surface air (9–10 °C). Consequently, the ventilation almost ceased and the pCO_2 in the cave began to increase. Hence, the variability in the cave air pCO_2 followed changes in the SAT driven by climate dynamics which were evidenced by a strong correlation between exterior temperature and the cave pCO_2 ($\rho = 0.71$, p-value < 0.001, n = 22).

5.4.2. $\delta^{18}O$ and δD of precipitation and dripwaters

The values of δD in the precipitation (δD_p) ranged between −139.24 and 4.09 (mean = −52.38, s = 27.28) ‰ V-SMOW while those of $\delta^{18}O$ ranged between −20.54 and 0.01 (mean = −7.86, s = 3.75) ‰ V-SMOW (blue circles, Fig. 5.4.A). Some precipitation samples indicated extremely high values for both δD and $\delta^{18}O$. These exhibited evaporation associated with delayed sampling during high summer temperatures and were excluded from the calculations (grey colour, Fig. 5.4.A and 5.4.B).

Seasonality was the main pattern with regard to the distribution of $\delta^{18}O_p$ and δD_p and was clearly indicated by changes in the mean SAT during precipitation events, with high temperatures coinciding with events of high isotope values (red and orange colours, Fig. 5.4B) while lower temperatures (violet and blue colours, Fig. 5.4B) dominated in the lower isotope values. The mean values for $\delta^{18}O_p$ were −6.92 ± 0.29 in spring, −4.04 ± 0.39 in summer, −8.74 ± 0.47 in autumn, and −10.02 ± 0.45 in winter, all in ‰ V-SMOW. Hence, the stable isotopes in precipitation indicate seasonality with higher values in summer and lower during autumn to spring.

The δD and $\delta^{18}O$ of precipitation were closely correlated. The linear regression between both variables (δD-$\delta^{18}O$ relationship) established the global meteoric water line (GMWL) (Craig, 1961; Dansgaard, 1964). However, different factors at the local scale changed the global pattern established by the GMWL. Hence, data of daily precipitation from January 2010 to June 2015 (n = 258) were used to determine a local meteoric water line (LMWL) which improved upon the previously published line for this area with

fewer samples (Moreno et al., 2014). The LMWL was determined by Eq. (2):

$$\delta D\ (‰\ V\text{-}SMOW) = 6.94\ (\pm 0.14)\ \delta^{18}O + 2.15\ (\pm 1.18) \quad (2)$$

The slope, determined by the ratio of the $\delta D/\delta^{18}O$, was 6.94 while the LMWL intercept for y-axis indicated a value of 2.15.

The values of δD in the dripwaters of the 12 drip sites in the cave ranged between −74.48 and −22.84 (mean = −63.42, s = 7.68) ‰ VSMOW, and between −13.41 and 8.98 (mean = −9.14, s = 2.30) ‰ VSMOW for $\delta^{18}O$. Their variability was much lower than that observed in the rainfall samples. In general, from February to October 2014, drips (n = 10) were marked by high values of both $\delta^{18}O$ and δD and extremely low *d-excess* that seemed to exhibit enhanced degassing and fractionation out of equilibrium (Fig. 5.4A and Table 5.3). Therefore, these were excluded from the calculations.

The mean seasonal $\delta^{18}O_d$ values were −9.59 ± 0.20 in spring, −9.47 ± 0.21 in summer, −9.24 ± 0.09 in autumn, and −9.66 ± 0.13 in winter, all in ‰ V-SMOW. Therefore, the seasonality seen in the precipitation was also observed in the dripwaters, although, it was much more reduced. The mean $\delta^{18}O$ of all drips, regardless of seepage or seasonal class, was in the range between −10 and −9‰, with the exception of EJ-6 which showed values close to −8‰ (Fig. 5.5B). The mean $\delta^{18}O_d$ ranged from −10 to −9‰ which was lower than the mean amount-weighted rainfall (8.02 ± 1.01 ‰ V-SMOW).

Using the classification based on discharge rates and coefficient of variation (CV) (Smart and Friedrich, 1987; Baker et al., 1997) for data collected from the 12 drips over a period of four years, two main types of groups emerged: seepage flow and seasonal drips (Fig. 5.5A). The inter-annual variation in discharge was much greater than the intra-annual variation. To calculate the CV, the relative standard deviation for both inter- and intra-annual variation was used to avoid sites classified as seepage in one year from being reclassified as seasonal in another year (Baker et al., 1997).

Seepage flow drips showed low temporal variability in discharge while the seasonal drips recorded variations higher than 50% of the intra- or inter-annual variation in discharge. High dissimilarities were found in seasonal drips which supports the existence of three subgroups of drips evidenced by: a) low discharge and medium variability, b) medium variability and medium discharge, and c) high discharge and high variability (Fig. 5.5A).

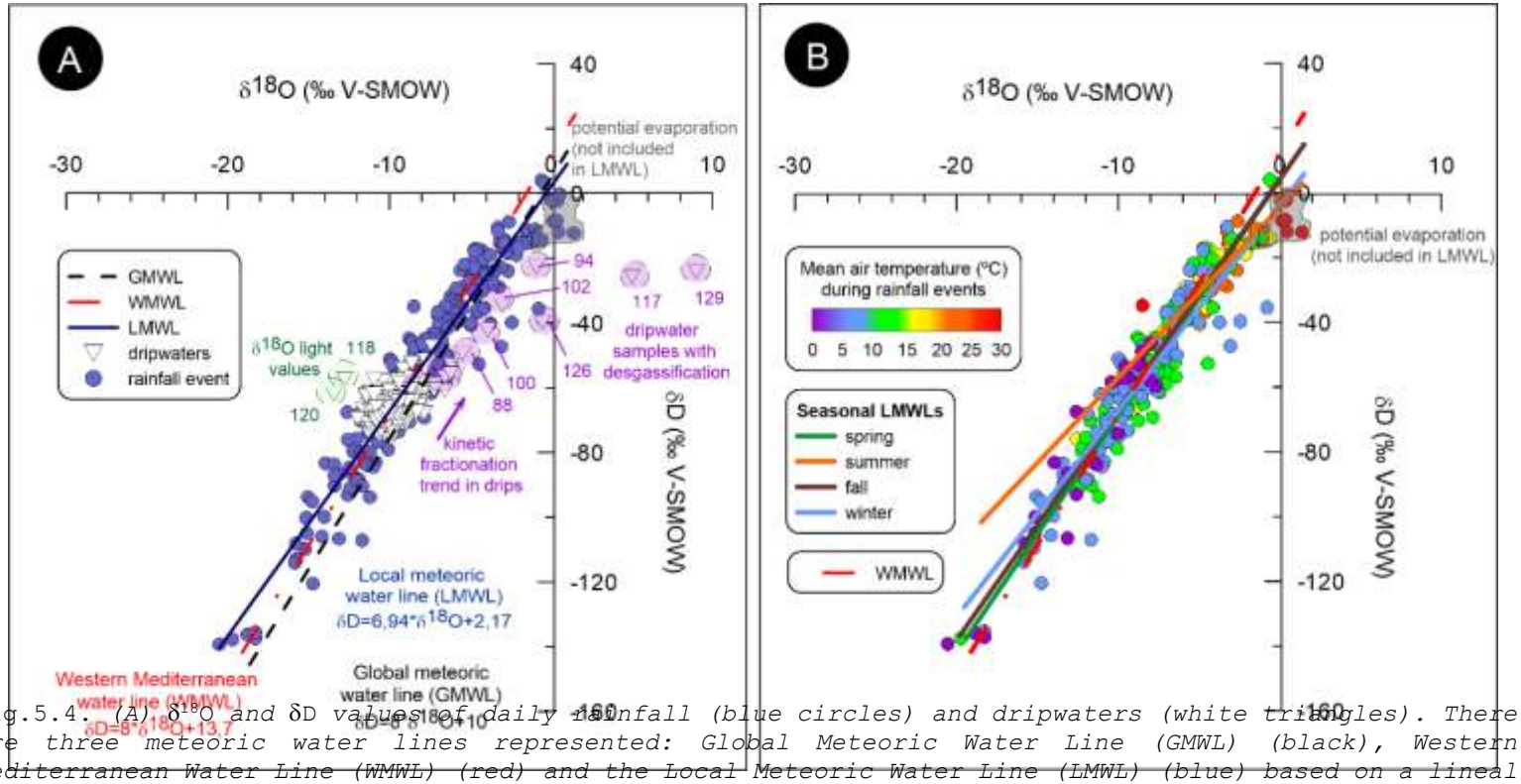

Fig.5.4. *(A) $\delta^{18}O$ and δD values of daily rainfall (blue circles) and dripwaters (white triangles). There are three meteoric water lines represented: Global Meteoric Water Line (GMWL) (black), Western Mediterranean Water Line (WMWL) (red) and the Local Meteoric Water Line (LMWL) (blue) based on a lineal regression of the isotope values of local rainfall. The samples out of equilibrium have been taken out from the calculation of the LMWL (samples in grey shape). Likewise, some dripwaters exhibit conditions far from equilibrium (samples in violet circles). (B) Mean temperature of the air during the day of each rainfall. Using seasonally ordered samples, four meteoric water lines for every season have been calculated and compared with the WMWL (red).*

Event	Date (mm/dd/yy)	δD_{drip}	$\delta^{18}O_{drip}$	*d–excess*	Drip label	Season	Comments
1	01/10/2013	−70.77	−10.73	15.07	EJ−1	winter	
2	01/10/2013	−74.48	−11.18	14.96	EJ−2	winter	
3	01/10/2013	−70.20	−11.58	22.44	EJ−4	winter	
4	01/10/2013	−71.50	−10.99	16.42	EJ−7	winter	
5	01/10/2013	−69.30	−10.37	13.66	EJ−8	winter	
6	01/10/2013	−70.80	−10.06	9.68	EJ−9	winter	
7	02/14/2013	−68.32	−11.07	20.24	EJ−1	winter	
8	02/14/2013	−67.43	−10.32	15.13	EJ−2	winter	
9	02/14/2013	−66.39	−10.26	15.69	EJ−4	winter	
10	02/14/2013	−67.03	−10.66	18.25	EJ−7	winter	
11	02/14/2013	−67.52	−10.19	14.00	EJ−8	winter	
12	02/14/2013	−64.47	−10.99	23.45	EJ−9	winter	
13	03/22/2013	−65.89	−10.95	21.71	EJ−1	winter-to-spring	
14	03/22/2013	−65.43	−11.28	24.81	EJ−2	winter-to-spring	
15	03/22/2013	−62.53	−11.46	29.15	EJ−4	winter-to-spring	
16	03/22/2013	−62.51	−11.23	27.33	EJ−7	winter-to-spring	
17	03/22/2013	−66.53	−11.62	26.43	EJ−8	winter-to-spring	
18	03/22/2013	−66.85	−11.22	22.91	EJ−9	winter-to-spring	
19	05/09/2013	−66.62	−8.85	4.18	EJ−1	spring	
20	05/09/2013	−68.38	−9.58	8.26	EJ−2	spring	
21	05/09/2013	−65.02	−9.86	13.86	EJ−4	spring	
22	05/09/2013	−64.57	−9.68	12.87	EJ−7	spring	
23	05/09/2013	−68.91	−9.86	9.97	EJ−8	spring	
24	05/09/2013	−67.21	−9.90	11.99	EJ−9	spring	
26	06/18/2013	−68.38	−9.70	9.22	EJ−1	sp.-to-summer	
27	06/18/2013	−67.72	−9.87	11.24	EJ−2	sp.-to-summer	
28	06/18/2013	−64.55	−9.94	14.97	EJ−4	sp.-to-summer	
29	06/18/2013	−67.58	−10.42	15.78	EJ−7	sp.-to-summer	
30	06/18/2013	−63.43	−10.10	17.37	EJ−8	sp.-to-summer	
31	06/18/2013	−66.14	−9.89	12.98	EJ−9	sp.to-summer	
32	08/07/2013	−71.06	−9.61	5.82	EJ−1	summer	
33	08/07/2013	−67.63	−9.04	4.69	EJ−2	summer	
34	08/07/2013	−66.70	−9.20	6.90	EJ−4	summer	
35	08/07/2013	−66.79	−9.25	7.21	EJ−7	summer	
36	08/07/2013	−68.93	−9.11	3.95	EJ−8	summer	
37	08/07/2013	−71.10	−9.08	1.54	EJ−9	summer	
38	09/18/2013	−69.03	−9.51	7.05	EJ−1	summer-to-fall	
39	09/18/2013	−70.24	−9.35	4.56	EJ−2	summer-to-fall	
40	09/18/2013	−70.21	−9.52	5.95	EJ−4	summer-to-fall	

Table 5.3 (cont. in next pages). *Isotopic data of the drip sites. All data are in per mil (‰) relative to V-SMOW. The analytical precision is ±0.1 ‰ in* $\delta^{18}O$ *and ±1 ‰ in* δD*. In the column 'comments', the '*$\delta^{18}O$ *low values' refer to the results that exhibit unusual low*

$\delta^{18}O$ and high d-excess, and 'kinetic fract.' to the results that exhibit unusual high $\delta^{18}O$ and low d-excess.

41	09/18/2013	−65.34	−8.92	6.02	EJ−7	summer-to-fall	
42	09/18/2013	−66.24	−9.11	6.64	EJ−9	summer-to-fall	
43	11/06/2013	−63.86	−9.73	13.98	EJ−1	fall	
44	11/06/2013	−67.93	−9.92	11.43	EJ−2	fall	
45	11/06/2013	−67.43	−9.81	11.05	EJ−3	fall	
46	11/06/2013	−67.80	−10.35	15.00	EJ−4	fall	
47	11/06/2013	−70.95	−10.83	15.69	EJ−5	fall	
48	11/06/2013	−64.09	−9.68	13.35	EJ−6	fall	
49	11/06/2013	−62.78	−9.33	11.86	EJ−7b	fall	
50	11/06/2013	−61.60	−8.95	10.00	EJ−8	fall	
51	11/06/2013	−64.84	−8.55	3.56	EJ−9	fall	
52	11/06/2013	−56.97	−8.33	9.67	EJ−10	fall	
53	11/06/2013	−57.47	−8.39	9.65	EJ−10b	fall	
54	12/19/2013	−63.01	−8.88	8.03	EJ−1	fall-to-winter	
55	12/19/2013	−63.91	−8.93	7.53	EJ−2	fall-to-winter	
56	12/19/2013	−64.13	−9.60	12.67	EJ−3	fall-to-winter	
57	12/19/2013	−59.15	−9.13	13.89	EJ−4	fall-to-winter	
58	12/19/2013	−61.98	−9.43	13.46	EJ−5	fall-to-winter	
59	12/19/2013	−60.31	−8.64	8.81	EJ−6	fall-to-winter	
60	12/19/2013	−63.85	−8.97	7.91	EJ−7b	fall-to-winter	
61	12/19/2013	−64.38	−8.86	6.50	EJ−8	fall-to-winter	
62	12/19/2013	−64.52	−8.25	1.48	EJ−9	fall-to-winter	
63	12/19/2013	−63.56	−8.36	3.32	EJ−10	fall-to-winter	
64	12/19/2013	−58.28	−7.84	4.44	EJ−10b	fall-to-winter	
65	02/19/2014	−69.30	−10.33	13.34	EJ−1	winter	
66	02/19/2014	−68.75	−10.13	12.29	EJ−2	winter	
67	02/19/2014	−56.72	−6.54	−4.40	EJ−3	winter	
68	02/19/2014	−64.41	−9.92	14.95	EJ−4	winter	
69	02/19/2014	−51.53	−7.78	10.71	EJ−5	winter	
70	02/19/2014	−55.48	−5.81	−9.00	EJ−6	winter	kinetic fract.
71	02/19/2014	−63.84	−9.68	13.60	EJ−7	winter	
72	02/19/2014	−59.06	−10.69	26.46	EJ−8	winter	
73	02/19/2014	−62.75	−10.77	23.41	EJ−9	winter	
74	02/19/2014	−69.38	−10.82	17.18	EJ−10	winter	
75	02/19/2014	−69.45	−11.96	26.23	EJ−10b	winter	
76	04/02/2014	−61.50	−11.24	28.42	EJ−1	spring	
77	04/02/2014	−47.43	−7.32	11.13	EJ−2	spring	
78	04/02/2014	−62.47	−11.42	28.89	EJ−3	spring	
79	04/02/2014	−51.78	−7.59	8.94	EJ−4	spring	
80	04/02/2014	−67.08	−11.03	21.16	EJ−5	spring	

81	04/02/2014	−68.33	−10.15	12.87	EJ−6	spring	
82	04/02/2014	−70.94	−10.84	15.78	EJ−7	spring	
83	04/02/2014	−70.82	−11.36	20.06	EJ−8	spring	
84	04/02/2014	−72.54	−11.13	16.50	EJ−9	spring	
85	04/02/2014	−71.16	−10.85	15.64	EJ−10	spring	
86	04/02/2014	−58.89	−7.19	−1.37	EJ−10b	spring	
87	05/13/2014	−60.92	−8.29	5.40	EJ−1	spring	
88	05/13/2014	−49.55	−5.45	−5.95	EJ−2	spring	
89	05/13/2014	−61.83	−8.21	3.85	EJ−3	spring	
90	05/13/2014	−63.51	−7.98	0.33	EJ−4	spring	
91	05/13/2014	−61.28	−8.42	6.08	EJ−5	spring	
92	05/13/2014	−59.21	−8.57	9.35	EJ−6	spring	
93	05/13/2014	−61.28	−8.93	10.16	EJ−7b	spring	
94	05/13/2014	−22.84	−0.88	−15.80	EJ−8	spring	Kinetic fract.
95	05/13/2014	−63.13	−8.17	2.23	EJ−9	spring	
96	05/13/2014	−64.71	−8.42	2.65	EJ−10	spring	
97	05/13/2014	−63.46	−8.51	4.62	EJ−10b	spring	
98	06/27/2014	−61.93	−7.93	1.51	EJ−1	summer	
99	06/27/2014	−64.70	−8.16	0.58	EJ−2	summer	
100	06/27/2014	−42.20	−3.91	−10.92	EJ−3	summer	kinetic fract.
101	06/27/2014	−65.97	−8.25	0.03	EJ−4	summer	
102	06/27/2014	−34.64	−3.01	−10.56	EJ−5	summer	kinetic fract.
103	06/27/2014	−61.50	−7.99	2.42	EJ−6	summer	
104	06/27/2014	−53.06	−6.17	−3.70	EJ−7	summer	
105	06/27/2014	−63.32	−8.15	1.88	EJ−7b	summer	
106	06/27/2014	−64.24	−8.22	1.52	EJ−8	summer	
107	06/27/2014	−64.87	−8.31	1.61	EJ−9	summer	
108	06/27/2014	−55.60	−6.22	−5.84	EJ−10	summer	
109	06/27/2014	−60.79	−6.59	−8.07	EJ−10b	summer	kinetic fract.
110	08/20/2014	−56.82	−9.05	15.58	EJ−1	summer	
111	08/20/2014	−57.31	−9.56	19.17	EJ−2	summer	
112	08/20/2014	−57.36	−10.01	22.72	EJ−3	summer	
113	08/20/2014	−57.42	−10.34	25.30	EJ−4	summer	
114	08/20/2014	−57.97	−10.37	24.99	EJ−5	summer	
115	08/20/2014	−54.04	−7.80	8.36	EJ−6	summer	
116	08/20/2014	−64.01	−9.36	10.87	EJ−7b	summer	
117	08/20/2014	−25.77	5.01	−65.85	EJ−8	summer	kinetic fract.
118	08/20/2014	−57.33	−12.79	44.99	EJ−9	summer	$\delta^{18}O$ low values
119	08/20/2014	−57.43	−10.96	30.25	EJ−10	summer	
120	08/20/2014	−62.07	−13.41	45.21	EJ−10b	summer	$\delta^{18}O$ low values
121	09/30/2014	−56.65	−9.11	16.23	EJ−1	fall	
122	09/30/2014	−57.76	−9.45	17.84	EJ−2	fall	
123	09/30/2014	−57.94	−9.61	18.94	EJ−3	fall	

124	09/30/2014	−54.33	−9.11	18.55	EJ−4	fall	
125	09/30/2014	−52.39	−8.61	16.49	EJ−5	fall	
126	09/30/2014	−39.81	−0.53	−35.57	EJ−6	fall	kinetic fract.
127	09/30/2014	−61.25	−8.56	7.23	EJ−7	fall	
128	09/30/2014	−61.10	−8.34	5.62	EJ−7b	fall	
129	09/30/2014	−24.17	8.98	−96.01	EJ−8	fall	kinetic fract.
130	09/30/2014	−62.32	−8.64	6.80	EJ−9	fall	
131	09/30/2014	−59.67	−9.24	14.25	EJ−10	fall	
132	09/30/2014	−57.05	−8.71	12.63	EJ−10b	fall	
133	11/11/2014	−62.92	−9.05	9.48	EJ−1	fall	
134	11/11/2014	−62.86	−9.20	10.74	EJ−2	fall	
135	11/11/2014	−63.96	−9.63	13.08	EJ−3	fall	
136	11/11/2014	−64.80	−9.60	12.00	EJ−4	fall	
137	11/11/2014	−62.56	−9.63	14.48	EJ−5	fall	
138	11/11/2014	−62.35	−9.03	9.89	EJ−6	fall	
139	11/11/2014	−64.27	−9.33	10.37	EJ−7	fall	
140	11/11/2014	−63.71	−9.37	11.25	EJ−7b	fall	
141	11/11/2014	−63.07	−9.23	10.77	EJ−8	fall	
142	11/11/2014	−64.14	−9.26	9.94	EJ−9	fall	
143	11/11/2014	−63.88	−9.17	9.48	EJ−10	fall	
144	11/11/2014	−62.73	−8.84	7.99	EJ−10b	fall	
145	12/17/2014	−61.82	−8.80	8.58	EJ−1	fall-to-winter	
146	12/17/2014	−61.66	−8.71	8.02	EJ−2	fall-to-winter	
147	12/17/2014	−63.76	−9.37	11.20	EJ−3	fall-to-winter	
148	12/17/2014	−65.56	−9.59	11.16	EJ−4	fall-to-winter	
149	12/17/2014	−62.63	−9.32	11.93	EJ−5	fall-to-winter	
150	12/17/2014	−62.31	−8.87	8.65	EJ−6	fall-to-winter	
151	12/17/2014	−65.82	−9.72	11.94	EJ−7	fall-to-winter	
152	12/17/2014	−59.65	−8.95	11.95	EJ−7b	fall-to-winter	
153	12/17/2014	−67.37	−9.79	10.95	EJ−8	fall-to-winter	
154	12/17/2014	−62.66	−9.06	9.82	EJ−9	fall-to-winter	
155	12/17/2014	−64.24	−9.28	10.00	EJ−10	fall-to-winter	
156	12/17/2014	−62.68	−8.97	9.08	EJ−10b	fall-to-winter	
157	02/12/2015	−65.95	−9.90	13.25	EJ−1	winter	
158	02/12/2015	−69.70	−10.02	10.46	EJ−2	winter	
159	02/12/2015	−69.22	−9.90	9.98	EJ−3	winter	
160	02/12/2015	−68.35	−9.69	9.17	EJ−4	winter	
161	02/12/2015	−61.56	−9.18	11.88	EJ−5	winter	
162	02/12/2015	−63.04	−8.37	3.92	EJ−6	winter	
163	02/12/2015	−69.14	−9.86	9.74	EJ−7	winter	
164	02/12/2015	−64.81	−9.21	8.87	EJ−7b	winter	
165	02/12/2015	−72.97	−10.64	12.15	EJ−8	winter	
166	02/12/2015	−67.10	−9.89	12.02	EJ−9	winter	
167	02/12/2015	−70.10	−9.95	9.50	EJ−10	winter	

168	02/12/2015	−67.37	−9.48	8.47	EJ−10b	winter
169	03/07/2015	−68.66	−10.15	12.54	EJ−1	winter
170	03/07/2015	−74.54	−10.60	10.26	EJ−3	winter
171	03/07/2015	−67.74	−7.99	−3.82	EJ−4	winter
172	03/07/2015	−74.40	−10.34	8.32	EJ−5	winter
173	03/07/2015	−72.27	−10.08	8.37	EJ−6	winter
174	03/07/2015	−69.65	−9.64	7.47	EJ−7	winter
175	03/07/2015	−69.19	−9.28	5.05	EJ−7b	winter
176	03/07/2015	−73.19	−10.10	7.61	EJ−8	winter
177	03/07/2015	−75.90	−9.90	3.30	EJ−9	winter
178	03/07/2015	−71.82	−9.74	6.10	EJ−10	winter
179	03/07/2015	−60.47	−8.67	8.89	EJ−10b	winter
180	05/20/2015	−65.24	−9.65	11.96	EJ−1	spring
181	05/20/2015	−68.19	−9.50	7.81	EJ−2	spring
182	05/20/2015	−68.94	−9.28	5.30	EJ−3	spring
183	05/20/2015	−72.29	−9.78	5.95	EJ−4	spring
184	05/20/2015	−65.78	−9.64	11.34	EJ−5	spring
185	05/20/2015	−69.01	−9.23	4.83	EJ−6	spring
186	05/20/2015	−68.88	−9.50	7.12	EJ−7	spring
187	05/20/2015	−64.68	−8.95	6.92	EJ−7b	spring
188	05/20/2015	−70.43	−9.61	6.45	EJ−8	spring
189	05/20/2015	−68.92	−9.62	8.04	EJ−9	spring
190	05/20/2015	−70.64	−10.38	12.40	EJ−10	spring
191	05/20/2015	−66.13	−9.84	12.59	EJ−10b	spring
192	06/17/2015	−66.08	−9.69	11.44	EJ−1	sp.-to-summer
193	06/17/2015	−71.30	−10.06	9.18	EJ−2	sp.-to-summer
194	06/17/2015	−74.25	−10.25	7.75	EJ−3	sp.-to-summer
195	06/17/2015	−67.61	−10.27	14.55	EJ−4	sp.-to-summer
196	06/17/2015	−66.62	−10.01	13.46	EJ−5	sp.-to-summer
197	06/17/2015	−66.64	−9.37	8.32	EJ−6	sp.-to-summer
198	06/17/2015	−69.25	−9.78	8.99	EJ−7	sp.-to-summer
199	06/17/2015	−70.95	−8.99	0.97	EJ−7b	sp.-to-summer
200	06/17/2015	−73.78	−10.73	12.06	EJ−8	sp.-to-summer
201	06/17/2015	−69.44	−10.01	10.64	EJ−9	sp.-to-summer
202	06/17/2015	−71.15	−10.27	11.01	EJ−10	sp.-to-summer
203	08/24/2015	−65.38	−7.98	−1.54	EJ−1	summer
204	08/24/2015	−66.86	−9.27	7.30	EJ−2	summer
205	08/24/2015	−61.87	−9.39	13.25	EJ−3	summer
206	08/24/2015	−64.91	−10.56	19.57	EJ−4	summer
207	08/24/2015	−64.59	−10.60	20.21	EJ−5	summer
208	08/24/2015	−61.82	−10.70	23.78	EJ−6	summer
209	08/24/2015	−67.84	−10.09	12.88	EJ−7	summer
210	08/24/2015	−68.38	−9.76	9.70	EJ−7b	summer
211	08/24/2015	−70.41	−10.43	13.03	EJ−8	summer
212	08/24/2015	−68.46	−10.52	15.70	EJ−9	summer

213	08/24/2015	−73.24	−10.51	10.84	EJ−10	summer
214	10/22/2015	−67.81	−10.21	13.87	EJ−1	fall
215	10/22/2015	−70.59	−10.52	13.57	EJ−2	fall
216	10/22/2015	−69.64	−9.76	8.44	EJ−3	fall
217	10/22/2015	−69.45	−10.07	11.11	EJ−4	fall
218	10/22/2015	−67.11	−9.81	11.37	EJ−5	fall
219	10/22/2015	−65.07	−8.91	6.21	EJ−6	fall
220	10/22/2015	−66.38	−9.18	7.06	EJ−7	fall
221	10/22/2015	−64.23	−10.12	16.73	EJ−7b	fall
222	10/22/2015	−62.84	−9.93	16.60	EJ−8	fall
223	10/22/2015	−68.91	−10.18	12.53	EJ−9	fall
224	10/22/2015	−66.04	−9.22	7.72	EJ−10	fall
225	10/22/2015	−64.70	−8.06	−0.22	EJ−10b	fall
226	11/27/2015	−64.13	−8.56	4.35	EJ−1	fall
227	11/27/2015	−67.40	−9.15	5.80	EJ−2	fall
228	11/27/2015	−69.34	−9.97	10.42	EJ−3	fall
229	11/27/2015	−67.99	−10.60	16.81	EJ−4	fall
230	11/27/2015	−70.94	−9.32	3.62	EJ−5	fall
231	11/27/2015	−65.45	−8.16	−0.17	EJ−6	fall
232	11/27/2015	−67.79	−7.84	−5.07	EJ−7	fall
233	11/27/2015	−65.40	−8.93	6.04	EJ−7b	fall
234	11/27/2015	−68.24	−9.65	8.96	EJ−8	fall
235	11/27/2015	−68.73	−9.87	10.23	EJ−9	fall
236	11/27/2015	−66.22	−8.72	3.54	EJ−10	fall
237	11/27/2015	−63.57	−9.37	11.39	EJ−10b	fall
238	01/08/2016	−66.83	−9.78	11.41	EJ−1	winter
239	01/08/2016	−68.57	−9.97	11.19	EJ−2	winter
240	01/08/2016	−71.17	−10.28	11.07	EJ−3	winter
241	01/08/2016	−75.71	−9.87	3.25	EJ−4	winter
242	01/08/2016	−73.76	−9.79	4.56	EJ−5	winter
243	01/08/2016	−70.93	−9.27	3.23	EJ−6	winter
244	01/08/2016	−67.84	−9.47	7.92	EJ−7	winter
245	01/08/2016	−63.63	−8.73	6.21	EJ−7b	winter
246	01/08/2016	−67.34	−8.29	−1.02	EJ−8	winter
247	01/08/2016	−67.77	−9.13	5.27	EJ−9	winter
248	01/08/2016	−69.67	−9.04	2.65	EJ−10	winter
249	02/09/2016	−60.90	−10.01	19.18	EJ−1	winter
250	02/09/2016	−62.30	−10.93	25.14	EJ−2	winter
251	02/09/2016	−65.98	−10.81	20.50	EJ−3	winter
252	02/09/2016	−70.67	−10.74	15.25	EJ−4	winter
253	02/09/2016	−70.68	−10.11	10.20	EJ−5	winter
254	02/09/2016	−65.00	−9.78	13.24	EJ−6	winter
255	02/09/2016	−64.88	−9.87	14.08	EJ−7	winter
256	02/09/2016	−58.38	−9.39	16.74	EJ−7b	winter

257	02/09/2016	−63.94	−8.56	4.54	EJ−8	winter
258	02/09/2016	−68.71	−9.34	6.01	EJ−9	winter
259	02/09/2016	−68.24	−9.27	5.92	EJ−10	winter
260	04/09/2016	−65.99	−9.56	10.49	EJ−1	spring
261	04/09/2016	−69.00	−10.32	13.56	EJ−2	spring
262	04/09/2016	−69.63	−10.53	14.61	EJ−3	spring
263	04/09/2016	−69.90	−9.28	4.34	EJ−4	spring
264	04/09/2016	−70.10	−9.42	5.26	EJ−5	spring
265	04/09/2016	−66.32	−8.90	4.88	EJ−6	spring
266	04/09/2016	−67.99	−9.14	5.13	EJ−7	spring
267	04/09/2016	−64.29	−8.90	6.91	EJ−7b	spring
268	04/09/2016	−69.99	−9.63	7.05	EJ−8	spring
269	04/09/2016	−63.92	−9.39	11.20	EJ−9	spring
270	04/09/2016	−67.48	−9.55	8.92	EJ−10	spring
271	06/19/2016	−65.17	−9.54	11.15	EJ−1	sp.-to-summer
272	06/19/2016	−67.32	−9.62	9.64	EJ−2	sp.-to-summer
273	06/19/2016	−68.17	−9.60	8.63	EJ−3	sp.-to-summer
274	06/19/2016	−67.90	−9.84	10.82	EJ−4	sp.-to-summer
275	06/19/2016	−68.73	−10.27	13.43	EJ−5	sp.-to-summer
276	06/19/2016	−66.10	−9.75	11.90	EJ−6	sp.-to-summer
277	06/19/2016	−66.99	−9.94	12.53	EJ−7	sp.-to-summer
278	06/19/2016	−63.24	−9.64	13.88	EJ−7b	sp.-to-summer
279	06/19/2016	−64.23	−9.35	10.57	EJ−8	sp.-to-summer
280	06/19/2016	−68.65	−10.06	11.83	EJ−9	sp.-to-summer
281	06/19/2016	−60.56	−7.22	−2.80	EJ−10	sp.-to-summer

Table 5.3. *Isotopic data of the drip sites. All data are in per mil (‰) relative to V-SMOW. The analytical precision is ±0.1 ‰ in* $\delta^{18}O$ *and ±1 ‰ in* δD. *In the column 'comments', the '*$\delta^{18}O$ *low values' refer to the results that exhibit unusual low* $\delta^{18}O$ *and high d-excess, and 'kinetic fract.' to the results that exhibit unusual high* $\delta^{18}O$ *and low d-excess.*

5.4.3. Hydrochemistry of dripwaters

Dripwaters are calcium-bicarbonate type and are mainly composed of Ca^{2+}, Mg^{2+}, CO_3^{2-}, and HCO_3^-. The concentrations of Ca^{2+} ranged from 59.0 to 96.6 ppm (mean = 80.8 ppm), Mg^{2+} ranged from 5.7 to 9.2 ppm (mean = 7.4 ppm), CO_3^{2-} from 0 to 19.0 ppm (mean = 5.5 ppm), and HCO_3^- from 201.7 to 256.2 ppm (mean = 220.1 ppm) (Table 5.4). Ca^{2+}, HCO_3^-, and CO_3^{2-} showed seasonality; minima for Ca^{2+} occurred during the periods of low infiltration in late spring through early autumn. Because Mg^{2+} featured less variation and no clear seasonal cycle, Mg/Ca increased at each Ca minima.

The pH measurements ranged from 6.9 to 9.2, showed no clear seasonal pattern, and exhibited lower values in 2013 and higher in 2014. The EC ranged from 350 to 645 mS, while the temperature of the dripwaters ranged from 11.3 to 13 °C. The PHREEQC code for determination of saturation index of calcite (SI_{ct}) indicated waters supersaturated with respect to calcite during most of the study period, although, with some negative values, a mean SI_{ct} of 0.4 was indicated (Table 5.4).

The periods with higher SI_{ct} were May, September, and December 2014. The pCO_2 in the dripwaters showed high values in all seasons; thus, any degasification should imply calcite precipitation.

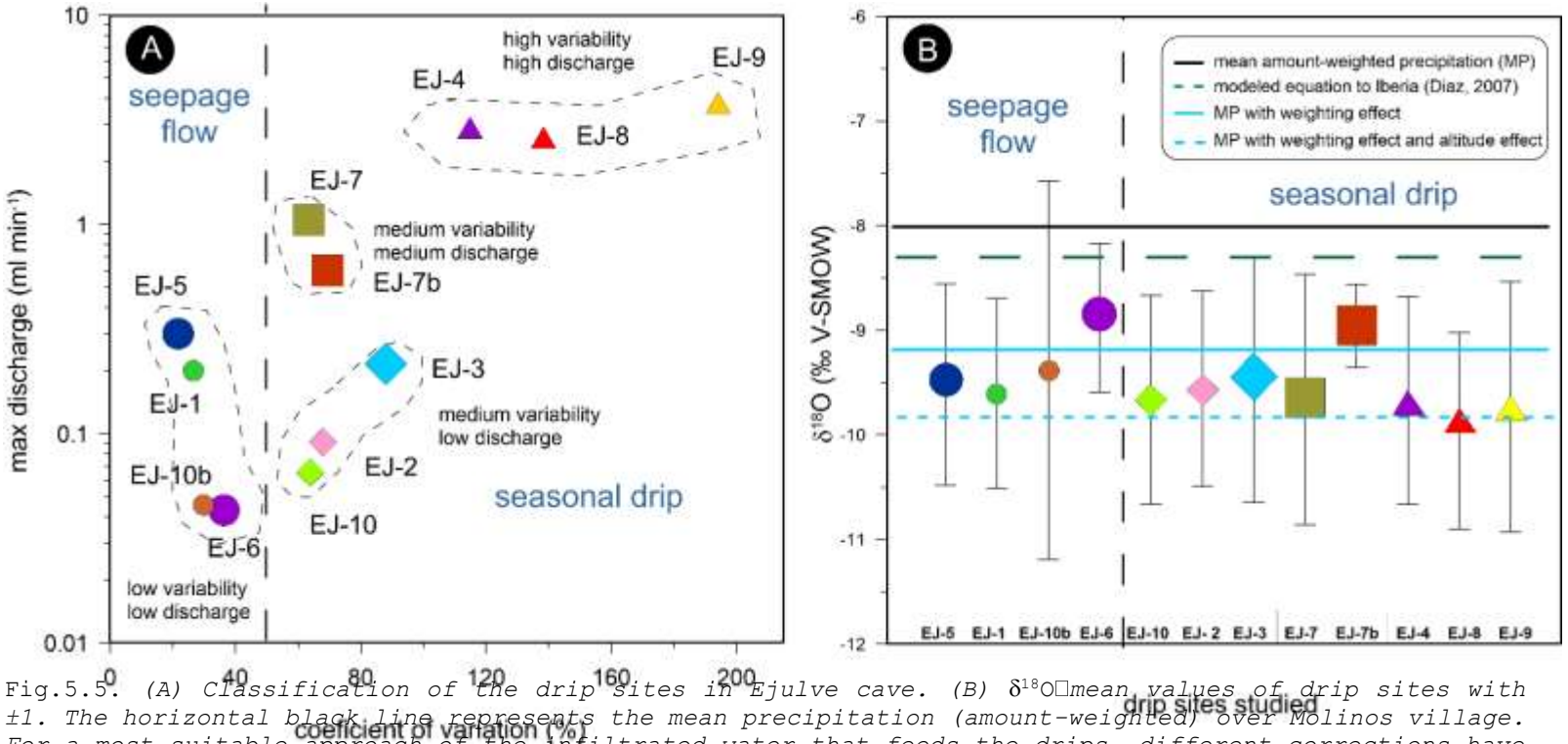

Fig.5.5. *(A) Classification of the drip sites in Ejulve cave. (B) $\delta^{18}O$ mean values of drip sites with ±1. The horizontal black line represents the mean precipitation (amount-weighted) over Molinos village. For a most suitable approach of the infiltrated water that feeds the drips, different corrections have been applied to the $\delta^{18}O$ of the precipitation, attending to the weighting effect (i.e. using the precipitation of only the months with effective infiltration) (blue line), and the altitude effect (the sampling site of rainfall is 500m below the cave) using a gradient of -0.15 ‰/100 m (blue dashed line). Finally, the mean precipitation for the Iberian Peninsula, modeled according the equation of Diaz et al., (2007), has been represented (green dashed line). The drip sites that records higher amount of carbonate precipitates are remarked with bigger symbols.*

date	pH	tem	EC	Ca^{2+}	Mg	CO_3	HCO_3	SI_{ct}	*p*CO
01/11/1	-	-	633	65.2	8.2	9.7	224.3	-	-
02/14/1	6.85	11.7	468	84.4	9.2	4.0	221.5	−0.5	−1.5
03/22/1	7.73	11.3	502	83.3	7.1	3.0	217.1	0.36	−2.4
05/09/1	7.38	11.6	610	78.6	6.9	7.2	217.4.	−0.0	−2.1
06/18/1	7.44	12.4	550	59.0	8.1	19.0	201.9	0.40	−2.5
08/08/1	7.04	11.5	380	65.6	7.0	8.0	214.7	−0.4	−1.7
11/06/1	6.88	11.8	400	79.2	7.4	0.0	215.9	−0.5	−1.6
12/20/1	7.00	12.4	-	82.5	7.3	0.0	228.8	−0.3	−1.7
02/19/1	7.00	11.4	-	82.8	7.5	9.0	214.1	−0.3	−1.7
04/02/1	7.25	12.1	-	87.6	7.1	6.5	211.7	−0.1	−2.0
05/13/1	8.55	11.6	-	89.2	7.4	10.1	225.5	1.20	−3.2
06/27/1	8.24	11.7	645	84.4	7.2	7.9	217.0	0.87	−2.9
08/20/1	7.54	13.0	477	71.5	7.0	-	-	-	-
09/30/1	9.20	12.1	415	86.3	7.0	10.0	227.0	1.71	−4.0
11/11/1	7.84	12.1	-	84.7	7.9	7.0	222.0	0.50	−2.5
12/17/1	9.01	12.7	460	92.6	7.1	3.0	235.5	1.60	−3.8
02/17/1	8.11	11.4	380	89.8	7.6	10.7	225.2	0.79	−2.8
04/07/1	7.94	12.1	350	73.4	7.4	0.0	209.9	0.49	−2.7
05/20/1	-	-	-	94.6	7.6	0.0	209.9	-	-
06/17/1	-	-	-	87.3	6.7	6.8	213.4	-	-
08/24/1	-	-	-	84.3	7.4	6.0	203.2	-	-
10/29/1	-	-	-	72.2	7.4	0.0	204.4	-	-
11/27/1	-	-	-	84.0	7.7	0.0	204.4	-	-
01/08/1	-	-	-	84.2	7.6	0.0	201.7	-	-
02/09/1	-	-	-	87.6	7.8	9.5	235.5	-	-
04/09/1	-	-	-	64.1	7.2	-	256.2	-	-
06/19/1	-	-	-	96.6	7.5	6.3	236.3	-	-
10/04/1	-	-	-	67.4	5.7	0.0	246.5	-	-

Table 5.4. *Hydrochemistry data of Ejulve cave. The results are the mean of the values from two drip sites, EJ-7 and EJ-2. The data are in ppm, except for the temperature (°C) and conductivity (mS).*

5.4.4. Stable isotopes and growth rate of carbonate precipitates

The $\delta^{18}O_{ct}$ for farmed carbonate ranged from −9.3 to −7.3 (mean = −8.26, s = 0.42) ‰ Pee Dee Belemnite (PDB) with $\delta^{13}C$ ranging from −11.5 to −7.2 (mean = −9.85, s = 0.94) ‰ PDB (Table 5.5). Seasonally, $\delta^{18}O_{ct}$ averaged across all drip sites was −8.20 ± 0.07 for spring, −8.18 ± 0.09 in summer, −8.30 ± 0.07 in autumn, and −8.27 ± 0.07 in winter (all in ‰ PDB) which were identical within analytical uncertainty. Therefore, the seasonality seen in precipitation and dripwaters was not observed in the $\delta^{18}O$ of farmed carbonate. The $\delta^{18}O_{ct}$ was similar in both seepage and seasonal drip groups (−8.19‰ and −8.25‰, respectively) (Fig. 5.6A).

In case of $\delta^{13}C_{ct}$, the seasonal averages across all drip sites were −9.77 ± 0.13 for spring, −9.73 ± 0.20 in summer, −9.89 ± 0.15 in autumn, and −9.97 ± 0.16 in winter, all in ‰ PDB. Higher values were recorded in summer and autumn; thus, reflecting some degree of seasonality. The $\delta^{13}C_{ct}$ for seasonal drips was lower than that from seepage drips (−9.93‰ and −9.76‰, respectively) (Fig. 5.6B).

The growth rate of carbonate precipitates has been shown by each drip site (rows) and season (column) in Table 5.6. The drip sites EJ-3, EJ-5, EJ-7, and EJ-7b, with a maximum drip discharge between 0.2 and 1 ml/min, recorded the highest amount of carbonate precipitates with wide variances between seasons. On the other hand, drip sites EJ-1, EJ-4, EJ-8, and EJ-10b recorded lower amounts. Higher amounts of calcite precipitate were observed in winter and spring (31.8% and 37.9% of the total, respectively), while fall and summer exhibited less calcite precipitation (11.82% and 18.45%, respectively).

It should be noted that the year 2016 was excluded in these results due to the lack of data during summer and autumn. There was no clear relationship between growth rate and the isotopes results in our data.

While two sites of high growth rate of precipitates were characterized by lower values of $\delta^{18}O_{ct}$ (EJ-5 and EJ-3), the rest exhibited the highest values of $\delta^{18}O_{ct}$ (EJ-6, EJ-7, and EJ-7b). With regard to $\delta^{13}C_{ct}$, three sites of higher growth rate (EJ-5, EJ-3, and EJ-7) exhibited low isotopic values while EJ-6 and EJ-7b recorded high $\delta^{13}C_{ct}$ values (Fig. 5.6).

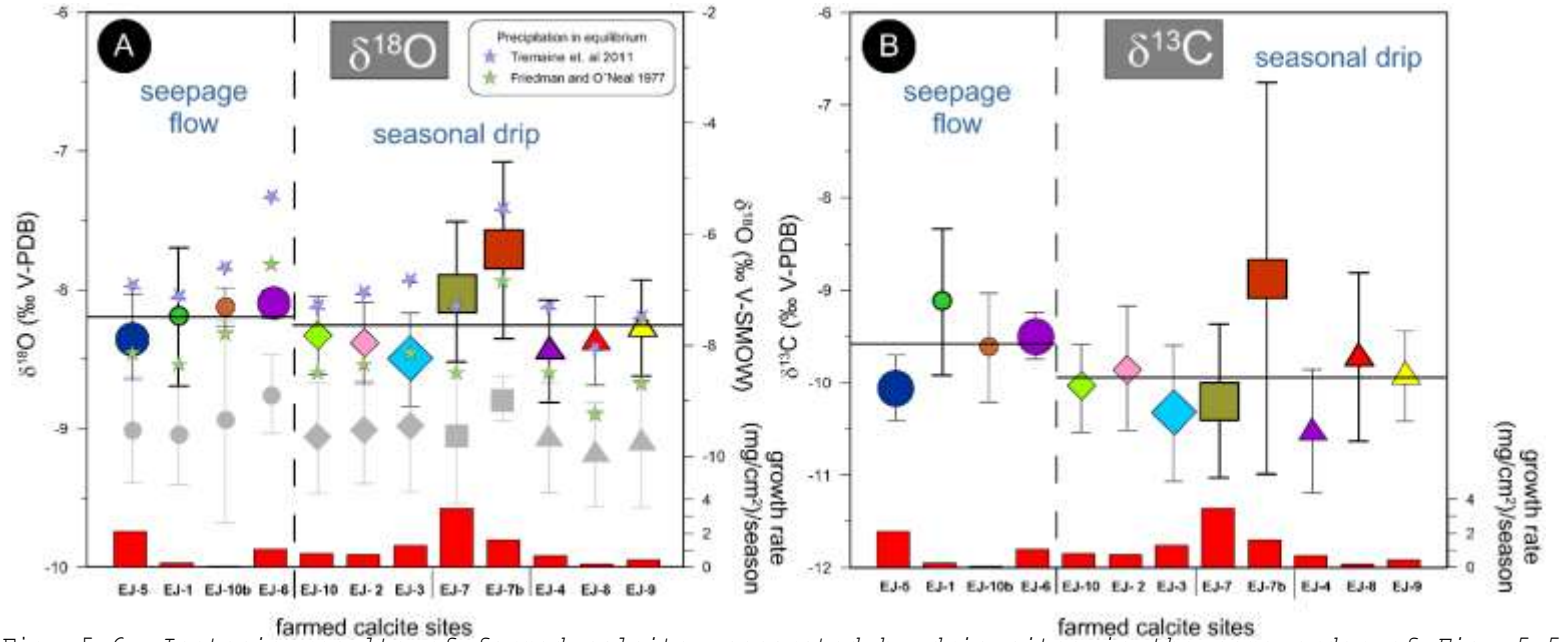

Fig. 5.6. *Isotopic results of farmed calcite, separated by drip sites in the same order of Fig. 5.5 attending to drip classification. (A) $\delta^{18}O$ mean values of farmed calcite from each group are represented by the black lines. The precipitation in equilibrium is calculated for each drip (blue and green stars). The symbols and standard deviation shadowed are the values of dripwaters. (B) $\delta^{13}C$ mean values of farmed calcite from each group are represented by the black lines. The higher size of symbols in drips EJ-5, EJ-6, EJ-3, EJ-7 and EJ-7b remarks the higher precipitation rates of carbonate resulting from these drips. The data with error bars in bold show the drips that exhibit higher standard deviation than the mean drip values. Below, the mean growth rate of the carbonate precipitates is shown for each drip site.*

Carbonate $\delta^{18}O$

		EJ–1	EJ–2	EJ–3	EJ–4	EJ–5	EJ–6	EJ–7	EJ–7b	EJ–8	EJ–9	EJ–10	EJ–10b
2013	WI	−8.5	−8.7	−8.2	−8.1	−8.3	−8.1	−8.2	**	−7.9	−7.5	**	**
	SP	−8.5	−8.3	−7.9	−8.0	−8.3	−8.0	−7.8	**	−8.1	*	**	**
	SU	−8.4	−8.4	*	*	−8.6	−8.2	−8.0	**	−7.9	*	**	**
	AU	−8.0	−8.4	−8.1	−8.3	−8.2	−8.1	−7.9	−8.4	−8.4	−7.9	−7.9	*
2014	WI	−8.4	−8.2	−8.4	−8.4	−7.9	−8.1	−8.2	−8.2	−8.6	−8.0	−8.4	−8.0
	SP	−8.2	−8.0	−8.2	−8.6	−7.7	−8.0	−8.0	−8.1	−8.4	−8.2	*	*
	SU	−8.2	−8.4	−8.3	−8.6	−8.2	−7.9	−8.4	−8.2	−7.5	−8.5	−8.0	*
	AU	−8.0	−7.7	−8.6	−8.6	−8.2	−8.2	−8.5	−8.3	−8.9	−8.1	−8.7	*
2015	WI	−8.5	−8.4	−8.8	−8.9	−8.2	−8.0	−8.2	−6.7	−8.7	−8.2	−8.5	−8.2
	SP	−8.2	−8.4	−8.6	−8.9	−8.5	−8.2	−8.4	−8.2	−8.7	−8.6	−8.0	*
	SU	−6.6	−8.5	−8.9	−8.5	−8.7	−8.2	−7.3	−7.6	*	−8.7	−8.5	*
	AU	−8.6	−8.6	−8.9	−8.9	−8.7	−8.0	−8.4	−7.1	−8.2	−8.5	−8.5	*
2016	WI	−8.4	−8.9	−9.0	−8.5	−8.4	−8.2	−8.3	−7.0	−8.3	−8.5	−8.6	*
	SP	−8.3	−8.5	−8.7	−7.7	−8.8	−8.3	−6.6	−7.0	−8.5	−8.6	−8.2	*

Carbonate $\delta^{13}C$

		EJ–1	EJ–2	EJ–3	EJ–4	EJ–5	EJ–6	EJ–7	EJ–7b	EJ–8	EJ–9	EJ–10	EJ–10b
2013	WI	−9.7	−10.1	−9.2	−10.3	−10.0	−9.5	−10.6	**	−9.9	−9.2	**	**
	SP	−9.6	−9.5	−8.6	−9.7	−10.2	−9.3	−10.3	**	−10.2	*	**	**
	SU	−9.0	−9.6	*	*	−10.2	−9.9	−10.4	**	−9.2	*	**	**
	AU	−8.4	−9.9	−9.7	−10.7	−10.0	−9.4	−9.9	−11.0	−10.2	−10.0	−9.9	*
2014	WI	−9.2	−9.8	−10.5	−11.0	−9.7	−9.6	−10.4	−10.7	−10.4	−9.8	−10.7	−9.9
	SP	−9.2	−9.1	−10.5	−11.0	−9.6	−9.6	−10.1	−10.8	−10.0	−9.8	*	*
	SU	−9.6	−10.2	−10.6	−10.8	−10.1	−9.5	−10.7	−10.8	−7.2	−10.4	−9.5	*
	AU	−8.8	−8.3	−10.8	−10.7	−9.8	−9.4	−10.9	−10.5	−10.9	−9.1	−10.8	−7.1
2015	WI	−9.9	−10.7	−11.1	−11.5	−10.1	−8.9	−10.8	−6.2	−10.2	−9.3	−10.6	−9.8
	SP	−9.0	−10.0	−10.2	−10.8	−10.2	−9.7	−10.6	−10.2	−10.0	−10.1	−9.1	*
	SU	−6.7	−10.0	−10.8	−9.4	−10.4	−9.7	−8.5	−8.7	*	−10.3	−10.2	*
	AU	−9.6	−9.9	−10.8	−11.0	−9.6	−9.1	−10.7	−7.3	−9.3	−10.2	−10.1	*
2016	WI	−9.6	−11.2	−11.1	−10.6	−9.9	−9.7	−10.5	−6.2	−9.4	−10.6	−10.7	*
	SP	−9.4	−9.7	−10.4	−9.3	−10.9	−9.5	−8.2	−6.5	−9.5	−10.3	−9.6	*

Table 5.5. *Isotopic data of the farmed calcite. * Data not available due to low amount of calcite precipitate*

*** Sampling started in fall of 2013*

Growth rate of farmed calcite (mg/cm²)/season

	Win 2013	Spr 2013	Sum 2013	Fall 2013	Win 2014	Spr 2014	Sum 2014	Fall 2014	Win 2015	Spr 2015	Sum 2015	Fall 2015	Win 2016	Spr 2016	Sum 2016
EJ-1	0.59	1.47	0.04	0.18	0.09	0.25	0.03	0.03	0.33	0.06	0.02	0.13	0.22	0.04	0.01
EJ-2	0.28	1.06	0.03	0.92	1.85	0.59	0.16	0.08	1.32	0.54	0.44	0.70	0.54	0.29	2.21
EJ-3	0.13	0.68	0	2.74	1.98	2.56	1.28	1.41	2.60	1.80	0.99	0.69	1.06	0.75	0.39
EJ-4	0.63	2.14	0.32	0.55	0.85	1.01	0.61	0.31	1.18	1.17	0.25	0.27	0.43	0.06	0.12
EJ-5	3.08	4.61	0.20	1.15	3.72	4.74	1.48	0.72	3.64	1.49	1.68	1.33	1.88	0.75	1.18
EJ-6	2.44	2.34	1.59	1.07	1.18	1.36	0.50	0.47	0.86	0.67	0.87	1.09	0.76	0.27	0.25
EJ-7	1.52	9.05	2.07	3.47	4.50	3.21	2.04	2.30	4.69	3.70	3.33	3.93	4.06	3.78	0.50
EJ-7b	*	*	*	1.12	3.17	5.43	4.41	1.17	0.24	0.82	2.55	0.19	0.08	0.04	0
EJ-8	0.03	0.91	0.02	0.32	0.25	0.39	0.03	0.03	0.31	0.04	**	0.09	0.01	0.02	0
EJ-9	0	0.22	0	0.58	0.67	0.86	0.23	0.39	1.03	0.35	0.15	0.78	0.64	0.30	0.14
EJ-10	*	*	*	0.72	0.95	0.86	0.87	0.27	1.87	0.76	0.58	0.79	1.11	0.37	0.41
EJ-10b	*	*	*	0	0.18	0.03	0.01	0.02	0.07	***	***	***	***	***	***
TOTAL	8.7	22.5	4.3	12.8	19.4	21.3	11.7	7.2	18.2	11.4	10.9	10.0	10.8	6.7	5.2
% (1)	39	**100**	19	57	**86**	**95**	52	32	**81**	51	48	44	48	30	23

** monitoring tasks in these drips was started in fall of 2013.*
*** data not available.*
**** monitoring at this drip was stopped in spring of 2015 due to the low calcite precipitated seasonally.*
(1) the % reflects the amount of farmed calcite precipitated seasonally, using the 100% for the season of the highest amount of calcite precipitates (spring of 2013) and avoiding the drips EJ-7b, EJ-10 and EJ-10b due to the lack of data in the onset of the time series. Bold format remarks the seasons with higher amount of calcite precipitates (winter and spring).

Table 5.6. *Growth rate of farmed calcite (mg/cm²)/season.*

5.5 Discussion

The discussion will focus on three main points: a) rainfall, with an emphasis on the effects and environmental controls of $\delta^{18}O$ and □δD; b) dripwaters, including understanding the hydrological response of cave dripwaters with regard to the temporal and spatial characterisation of the dripwater composition; and c) farmed calcite, focusing on the recording of isotopic signal and its links with dripwater hydrochemistry, temperature, and cave ventilation. Finally, the implications of this study for future paleoclimate research in semi-arid karst regions will be summarised.

5.5.1. Isotopes in precipitation and controls at event and monthly scales

5.5.1.1. Characterisation of rainfall $\delta^{18}O$ and δD

The δD-$\delta^{18}O$ relationship was determined by the slope of linear regression and the deuterium intercept. The differences between water lines, both in the slope and in the deuterium intercept, were due to the origin of vapour source or complex processes such as mixing, vapour recycling or evaporation.

The slopes of LMWLs generally range from ~ 8 to ~ 5 (Rozanski et al., 1993), with lower values as an evidence of raindrop evaporation beneath the cloud base during some rainfall events. In this study, a slope of 6.94 was estimated which lies in the range of other LMWL slopes around the IP (e.g., Santander, Valencia) and other Mediterranean sites (Genoa, Athens). However, it is in contrast to slopes in the range of 8 which are typical of central Europe (e.g., Germany, Switzerland) (IAEA/WMO, 2015).

The *d*-excess reflects the relative humidity and the air temperature of the area where the evaporation and cooling leads to rainfall; therefore, it is an effective tracer for moisture sources (Rozanski et al., 1993; Clark and Fritz, 1997) and vapour recycling over the continents (Gat et al., 1994). In this area, the *d*-excess was lower when the temperature was higher which is consistent with previous studies in other areas (Frohlich et al., 2002; Lambert and Aharon, 2010; Ma et al., 2012; Feng et al., 2013; Wang et al., 2015) suggesting a dominant effect of temperature and subcloud evaporation on the *d*-excess during summer (see Supplementary Annex).

5.5.1.2. Mechanisms and dominant effects in rainfall at event and monthly time scales

As indicated in a previous study, the main controls of $\delta^{18}O_p$ in the study area were *temperature effect*, *amount effect*, and *source effect* (Moreno et al., 2014). In this study, new rainfall data (125 new events during the years 2012-2015) were incorporated and analysed to further explore and quantify the effects influencing the isotope signal as part of the monitoring survey carried out in Ejulve cave.

5.5.1.2.1. Temperature effect

Equilibrium fractionation occurs during the condensation process and the removal of moisture from an air mass during Rayleigh distillation is temperature-dependent; therefore, temperature should be one of the main factors influencing $\delta^{18}O_p$. This is known as the *temperature effect* (Dansgaard, 1964; Fricke and O'Neil, 1999).

The relationship between $\delta^{18}O_p$ and the SAT ($\delta^{18}O_p$-T) was calculated using daily rainfall data (n = 258) and all monthly mean values (n = 47). The determination coefficient was relatively high in both cases (r^2 = 0.36, p-value < 0.001 and r^2 = 0.46, p-value < 0.001, respectively) (Fig. 5.7.A) supporting a clear relationship between $\delta^{18}O_p$ and the SAT at different scales of observation. In any case, the correlation between $\delta^{18}O_p$ and temperature was higher at the mean monthly scale (Fig. 5.7.B) than the other scales; an effect also seen in other domains (Meiliang et al., 2015).

Therefore, situations of unusually high/low $\delta^{18}O_p$ due to specific synoptic patterns or history of the air mass and their relationship with temperature are known to have less relevance at monthly to yearly scales. Therefore, it is more pertinent to use mean monthly values of temperature for the calculations of $\delta^{18}O_p$-T for this area (Fig. 5.7.B), as represented by Eq. (3):

$$\delta^{18}O_p \text{ (‰ V-SMOW)} = 0.35\ (\pm 0.05)\ T - 12.5\ (\pm 0.83)$$
$$(r^2 = 0.82,\ \text{p-value} < 0.001,\ n = 12) \quad (3)$$

where, T was calculated using mean monthly values of four years and the $\delta^{18}O_p$ was amount-weight corrected.

However, the Mediterranean climate is characterised by dry summers, and therefore, a high PET strongly limits the infiltration of rainfall water through the epikarst. As the PET is higher than the scarce summer precipitation in this area, the evapotranspiration in the dry soil should prevent the recharge of the epikarst. Therefore, it is useful to explore the $\delta^{18}O_p$-T excluding the months with no infiltration (Fig. 5.7.C).

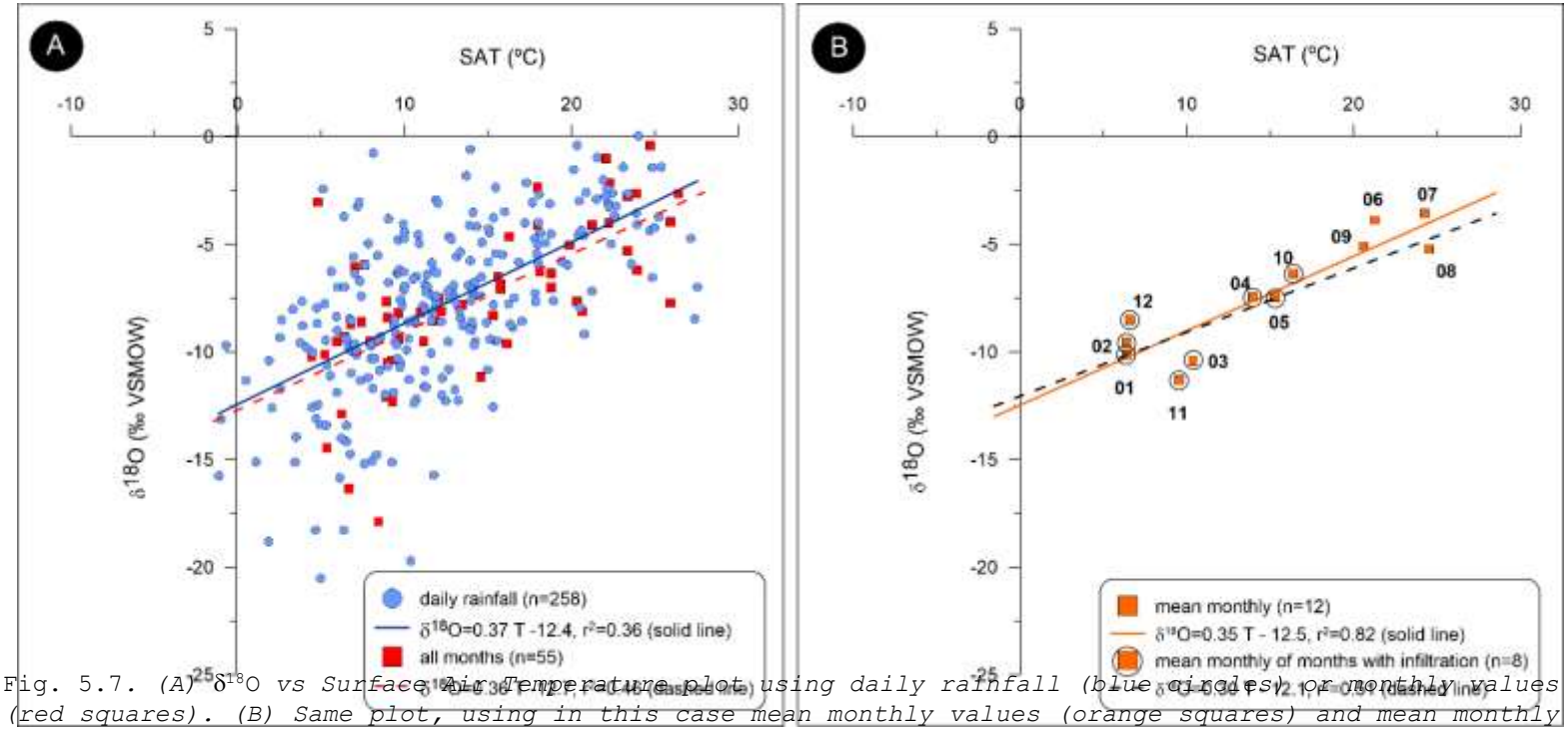

Fig. 5.7. *(A) $\delta^{18}O$ vs Surface Air Temperature plot using daily rainfall (blue circles) or monthly values (red squares). (B) Same plot, using in this case mean monthly values (orange squares) and mean monthly of months with effective infiltration (orange squares rounded). Each number is referred to the month of the sample.*

The results indicate that the determination coefficient remained high (r^2 = 0.51, p-value = 0.056), reinforcing this relationship despite excluding the months from June to September (Fig. 5..7B). The slopes obtained in this study, i.e., 0.35 ‰ $°C^{-1}$ and 0.30 ‰ $°C^{-1}$, were in the range or slightly higher than the slopes obtained for central and north IP (Domínguez-Villar et al., 2008; Stoll et al., 2015a). Nevertheless, temperature is insufficient to account for all observed isotopic variability in precipitation and other processes are explored below.

5.5.1.2.2. Amount effect

This effect is explained by a decrease in rainfall □ values with increased rainfall amount (Dansgaard, 1964; Rozanski et al., 1993). In this study, the relationship between $\delta^{18}O_p$ and monthly precipitation ($\delta^{18}O_p$-P) showed a weak coefficient of determination for all months during the monitoring period (r^2 = 0.06, p-value = 0.07, n = 55) (dots, Fig. 5.8) as well as for the mean monthly values (r^2 = 0.20, p-value = 0.15, n = 12) (green triangles, Fig. 5.8). In addition, a more realistic $\delta^{18}O_p$-P was calculated using only months with positive infiltration (green rounded triangles, Fig. 5.8) to indicate a low gradient of −0.004 ‰ mm^{-1} and a coefficient of determination of zero. Therefore, the amount effect showed a weak correlation with $\delta^{18}O_p$ and did not exert control on the $\delta^{18}O_d$ of Ejulve cave. It is worth noting that none of the coefficients exhibited high statistical significance.

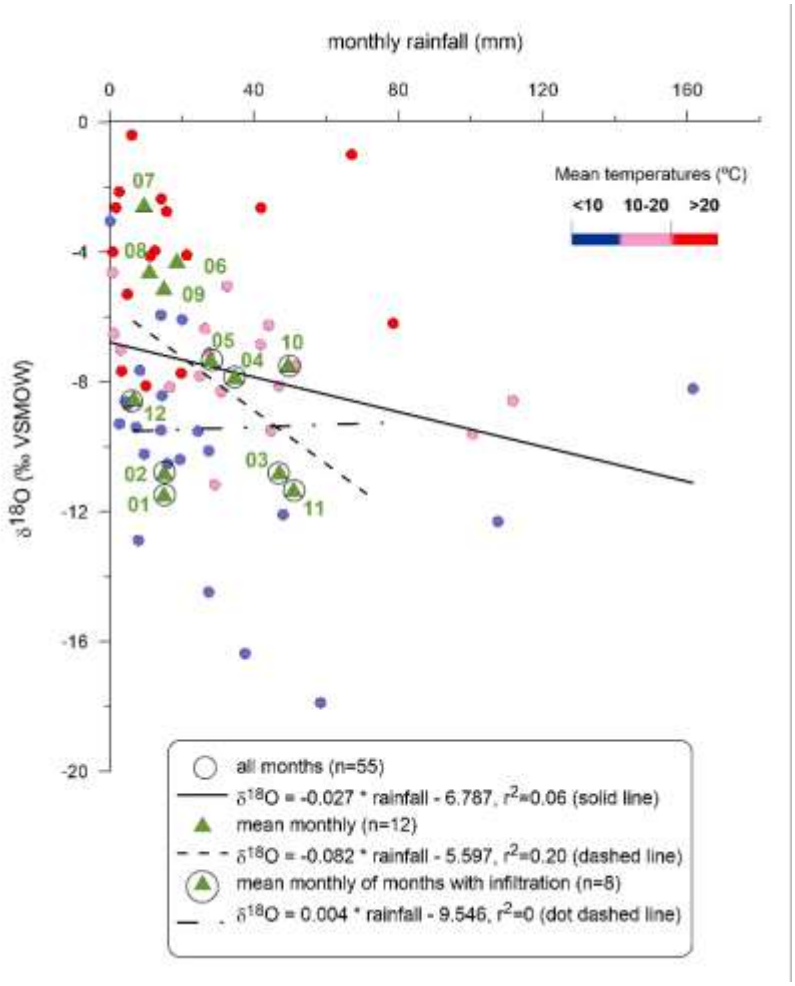

Fig.5.8. $\delta^{18}O$ *vs monthly rainfall plot of each month (circles) segregate by mean air temperature, with months of less than 10 °C (blue), between 10 and 20 °C (pink) and higher than 20 °C (red), mean monthly values (green triangles) and mean monthly of months with effective infiltration (green triangles rounded).*

5.5.1.2.3. Additional effects

In this study, other effects such as sources of moisture, rainfall components, continental, and altitude effects were also analysed. The variability in precipitation isotopes may also reflect the difference in isotope values of air masses derived from different moisture sources such as regional differences in $\delta^{18}O$ of the ocean and different air mass histories and temperatures (LeGrande and Schmidt, 2006). These are described as the *source effect* (Dansgaard, 1964; Rozanski et al., 1993).

The moisture source for precipitation in the study region could be the North Atlantic Ocean characterised by low rainfall $\delta^{18}O$ and the Western Mediterranean characterised by a high $\delta^{18}O$ (Celle-Jeanton et al., 2001; Moreno et al., 2014). However, that analysis should be polished through the rainfall component, using the synoptic pattern of precipitation. Previous studies have shown that rainfall from the Atlantic fronts, occurring from September to April, exhibits lower $\delta^{18}O$ than convective rainfalls coming from the Mediterranean (Moreno et al., 2014). However, it is more pertinent to study the rainfall component rather than merely the source area to explain the $\delta^{18}O$ values. One example represents cyclogenesis that involves complex mesoscale convective system responsible for intense rainfall during late fall and winter (known as back-door cold fronts). In spite of its Mediterranean origin, it displays low $\delta^{18}O$ (Moreno et al., 2014).

Similarly, the lower values for the Atlantic rainfall in this area are also attributed to the large distance between the source vapour area and the rainout site above the cave, giving through Rayleigh distillation progressive depletion of $\delta^{18}O$ in the remaining moisture with the precipitation along the air mass trajectory, known as *continental effect* (Dansgaard, 1964; Rozanski et al., 1993; Clark and Fritz, 1997). Finally, the *altitudinal effect* (Clark and Fritz, 1997) that refers to the inverse relationship between rainfall isotopes and elevation when an airmass is orographically lifted and adiabatically cooled should be noted for the study area.

A compilation of 68 studies in different mountains around the world established a gradient of ~−0.28‰/100 m in a range that spans between −0.2 and −0.3‰/100 m (Lachniet, 2009). The large differences in altitude between the sampling site of rainfall (Molinos) and Ejulve cave (Fig. 5.1) justify an altitude-correction of $\delta^{18}O$ of the rainfall.

5.5.1.2.4. Modelling the dominant effects on $\delta^{18}O_p$

Integrating the temperature effect and the amount effect, a multiple regression model for $\delta^{18}O_p$ was proposed (Eq. (4)) in which the temperature effect exerted a clear dominant control. The temperature effect increased further if the calculations were performed using precipitation that led to effective infiltration instead of the total precipitation (Eq. (5)). Equations (4) and (5) explained 89% and 79%, respectively, of the variability of $\delta^{18}O_p$ in the study area with a high statistical significance (> 95% confidence interval for both equations).

$$\delta^{18}O_{year}\ (‰\ \text{V-SMOW}) = -0.04\ (\pm 0.01)\ A + 0.33\ (\pm 0.04)\ T - 11.11 \quad (r^2 = 0.89,\ \text{p-value} < 0.001) \qquad (4)$$

$$\delta^{18}O_{infiltrated}\ (‰\ \text{V-SMOW}) = -0.06\ (\pm 0.03)\ A + 0.51\ (\pm 0.12)\ T - 12.84\ (r^2 = 0.79,\ \text{p-value} = 0.02) \qquad (5)$$

where, A is the amount effect represented by monthly precipitation and T is the monthly temperature.

Moreover, to evaluate the importance of both effects, some considerations need to be accounted for. The amount effect was weaker in contrast to the temperature effect which was dominant in both equations. However, the influence of moisture source and continental effect on the temperature effect in the study area should be noted. This influence could not be accounted in the modelled equations and will be explored here.

The rainfall that occurs from autumn to spring could be derived from two source areas, the Atlantic (through the synoptic pattern of Atlantic fronts) or Mediterranean (back-door cold fronts) (Moreno et al., 2014). The rainfall from Atlantic fronts, together with the greater rainout distance, amplified the effect of low local temperature. During summer, convective rainfalls that exhibited high $\delta^{18}O$ were sourced from the Mediterranean and had a shorter rainout distance which amplified the effect of high temperatures. Thus, the high significance of the temperature effect in this area was amplified by confluence with the source area and continental effects. Therefore, using the speleothem $\delta^{18}O$ from this cave to reconstruct past climates could overestimate temperatures if source effect and rainfall components are not considered.

5.5.2. Hydrological response of the cave dripwaters to rainfall

5.5.2.1. Mean annual precipitation $\delta^{18}O$ infiltrating into the cave

To compare the cave dripwaters with the rainfall, the mean amount-weighted $\delta^{18}O_p$ (MP) was calculated using the values from January 2013 in advance (i.e., the overlap period with dripwater sampling). The result of −8.02 ‰ (black line, Fig. 5.5.B) is similar to the modelled value of −8.20 ‰ for $\delta^{18}O_p$ in the IP (green dashed line, Fig. 5.5.B). This is presented by Eq. (6) which only uses latitude and altitude as variables (Diaz et al., 2007).

$$\delta^{18}O_p \text{ (‰ V-SMOW)} = -0.013\ Lat^2 + 0.9507\ Lat - 0.0037\ Alt - 22.253 \quad (6)$$

where, *Lat* represents the latitude and *Alt* the altitude of the $\delta^{18}O_p$ sampling site (Molinos village in this case).

However, the MP result was decidedly conditioned by the high isotope values of summer rainfall and these events may not be recharging the epikarst because of the high PET. This issue, common in semi-arid regions, was identified as the 'weighting effect' by Wackerbarth et al. (2012). Therefore, the MP should be calculated using the months with effective infiltration (blue line, Fig. 5.5.B) which yielded a value of −9.08‰.

Secondly, it is necessary to apply a correction factor since the rainfall samples were collected in Molinos village at 838 m.s.n.m. and the cave is located at 1269 m.s.n.m. Therefore, lower $\delta^{18}O$ values were expected in the rainfall over Ejulve cave in comparison to the $\delta^{18}O$ of rainfall over Molinos village due to the difference in altitude (*altitudinal effect)*. Although, altitudinal gradients were not determined in this study area, an altitudinal correction was applied in the previously calculated $\delta^{18}O_p$ using a moderate gradient of −0.15‰/100 m (dashed blue line, Fig. 5.5.B) after the studies in Italian Alps (Johnston et al., 2013) and Appenines (Mussi et al., 1998; Giustini et al., 2016).

Therefore, the fitted $\delta^{18}O$ composition of the rainfall over Ejulve cave that infiltrates through the epikarst should be the MP with corrected weighting and altitude effects (blue dashed line, Fig. 5.5.B). Thus, the estimated $\delta^{18}O$ of the precipitation infiltrating at the cave site was −9.73 ‰.

This estimate is subject to two factors of uncertainty: the impact of the gradient used in the altitude effect and the possibility of some infiltration during high precipitation events during months of high PET. The mean $\delta^{18}O_d$ values for all

dripwater locations were estimated between the MP of months with effective infiltration and the altitude-adjusted MP of months with effective infiltration, except for EJ-6 and EJ-7b (Figure 5.5.B). This suggests that average dripwater composition is representative of the contemporary precipitation.

5.5.2.2. Seasonal variation in water isotopic composition

The lower variability in $\delta^{18}O$ and δD in dripwaters compared to rainfall is the result of the homogenisation process of waters in the epikarst (Jones and Banner, 2003; Cruz et al., 2005; Pape et al., 2010; Oster et al., 2012; Feng et al., 2014; Moreno et al., 2014; Affolter et al., 2015; Guo et al., 2015; Mischel et al., 2015; Dumitru et al., 2017). However, in some cave systems seasonal variation is completely homogenised (Yonge et al., 1985; Williams and Fowler, 2002). This homogenisation is not complete in Ejulve since dripwaters retain some of the seasonality present in the $\delta^{18}O_p$. A similar retention of attenuated seasonality in $\delta^{18}O_d$ with some homogenisation of the waters in the epikarst has been observed in other caves with low overlying bedrock thickness (10–15 m) (van Beynen and Febbroriello, 2006; Moreno et al., 2014).

There are different methods to explore the transit times of water in the vadose zone and the lag in the arrival to drips (Even et al., 1986; Cruz et al., 2006; Mattey et al., 2008; Genty et al., 2014). The analyses of the delay in drip response to rainfall events and the isotopic variations in dripwaters are presented in the following sections.

5.5.2.3. Delay in drip discharge rates

The discharge rate of Ejulve cave dripwaters showed marked differences between drip sites, but most drips were low flow with values in the typical range of 1 drip every 5–1000 s established by Baker et al. (1997). The events of discharge in both seasonal and seepage drip sites were not always in-phase with the daily rainfall but were related to the seasons of effective infiltration (blue bars, Fig. 5.9). The infiltration showed a lag ranging from a minimum of a few days/weeks to a maximum of 12 weeks (black arrows, Fig. 5.9) which was reached at the end of the water infiltration period (e.g., six weeks at the end of spring of 2014 and 12 weeks at the end of spring of 2015).

However, with the exception of the longer lags explained previously, the rest were within the uncertainties indicated by the periodicity of the sampling interval, usually done every six weeks. This lag time in the infiltration was applicable to both seasonal and seepage drips, although there were differences

in discharge rates between them (see the logarithmic scale in the seepage group) (Fig. 5.9).

Therefore, similar to other semi-arid karst environments, the increase in discharge in cave dripwaters of both drip groups seemed to be controlled by the seasons of effective infiltration rather than individual high rainfall events (Cuthbert et al., 2014). The rainfall that occurred in the dry season had no effect on the dripwater discharge, suggesting that it was absorbed by the soil in low moisture conditions or lost by evapotranspiration. On the contrary, high rainfall events during the seasons of effective infiltration, with the soil wetted, were prone to arrive to epikarst, thus, increasing the drip rates a few weeks later (e.g., March 2013 and November 2014, Fig. 5.9).

The simultaneous increase in discharge rates due to external rainfall suggests similar residence time and homogenisation of water that fed both groups of drips in the epikarst. However, although the selection of sampling sites of dripwaters was representative of the cave hydrology (i.e., combining drips of different discharge rates), there were some marked low-flow drips (< 0.01 ml min^{-1}) that were difficult to analyse (too low to count drips manually). Therefore, one of the points was measured continuously with a pluviometer to examine if it exhibited a similar behaviour to the other studied groups.

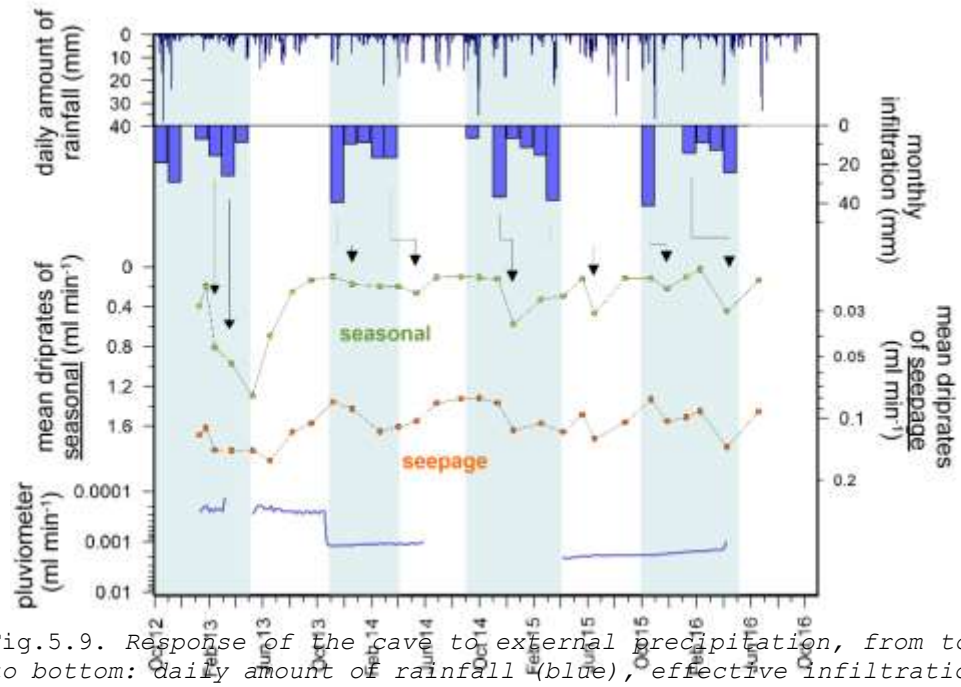

Fig.5.9. *Response of the cave to external precipitation, from top to bottom: daily amount of rainfall (blue), effective infiltration (blue bars), mean drip rate of seepage and seasonal drip groups*

(orange and green, respectively) -the vertical arrows represent the approached lag of the drip rate response to the precipitation-, and drip rate measured continuously of a seepage flow site (using a pluviometer) (blue line). Note the reversed axes in all variables and the logarithmic scale in seepage drips and pluviometer.

The results showed a very small variation in the drip rate, although the lack of data from summer of 2014 to spring of 2015 prevents any interpretation regarding the presence/absence of seasonality at this drip site (blue line, Fig. 5.9). The discharge rate suggests a higher residence time and homogenisation of the dripwater feeding this point and the changes seemed to be determined by thresholds of the amount of water infiltrated than the seasons of more infiltration.

Hence, only when the cumulative rainfall exceeded the given threshold, the fresh water arrived to the groundwater to feed this point and resulted in an increase in the discharge rate. This mechanism is similar to that seen in other karstic systems (Perrin et al., 2003; Guo et al., 2015). These considerations are important for future paleoclimate studies with speleothems derived from these dripwater points. As the infiltration was controlled by seasons of higher precipitation than PET and both seasonal and seepage drips responded simultaneously to external rainfall, therefore, a similar recording of the climate signal, biased to wet season, is suggested in both drip groups. However, it should be noted that some points that exhibited too low a discharge (< 0.01 ml min^{-1}) could likely represent inter-annual changes in rainfall.

5.5.2.4. Delay in the isotopic signal

The lower $\delta^{18}O$ values seen in the precipitation during winter, autumn, and spring (inferred as a, b, c, respectively, to represent the lags) were not in-phase with the $\delta^{18}O_d$ which showed a variable lag (a', b', c', black arrows, Fig. 5.10). If we accept that inference, low $\delta^{18}O_p$ values were recorded in dripwaters six to 21 weeks after the minima in $\delta^{18}O_p$ (see Supplementary Annex).

The response of the isotopic signal suggests a residence time between six to 21 weeks in the epikarst; in contrast, the delay in drip discharge suggests a faster response, up to a maximum of 12 weeks. This process is in concordance with the "piston flow" mechanism characterised by a rapid increase in drip discharge due to the hydraulic pressure from the arrival of "new" freshwater to the epikarst. Therefore, when the epikarst was being recharged, the "old" water was pushed down through the fracture network, as evidenced by the high conductivity of dripwaters during periods of high discharge (May 2013, Table

5.4 and Fig. 5.9). The behaviour observed in Ejulve cave, i.e., faster response in discharge rate but lagged isotope signal in the dripwaters with respect to the precipitation, is similar to other cave systems (Moreno et al., 2014; Affolter et al., 2015; Guo et al., 2015; Riechelmann et al., 2017).

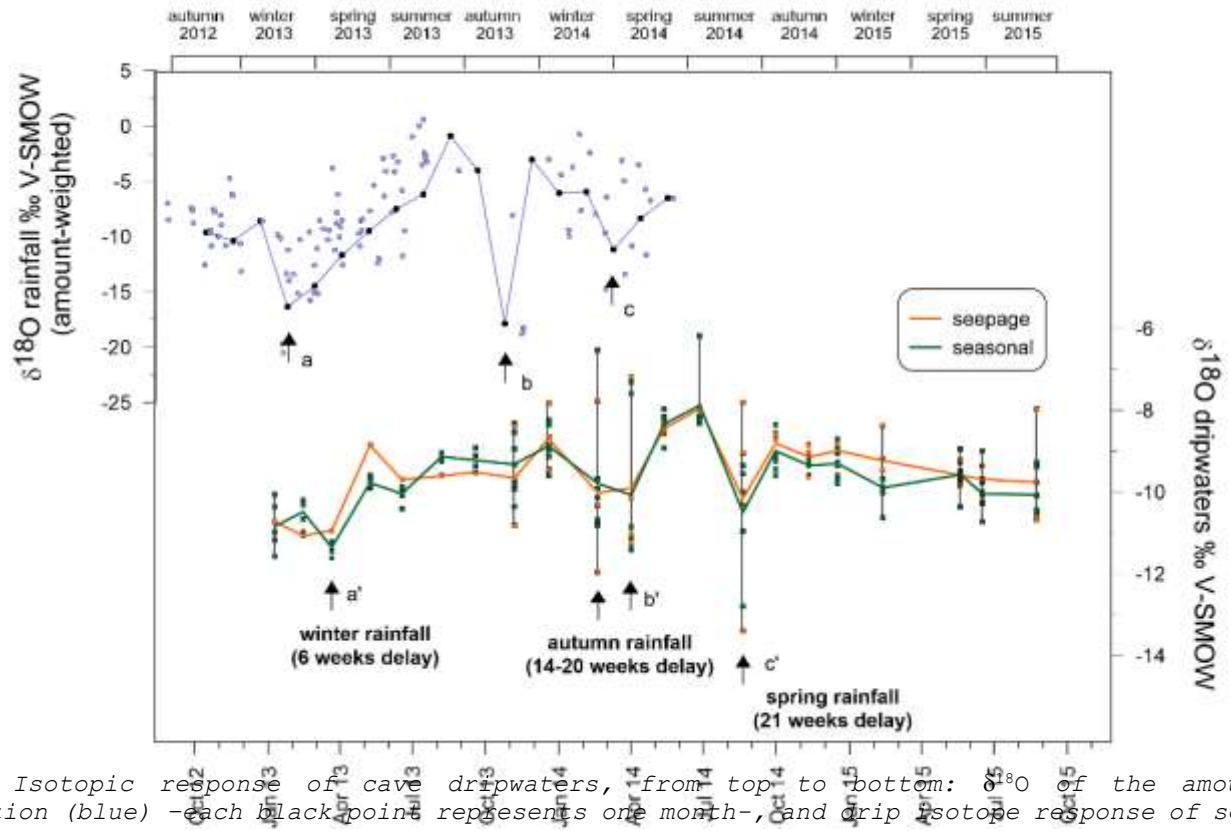

Fig.5.10. *Isotopic response of cave dripwaters, from top to bottom: $\delta^{18}O$ of the amount-weighted precipitation (blue) -each black point represents one month-, and drip isotope response of seepage drips (orange) and seasonal (green). The events a', b', and c' detected in drip samples could correspond to events a, b, and c seen in precipitation, reflecting the rainfall from winter of 2013, autumn of 2013 and spring of 2014, respectively.*

5.6. Isotopic transference to the cave farmed calcite

5.6.1. Growth rate of calcite precipitates linked to cave air ventilation and dripwater chemistry

The changes in cave ventilation patterns driven by the relative density of surface air and triggered by seasonal temperature variability (CO_2 lower in winter, higher in summer) observed in Ejulve cave are relatively common in other caves (Spötl et al., 2005; Banner et al., 2007; Frisia et al., 2011; Oster et al., 2012; Cowan et al., 2013). The calcite precipitation was linked to cave ventilation. Therefore, the seasons with higher calcite precipitation in Ejulve cave (brown shadow bars, Fig. 5.11) occurred when both the SAT and cave air pCO_2 were low, suggesting an enhanced ventilation. Thus, seasons with lower cave air pCO_2 favoured degassing of the solution supersaturated with respect to calcite and the precipitation of the carbonate (Spötl et al., 2005; Banner et al., 2007; Kowalczk and Froelich, 2010; Lambert and Aharon, 2010; Mattey et al., 2010; Miorandi et al., 2010; Boch et al., 2011; Frisia et al., 2011; Tremaine et al., 2011).

As shown in previous modelling studies, during the degassing process, the pH increases to approximately 8.5 and the majority (> 95%) of the carbonate in the solution is in the bicarbonate (HCO_3^-) form (Dreybrodt and Scholz, 2011); consequently, a rise in the SI_{ct} occurs with respect to calcite. The SI_{ct} was positive during the majority of the analyses in Ejulve cave dripwaters and should explain the presence of calcite precipitates throughout the year. Calcite precipitation was enhanced when the difference between the cave air pCO_2 and the dripwater pCO_2 was greatest due to lower cave air pCO_2 that favoured degassing, and/or due to an increased soil pCO_2 during the growth season (Genty et al., 2010; Kowalczk and Froelich, 2010). This mechanism contrasts with other perennially ventilated caves in the IP (e.g., Cueva Rosa) in which growth rate is not regulated by cave pCO_2 but by the dripwater chemistry and drip rate (Stoll et al., 2015a).

Although the calcite growth rate in Ejulve cave was controlled by cave air pCO_2, it could also be influenced by dripwater composition (Fairchild et al., 2006; Banner et al., 2007) because calcium ion concentration is recognised to be the primary determinant of speleothem growth rate (Baker et al., 1998; Dreybrodt, 1999; Baker et al., 2016). The higher growth rates in Ejulve cave showed in-phase changes with Ca^{2+}, HCO_3^-, and CO_3^{2-} in dripwaters (Fig. 5.11). This seasonal increase in Ca^{2+} accompanied by an increase in deposition rates suggests the dependence of Ca^{2+} on the soil CO_2 production which is determined by the SAT and soil moisture (Genty et al., 2001b).

The high Mg^{2+} in Ejulve cave dripwaters did not exhibit a clear seasonal pattern and may be explained by the interaction of the groundwater with the dolomite bedrock. Ca^{2+} and Mg^{2+} did not show a correlation ($\rho = 0.12$, p-value = 0.53, n = 28). However, during the dry season, an inverse correlation was observed between Ca^{2+} and the Mg/Ca ratio ($\rho = -1$, p-value < 0.001, n = 7) suggesting the PCP control of Ca^{2+} signature during the dry season. The role of the dripwater chemistry in Ejulve cave, although important, seemed to be dependent on the pCO_2. Therefore, higher concentrations of Ca^{2+} do not imply higher deposition rates if the pCO_2 levels were not low enough (October 2014, June 2016, Fig. 5.11).

The drip sites that recorded high growth rates in carbonate precipitates (EJ-3, EJ-5, EJ-6, EJ-7, and EJ-7b) (Table 5.6 and Fig. 5.5) were those that exhibited low to medium characteristics in both CV and maximum discharge. Therefore, drips with excessive variations in drip discharge during the year and major discharge were less prone to calcite precipitation, in contraposition to other caves, in which high drip rates also resulted in higher precipitation rates (Mühlinghaus et al., 2007; Romanov et al., 2008) or in which drip rates and drip rate variability had a minor contribution to modulating the amount of annual calcite formation (Miorandi et al., 2010).

Using drip rate, cave temperature, pCO_2, and Ca^{2+} data from Ejulve cave to model the carbonate precipitates in I-STAL (Stoll et al., 2012), the variables that exhibited major control over the carbonate growth were found to be pCO_2 and Ca^{2+}. As Ca^{2+} promoted higher deposition rates only when the pCO_2 was low, these findings confirm that cave air ventilation exerted a dominant control on calcite precipitation rates explaining the seasonal changes in growth rate while the effects if dripwater chemistry and drip rate as secondary controls were in accordance with other studies (Oster et al., 2012).

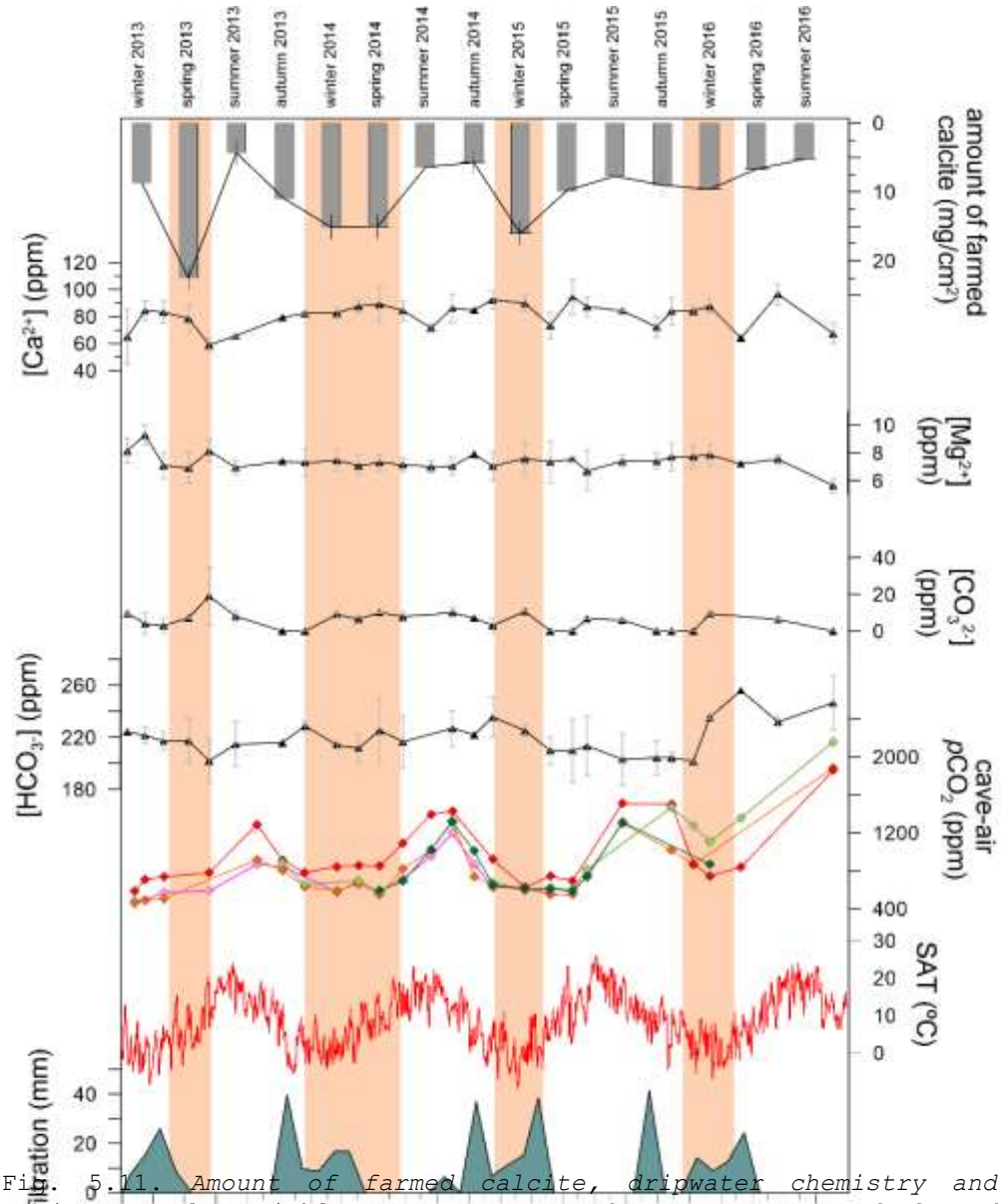

Fig. 5.11. Amount of farmed calcite, dripwater chemistry and environmental variables. From top to bottom: amount of farmed calcite of all drip sites seasonally reversed axes, mean Ca^{2+}, Mg^{2+}, CO_3^{2-} and HCO_3^- in dripwaters of sites EJ-2 and EJ-7 (ppm), with the SD in the error bars (1σ), pCO_2 inside the cave (ppm), Surface Air Temperature in Majalinos station and infiltration. The vertical brown shadow bars mark the seasons with higher calcite precipitation in Ejulve cave

5.6.2. Isotopic characterisation of farmed calcite

The oxygen and carbon isotope composition of calcite was influenced by both environmental conditions and processes in

the epikarst. While $\delta^{18}O$ of calcite depended mainly on $\delta^{18}O_d$, calcite growth rate, and the temperature of the cave, $\delta^{13}C$ was controlled by the infiltration pattern, the drip rate, and environmental factors (soil CO_2, cave ventilation, etc.) (Fairchild and Baker, 2012).

The standard deviation of $\delta^{18}O$ of calcite precipitates in Ejulve cave (1σ = 0.42) was lower than that observed in dripwaters (1σ = 2.3) and in rainfall (1σ = 3.75), reflecting a lower $\delta^{18}O$ amplitude in the calcite precipitates and a notably smooth signal (Figs. 5.10, 5.12). However, the amplitude exhibited differences between the drip sites (Fig. 5.6). The higher variability recorded in drips with medium and high discharge belonged to the seasonal group, with the exception of EJ-1 (Fig. 5.6.A).

Therefore, a high variation in discharge rate promoted a high variability in $\delta^{18}O_{ct}$, although the link between drip discharge and $\delta^{18}O_{ct}$ did not exert significant influence on $\delta^{18}O_{ct}$ values (ρ =□−0.15, p-value = 0.08, n = 135), showing similar mean values in seepage and seasonal sites (−8.19‰ and −8.25‰, respectively). In addition, data collected in this study lack evidence for a clear relationship between growth rate and the isotope values at this scale as three sites exhibiting a high growth rate of precipitates resulted in high $\delta^{18}O_{ct}$ while two sites indicated low $\delta^{18}O_{ct}$ values (Fig. 5.6.A).

Likewise, to understand the transference of the $\delta^{18}O$ signal, it is necessary to examine if the seasonality observed in the precipitation and dripwaters was also indicated for carbonate.

The mean variability of $\delta^{18}O_{ct}$ between seasons during the study period was 0.11‰ which is close to the analytical uncertainties; therefore, the effect of seasonality on $\delta^{18}O_{ct}$ cannot be concluded. Hence, the $\delta^{18}O_{ct}$ variability may reflect changes at timescales longer than seasonally or yearly. However, individual drip sites may reflect seasonal variability in calcite. This was inferred from the high $\delta^{18}O_{ct}$ values of some drips despite the related dripwaters not being enriched in $\delta^{18}O$ which was observed at EJ-1, EJ-7, and EJ-7b during summer in 2015 and EJ-7 and EJ-7b during spring in 2016 (Table 5.3, Table 5.5). Therefore, kinetic effects due to low drip rates could explain these values. This effect was more pronounced at drip sites EJ-7 and EJ-7b which exhibited the highest $\delta^{18}O_{ct}$ mean values despite the isotopic values of the related dripwater not being different to other drip sites (Fig. 5.6.A). Therefore, seasonality in $\delta^{18}O_{ct}$ in some drips appeared to track the summer conditions, not because the dripwater $\delta^{18}O_{ct}$ was enriched, but due to the kinetic effects.

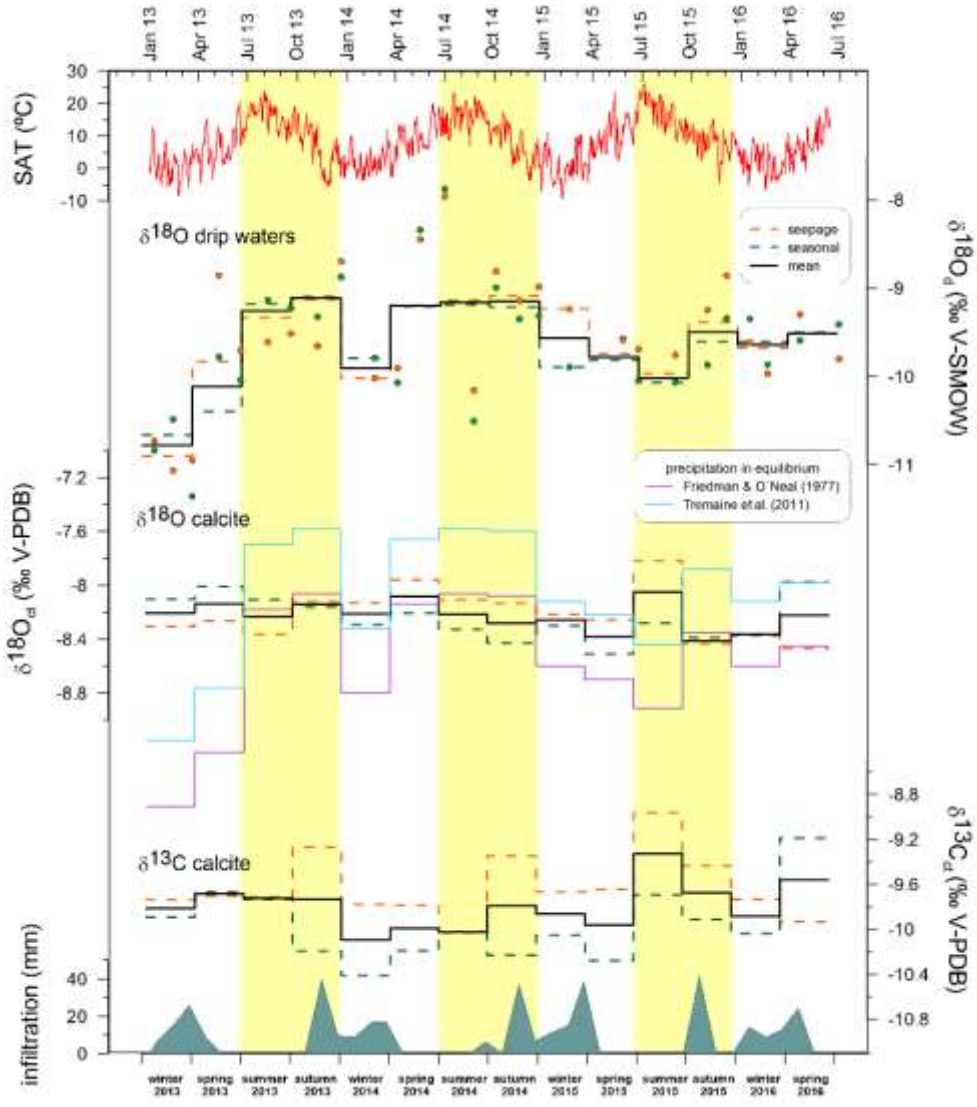

Fig. 5.12. *Isotope values of farmed calcite, from top to bottom: Surface Air Temperature in Majalinos station (red),* $\delta^{18}O$ *of dripwaters (seepage –orange, seasonal –green-, mean –black),* $\delta^{18}O$ *and* $\delta^{13}C$ *of farmed calcite (seepage -orange-, seasonal –green-, mean –black), and infiltration. The precipitation in equilibrium conditions of the* $\delta^{18}O$ *is following Friedman & O´Neal (1977) equation (violet line) and Tremaine et al (2011) (blue line). The vertical yellow bars mark the seasonal pattern in* $\delta^{13}C$ *highlighting higher isotopic values.*

The $\delta^{13}C_{ct}$ showed a standard deviation of 0.97, exhibiting higher variability than $\delta^{18}O_{ct}$, with different values among seepage and seasonal drip sites (Fig. 5.6.B). This pattern has been observed in other caves (Riechelmann et al., 2013) and is contrary to $\delta^{18}O_{ct}$ which showed similar values in seepage and seasonal groups. In addition, a clear seasonal pattern was seen for $\delta^{13}C_{ct}$ with low values in winter and spring and higher in summer and autumn (vertical bars, Fig. 5.12).

Additionally, a mean seasonal variability of 0.22‰ (up to 0.42‰ in the seepage group) (Table 5.5) was observed. An important inverse correlation existed between the drip rate and $\delta^{13}C_{ct}$ in Ejulve cave (ρ=−0.40, p-value < 0.001, n = 135) evidencing that drip rate was significant for determining the $\delta^{13}C_{ct}$ and was controlled by kinetics during degassing (Mattey et al., 2010; Meyer et al., 2014).

This dependence has been explored in Ejulve cave by attending to two parameters, i.e., drip class and seasonality (Table 5.7). The results indicate that drip rate of seepage drip sites tended to have a higher correlation with $\delta^{13}C_{ct}$, which is in agreement with more time between drops and, hence, greater duration of exposure to potential drip degassing. Moreover, higher correlations were reached during summer and autumn when the drip discharge was low, with high statistical significance in case of autumn at seasonal drip sites (Table 5.7). This suggests degassing during dry season as the explanatory mechanism for high isotopic values. The low seasonal values were in concordance with higher soil microbial activity and vegetation productivity linked to the seasons of effective infiltration.

Therefore, $\delta^{18}O_{ct}$ was likely controlled by $\delta^{18}O_{d}$. Neither the temperature in the cave, which was constant, nor calcite growth rate suggested any control on $\delta^{18}O_{ct}$ at the scale of this study. The kinetics of enhanced degassing could explain the higher values of $\delta^{18}O_{ct}$ in some drips that did not exhibit marked high values in the dripwaters (EJ-7 and EJ-7b). By contrast, the high values of $\delta^{13}C_{ct}$ during summer and autumn (enhanced by drip degassing) and lower in winter and spring were in concordance with higher soil microbial activity and vegetation productivity which could explain the seasonal pattern of $\delta^{13}C_{ct}$.

	Winter	*Spring*	*Summer*	*Autumn*
Seepage	−0.314 (0.28)	−0.497 (0.10)	−0.561 (0.12)	−0.587 (0.10)
Seasonal	−0.106 (0.61)	−0.365 (0.08)	−0.443 (0.09)	**−0.616** (0.002)

The p-value is indicated in parenthesis, and the higher statistical significance is highlighted in bold

Table 5.7. *Correlations* $\delta^{13}C$ – *drip rate.*

5.6.3. Fractionation effects during carbonate precipitation

In paleoclimate studies, the fractionation during carbonate precipitation has emerged as a key factor for interpreting the isotopic profile as a climate signal. The Hendy test (Hendy, 1971) is usually used for fossil-stalagmites, although, some studies suggest that this test is not sufficient to rule out kinetic fractionation (Mickler et al., 2006; Mühlinghaus et al., 2009). Moreover, if a speleothem fails the Hendy test, the calcite near the growth axis could be in isotopic equilibrium with the dripwater (Dorale and Liu, 2009; Dreybrodt and Scholz, 2011).

In the present-day conditions, it is important to compare the measured $\delta^{18}O$ of both dripwater and farmed calcite as well as the temperature of the cave with the values predicted for conditions of isotopic equilibrium. Only few studies have attempted to elucidate the isotopic fractionation between dripwater and recent calcite precipitates (McDermott et al., 2006; Mickler et al., 2006; Riechelmann et al., 2013; Feng et al., 2014; Pu et al., 2016). The results depended on the fractionation factor and the equation used. Here, we compare the following expressions:

$$1000 \ln \alpha = 2.78 \ (10^6 T^{-2}) - 2.89 \quad \text{(Friedman and O'Neil, 1977)} \quad (7)$$

$$1000 \ln \alpha = 18.03 \ (10^3 T^{-1}) - 32.42 \quad \text{(Kim and O'Neil, 1997)} \quad (8)$$

$$1000 \ln \alpha = 16.1 \ (10^3 T^{-1}) - 24.6 \quad \text{(Tremaine et al., 2011)} \quad (9)$$

The fractionation factor (α) was affected by temperature (T), pH of the solution, and growth rate of calcite. Hence, at constant temperature and precipitation rate, α decreased with increasing pH. If temperature and pH are constant, then, α decreases with elevated precipitation rates of calcite (Dietzel et al., 2009).

Equation (7) has been widely used due to consistent results between the calculated temperature and the measured temperature and is a well-accepted representation of the isotopic fractionation under natural cave conditions (McDermott et al., 2006). It was modified recently using the CO_2-calcite fractionation factor of 1,01025 as indicated in Eq. (8). Recently, Tremaine et al. (2011) used data for the Hollow Ridge Cave (USA) to propose oxygen isotope fractionation factors larger than those obtained from the laboratory experiments (Eq. (9)).

Our results indicate that the highest offsets were observed during winter and summer (Fig. 5.12), and seasonal drips precipitated in conditions closer to the equilibrium in contrast to seepage drips (Table 5.7). The offset in seasonal drips of Ejulve cave was calculated as ~0.35‰ PDB from Eq. (7), ~0.60‰ PDB from Eq. (8), and ~0.25‰ PDB from Eq. (9). These values were similar to those seen in seepage (~0.35‰ PDB from Eq. (7), 0.60‰ PDB from Eq. (8), and ~0.30‰ PDB from Eq. (9)). In general, these offsets were lower than those calculated in other studies (1 ± 0.5‰ PDB) (McDermott et al., 2006) or within 1.5‰ V-PDB (Pu et al., 2016).

Seasonally, Eq. (7) modelled $\delta^{18}O_{ct}$ closer to the measured $\delta^{18}O_{ct}$ in the cave during summer and autumn (except in 2015), and Eq. (9) during winter and spring (Fig 5.12, Table 5.8). There were marked differences between drips; while precipitates from low and medium drip discharge sites were more consistent with Eq. (7), those of high discharge were consistent with Eq. (9) (Fig. 5.6.A).

Moreover, most drip sites with higher standard deviation (data with error bars in bold, Fig. 5.6.A) displayed values closer to Eq. (9), indicating that the larger oxygen isotope fractionation factors in natural cave conditions, as used by Tremaine et al. (2011), reflected the conditions of the drip sites more accurately. By contrast, the results of drips with less drip discharge variability were more consistent with the fractionation factors from the laboratory experiments of Friedman and O´Neal (1977).

Carbonate precipitation was close to equilibrium (within analytical uncertainties) in seasonal drips during spring and autumn, and in seeping drips during spring, (Fig. 5.12 and Table 5.8). Therefore, precipitation close to the equilibrium was reached with intermediate levels of cave air pCO_2. These results are in agreement with previous studies which indicate that low cave air pCO_2 during winter promoted disequilibrium fractionation due to acceleration in the CO_2 degassing (Wiedner et al., 2008; Day and Henderson, 2011). Similarly, high pCO_2 during summer in Ejulve cave exhibited deviation from the isotopic equilibrium.

Additionally, unlike other caves, the decreasing precipitation rates and the lower pCO_2 contrasts suggested conditions closer to equilibrium than expected for the temperatures in the cave environment (Mattey et al., 2008; Johnston et al., 2013). On the other hand, the season of rapid calcite deposition (spring) and lower cave air pCO_2 achieved conditions closer to equilibrium which is in agreement with other studies (Feng et al., 2012).

Testing the $\delta^{18}O_{ct}$ precipitation in equilibrium

	Ejulve cave			Equations of equilibrium		
	$\delta^{18}O_d$ V–SMOW	$\delta^{18}O_{ct}$ V–PDB	$T_{measured}$ (°C)	Friedman and O'Neil (1977)	Kim and O'Neil (1997)*	Tremaine et al. (2011)
Seasonal drips						
Spring	−9.73	−8.17	11.2	−8.67	−8.96	**−8.19**
Summer	−9.48	−8.24	11.3	**−8.42**	−8.72	−7.93
Autumn	−9.31	−8.33	11.3	**−8.25**	−8.54	−7.77
Winter	−9.99	−8.27	11.2	−8.92	−9.22	**−8.45**
Seepage drips						
Spring	−9.57	−8.24	11.2	**−8.50**	−8.80	**−8.03**
Summer	−9.48	−8.10	11.3	**−8.42**	−8.72	−7.94
Autumn	−9.20	−8.23	11.3	**−8.13**	−8.44	−7.65
Winter	−9.96	−8.25	11.2	−8.90	−9.20	**−8.42**

Note that the $\delta^{18}O_{ct}$ V–PDB has been converted to V–SMOW using the expression $\delta^{18}O_{V-SMOW} = 1.03091 \square\delta^{18}O_{V-PDB} + 30.91$ (Coplen et al., 2002).

** corrected for conventional CO_2–calcite acid fractionation factor of 1,01025*
The results of the modeled equations highlighted in bold are the closest to the $\delta^{18}O_{ct}$ precipitates in Ejulve cave, and those underlined exhibit precipitation in equilibrium.

Table 5.8. *Testing the $\delta^{18}O_{ct}$ precipitation in equilibrium in the present-day carbonates.*

5.7. Implications for paleoclimate reconstructions

The understanding of climate controls of water isotopes and the particular cave features is crucial to accurately interpret past climate from speleothems. The results of this study indicate a sensitivity of the precipitation to the climate recorded as shown by the *temperature effect* (reaching a slope of 0.34‰ °C^{-1}). This slope was higher than that of the *cave temperature effect*, which represented the fractionation of oxygen isotopes between water and calcite during calcite precipitation and presented an opposite relationship (−0.177 ‰ °C^{-1} following Tremaine et al. (2011)). As the $\delta^{18}O_P$-T was higher than the *cave temperature effect*, the *temperature effect* was not annulled during calcite precipitation; thus, $\delta^{18}O$ in the calcite of Ejulve cave could reflect positive values at warmer temperatures (Dorale et al., 2002).

Nonetheless, at longer timescales, several processes could change the present-day relationships, including: a) differences in the seasonality of precipitation (Denton et al., 2005), b) changes in the vapour moisture source (Charles et al., 1994), c) changes in the isotopic composition of the ocean (Shackleton, 1987), and d) changes in the atmospheric circulation patterns and the routes of the air masses (Charles et al., 1994).

Therefore, the long-term $\delta^{18}O_P$-T calculations with instrumental records should be used cautiously to interpret isotopic records in mid and high latitudes during Holocene climate (Darling et al., 2006). Nonetheless, the low variability and lack of seasonal response made the interpretation of $\delta^{18}O_{ct}$ in present-day precipitates of Ejulve cave complex. For example, in the context of colder and drier climates, $\delta^{13}C_{ct}$ would exhibit higher values due to the dry climate and would be amplified by ventilation and the associated kinetic effects. However, the signal of $\delta^{18}O_{ct}$ (assuming temperature as a main control for isotopes as suggested by the monitoring results) would tend to lower values, thus, in a direction opposite to kinetics. This complex pattern can explain the use of $\delta^{13}C_{ct}$ (as opposed to $\delta^{18}O_{ct}$) as a paleoclimatic proxy under certain climates and time periods (Hodge et al., 2008; Genty et al., 2010; Scholz et al., 2012; Pérez-Mejías et al., 2017).

Additionally, the understanding of hydrogeological factors that exert influence on the oxygen isotopes of individual drips is necessary to correctly interpret temporal changes in the oxygen isotope composition of speleothems. Therefore, drip rate emerged as a key factor to unravel the climatic significance of speleothems fed by each drip site. The low discharge drip sites (< 0.1 ml/min) may be of interest to study hydrologic variability at decadal to millennial scales, with some

meteorological events smoothed in the long-term pattern (Baldini et al., 2006).

However, the drip sites of medium to high discharge (EJ-4, EJ-7b) (Fig. 5.6.B) were more sensitive to water excess/deficiency and might preserve a paleoseasonality signal. Therefore, a potential bias with regard to the drip rate was not identified as the dripwaters identified in Ejulve cave had medium-low discharge (> 2 ml/min) and were saturated with respect to calcite. Furthermore, the classification of drips with regard to the CV and maximum discharge needs to be accounted for. The seasonal drips in this study indicated less CV and, thus, were closer to seepage flow and could change the classification from seasonal to seepage at longer time scales as has been observed in other caves (Baker et al., 1997; Riechelmann et al., 2013, 2017).

Additionally, a potential bias with regard to calcite precipitation was linked to cave ventilation. The paleoclimate archives from Ejulve cave were biased from autumn to spring seasons rather than reflecting an annually averaged climate (as seen in a Holocene climate reconstruction from the stalagmite of this cave, Moreno et al., 2017), a pattern also observed in other caves (Banner et al., 2007; Oster et al., 2012; James et al., 2015).

5.8. Conclusions

The monitoring survey carried out in Ejulve cave allowed the study of the isotopic signal of precipitation ($\delta^{18}O$ and δD), cave dripwaters ($\delta^{18}O$ and δD), and farmed calcite ($\delta^{18}O$ and $\delta^{13}C$). The $\delta^{18}O$ and δD of rainfall were conditioned by temperature, with lower values in winter and higher in summer. In addition to the temperature effect, the rainfall component (convective versus rain front) was strongly linked to the temperature in the study area. Moreover, the amount effect explained the variability in $\delta^{18}O$ and δD of precipitation. Additionally, a new LMWL was calculated to include all isotopic data from rainfall and is expressed as follows:

$$\delta D\ (‰\ V\text{-}SMOW) = 6.94\ (\pm 0.14)\ \delta^{18}O + 2.15\ (\pm 1.18) \quad (10)$$

The $\delta^{18}O$ values of dripwaters were in concordance with those of the precipitation after correction of the "altitude affect" and the weighting correction (i.e. using the precipitation of only the months with effective infiltration) for precipitation isotopes. With regard to the maximum water discharge and the CV, the drips of Ejulve cave were classified in two groups: seasonal and seepage. Homogenisation of the waters was observed in the epikarst, however, the seasonality of $\delta^{18}O_p$ was still preserved, indicating similar values for both seasonal and seepage drip sites.

The response time of dripwater from both groups to isotopes in rainfall ranged from six to 21 weeks. However, the discharge rate response was faster and ranged between a few days to 12 weeks. These results suggest the existence of the "*piston effect*" in Ejulve cave which indicates that "new" water pushed down the "old" water pre-existent in the epikarst through the fracture network. With regard to the infiltration, the dripwater from both groups could reflect climatic signals at the seasonal scale with a bias to the wet season for all sites except those with a very low discharge (< 0.01 ml min^{-1}) which likely reflected inter-annual variability.

The cave exhibited ventilation which was driven by air density during autumn through spring, recording the lowest in-cave pCO_2 values and the highest calcite precipitation rates during that time. The growth rate was controlled primarily by cave ventilation and secondarily by dripwater chemistry and drip rate.

The results of the carbonate precipitates suggest the dependence of $\delta^{18}O_{ct}$ on $\delta^{18}O_d$, with a weak effect of drip rate on the $\delta^{18}O_{ct}$.The isotopic variability was not observed at a seasonal scale, therefore, any climatic interpretation of $\delta^{18}O_{ct}$ should be made for longer timescales. Nevertheless, a seasonal signal in

$\delta^{18}O_{ct}$ was observed in some drips and the high values during summer and autumn were explained by degassing kinetics and not by the high $\delta^{18}O$ of dripwaters.

On the contrary, $\delta^{13}C_{ct}$ showed seasonality with higher values during summer and autumn and lower in winter and spring. The inverse correlation between drip rate and $\delta^{13}C_{ct}$ was higher in seepage than seasonal drip sites, and higher in summer and autumn, suggesting longer time between drops and potential degassing as the mechanism behind the high $\delta^{13}C_{ct}$ values. Likewise, the low $\delta^{13}C_{ct}$ values were in agreement with high soil microbial activity, vegetation productivity, and water availability. Seasonally, calcite precipitation in the cave was close to equilibrium during spring and autumn. In general, while seasonal and seepage drip sites exhibited similar $\delta^{18}O_{ct}$ signals, they differed in the $\delta^{13}C_{ct}$ values, with higher values for seepage drip sites in contrast to seasonal ones.

Therefore, the monitoring of the cave environment offers an opportunity to understand the present-day relationships between environmental variables and rainfall, dripwaters, and farmed calcite for better understanding and accurate interpretation of speleothem records.

Supplementary Annex

of

Transference of isotopic signal from rainfall to dripwaters and farmed calcite in Mediterranean semi-arid karst

5.9. Analysis of the d-excess

The *d*-excess reflects the relative humidity and the air temperature of the area where the evaporation and cooling leads to rainfall, so it is an effective tracer for moisture sources (Dansgaard, 1964; Rozanski et al., 1993; Clark and Fritz, 1997; Celle-Jeanton et al., 2001; Vandenschrick et al., 2002) and vapour recycling over the continents (Gat et al., 1994). The *d*-excess of precipitation has a worldwide average of ~ 10, and values <10‰ are associated with high humidity conditions during the formation of moisture masses, while values >10‰ derived from recycled moisture evaporated under low humidity at the vapor source (Dansgaard, 1961; Craig, 1961; Clark and Fritz, 1997). Additionally, other local processes would modify the *d*-excess values such as subcloud evaporation of raindrops (Rozanski et al., 1993). In this way, this results in lower values of *d*-excess with lower slopes of LMWL are strongly associated with evaporative environments (Rozanski et al., 1993) in which the evaporation of the samples, mostly in summer, occurs beneath cloud base in warm-dry atmospheres (Araguás-Araguás et al., 2000; Onac et al., 2008; Lachniet and Patterson, 2009; Moreno et al., 2014).

Our results of *d*-excess show seasonality, with lower values in summer (7.72‰) with respect to the rest of the year (11.26‰). Taking into account the dominance of Mediterranean vapor source for summer precipitation in this area (Moreno et al., 2014), our low *d*-excess in summer seems to contradict the high values, usually higher than 10, seen in other Mediterranean areas (Celle-Jeanton et al., 2001). In order to disaggregate the seasonal processes, the regression lines for each season have been plotted (Fig. 5.4.B). Spring and fall show higher slope and intercept, close to the Western Mediterranean Water Line. During these seasons, the evaporation effect appears to be negligible. On the contrary, winter exhibit slightly lower slope and intercept, explained by rainfall samples located below the LMWLs that could be affected by evaporation at high humidity conditions in the source area (Lachniet, 2009). Finally, the summer line reflects the lowest slope and intercept, confirming the evaporation of samples in the subcloud layer as the main process explaining those values.

Therefore, two possible explanations can be established for the results of *d*-excess; firstly, the low humidity in North Atlantic source area gives as a result high values of *d*-excess during the wet season (autumn through spring); secondly, the elevated evaporation due to the high temperatures of air during summer, supported by the low slope in the LMWL, triggers unusual low values of *d*-excess usually in events of low amount of precipitation. Hence, in this area the *d*-excess could be controlled by temperature that triggers subcloud evaporation during summer, and then the moisture source fingerprint of the Mediterranean is masked. In that way, *d*-excess values are lower when temperature is higher, consistent with previous studies in other areas (Frohlich et al., 2002; Lambert and Aharon, 2010; Ma et al., 2012; Feng et al., 2013; Wang et al., 2015).

5.10. Variable lag in the transference of the isotopic signal from precipitation to dripwaters

The event "a" (Fig. 5.10) exhibit a faster response in the dripwaters compared to events "b" and "c", and could be explained by the intense rainfalls during October and November of 2012 (Fig. 5.9) that favors further infiltration, hence, a more effective infiltration and transmission of the isotopic signal occurs in a wetted soil.

While in some periods all the drips show similar isotopic values (e.g. event a', Fig. 5.10), in which the local processes in the epikarst seem not to modify differently the dripwater isotopic signal, in other periods the differences between drips are notable (e.g. event b' and c', Fig. 5.10). These periods of big differences do not coincide with those of more discharge (Fig. 5.9) evidencing a more complex behavior. A special case is represented by two dripwater samples (EJ-9 ad EJ-10b) that exhibit clearly lower values of $\delta^{18}O_d$ reached during the summer of 2014 (#118 and #120, Table 5.3) than the other dripwater sites. Although there are some rainfall events in March-April of 2014 with lower $\delta^{18}O$ (Fig. 9), the results of these two dripwater samples are lower than the weight-averaged precipitation.

Most drips during that time show unusual values close to −10‰ (e.g. #112, #113, #114, #119, Table 5.3), suggesting a general recharge of the epikarst with water with a remarked low $\delta^{18}O_p$ values. However, the mixing in the epikarst with the pre-existing groundwaters depends on the type of flow, the route, the response time, and other local factors (Lachniet, 2009) resulting in lower $\delta^{18}O_d$ values in the case of #118 (drip EJ-9, seasonal) and #120 (drip EJ-10b, seepage) (Table 5.3).

As one drip belongs to seasonal and the other to seepage group, and in general all drips exhibit low $\delta^{18}O$ values during that time, both drip groups may be connected to common groundwater microreservoirs, suggesting an internal structure of the host rock composed mainly by micro pores feeding the seepage drippings, with less discharge rates, and should be accompanied by joints, fractures or fissures that favored the preferential flow in the drips with higher discharge rate and variability.

	EJ-1	EJ-2	EJ-3	EJ-4	EJ-5	EJ-6	EJ-7	EJ-7b	EJ-8	EJ-9	EJ-10	EJ-10b
1/10/13	2,3	-	3,8	14,0	4,3	0,7	8,6	-	6,0	7,0	-	-
1/25/13	2,3	1,8	3,3	8,6	3,8	0,7	4,8	-	4,0	0,7	-	-
2/14/13	2,7	0,9	3,8	24,0	5,0	0,9	-	-	22,0	30,0	-	-
3/23/13	3,0	0,6	4,3	58,0	5,0	0,7	4,0	-	6,0	44,0	-	-
5/9/13	4,0	0,5	0,1	58,0	4,0	0.6	13,0	-	8,0	76,0	-	-
6/18/13	3,0	0,6	0,0	34,0	6,0	0,6	14,0	-	4,6	30,0	-	-
8/7/13	2.86	0,3	0,0	15,0	3,5	0,6	10,0	-	1,4	3,3	-	-
9/18/13	2,6	0,3	static	3,3	3,3	0,4	10,0	-	static	2,1	-	-
11/6/13	2,9	0,6	0,7	0,9	3,0	0,3	-	10,0	static	0,9	0,3	0,5
12/19/13	2,9	0,4	1,2	4,6	3,5	0,5	8,6	8,6	2,9	1,0	0,5	0,3
2/19/14	2,7	1,1	1,3	7,5	5,5	0,6	-	8,6	6,7	1,0	1,3	0,5
4/2/14	2,7	0,2	1,3	8,0	4,6	0,6	10,0	-	6,0	1,0	1,1	0,9
5/13/14	2,6	0,8	1,2	6,0	4,3	0,6	18,0	12,0	2,2	1,0	0,6	0,8
6/27/14	2,6	0,6	0,9	2,4	3,2	0,4	3,8	7,5	0,6	1,0	0,4	0,6
8/20/14	2,5	-	0,7	1,0	3,2	0,3	3,3	7,5	static	0,9	0,3	0,5
9/30/14	2,4	-	1,1	0,2	3,2	0,4	6,7	6,0	static	0,8	0,2	0,4
11/11/14	2,4	-	0,8	1,8	3,5	0,3	6,0	7,5	0,0	1,0	0,2	0,6
	EJ-1	EJ-2	EJ-3	EJ-4	EJ-5	EJ-6	EJ-7	EJ-7b	EJ-8	EJ-9	EJ-10	EJ-10b
12/17/14	2,4	-	1,7	20,0	5,5	0,6	3,0	1,1	52,0	1,0	1,3	0,7
2/17/15	2,3	-	1,3	11,0	4,6	0,6	21,0	0,1	10,0	1,0	1,3	0,9
4/7/15	3,0	-	0,9	22,0	5,0	0,6	12,0	0,1	4,0	1,0	0,9	0,7
5/20/15	2,9	-	1,1	5,0	3,5	0,6	8,6	0,1	1,2	1,0	0,5	0,8
6/17/15	2,6	-	1,6	15,0	6,0	0,6	20,0	1,0	26,0	1,0	0,6	0,9
8/24/15	2,5	-	1,1	5,0	4,3	0,6	6,7	0,8	1,0	0,9	0,3	1,0
10/22/15	2,4	-	0,7	1,7	3,3	0,3	12,0	0,3	static	0,9	0,3	0,5
11/27/15	2,4	-	1,1	6,7	4,3	0,6	20,0	0,2	0,9	1,0	0,5	1,0
1/8/16	2,3	-	0,8	2,1	3,3	0,3	10,0	0,1	static	1,0	0,3	-
2/9/16	2,3	-	0,6	0,9	3,0	0,2	0,2	0,1	static	0,9	0,3	-
4/9/16	2,2	-	2,1	0,4	5,5	0,6	12,0	0,1	46,0	1,0	1,3	-

6/19/16	1,8	-	1,4	1,4	3,3	0,4	15,0	0,1	static	1,0	0,4	-
10/4/16	1,9	-	0,4	static	4,0	0,2	10,0	-	static	0,9	0,2	-

5.9. Table of drip rates. *The units are drips minute^{-1}. When a drip does not exhibit any discharge during 15 minutes, we refer it as a "static".*

'Work, finish, publish!'

-Michael Faraday

Chapter

Paleoclimatology

A. Abrupt climate changes during Termination III in Southern Europe

Significance

We present an outstanding speleothem record that reconstructs the vegetation activity and hydrological availability during Termination III (T-III) in Southern Europe throughout $\delta^{13}C$, $\delta^{18}O$, and Mg/Ca variations. The results reveal for the North Atlantic region the sequence of abrupt stadial events during T-III, in close analogy to the Asian Monsoon changes reconstructed from Chinese speleothems. The two stadials identified in this record (S8.1 and S8.2) have similarities with Heinrich 1 and Heinrich 2 events in Termination I in terms of changes in the phasing of benthic $\delta^{18}O$, rise of semidesert pollen taxa, and ice-rafted debris release.

Abstract

The Late Quaternary glacial–interglacial transitions represent the highest amplitude climate changes over the last million years. Unraveling the sequence of events and feedbacks at Termination III (T-III), including potential abrupt climate reversals similar to those of the last Termination, has been particularly challenging due to the scarcity of well-dated records worldwide.

Here, we present speleothem data from southern Europe covering the interval from 262.7 to 217.9 kyBP, including the transition from marine isotope stage (MIS) 8 to MIS 7e. High-resolution $\delta^{13}C$, $\delta^{18}O$, and Mg/Ca profiles reveal major millennial-scale changes in aridity manifested in changing water availability and vegetation productivity. uranium–thorium dates provide a solid chronology for two millennial-scale events (S8.1 and S8.2) which, compared with the last two terminations, has some common features with Heinrich 1 and Heinrich 2 in Termination I (T-I).

Keywords

Terminations | *stalagmite* | *stadial event* | *stable isotopes* | *Iberian Peninsula*

Interpreting the processes responsible for glacial terminations and the accompanying feedbacks requires a detailed chronology across different elements of the climate system. Because of the varying orbital configurations among glacial terminations, it is instructive to compare the sequence of events in different terminations to distinguish common processes and those which are unique. Using records in different parts of the climate system to compare the expression

of abrupt climate events at different latitudes may help to diagnose the mechanisms that triggered those transitions.

However, it has been difficult to obtain climate records for older terminations, such as Termination III (T-III), with sufficient resolution to capture the abrupt climate events that in some c ases result from deglacial meltwater release (Martrat et al., 2014), and to assess which of them are expressed worldwide. In Europe and the Middle East, long lacustrine sequences reveal abrupt changes in sedimentology and vegetation cover over T-III (Tzedakis et al., 1997; Tzedakis, 2005; Kwiecien et al., 2014). Unfortunately, the absence of absolute dates precludes the construction of independent chronologies for these changes and their correlation with marine records of ice volume.

To date, most of the marine and also terrestrial available chronologies of the marine isotope stage (MIS) 8 to MIS 7 transition have been built by either directly or indirectly tuning to orbital configurations (Desprat et al., 2007) or using Antarctic chronologies aligning the benthic $\delta^{18}O$ to deuterium/hydrogen records from Antarctic ice cores (Tzedakis, 2004). Independent chronologies on the marine T-III period, for example in benthic $\delta^{18}O$ records, feature high uncertainty (239 ± 10 ky) (Huybers and Wunsch, 2005). Antarctic ice sheet chronologies for T-III based on changes in δD and atmospheric gases have uncertainties estimated at 3–4 ky (Bazin et al., 2013). The absolute chronologies independent of orbital forcing are critical to determine the relationship between paleoclimate records and insolation and to understand ocean-atmosphere feedbacks responsible for deglacial changes. So far, other terrestrial absolute chronologies for T-III are available only in $\delta^{18}O$ records of summer monsoon intensity from Chinese caves (Cheng et al., 2009; Cai et al., 2015) and in a $\delta^{18}O$ record of temperature changes from Spannagel Cave in the Alps (Spotl et al., 2008), although this last record starts during early MIS 7e.

Here, we present a speleothem geochemical record that covers the full duration of the T-III period in southern Europe, providing a well-dated high-resolution reconstruction of aridity and vegetation productivity which can be related to abrupt stadial events in the North Atlantic caused by glacial meltwater discharges. The studied speleothem comes from the Ejulve cave (40°45´34´´N, 0°35´07´´6W, 1,240 m above sea level) (Fig. 6.1), located in the Iberian Range, NE Spain, under a Mediterranean temperate climate with strong continentality.

Results from a 3-y monitoring survey of farmed calcite show that the seasons of positive water balance, autumn through spring, feature low-calcite $\delta^{13}C$ in the precipitated carbonate

because soil CO_2 is enhanced by productive vegetation in association with rainy seasons (Camarero et al., 2015) and prior calcite precipitation is minimized.

In contrast, high $\delta^{13}C$ occurs during drier periods, and coincides with high Mg/Ca ratios, low amount of in situ farmed calcite, and high temperatures with minima water availability over the cave (Supplementary annex). These seasonal oscillations confirm a water availability signal in $\delta^{13}C$ and Mg/Ca ratio; on long time scales changes in the mean temperature during the growth season may also affect vegetation activity and thus $\delta^{13}C$. Therefore, $\delta^{13}C$ record in Ejulve stalagmites is interpreted as a proxy for vegetation productivity since it is controlled by plant root respiration and microbial activity, and thus conditioned by temperature and especially by humidity.

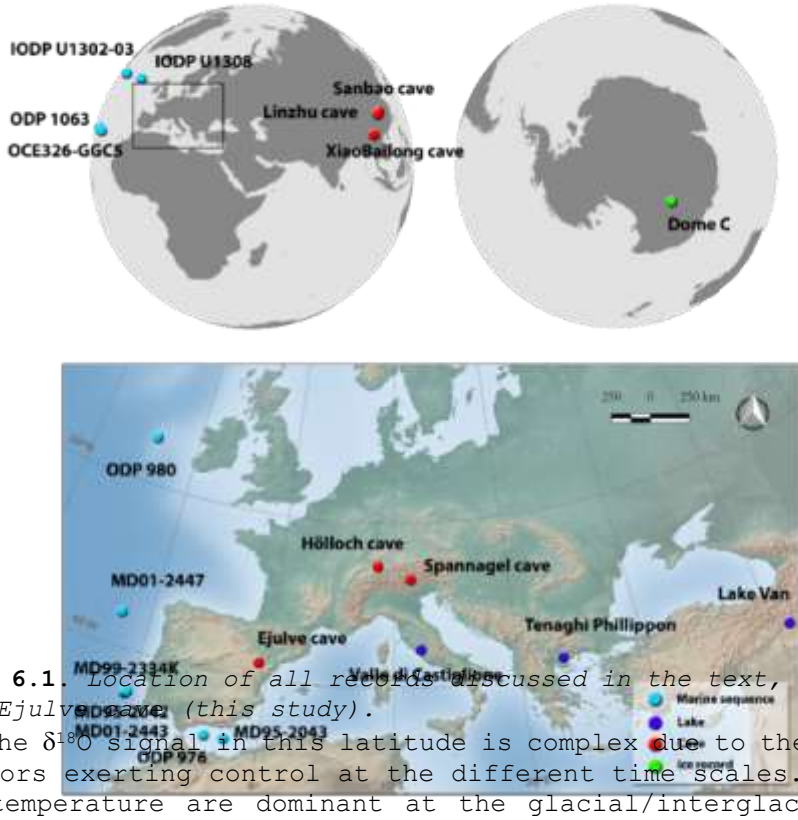

Fig. 6.1. *Location of all records discussed in the text, including the Ejulve cave (this study).*

The $\delta^{18}O$ signal in this latitude is complex due to the diverse factors exerting control at the different time scales. Changes in temperature are dominant at the glacial/interglacial time scales while the source of moisture (e.g., freshwater input) has been detected to be important during short events (Supplementary annex). Calcite precipitates in artificial supports are found throughout the year, but are reduced in summer, a season with water deficit. Thus, a mixing in the

isotopic signal of the seasonal values, biased to the higher calcite growth seasons, is expected to be found in fossil speleothems.

6.1. Age Model

The 350-mm-long ARTEMISA stalagmite grew from 262.7 to 217.9 kyBP (Fig. 6.2) with a period of particularly fast growth rate during 240–238 ky, corresponding to the transition from MIS 8 to MIS 7. The chronology is provided by 24 uranium–thorium (U/Th) dates (suppl. annex, Table 6.1), with two reversals (at 45 and 255 mm from the bottom) that were excluded from the age model.

From 15 to 65 cm, corresponding to 260–240 ky, U/Th dates fitted by StalAge yield a linear age model and constant slow rates of growth. Dramatically faster growth rates occur over the subsequent 16 cm (70 to 230 mm from base) during MIS 7e. The fast growth rate and absolute age uncertainties of ±2 ky, characteristic of the 1% of uncertainty in age given by the analytical uncertainties propagated through the age equation, complicate a single age interpolation of the entire stalagmite with standard algorithms such as OXCAL software (Ramsey, 2008) (orange line, Fig. 6.2.A) and StalAge (Scholz and Hoffmann, 2011) (red line, Fig. 6.2.A).

The final model we use (green line, Fig. 6.2.B) is generated using StalAge for the base (seven dates) and top (nine dates) sections of the Stalagmite but adding a linear interpolation to connect both parts. This approach provides a more realistic growth post-T-III during earlier MIS 7e and also considers the maximum potential uncertainty given by the U/Th datings (i.e., 2 ky). The fast-growing section permits a resolution of 37 y in the stable isotope record, while the slower-growing glacial and deglacial phases permit 160-y resolution.

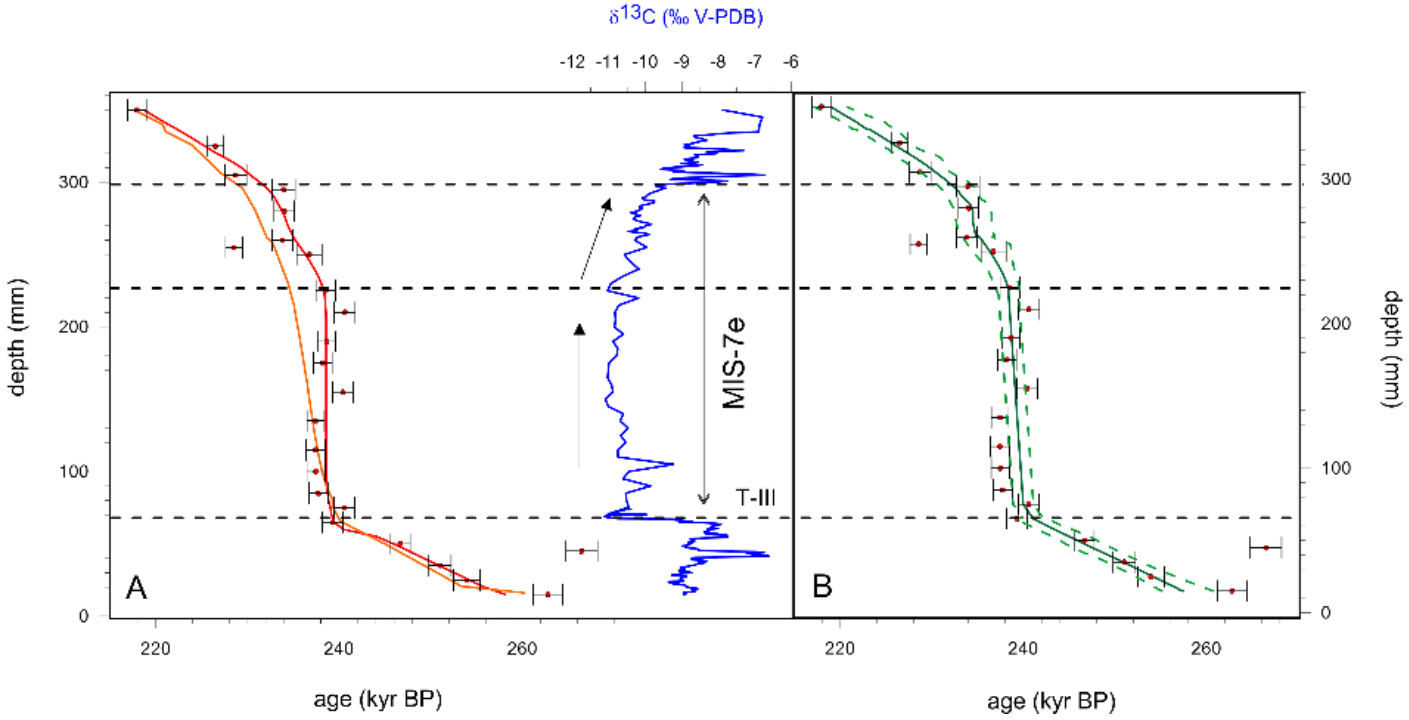

Fig. 6.2. *Age model for ARTEMISA stalagmite. (A) Blue line represents $\delta^{13}C$ values to trace the timing of MIS 7e versus depth; red line is the age model constructed by StalAge software (Scholz and Hoffmann, 2011), and orange line is the model provided by OxCal (Ramsey, 2008). (B) Final model adopted for the stalagmite. Dashed line in the age model represents age uncertainty, provided by StalAge in the top and base parts, and an average dating error used in the lineal interpolation. Horizontal dashed lines establish the glacial-interglacial transitions and the two phases in MIS 7e, according to the changes in growth rate in the age model and the $\delta^{13}C$ profile.*

6.2. Results and Discussion

Intense isotopic changes in the Ejulve cave speleothem, mostly the change toward more negative $\delta^{13}C$ values, mark the transition from MIS 8 to MIS 7, suggesting a rapid evolution from a generally more arid glacial state with low biological activity to a more humid interglacial with enhanced vegetation productivity (Fig. 6.3). During this time, the $\delta^{18}O$ values vary from the mínimum values of the termination (-9.3 ‰) at about 243 ky to the maximum in the record (−6.5 ‰) at 235 kyr. The low growth rates during glacial times (3 mm/kyr) are consistent with low water availability in the cave during the cold conditions of MIS 8. Afterward, the onset of MIS 7e is characterized by a rapid $\delta^{13}C$ decrease to −11.1 ‰, a gradual rise in the $\delta^{18}O$, and a dramatic increase in growth rate to 91 mm/kyr (Fig. 6.3).

Following this exceptional increase, growth rates remain higher (20–30 mm/kyr) than those of the glacial until 234 ± 2.0 kyr before descending to rates near to 6 mm/ky, which are similar to those of MIS 8. This growth rate pattern is consistent with more humid and vegetated interglacial. Likewise, the minima in $\delta^{234}U$ (Fig. 6.3) between 240 ± 1.1 and 234 ± 2.0 ky compared with previous and following values suggest shorter water residence times in the epikarst during the interglacial (Hellstrom and McCulloch, 2000). The delay of 1 kyr in $\delta^{234}U$ with respect to $\delta^{13}C$ and metal ratios at the end of the glacial period indicates a climatic-dependent signal, as seen in other records (Hellstrom and McCulloch, 2000).

Two abrupt excursions to more positive $\delta^{13}C$ preceed the main deglacial $\delta^{13}C$ depletion from 244.7 ± 2.1 to 241 ± 1.5 and from 249 ± 1.9 to 247.4 ± 2.0 ky [labeled here as Stadial 8.1 and 8.2 events, respectively, identified previously in ice-rafted debris (IRD) layers (Channell et al., 2012)] which are also marked as transient increases in Mg/Ca and, at least the 8.1 Stadial, as decrease in $\delta^{18}O$ (Fig. 6.3). Those two events were previously found in Chinese caves (Fig. 6.3).

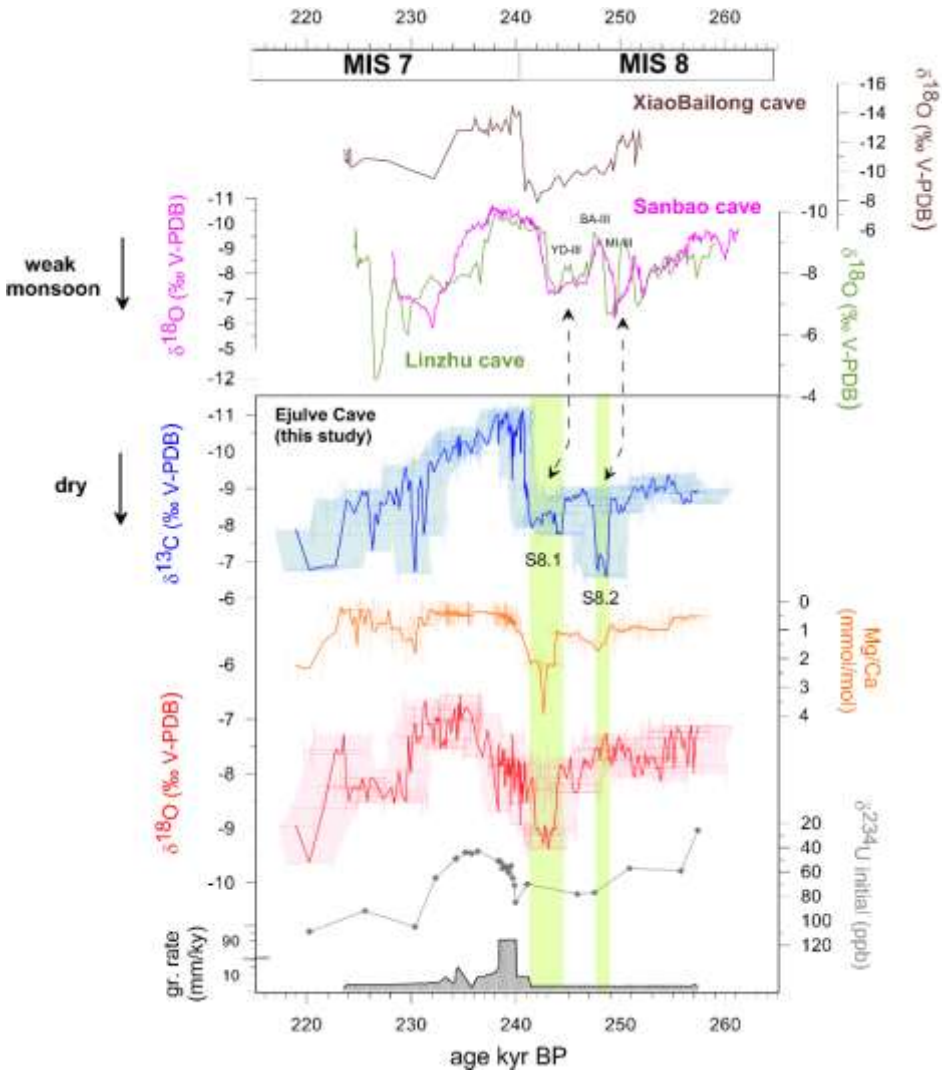

Fig. 6.3. *Results of ARTEMISA stalagmite compared with other records of T-III, from top to bottom:* $\delta^{18}O$ *profiles from XiaoBailong cave (Cai et al., 2015) (dark brown), Linzhu cave (Cheng et al., 2009) (light green), and Sanbao cave (Cheng et al., 2009) (pink) [the events YD-III, BA-III, and MI-III identified by Cheng et al. (2009) are indicated]. The axes in the Chinese caves are reversed; the results of this study are composed of* $\delta^{13}C$ *(blue) and* $\delta^{18}O$ *(red) profiles (the shadow area represents uncertainty range in the chronology) and Mg/Ca (orange) metal ratio (both with axes reversed),* $\delta^{234}U$ *initial (gray) and growth rate (black and gray). All of the axes are reversed except the growth rate one. Green band indicates dry events, highlighting S8.1 and S8.2, characterized by a trend to higher* $\delta^{13}C$ *and Mg/Ca values and lower* $\delta^{18}O$ *in S8.1.*

6.3. Abrupt climatic changes and forcing mechanisms during T-III

Glacial terminations appear to be explained not only by rising high latitude or northern Hemisphere insolation (Denton et al., 2010), but also due to feedbacks from changes in ocean circulation and the carbon cycle (Lang and Wolff, 2011; Past Interglacials Working Group of PAGES, 2016). When orbital forcing initiates significant melting of a large NH ice sheet, it provides enough meltwater to produce a collapse on the Atlantic Meridional Overturning Circulation (AMOC) (Denton et al., 2010; Past Interglacials Working Group of PAGES, 2016) which in turn through the bipolar seesaw accelerates Southern Ocean warming and alters wind regimes leading to rapid release of CO_2 from upwelled deep ocean waters to the atmosphere. This greenhouse forcing may be a key impulse making a termination inevitable.

While the conditions for an interglacial onset are conditioned by astronomical pacing (high insolation–low precession), the precise (millennial-scale) timing of each termination and the strength of the following interglacial varies, influenced by key global climate parameters (e.g., ice volume, regional Surface temperature, greenhouse gases) (Past Interglacials Working Group of PAGES, 2016). The role of such feedbacks and short oscillations has been well characterized for T-I and more recently for Termination II (T-II) (Marino et al., 2015), but their role in the T-III has not been previously described.

The orbital configuration of T-III, with an ~10-kyr lag between maximum in obliquity and minimum in precession (Fig. 6.4), is very distinctive from that of T-II and T-I (Cheng et al., 2009; Denton et al., 2010). T-III is a low-amplitude termination (Lang and Wolff, 2011) that leads to a weak interglacial, with a rapid return to near full glacial benthic $\delta^{18}O$ within 20 kyr after the termination. However, in terms of the sequence of abrupt climate events associated with the termination, T-III has been considered similar to T-I (terminations interrupted by stadials) and different from T-II and Termination IV (T-IV) (uninterrupted or minimally interrupted terminations) according to the study of Chinese stalagmites (Cheng et al., 2009).

The freshwater glacial melt release and AMOC shutdown leave a clear climatic fingerprint on the Iberian Peninsula during stadial events of T-I and MIS 3 because weakened heat transport shifted storm tracks and led to extremely dry conditions (Moreno et al., 2005; Fletcher and Sánchez Goñi, 2008). This connection results from the expansion of the polar vortex during AMOC shutdowns, which lead to the southward arrival of polar or

continental air outbreaks. Several pollen sequences have demonstrated the synchrony of shifts to arid-adapted vegetation in the Iberian Peninsula and the marine cooling (Goñi et al., 2002; González-Sampériz et al., 2006). A further proof for this tight AMOC–Iberia connection during T-I is provided by an accurately dated speleothem record from the southern Pyrenees which shows parallel changes in humidity and AMOC intensity along the Younger Dryas period (YD) (Bartolomé et al., 2015).

We propose that the millennial-scale aridity events detected in the Ejulve record at the onset and within the T-III (S8.1 and S8.2 events) are likewise related to AMOC slowdowns or shutdowns. The arid events recorded by high $\delta^{13}C$ and high Mg/Ca in the Ejulve T-III record provide an absolute chronology for the marine record of abrupt changes, where arid events are manifest by the dominance of semidesert pollen in Iberian margin sediments (Fig. 6.4.J) and are coincident with enhanced IRD deposition (Fig. 6.4.I).

Our T-III record shows a two-phase structure, with a first extreme arid event (S8.2) at 249–247.4 kyr, a return to more humid conditions, and a second arid event (S8.1) at 244.7–241 kyr (Fig. 6.4.D). The imprint of the $\delta^{18}O$ differs between both events and only the S8.1 event is pointed out with extremely low values. The sudden arrival of fresh (^{18}O-depleted) meltwater to North Atlantic intermediate latitudes and entrance in the Mediterranean Sea would provide a mechanism to explain the low $\delta^{18}O$ signal during S8.1 in an analogous way that occurred during T-I (Heinrich 1) and T-II (Heinrich 11) (Jiménez-Amat and Zahn, 2015).

Other records in the Iberian Peninsula have reported a similar isotopic response to the arrival of fresh water to North Atlantic (e.g. during the 8.2-kyr event) (Domínguez-Villar et al., 2009), reinforcing the hypothesis that changes in North Atlantic and Mediterranean sea water may modify rainwater isotopic composition in the Iberian Peninsula and, consequently, $\delta^{18}O$ in speleothems.

The shift to low values in $\delta^{18}O$ of ARTEMISA during event S8.1 is very similar to the change reported previously for the Holocene stalagmite [1.7‰ in S8.1 with respect to 2‰ in the 8,200-y event (Domínguez-Villar et al., 2009)]. On the contrary, $\delta^{18}O$ values do not change during the S8.2 event. That event has more enriched $\delta^{13}C$ values than S8.1, pointing out a lower vegetation activity in our area, in coherence with the record from Chinese caves with weaker monsoon in S8.2 with respect to S8.1 (Fig. 6.3).

A similar structure for the T-III in two phases has already been described in Asian monsoon speleothems (Cheng et al., 2009). Therefore, Ejulve Stadials that are correlated within

the dating uncertainty with two similar events of weak summer monsoon in the $\delta^{18}O$ signal from Sanbao Cave (Fig. 6.3) are the first expression of those abrupt climate changes during T-III in a continental record from Europe.

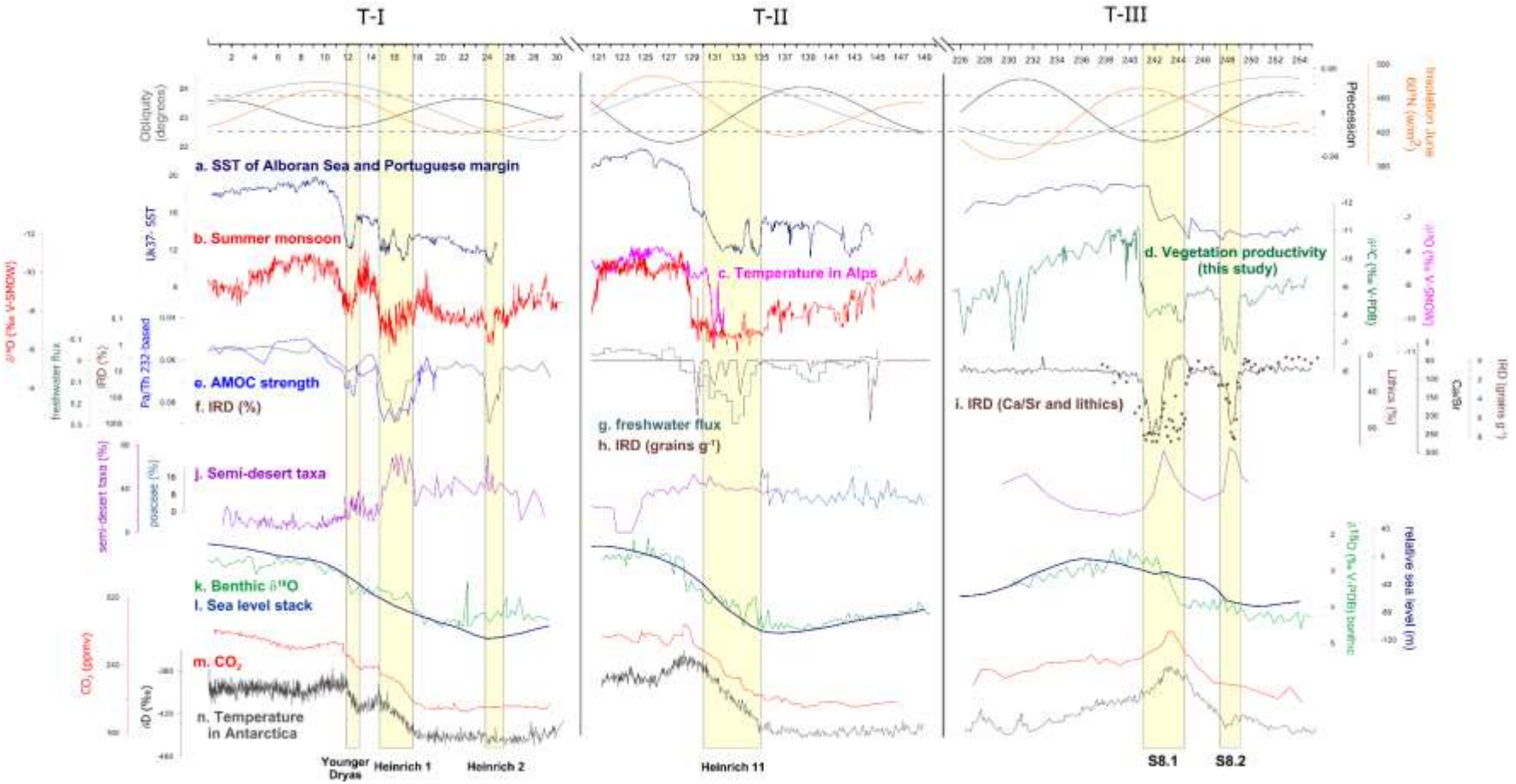
T-I
T-II
T-III
Obliquity (degrees)
Precession
Insolation June 60°N (W/m²)
a. SST of Alboran Sea and Portuguese margin
b. Summer monsoon
c. Temperature in Alps
d. Vegetation productivity (this study)
e. AMOC strength
f. IRD (%)
g. freshwater flux
h. IRD (grains g⁻¹)
i. IRD (Ca/Sr and lithics)
j. Semi-desert taxa
k. Benthic δ¹⁸O
l. Sea level stack
m. CO₂
n. Temperature in Antarctica
Younger Dryas
Heinrich 1
Heinrich 2
Heinrich 11
S8.1
S8.2

There are clear teleconnections between the monsoon system and our latitudes, both responding to changes in North Atlantic oceanic conditions that would explain this covariation between records. During the ice-sheet disintegration, the cold anomalies in the ocean generate an influx of meltwater and iceberg discharges in the North Atlantic, triggering the reduction or shutdown of the AMOC and the associated northward surface-ocean transport of heat. The extensive ice cover would seal off the escape of heat to the atmosphere, triggering cold anomalies during winter that probably advected eastward into Asia, affecting the summer monsoon (Cheng et al., 2009; 2016). Thus, both Chinese speleothems and our record respond to common mechanisms of climate forcing.

Fig. 6.4. *Comparison of T-I, T-II, and T-III, from top to bottom: orbital forcing including obliquity (gray), precession (black), and insolation curves in June at 65°N (W/m2) (orange); (A) Uk^{37} SST from marine cores ODP 976 (Alboran Sea) in T-I (Martrat et al., 2014) and T-II (Marino et al., 2015), and MD01-2443 (Portuguese margin) in T-III (Martrat et al., 2007) (navy blue); (B) $\delta^{18}O$ composite from Chinese caves as a proxy of summer monsoon intensity (Cheng et al., 2016) (red); (C) $\delta^{18}O$ profile of Hölloch cave (Moseley et al., 2015) (pink); (D) $\delta^{13}C$ of ARTEMISA from Ejulve cave (forest green); (E) Pa/Th 232-based as AMOC intensity proxy (McManus et al., 2004) (blue); (F) IRD from MD99-2334K (Skinner and Shackleton, 2004) (dark brown); (G) freshwater flux reconstruction (Marino et al., 2015) (moss green); (H) IRD discharge in ODP-1063 (Deaney et al., 2017) (dark brown); (I) Ca/Sr from IODP U1302-03 (Channell et al., 2012) (black line) and lithics from IODP 1308 (Obrochta et al., 2014) (dots, dark brown) in percent; (J) semidesert taxa of pollen in MD95-2043 and MD95-2042 (Goñi et al., 1999; Fletcher and Sánchez Goñi, 2008) in T-I and T-II (purple), poaceae taxa in MD01-2444 (Margari et al., 2014) (blue), and semidesert taxa of pollen in MD01-2447 (Desprat et al., 2006) in T-III (purple); (K) $\delta^{18}O$ of benthic foraminifera in IODP U1308 (Hodell et al., 2008) (forest green), (L) sea-level stack (Spratt and Lisiecki, 2016) (deep navy blue); (M) CO_2 (ppmv) (Lüthi et al., 2008) (red); and (N) δD (Jouzel et al., 2007) (gray) both in Dome C, Antarctica. Yellow vertical bars represent YD, Heinrich 1, and Heinrich 2 in T-I; Heinrich 11 in T-II; and S8.1 and S8.2 stadials in T-III established in ARTEMISA from the Ejulve cave. Due to the lack of absolute chronologies in the pollen record of T-III, that profile from Iberian Margin has been tuned to the age model of ARTEMISA, using tie points anchored to S8.2, S8.1, and at the end of the MIS 7e. The profile with the original ages can be found in suppl. annex, Fig. 6.11.*

6.4. Millennial-scale stadial events in the context of last three Terminations

Taking into account the similar structure established in monsoon records between terminations interrupted by stadials (T-I and T-III) on one hand, and uninterrupted or minimally interrupted terminations (T-II and T-IV) on the other hand, Cheng et al. (2009) suggested that in the last four terminations only T-I and T-III show abrupt events in their structure. The possible cause of this different structure among the terminations is associated with the relatively low insolation shifts and rates of insolation change in T-I and T-III, in opposition to the high shifts and rates reported from uninterrupted terminations (T-II and T-IV) (Cheng et al., 2009). In T-III, whereas the two abrupt weak monsoon events were previously considered analogous to the Mystery Interval and YD (Fig. 6.3), our direct correlation of the Iberian arid events to the regional marine sequences, the benthic $\delta^{18}O$ record, and the IRD discharges, suggests instead that they are more analogous to the Heinrich 2 (HS-2) and Heinrich 1 (HS-1) in spite of some dissimilarities are also observed (Fig. 6.4). One of the reasons to make an analogy with Ejulve stadials S8.1 and S8.2 during T-III, with HS-1 and HS-2, lies in their correspondence with two strong IRD events in the North Atlantic Ocean (Fig. 6.4.I), which have an intensity similar to those of the MIS 3 (Birner et al., 2016). In a similar way, HS-1 and HS-2 events preceding the T-I are synchronous with a strong IRD event, while no IRD occurs during the YD (Fig. 6.4.F).

The AMOC slowdown during the HS-1 (Fig. 6.4.E) is coincident with the first appreciable shift in $\delta^{18}O$ of benthic foraminifera (Fig. 6.4.K) due to a massive arrival of meltwater to the North Atlantic latitudes and its penetration into the deep ocean. During T-III, the first rise in $\delta^{18}O_{benthic}$ occurs during S8.1 (Fig. 6.4.K), indicating the arrival of a large volume of meltwater also coincident with an AMOC slowdown in a similar way to that of T-I, underscoring the similarities between HS-1 and S8.1. However, the arid event and AMOC slowdown of S8.2 were not coincident nor preceded by an appreciable $\delta^{18}O_{benthic}$ change, more analogous to the HS-2, where a small volume of meltwater not appreciable in $\delta^{18}O_{benthic}$ released in particularly sensitive locations was able to accomplish AMOC slowdown. Likewise during T-II, the sea-surface temperatures show during HS-11 (Marino et al., 2015) a similar structure to HS-1 (Fig. 6.4.A), being thus similar to the S8.1 event found in ARTEMISA stalagmite in terms of IRD discharge and arrival of freshwater (Fig. 6.4.G,H). On the contrary, arid conditions were not reported from the pollen taxa, albeit it can be due to the scarce pollen records in this area during MIS 6 (Goñi et al., 1999; Margari et al., 2014). Moreover, stadial events similar to S8.2 during T-II have not

been found in marine sequences, European or Chinese caves (Fig. 6.4.A–C). Hence, more data of T-II are needed to confirm or discard the existence of two stadial events or only one in that termination.

Therefore, the similitudes between stadial events S8.1 and S8.2 to HS-1 and HS-2 are defined by the intense IRD discharges, the existence of arid events interpreted from the pulses of dominance of semidesert taxa, and the similar phasing of the benthic $\delta^{18}O$, features not seen during the YD. However, there are also some dissimilarities between S8.1 and HS-1 that should be taken into account and suggest that the analogy between S8.1 and HS-1 is not as strong as between S8.2 and HS-2. Due to the timing of the deglaciation, the relative sea level and the summer insolation differs between S8.1 and HS-1, on which the glacier conditions are more evident. However, the Antarctic warming and the forcing of the CO_2 linked to the AMOC strength (Deaney et al., 2017) differ in the last three terminations (Fig. 6.4.M,N). While in T-I the rise in Antarctic temperatures is interrupted by the Bølling–Allerød warm period in the North Hemisphere, conforming a two-peak structure in δD and CO_2, on the contrary T-II and T-III exhibit an uninterrupted rise in Antarctic temperaturas following the termination. The AMOC strength is known to be crucial in the development (or not) of a YD-like event in the moment of meltwater discharge due to the deglaciation (Carlson, 2008). In that way, the dissimilarities between YD and S8.1 do not rule out definitely the hypothesis of an analog of the YD event in T-III, but are in line with the view of the YD as a very particular abrupt change triggered by complex and multiple processes (Renssen et al., 2015).

6.5. Concluding Remarks

The stalagmite ARTEMISA from the Ejulve cave covers the full duration of T-III, which in contrast to T-I and T-II is poorly known due to the scarcity of high precision and well-dated records. This speleothem reconstructs abrupt arid events using $\delta^{13}C$ and Mg/Ca, which have been verified as aridity proxies in the cave by 3 years of cave monitoring. Variation in $\delta^{18}O$ also marks the latest (S8.1) of those two events, indicating a change in the $\delta^{18}O$ composition of the sea water in the source of moisture, probably associated with the entrance of freshwater. Due to the latitudinal and geographical location of the Iberian Peninsula, the sensitivity of this area to AMOC changes during T-I and MIS 3 has been demonstrated.

Now, the results of ARTEMISA presented here identify two millennial-scale events (S8.1 and S8.2) that are also related to AMOC slowdowns during MIS 8. The stadial events have some similarities with HS-1 and HS-2, respectively, rather than to YD and HS-1 of the T-I. These similarities, after comparing with T-I and T-II records, are supported by intense IRD discharges, the dominance of semidesert taxa that characterize these event as arid intervals, and the similar phasing of the benthic $\delta^{18}O$. However, changes in sea level and insolation during S8.1 are more similar to YD than HS-1, precluding the identification of the YD as a unique feature of the most recent termination.

6.6. Methods

ARTEMISA is a 415-mm-long stalagmite from Ejulve cave (we work with the first 350 mm from base) collected in situ. No active drip was found over the stalagmite. The location of the sample inside the cave can be found in suppl. annex. The sample was cut with a diamond saw along the growth axis, and polished before sampling. The sample shows a change in the growing edge at 255 mm, probably due to locally hydrological factors. Several thin sections were prepared along the stalagmite, and samples were drilled to U/Th dating, stables isotopes, trace element, and X-ray diffraction (XRD). A total of 236 samples were drilled to stable isotopes with a 0.5-mm microdrill tip in different intervals, 0.5 mm during periods of low growth (from 15 to 75 mm and from 260 to 305 mm from bottom) and 5 mm during faster growth periods (from 75 to 260 mm). The temporal resolution for stables isotopes varies between 37 and 1,406 y, with an average resolution of 194 y.

To analyze trace metals, 168 samples were drilled using a 1-mm microdrill tip in equal intervals of 1 mm. In the case of U/Th dating, 24 samples were drilled at different intervals covering the whole stalagmite growth, focusing on identifying potential hiatus or low-growth periods. Stable isotope analyses were performed at the University of Barcelona (Scientific-Technical Services), and University of Oviedo, using a Finnigan-MAT 252 mass spectrometer fitted with a Kiel Carbonate Device I. Standards were run every 6–10 samples with a reproducibility of 0.02‰ for $\delta^{13}C$ and 0.06‰ for $\delta^{18}O$. Values are reported as $\delta^{18}O$ (‰) and $\delta^{13}C$ (‰) with respect to the Vienna Pee Dee Belemnite standard. Trace metals analysis was performed in Instituto Pirenaico de Ecologia, Spanish Scientific Research Council (IPE-CSIC) laboratories with an atomic emission spectroscopy (ICP-AES) (Thermo Scientific iCAP DUO 6300) using molar ratios of Mg and Sr in relation to Ca.

U/Th datings were analyzed in a multi-collector mass spectrometry (MC-ICP-MS) (Thermo-Finnigan Neptune) at the University of Minnesota following the methodology described in Cheng et al. (2013). Thin sections were elaborated in University of Zaragoza (rock preparation services). XRD analyses were performed in the Jaume Almera Institute of the CSIC with a Bruker-AXS D5005 powder diffractometer configured in theta-2theta geometry.

Supplementary Annex

of

Abrupt climate changes during Termination III in Southern Europe

6.7. Climate, vegetation and cave settings

Ejulve cave (40°45'34''N 0°35'07''W, 1240 m asl) (Fig. 6.1) is located in the Iberian Range, NE Spain, under a Mediterranean temperate climate with strong continentality. Average temperatures are 5 °C in winter and 22 °C in summer while mean seasonal distribution of rainfall is 600 mm, mostly during spring and fall, originating from Atlantic fronts (43%), backdoor cold fronts (21%) and highly convective storms (36%) (Moreno et al., 2014).

Vegetation cover in this area is growing in patchy calcic cambisols, composed basically of *Quercus ilex, Genista scorpius, Thymus vulgaris, Rosmarinus officinalis* and *Pinus halepensis*. Ejulve Cave is 794 m long and 55 m depth, developed in dolomitic limestones of Upper Cretaceous in age, with an epikarst thickness above the cave around 10 m. It is a relatively small cave with vertical development guided by fracturing network developing a maze passages. Narrow conduits, cupolas and cups are frequent. Ejulve cave is decorated with different speleothems and current formation of soda-straws has been also observed.

Sample Number	^{238}U (ppb)		^{232}Th (ppt)		^{230}Th / ^{232}Th (atomic x10^{-6})		$\delta^{234}U$* (measured)		^{230}Th / ^{238}U (activity)		$\delta^{234}U_{Initial}$** (corrected)		^{230}Th Age (yr BP)*** (corrected)	
ART-15	183	±0	1102	±22	2536.4	±51.1	12.3	±1.5	0.9248	±0.0020	26	±3	26277	±3213
ART-20	146.9	±0.2	8428	±169	270	±5	29.0	±1.5	0.9377	±0.0018	59	±3	25392	±2890
ART-35	117	±0	1648	±33	1090.0	±21.9	27.9	±1.3	0.9325	±0.0018	57	±3	25101	±2436
ART-45	78	±0	1515	±30	815.2	±16.4	36.2	±1.5	0.9563	±0.0023	77	±3	26647	±3428
ART-50	84.7	±0.1	671	±13	1959	±39	39.0	±1.4	0.9407	±0.0015	78	±3	24668	±2116
ART-65	108	±0	4394	±88	378.6	±7.6	35.7	±1.4	0.9301	±0.0017	70	±3	23930	±2248
ART-75	126.5	±0.1	311	±6	6289	±127	43.1	±1.5	0.9388	±0.0018	85	±3	24057	±2267
ART-85	144.2	±0.1	581	±12	3799	±76	36.5	±1.5	0.9283	±0.0015	71	±3	23774	±2038
ART-100	144.7	±0.2	469	±9	4698	±95	33.0	±1.2	0.9240	±0.0017	65	±2	23748	±2008
ART-115	150.4	±0.1	294	±6	7749	±157	28.2	±1.5	0.9185	±0.0015	55	±3	23743	±2073
ART-135	193.3	±0.2	291	±6	10089	±205	31.4	±1.3	0.9221	±0.0015	61	±3	23744	±1904
ART-155	177.4	±0.2	782	±16	3453	±70	28.8	±1.2	0.9225	±0.0019	57	±2	24039	±2247
ART-175	173.0	±0.2	175	±4	14991	±306	28.1	±1.4	0.9192	±0.0015	55	±3	23821	±2022
ART-190	155.4	±0.2	488	±10	4835	±97	28.9	±1.4	0.9207	±0.0015	57	±3	23863	±1992
ART-210	172	±0	161	±3	16267.	±330.6	26.1	±1.5	0.9195	±0.0017	51	±3	24061	±2298
ART-225	188.9	±0.2	232	±5	12316	±250	26.1	±1.4	0.9173	±0.0017	51	±3	23852	±2145
ART-250	147.2	±0.2	194	±4	11380	±231	22.1	±1.6	0.9109	±0.0024	43	±3	23673	±2746
ART-255	151.1	±0.2	338	±7	6649	±134	23.7	±1.3	0.9034	±0.0017	45	±2	22853	±1845
ART-260	317.1	±0.4	459	±9	10348	±209	22.7	±1.5	0.9083	±0.0019	44	±3	23382	±2265
ART-280	128.3	±0.1	1774	±36	1088	±22	25.5	±1.6	0.9121	±0.0016	49	±3	23400	±2204
ART-295	161.0	±0.2	258	±5	9477	±192	33.3	±1.6	0.9203	±0.0022	65	±3	23394	±2496
ART-305	151.9	±0.3	128	±3	18377	±377	54.9	±1.5	0.9381	±0.0024	105	±3	22871	±2337
ART-325	143.2	±0.1	152	±3	14447	±294	48.7	±1.5	0.9285	±0.0016	92	±3	22648	±1855
ART-345	97	±0	1919	±38	777.6	±15.7	59.1	±1.6	0.9292	±0.0021	109	±3	21792	±2038

Table 6.1. ^{230}Th dating results. The error is 2σ. Sample numbers are referred to mm from bottom. Outliers are remarked in italics.

Corrected ^{230}Th ages assume the initial $^{230}Th/^{232}Th$ atomic ratio of 4.4 ±2.2 x10^{-6}. Those are the values for a material at secular equili bulk earth

$^{232}Th/^{238}U$ value of 3.8. The errors are arbitrarily assumed to be 50%.

***B.P. stands for "Before Present" where the "Present" is defined as the year 1950 A.D.

*$\delta^{234}U = ([^{234}U/^{238}U]_{activity} - 1)$x1000.

** $\delta^{234}U_{initial}$ was calculated based on ^{230}Th age (T), i.e., $\delta^{234}U_{initial} = \delta^{234}U_{measured} \times e^{\lambda 234 \times T}$.

6.8. Isotopic equilibrium of calcite

The use of stalagmites as a paleoclimatic archives, once discarded diagenetic processes, relies on the deposition of calcite in isotopic equilibrium, otherwise, the kinetic processes may modify the original environmental signal. The Hendy test (Hendy, 1971) was traditionally used to evaluate the isotopic equilibrium of calcite. In ARTEMISA stalagmite, the weak negative correlation between $\delta^{13}C$ and $\delta^{18}O$ (ρ=-0.17, p-value=0.007, n=236) suggest that the isotopic equilibrium was reached when the carbonate deposition occurs, evidencing absence of kinetic fractionation processes. Moreover, the correlation between $\delta^{13}C$ and $\delta^{18}O$ has been applied with the record split up between glacial and interglacial values, in order to explore the isotopic equilibrium in each period.

The results are ρ=-0.13 (p-value=0.16, n=105) in glacial period and ρ=-0.038 (p-value=0.66, n=131) for interglacial period, thus confirming the results obtained previously. Additionally, different procedures have been used to test any hypothetical influence of kinetics during post-depositional processes. In that way, mineralogy and thin-sections on different areas of the stalagmite were analysed to identify the crystal fabrics and textures (Fig. 6.5).

ARTEMISA stalagmite consists almost exclusively of calcite as inferred from X-ray diffraction analysis. Sometimes minimal amounts of quartz have been detected. The whole stalagmite displays a visible internal laminated structure, very well marked at some parts differentiating white porous laminae (WPL) and dark compact laminae (DCL), according the terminology by Genty, et al., (1997).

Laminated structure along the axis of stalagmite growth is basically made of columnar fabrics (Frisia et al., 2000; Frisia and Borsato, 2010) forming a palisade of calcite crystals perpendicular to the growth surface. Further two subtypes of columnar fabric have been identified. Microcristalline columnar fabric is dominant showing irregular and serrated boundaries among crystals and uniform and patchy extinction (Fig. 6.5.A).

Fig. 6.5. *ARTEMISA stalagmite and thin-sections photographs of calcite fabrics. In the stalagmite, the lines at the bottom represent the onset of S8.2 (normal line) and the onset of S8.1 (dashed line). The thin-sections represent: a) Microcristalline columnar fabric showing serrated boundaries and uniform extinction (crossed polars). b) Elongated columnar fabric showing straight boundaries and uniform extinction (crossed polars). c) Elongated columnar fabric calcite showing straight boundaries and uniform extinction (right side), and sweeping extinction (se) and pores (p) between crystals (left side) (crossed polars). Note in this case*

that fabric differences are related to visible laminae and blurred laminae respectively.

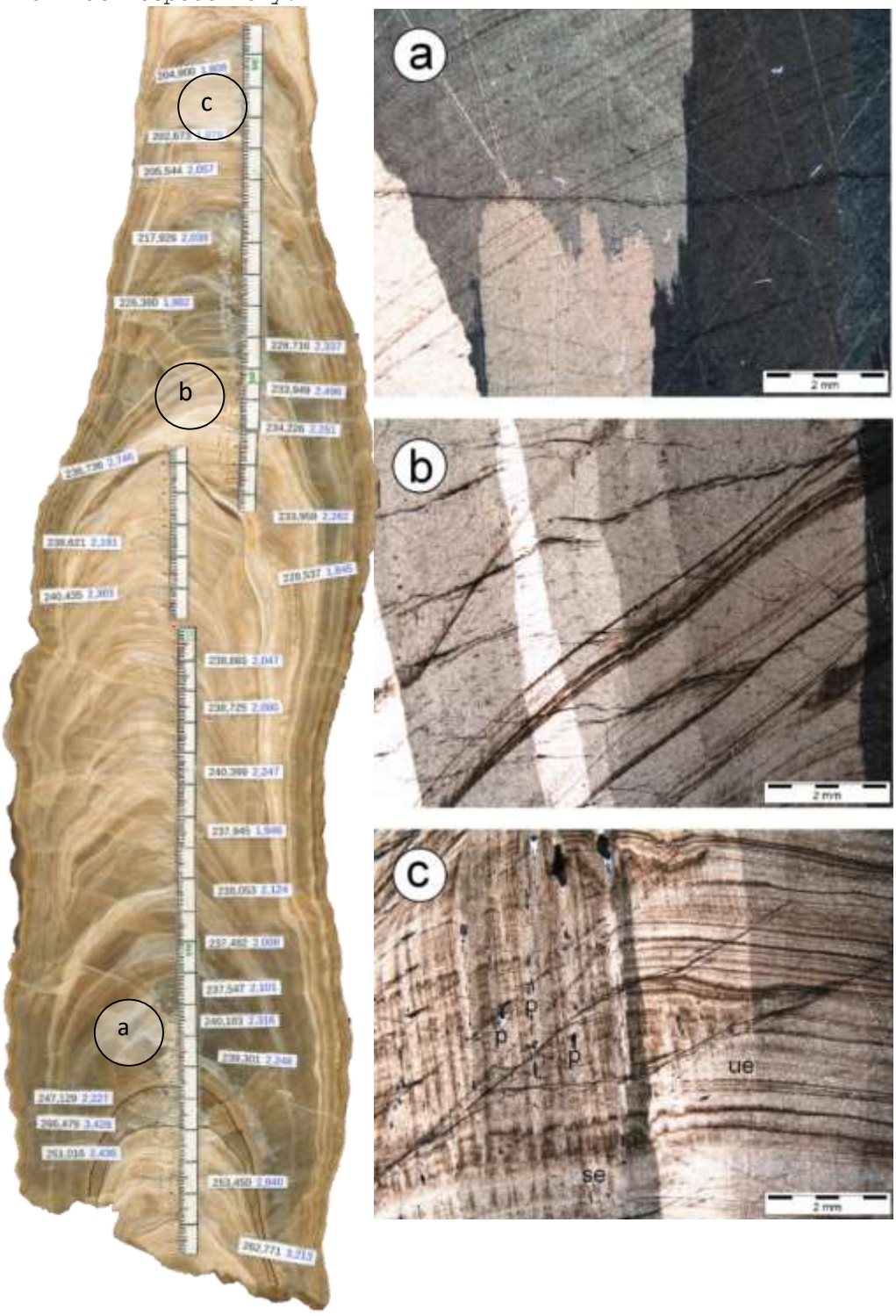

On the other hand, elongated columnar fabrics, showing a trend to straight crystals boundaries and uniform extinction have been identified (Fig. 6.5.B). However, elongated columnar fabrics also show sweeping extinction and pores between crystals when lamination appears blurred. Both elongated columnar calcite fabrics can appear laterally related (Fig. 6.5.C). These columnar fabrics indicate quasi-equilibrium conditions for calcite formation and related isotope composition (Frisia et al., 2000; Frisia and Borsato, 2010).

6.9. Interpreting the $\delta^{13}C$ climate signal

Long-term changes in $\delta^{13}C$ are due to: a) changes in the relative abundance of C3 and C4 plants (Hellstrom et al., 1998; McDermott, 2004); b) soil CO_2 controlled by microbial activity, vegetation respiration and atmospheric CO_2 (Hellstrom et al., 1998; Genty et al., 2003) and c) partial degassing or prior calcite precipitation during dry periods (Fairchild et al., 2000). Usually the $\delta^{13}C$ variations in southern Europe are interpreted as variations in the amount of isotopically light soil CO_2 production (Genty et al., 2003; Hodge et al., 2008) and PCP during periods of low rainfall and thus low carbonate precipitation, while relative changes in C3/C4 are discarded due to the minimal presence of C4 plants in the Mediterranean area. In addition, a strong temperature control on soil pCO_2 and speleothem $\delta^{13}C$ has been recognized in modern altitudinal temperature gradients in the Italian Alps, yielding more enriched speleothem $\delta^{13}C$ at colder, high elevation caves with less vegetation and lower soil pCO_2 (Johnston et al., 2013; Borsato et al., 2015).

PCP effect would modify the $\delta^{13}C$ in the same direction as the soil CO_2 climatic signal during dry periods, or dry and cold periods (i.e. leading to higher $\delta^{13}C$ values). PCP enables the preferential precipitation of light carbon atoms in the epikarst or in the cave ceiling, hence, enriching the aqueous solution in ^{13}C. In the same direction, low biological activity during dry periods would decrease the $\delta^{13}C$ content in soil CO_2. The variations of Mg/Ca and Sr/Ca among modern dripwaters in Ejulve Cave during 2013 do not exhibit the inverse correlation with $[Ca^{2+}]$ expected from PCP, and there is no correlation between Mg/Ca vs Sr/Ca ratios (Fig. 6.6).

For these reasons, we conclude that $\delta^{13}C$ in this cave is controlled by plant root respiration and microbial activity, thus, conditioned by temperature and humidity, as other stalagmite records in similar latitude (Genty et al., 2006b) and climate context (Moreno et al., 2017).

Additionally, the monitoring survey of three years in Ejulve cave allows the comparison of dripwater and farmed calcite data in seasonal drips with different environmental variables (Fig. 6.7).

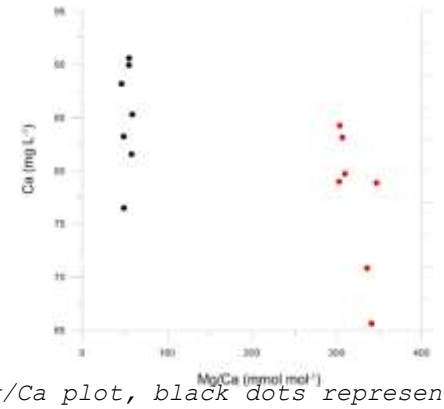

Fig. 6.6. *Ca vs Mg/Ca plot, black dots represents a fast drip and red dotes a slow drip.*

Air temperature and amount of rainfall was measured at Majalino meteorological station, located in the same mountains than Ejulve cave, about 300 m above. The amount of farmed calcite, stables isotopes and trace metals were analyzed seasonally. The location of the sampling sites can be observed in Fig. 6.8.

Hence, the results of seasonal drips during summer exhibit highest $\delta^{13}C$ values of farmed calcite coinciding with high values of Mg/Ca and Sr/Ca, high CO_2 inside the cave, high air temperature outside and minima moisture availability (Fig. 6.7). In this season, the amount of farmed calcite is low. On the other hand, during fall-winterspring, low $\delta^{13}C$ values of farmed calcite correlates with low values of Mg/Ca and Sr/Ca ratios, low CO_2, low air temperature and effective moisture (net rainfall). The amount of farmed calcite is variable depending on other factors (e.g. PCP, calcite saturation index-SIc) but is higher when the moisture availability is effective. In this way, in this Mediterranean region the available moisture, rather than temperature, is the key limiting factor for stalagmite growth (and thus the vegetation activity) as other authors pointed out (Hodge et al., 2008).

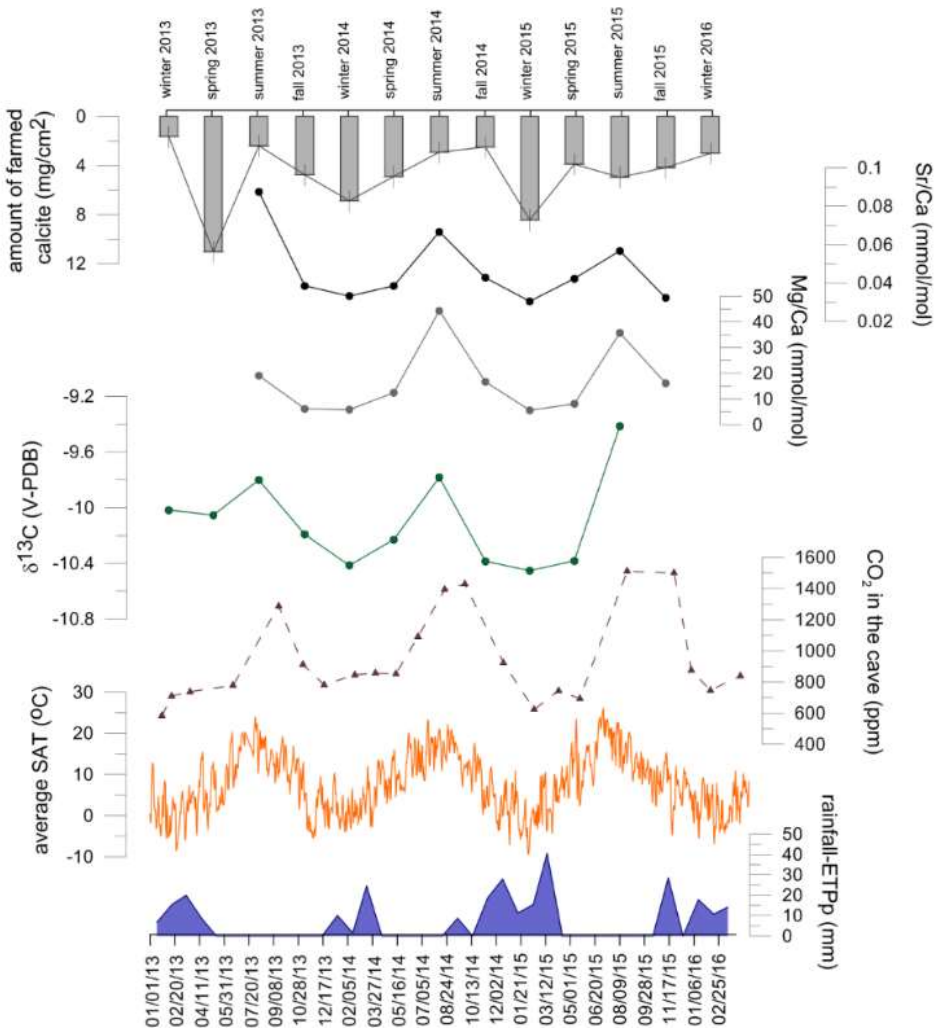

Fig. 6.7. *Data from monitoring survey in Ejulve cave covering from 2013-2016, from top to bottom: amount of farmed calcite (mg/cm²) recovered seasonally from glass plates; Sr/Ca, Mg/Ca and □δ¹³C of farmed calcite recovered seasonally; CO_2 measurements inside the cave; average surface air temperature (SAT) (°C) in nearby Majalinos meteorological station; and moisture availability (rainfall – ETPp), were rainfall was recovered on Majalinos station and potential ETP was calculated monthly through Thornthwaite equation.*

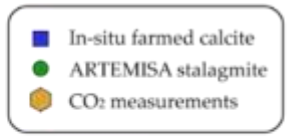

Fig. 6.8. *Topography of Ejulve cave with the location of sites for in-farmed calcite sampling, CO_2 measurements and the ARTEMISA stalagmite used in this study.*

6.10. Understanding the $\delta^{18}O$ signal

The $\delta^{18}O$ signal of a stalagmite, once post-depositional processes are discarded, is influenced by diverse factors influencing the rain and dripwater $\delta^{18}O$ such as temperature (Rozanski et al., 1993; Fricke and O'Neil, 1999) along the moisture trajectory, rainfall amount effect (Dansgaard, 1964; Rozanski et al., 1993), source effect (Dansgaard, 1964; Rozanski et al., 1993), changes in seasonality (Denton et al., 2005) and seawater $\delta^{18}O$ composition or ice-volume effect (Lachniet, 2009). In addition, cave temperature influences stalagmite $\delta^{18}O$ during calcite precipitation. In the case of the Ejulve setting over MIS 8 to MIS 7, we infer the dominant influence to be the temperature effect and the seawater $\delta^{18}O$ composition or ice-volume effect.

The modern rainwater observations between 2010 to 2012 reveal a positive correlation (Spearman's rank) between precipitation $\delta^{18}O$ values ($\delta^{18}O_p$) and surface air temperature (SAT) which is statistically significant (ρ=0.33) (Moreno et al., 2014). Calculations of the relationship between $\delta^{18}O_p$ and SAT ($d^{18}O_p/dT$) in this area give as a result a slope of 0.40‰/°C (r^2=0.39, p-value<0.0001, n=241). This slope is larger than the cave temperature effect (representing the temperature dependent fractionation of oxygen isotopes between water and calcite during the precipitation of the latter, expressed as $d^{18}O_{ct}/dT$) with a fractionation dependence of temperature of -0.24‰/°C established by Friedman and O´Neil (1977) or more recently -0.177‰/°C by Tremaine et al. (2011).

Combining both $d^{18}O_p/dT$ and $d^{18}O_{ct}/dT$ give as a result a single relationship of 0.16‰/°C for Ejulve cave. As the $d^{18}O_p$-SAT dependence is higher than the cave temperature effect, the $\delta^{18}O_{ct}$ in present-day should reflect the SAT signal with more positive values indicating warmer temperatures (Dorale et al., 2002). Nonetheless, the $d^{18}O_p/dT$ dependence show variations over time, especially in a scale of hundreds of thousand years, as a result of changes in seasonality of precipitation (Denton et al., 2005) and/or changes in moisture source (Charles et al., 1994). In the rainfall $\delta^{18}O$, there is no evidence of a strong amount effect as in tropical regions which feature a decrease in rainfall values with increased rainfall amount (Dansgaard, 1964). At Ejulve, a weak negative correlation exists between monthly amount of rainfall and the $\delta^{18}O_p$ values (ρ=-0.19) (Moreno et al., 2014). Then, the amount effect is expected to be of little importance in the record, but could modulate the $\delta^{18}O$ signal in some circumstances.

The $\delta^{18}O$ in the Ejulve stalagmite is characterized by more positive values in the interglacial period than the glacial,

similar to other high-altitude records as Spannagel Cave (Fig. 6.9). The 2.8‰ deglacial rise in $\delta^{18}O$ from the minima at S8.1 to the peak is much more gradual than that of carbon, peaking at 231 ± 2.1 kyr BP. The values in the glacial period have low variability in Ejulve cave and, unfortunately, cold conditions prevented the stalagmite growth in Spannagel Cave avoiding the comparison for the period previous to T-III.

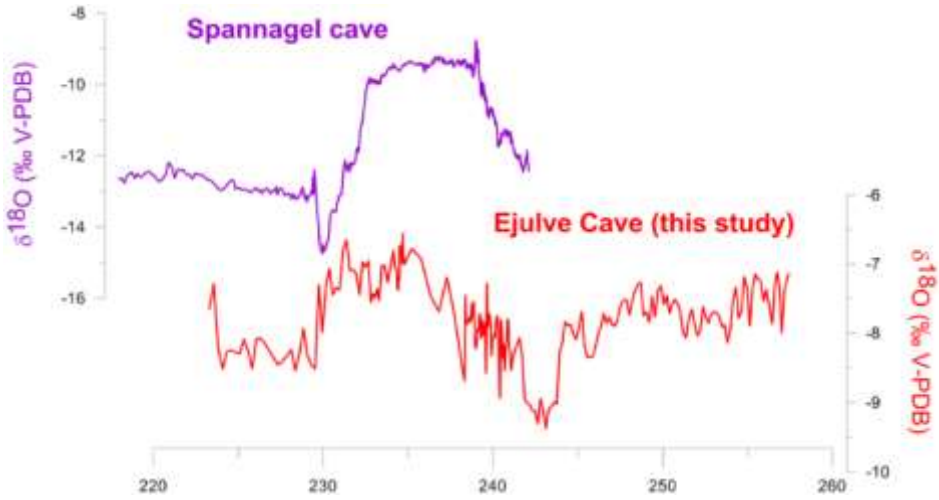

Fig. 6.9. *Comparison of* $\delta^{18}O$ *from Ejulve cave and Spannagel cave*

The transition to higher $\delta^{18}O$ during the interglacial compared to the glacial is consistent with a dominant temperature control over speleothem $\delta^{18}O$, in which, similar to modern observations, the warm temperatures drive significantly more positive rain $\delta^{18}O$, exceeding the opposite influence of cave temperature on oxygen isotope fractionation in calcite. We infer that the deglacial shift in $\delta^{18}O$ of the seawater source area is also manifest in the speleothem $\delta^{18}O$.

The time period of S8.1 is characterized to a shift to some of the most depleted speleothem $\delta^{18}O$ of the entire record, and appears to coincide with the major deglacial sea level rise and meltwater release, causing a shift to more negative $\delta^{18}O$ in the Atlantic and Mediterranean ocean source regions. The preceding S8.2 did not coincide with a release of meltwater sufficient to raise sea level or leave an imprint on benthic $\delta^{18}O$, and may not have been accompanied by such a pronounced shift in the $\delta^{18}O$ of the source areas nor accompanying shift in rainfall□$\delta^{18}O$.

The interglacial enrichment in stalagmite $\delta^{18}O$ and depletion in□$\delta^{13}C$ during the period of fast growth in MIS 7e (known as MIS 7e-I in Fig. 6.10), produces isotopic values similar to the

present-day in farmed calcite generated during the modern interglacial period of warmth and high vegetation activity. In fact, a similar $\delta^{18}O$ signal and slightly lower $\delta^{13}C$ of ARTEMISA in MIS 7e-I suggests controlling factors of the isotopic signal similar to present-day, probably with more vegetation activity.

On the other hand, during the period of reduced growth rate of MIS 7e (known as MIS 7e-II in Fig. 6.10) with the insolation in a clearly lowering trend, there is a notable excursion to higher values of $\delta^{18}O$. This is probably due to a combination of longer groundwater residence time as a response to lower rainfall and/or the vapor source displaced to lower latitudes of North Atlantic, due to the enhanced continental ice volume during the cold conditions prevailing in the North Atlantic ocean (Fig. 6.4), despite a predominant Mediterranean signal in $\delta^{18}O$ during this time cannot be discarded. Therefore, the differences in $\delta^{18}O$ between MIS 7e-I and MIS 7e-II seem to be controlled by changes in atmospheric circulation and vapor source rather than local temperature changes, in agreement with Asian records that reflect weakening in summer monsoon intensity during MIS 7e-I to MIS 7e-II transition.

.

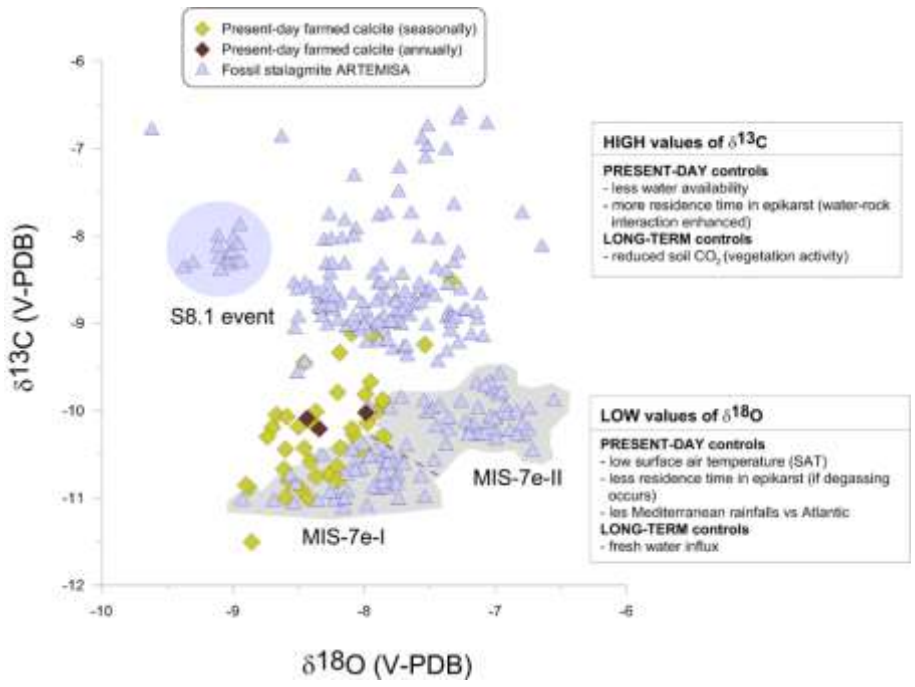

Fig. 6.10. *Values of in-situ farmed calcite (diamonds) and ARTEMISA (triangles). The green diamonds are samples recovered during each season, while brown diamonds represents the average of each year during 2013 to 2015. Additionally, are remarked the controls of high* $\delta^{13}C$ *and* $\delta^{18}O$ *in Ejulve cave.*

In summary, the $\delta^{18}O$ signal during this time in this latitude is mostly related to SAT and source effect, modulated punctually by amount of precipitation, and at longer time scales, by changes in the $\delta^{18}O$ of the seawater and by the input of freshwater. In contrast, $\delta^{13}C$ and Mg/Ca ratio appear as robust proxies of vegetation productivity and water availability

6.11. Comparing ARTEMISA with pollen and marine records in Europe

The two-events structure of T-III stablished in Ejulve are detected also in other sequences from the Portuguese Margin (pollen and foraminifera association records) (Fig. 6.11). These records have been tuned to the chronology of ARTEMISA using tie points anchored to S.8.2, S.8.1 and the end of MIS 7e, but in Fig. 6.11 are plotted respect to their original chronology. The signal representing stadials in the different records (eg. increase of semi-desert taxa) is indicated by black arrows (Portuguese Margin) in Fig. 6.11 highlighting the small lag among the sequences, always within dating uncertainty. This, together with the lack of absolute chronologies in the marine records, suggested us tuning those sequences to Ejulve stalagmite chronology.

The shape of MIS 7e period with wet conditions in Ejulve is in agreement with other pollen records in Europe (MD01-2447 (Desprat et al., 2006), Tenaghi Phillippon (Tzedakis et al., 2003), Valle di Castiglione (Follieri et al., 1988) , Fig. 6.11). Although there is a lack of data during MIS 8 in arboreal pollen due to the extremely cold/dry conditions, during MIS 7e the arboreal pollen increases up to 60 to 80 % of total, a pattern seen in eastern Europe (Tenaghi Phillippon, Greece) as in western (Valle di Castiglione, Italy and MD01-2447, Portuguese Margin) (Fig. 6.11). This percentage dramatically ceases in the transition to cold MIS 7d, during 231.5 kyr dated in Ejulve cave. This general agreement in the main patterns supports our interpretation of $\delta^{13}C$ as a proxy for vegetation productivity in Ejulve cave.

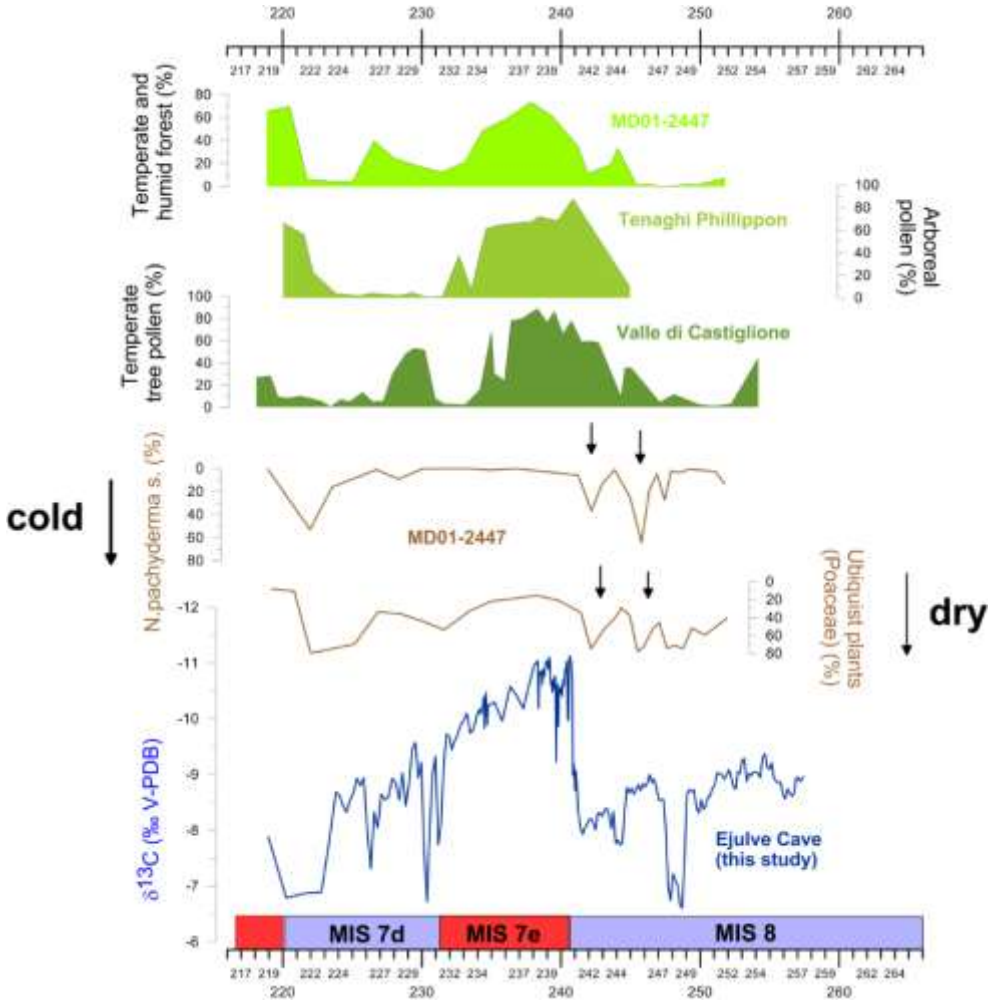

Fig. 6.11. *Comparison of* $\delta^{13}C$ *of ARTEMISA with pollen and marine records in Europe, from top to down: temperate and humid forest in MD01-2447 (Desprat et al., 2006) (Portuguese Margin), arboreal pollen in Tenaghi Phillippon (Tzedakis et al., 2003), temperate tree pollen in Valle di Castiglione (Follieri et al., 1988), N.pachyderma s. and ubiquist plants including Poaceae with the original ages (Desprat et al., 2006), both in Portuguese Margin, and* $\delta^{13}C$ *profile of ARTEMISA, Ejulve cave.*

B) Orbital-to-millenial scale climate variability during Marine Isotope Stages 5 to 3 in NE Spain

Significance

- *First continuous speleothem record from Europe covering MIS 5e to 3.*

- Precession-paced control of first order $\delta^{18}O$ *variability during MIS 5.*

- Enhanced drip water degassing controlled $\delta^{18}O$ *and* $\delta^{13}C$ *millennial variability during MIS 4 and 3.*

- Late demise of the Eemian forest stage in Southern Europe.

- New insights into the climate variability during Heinrich 6.

Abstract

The climate during the last glacial cycle was characterized by abrupt millennial-scale changes superimposed on long-term orbital control. This study examines this climate variability for southeast Spain for the time interval 118.9 to 36.9 kyr using a multi-proxy approach ($\delta^{18}O$, $\delta^{13}C$ and Mg/Ca) applied to a stalagmite that covers this period continuously. During Marine Isotope Stage (MIS) 5, $\delta^{18}O$ is controlled by orbital pacing, with low precession peaks leading wet conditions. In contrast, during MIS 4 and 3, $\delta^{18}O$ is decoupled from precession and co-varies with $\delta^{13}C$, suggesting a common control of both isotopes by enhanced degassing of drip waters during dry periods. $\delta^{13}C$ shows a positive correlation with the Mg/Ca reflecting water availability, vegetation productivity and microbial activity in the catchment of the cave´s drip water. The $\delta^{13}C$ values record the cold marine events C26 to C23 as well as Dansgaard-Oeschger (D-O) oscillations and Heinrich events. The speleothem record supports previous studies showing a late demise of the Eemian forest stage in southern Europe at 108.6 ± 0.3 to 108.3 ± 0.3 kyr. We also explored the intra-Heinrich variability and identified two periods with a marked "W-shape" pattern in the $\delta^{13}C$. These periods were characterized by the response of $\delta^{13}C$ to the weak D-O cycles 15 and 18. Both W-shape events show a similar intensity between them, attending to the drop in the $\delta^{13}C$ values, but a different timing, longer in the first event contemporary with HS-6. We identified two phases within the older W-event (D-O 18), a first one with dry-cold conditions before 63 kyr BP, and a second one with wet-cold conditions afterwards. The younger W-event (D-O 15) is in concordance with the reinforcement of the northeasterly trade winds (NAO+ phase) giving rise to a dry climate in Southern Europe at that time.

Keywords
stalagmite | *stable isotopes* | *orbital-millennial scale* | *Last Glacial Period* | *western Mediterranean*

6.12. Introduction

Rapid abrupt changes characterized the climate during the Last Glacial period. These Dansgaard-Oeschger (D-O) cycles were the most notable expression of the atmospheric changes over Greenland, while the massive iceberg discharges into the North Atlantic (Heinrich events) represented a notable feature in the adjacent ocean (Rasmussen et al., 2014). Our knowledge of the terrestrial response in Europe to those abrupt events has increased during last decade, but is still sparse. Previous studies on the Iberian Margin (Sánchez-Goñi et al., 2008; Naughton et al., 2009) and in the Mediterranean Sea, including the Alborán Sea (Goñi et al., 2002; Moreno et al., 2002; Sierro et al., 2005; Fletcher and Sánchez Goñi, 2008; Frigola et al., 2008), emphasize the sensitivity of the Iberian Peninsula (IP) to climate change in the North Atlantic realm. Unfortunately, only few reliable records have been published for the time before 50 kyr (Frigola et al., 2008; Fletcher et al., 2010). In the terrestrial realm, speleothems and lacustrine sediments from the IP and the remainder of Europe covering this time period are generally scarce and cover only short periods of time. An exception is the long lacustrine sequences of Lago Grande di Monticchio and Tenaghi Philippon, anchored by tephra datings (Martin-Puertas et al., 2014; Wulf et al., 2018). Speleothems are not an exception to this rule, as they preferentially form during warm/wet periods and commonly stop growing when the climate turns cold/dry (e.g. Genty et al., 2010; Boch et al., 2011; Vansteenberge et al., 2016).

There is clearly a need for long, well-dated terrestrial records to explore the mechanisms of climate change at a different scales during the Last Glacial period. Since the penultimate glaciation, a great climate variability has been identified, from the end of the interglacial to a more glacial conditions during MIS 3 and the succession of D-O or Heinrich events. The mechanisms influencing in the climate vary depending on the time scale, hence, the discrimination between the climate controls on orbital to (sub) millennial scale is essential. The dramatic rapid abrupt changes may alter the sequence of the dominant mechanisms controlling the $\delta^{18}O$ of the speleothems (e.g. rainfall amount, temperature, changes in seasonality). Paradoxically, the complexities to unravel the climate significance of the $\delta^{18}O$ seen in areas such as mid latitudes, due to the existent competing factors (Scholz et al., 2012; Pérez-Mejías et al., 2017), could help us to test whether any of those factors would change in a long time series.

Here we present a stalagmite record from Ejulve cave, northeastern Iberia, covering continuously the time between the end of the last interglacial (MIS 5e) and MIS 3, making this record exceptional to evaluate the terrestrial mid-latitude response to forcing mechanisms across several climate transitions.

6.13. Study area

Ejulve cave (40°45´34´´N, 0°35´07´´W, 1240 m a.s.l.) is located in the Iberian Range, NE Spain (Fig. 6.12). The cave developed in folded and thrusted Upper Cretaceous dolomitic limestones and dolostones and comprises 794 m of galleries, reaching a maximum depth of 55 m. The thickness of the rock above the cave in the shallow areas is less than 10 m.

The area above the cave is covered by poorly developed soil composed by patchy aridisols with shallow and stony soils supporting a vegetation composed mainly of sparse evergreen oak (*Quercus coccifera, Quercus ilex),* heliophytic shrubs (*Genista scorpius, Thymus vulgaris,* and sparse *Sideritis spinulosa* and *Rosmarinus officinalis*) and *Pinus halepensis*. The local climate is continental Mediterranean, with a mean annual rainfall of 547 mm (1981-2010) and a mean annual air temperature of 12.3 °C (2003-2012). The mean temperature in winter is 7.4 °C and 20.3 °C in summer, with high evapotranspiration from March to October.

6.14. Methods

The studied stalagmite (dubbed ANDROMEDA) was cut along the growth axis with a diamond saw and polished. A total of 739 samples were drilled for stable isotope analysis along the extension axis using a 0.5 mm microdrill, 558 samples of them in a continuous-sampling mode at 0.2 mm increments, and the remaining 181 samples at 1 mm resolution. For trace metals, 168 samples were sampled at 1 mm increments. 26 samples were drilled for U-Th at different intervals focusing on identifying potential hiatuses ad slow-growth periods. Thin sections covering the whole surface of the stalagmite were prepared and examined using transmitted-light microscopy.

X-ray diffraction (XRD) analyses were performed on 5 samples at the Jaume Almera Institute (ICTJA-CSIC) using a Bruker-AXS D5005 powder diffractometer configured in theta-2theta geometry. Sample were also examined on palladium-coated slabs using a Field Emission Scanning Electron Microscope (FE-SEM, CSEM-FEG INSPECT 50) equipped with an EDX detector at the Advanced Microscopy Laboratory-INA (Zaragoza). Epifluorescence observations of the thin sections were performed at the Theoretical and Experimental Ecology Station (CNRS) using a

Fluorescence Stereo Microscope (ZEISS Axio Zoom V16) with a HXP 200C illuminator.

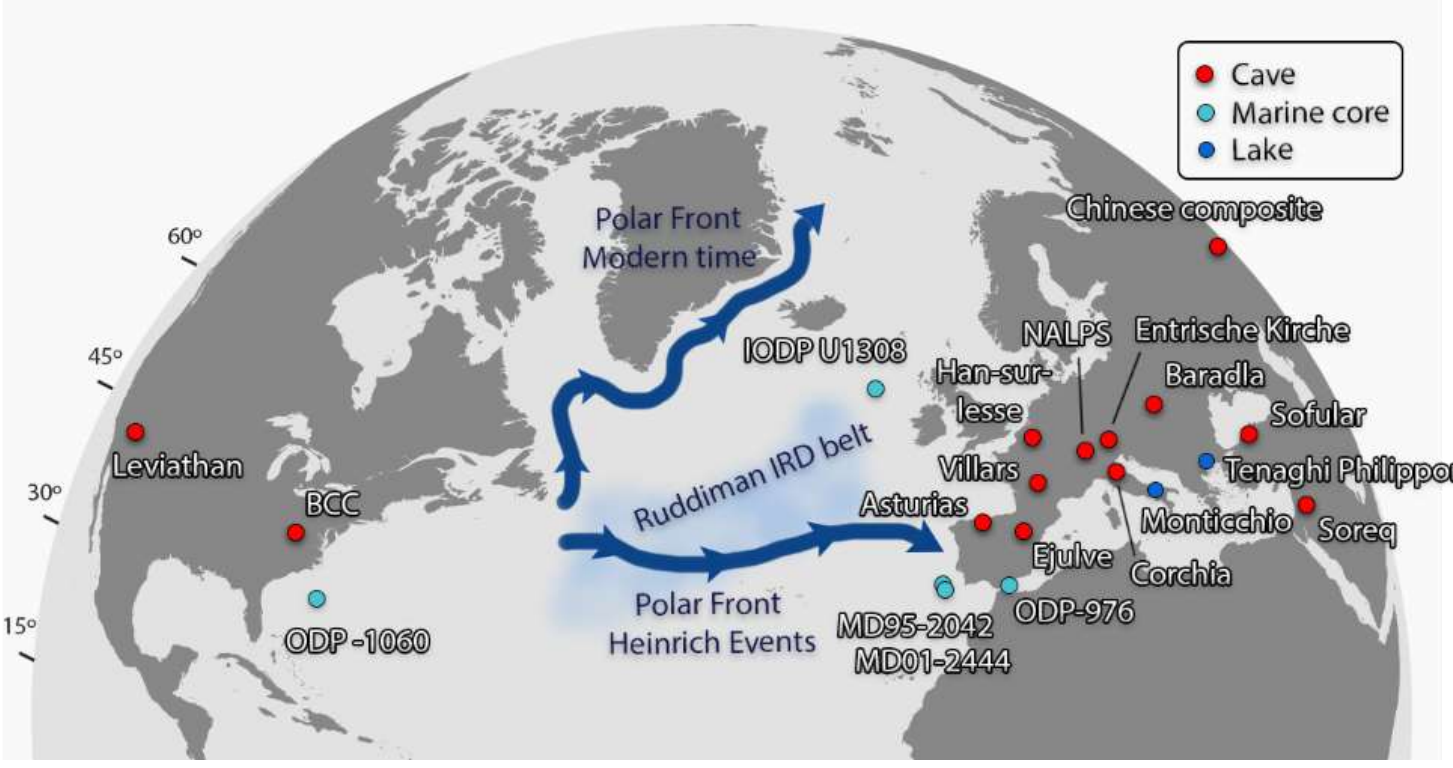

Fig. 6.12. *Location of Ejulve cave and records discussed in the text. The position of the polar front is marked for the present day (Eynaud et al., 2009) and reconstructed for Heinrich events (Eynaud et al., 2009; Voelker and Abreu, 2011).*

Stable isotopes analyses were performed at the University of Innsbruck using a ThermoFisher Delta V Plus mass spectrometer linked to a Gasbench II, following the methodology described in Spötl (2011), and at the University of Barcelona using a Finnigan MAT 252 mass spectrometer, equipped with a Kiel Carbonate Device III. Values are reported as $\delta^{18}O$ (‰) and $\delta^{13}C$ (‰) with respect to the Vienna Pee Dee Belemnite (V-PDB) standard. Long-term precision for $\delta^{13}C$ and $\delta^{18}O$ was 0.06‰ and 0.08‰ for the Innsbruck laboratory and 0.04‰ and 0.08‰ for the Barcelona laboratory, respectively. Trace-metal analysis was performed in the IPE-CSIC laboratories using an ICP-AES (ThermoFisher iCAP DUO 6300) using molar ratios of Mg in relation to Ca. U-Th samples were analyzed using a MC-ICP-MS (ThermoFisher Neptune Plus) at the University of Minnesota and at the Xi'an Jiaotong University following the methodology described in Cheng et al. (2013). The depth-age model was constructed using Bayesian chronological modeling with OxCal (Ramsey, 2008).

6.15. Results

6.15.1. Petrography and mineralogy

ANDROMEDA is 41 cm long, 9 cm wide at the base and 5 cm wide at the top, showing a conical external shape (Fig. 6.13.a). It is composed of radiating columnar calcite crystals showing macroscopically visible laminae in the lower half of the stalagmite, although the laminae have limited lateral continuity (Fig. 6.14).

ANDROMEDA is composed of calcite and no traces of other minerals were identified by XRD. Thin sections reveal a fabric of polycrystals 11 to 20 mm long and a 3 to 5 mm wide (L/W ratio below 6:1) showing uniform extinction with patches (Fig. 6.13.b). The smaller crystals forming the polycrystals are 1 to 7 mm long and about 1 mm wide. The intercrystalline borders are irregular and the fabric is compact and shows low porosity (Fig. 6.13.c). These characteristics correspond to the columnar microcrystalline fabric described by Frisia (2015).

All thin sections show weak homogeneous epifluorescence with no evidence of layering or changes in composition (Fig. 6.13.d). In the upper part hiatus 3 (Fig. 6.13) is marked by a micritic layer showing more intensive fluorescence.

FE-SEM images of freshly broken surfaces showed a homogeneous crystal fabric. EDX point analyses of the polished surfaces indicate low-Mg calcite, with an average 0.2 wt.% of Mg, while Sr was below the detection limit.

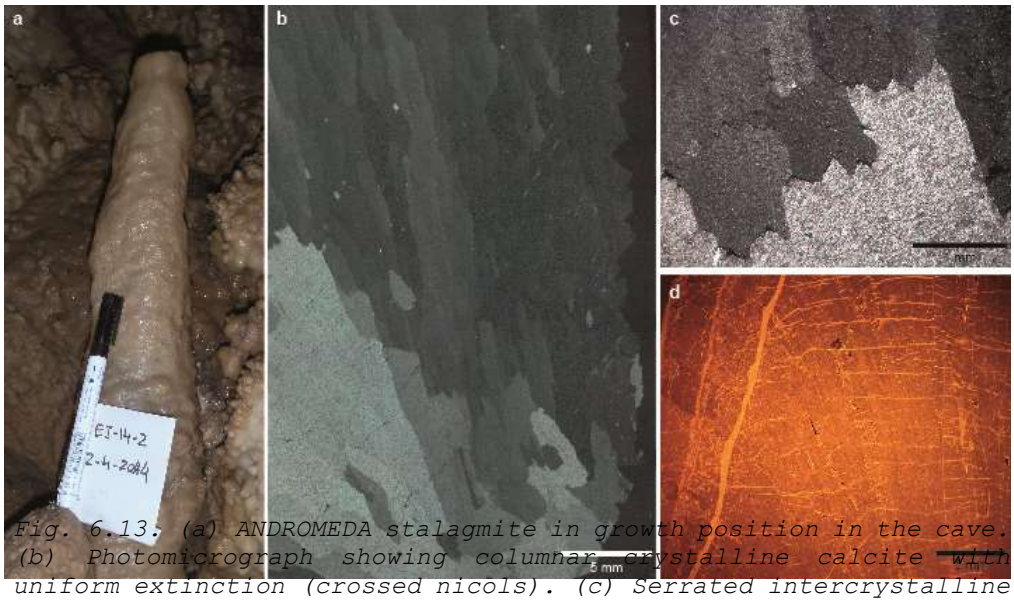

Fig. 6.13. (a) ANDROMEDA stalagmite in growth position in the cave. (b) Photomicrograph showing columnar crystalline calcite with uniform extinction (crossed nicols). (c) Serrated intercrystalline boundaries (crossed nicols). (d) Epifluorescence image of the calcite crystals. The bright line on the left corresponds to hiatus 3.

6.15.2. Age model and growth rate

The chronology of ANDROMEDA is anchored by 26 U-Th ages (Table 1), with analytical errors in the range of 2 to 4‰. ^{232}Th is general lower than 500 ppt. The ^{238}U content is mostly between 100 to 200 ppb, similar to values from other stalagmites in this cave (Moreno et al., 2017; Pérez-Mejías et al., 2017). The depth-age model was constructed using 21 U-Th ages, in the area between hiatus 1 and 2 (Fig. 6.14). The mean uncertainty of the record is of 162 yr (minimum 14 yr, maximum 641 yr).

The stalagmite exhibits three hiatuses, two of them are visible with the naked eye and confirmed by U-Th ages. The third hiatus (no. 1) is located close to the base of the stalagmite and shows no clear visible expression (Fig. 6.14). The hiatus 2 spans from 36.9 ± 0.11 to 13.9 ± 0.04 kyr, and hiatus 3 from 10.8 ± 0.15 to 5.1 ± 0.03. In the present work we discuss the data from 40 mm (post-hiatus 1) until 340 mm above the base (before hiatus 2).

Growth rate ranges from 1.0 mm/kyr during 96-81 kyr to 11.6 mm/kyr during 81-76 kyr with a mean of 5.2 mm/kyr (Fig. 6.14). Overall, it shows four stages of slow growth and three of high growth (Fig. 6.14). The former span 119-113 kyr, 99-81 kyr, 76-52 kyr and 46-36 kyr, corresponding to MIS 5e-d, 5b, 4 and the cold spells of MIS 3 (following Rasmussen et al., 2014). The

fast growth periods span 113-99 kyr, 81-76 kyr and 52-45 kyr (slighty lower during 48-46 kyr), corresponding to MIS 5c, 5a and 3 (Fig. 6.14).

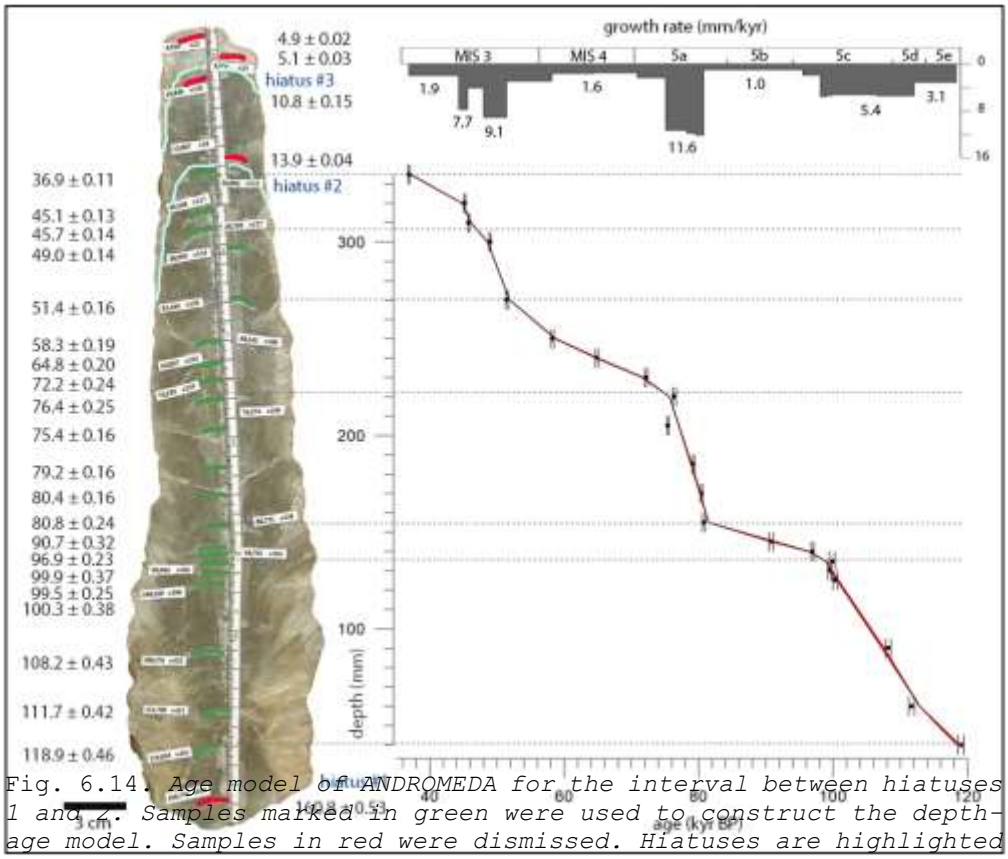

Fig. 6.14. *Age model of ANDROMEDA for the interval between hiatuses 1 and 2. Samples marked in green were used to construct the depth-age model. Samples in red were dismissed. Hiatuses are highlighted by blue lines, except for hiatus 1 which is not visible macroscopically. Also shown are changes in growth rate. Age model and uncertainty are shown in red.*

Sample Number	^{238}U (ppb)		^{232}Th (ppt)		^{230}Th / ^{232}Th (atomic x10^{-6})		$\delta^{234}U$* (measured)		^{230}Th / ^{238}U (activity)		$\delta^{234}U_{Initial}$** (corrected)		^{230}Th Age (yr BP)*** (corrected)	
AND-12	73.4	±0.1	2443	±49	576	±12	421.3	±1.6	1.1626	±0.0020	663	±3	160776	±829
AND-40	160.4	±0.2	573	±12	4533	±91	415.2	±1.7	0.9825	±0.0018	581	±2	118934	±460
AND-58	191	±0	706	±14	4479.6	±90.1	491.2	±1.6	1.0021	±0.0020	673	±2	111700	±423
AND-89	171.0	±0.2	234	±5	11183	±226	414.3	±1.8	0.9269	±0.0019	562	±3	108169	±433
AND-125	192.6	±0.2	308	±6	9337	±189	446.2	±1.8	0.9057	±0.0019	592	±2	100332	±383
AND-130	173.9	±0.2	435	±9	5978	±120	455.3	±1.4	0.9071	±0.0011	603	±2	99497	±251
AND-135	186.3	±0.2	889	±18	3435	±69	580.0	±1.8	0.9941	±0.0020	769	±3	99865	±369
AND-140	157.4	±0.1	750	±15	3273	±66	536	±1.4	0.9457	±0.0011	705	±2	96935	±232
AND-144	140	±0	1003	±20	2151.2	±43.3	587.4	±2.0	0.9376	±0.0018	759	±3	90714	±317
AND-154	125	±0	563	±11	3436.1	±69.1	720.9	±1.8	0.9421	±0.0016	906	±2	80772	±238
AND-170	122	±0.1	205	±4	8581	±173	606	±1.3	0.8724	±0.0010	761	±2	80420	±164
AND-185	143.5	±0.1	193	±4	11320	±229	708.2	±1.4	0.9214	±0.0011	886	±2	79210	±160
AND-205	133	±0.1	178	±4	10697	±217	671.7	±1.4	0.8690	±0.0011	831	±2	75397	±157
AND-220	151	±0	200	±4	9365.4	±189.3	440.2	±1.6	0.7486	±0.0015	546	±2	76374	±250
AND-230	165.0	±0.2	286	±6	7731	±156	617.1	±2.0	0.8124	±0.0017	757	±3	72153	±239
AND-240	142.0	±0.2	195	±4	9778	±198	754.4	±2.0	0.8162	±0.0017	906	±2	64782	±200
AND-248	95	±0	327	±7	3080.8	±62.3	504.9	±1.8	0.6404	±0.0014	595	±2	58257	±190
AND-271	121.5	±0.2	163	±3	7796	±158	636.8	±1.9	0.6333	±0.0013	736	±2	51444	±155
AND-300	134.7	±0.1	200	±4	6150	±125	494.2	±1.8	0.5533	±0.0010	568	±2	48960	±137
AND-309	132.7	±0.1	131	±3	9577	±195	636.9	±1.8	0.5751	±0.0012	725	±2	45725	±136
AND-318	119.1	±0.1	78	±2	14428	±296	650.9	±1.9	0.5738	±0.0011	739	±2	45112	±127
AND-338	69.1	±0.1	187	±4	3371	±69	884.1	±2.0	0.5546	±0.0013	981	±2	36856	±112
AND-349	82	±0	150	±3	2366.5	±48.4	1171.2	±2.0	0.2636	±0.0007	1218	±2	13867	±44
AND-390	51	±0	611	±12	240.4	±4.9	799.1	±1.8	0.1753	±0.0008	824	±2	10840	±145
AND-400	246	±0	571	±11	601.6	±12.3	826.2	±2.1	0.0847	±0.0004	838	±2	5064	±35
AND-410	168.8	±0.2	194	±4	1169	±24	807.3	±2.0	0.0816	±0.0003	819	±2	4936	±23

Table 6.2. ^{230}Th dating results. The error is 2□□□Sample number are refered to mm from bottom. *□^{234}U = ([$^{234}U/^{238}U]_{activity}$ – 1)x10(
** □$^{234}U_{initial}$ was calculated based on ^{230}Th age (T), i.e., □$^{234}U_{initial}$ = □$^{234}U_{measured}$ x e$^{□234xT}$
Corrected ^{230}Th ages assume the initial $^{230}Th/^{232}Th$ atomic ratio of 4.4 ±2.2 x10^{-6}. Those are the values for a material at secu
equilibrium,
with the bulk earth $^{232}Th/^{238}U$ value of 3.8. The errors are arbitrarily assumed to be 50%.
***B.P. stands for "Before Present" where the "Present" is defined as the year 1950 A.D.

6.15.3. Isotopic and trace-metal geochemistry

The resolution for stable isotopes varies between 22 years during the fast growth period of MIS 3 (52-45 kyr) and 1000 years during the slow growth phase of MIS 5b (99-81 kyr, Fig. 6.14). The average resolution is 109 years.

The $\delta^{18}O$ record of ANDROMEDA, corrected for the ice-volume effect (cf. Bintanja et al., 2005) (Fig. 6.15), shows values between −9.17 and −6.51 ‰ (mean −8.08 ± 0.38 ‰). $d^{13}C$ values range from −9.97 to −3.25 ‰ (mean −7.24 ±1.48 ‰). The highest and lowest $\delta^{18}O$ values occur during MIS 5 (117 and 107 kyr, respectively) (Fig. 6.16a). The lowest $\delta^{13}C$ values were also reached during this time interval (118 kyr), while the highest values were reached at 39 kyr (Fig. 6.16b). The geometry of the stalagmite shows a similar trend, whereby the diameter is larger at the base (9 cm) and narrows towards the top (5 cm) (Fig. 6.14).

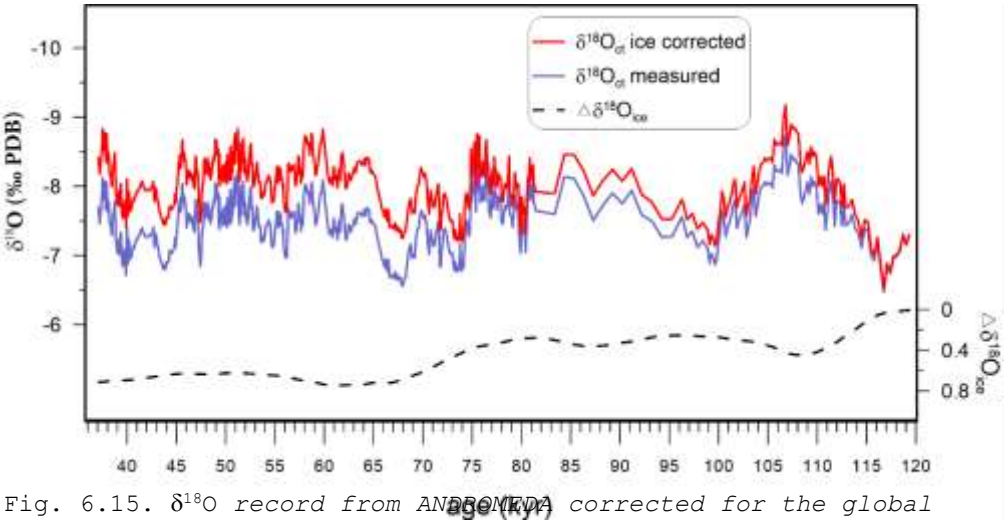

Fig. 6.15. $\delta^{18}O$ *record from ANDROMEDA corrected for the global ice-volume effect following Bintanja et al. (2005).*

The isotopic variability shows marked changes during the long growth history of the stalagmite. During MIS 4 and 3 the variability in $\delta^{18}O$ is 1.59‰ compared to 2.66‰ during MIS 5. In contrast, $\delta^{13}C$ shows the highest variability during the D-O oscillations of MIS 4 and 3 (5.62‰), while the variability during MIS 5 was lower (3.30‰). $\delta^{18}O$ and $\delta^{13}C$ show a variable degree of covariation along the growth axis, with no correlation during MIS 5 ($\underline{\rho}$ = 0.01, p-value = 0.83, n=235) and a statistically significant correlation (ρ = 0.53, p-value < 0.001, n=500) in MIS 4 and 3.

The Mg/Ca ratio (Fig. 6.16c) shows a highly positive correlation with $\delta^{13}C$ (ρ = 0.75, p-value = 0.02, n = 295), e.g., in the MIS 4 and 3 sections (Fig. 6.16). In spite of the low resolution of the $\delta^{234}U$ record, high values co-vary with high values in Mg/Ca (Fig. 6.16d).

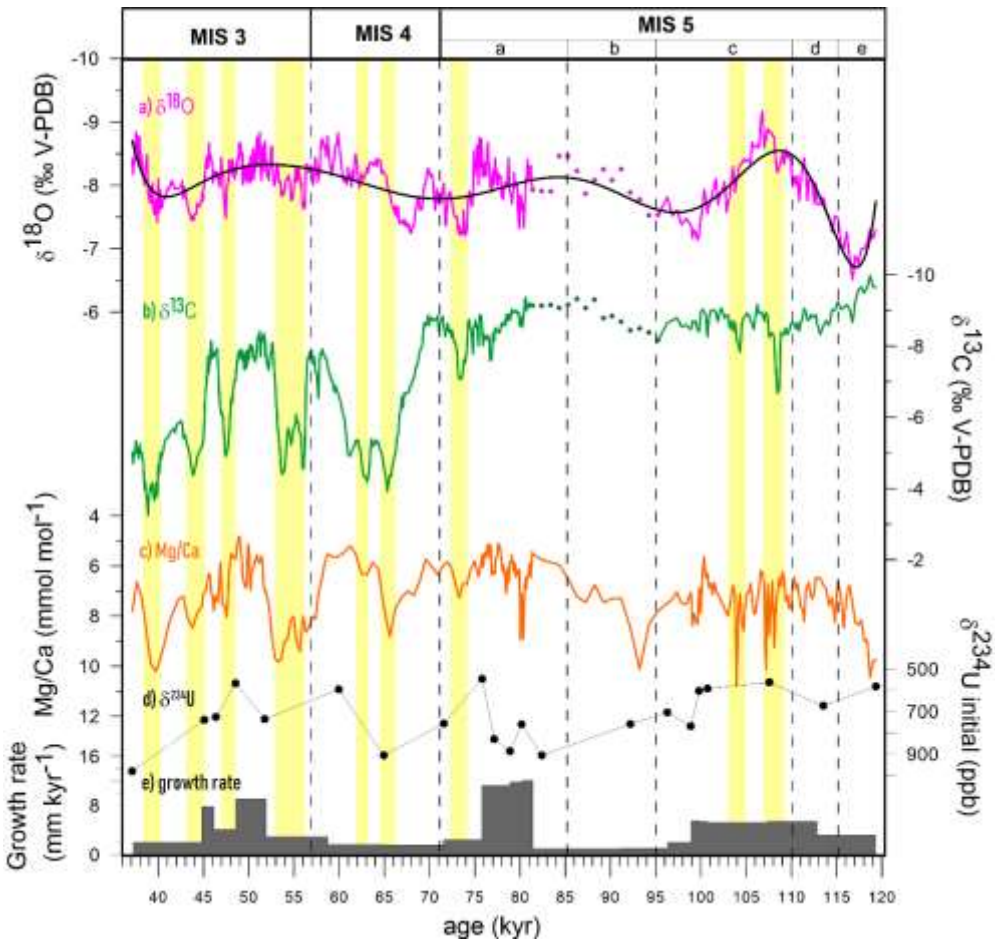

Fig. 6.16. *ANDROMEDA proxy record from Ejulve cave. From top to bottom: a) $\delta^{18}O$ corrected for changes in global ice volume (pink), polynomial fit (black), b) $\delta^{13}C$ (green), c) Mg/Ca (orange), d) $\delta^{234}U$ initial (grey) and e) growth rate. The vertical yellow bars mark maxima of both $\delta^{13}C$ and Mg/Ca.*

6.16. Discussion

In this work we use ANDROMEDA stalagmite for palaeoenvironmental proposals. Consequently, it is essential to assess the primary mineralogy (calcite or aragonite) of the stalagmite to interpret properly the speleothemic timing and the palaeoclimatic geochemical indicators recorded. Although columnar fabric is often considered an unaltered archive of geochemical signals (Frisia et al., 2018) it could be a result of early diagenesis which may re-set the original geochemical signals (Martín-García et al., 2009; Frisia and Borsato, 2010; Fairchild and Baker, 2012; Scholz et al., 2014; Bajo et al., 2016; Domínguez-Villar et al., 2017). Aragonite can last over time (10^5-10^6 years) (Alonso-Zarza et al., 2011), even though the diagenetic replacement can occur in a short period (< 1 kyr) (Frisia et al., 2002).

Diagenetic transformation affecting primary aragonite in open system conditions can introduce modifications in the timing deposition provided by U/Th dating series (Ortega et al., 2005; Lachniet et al., 2012) but also in the palaeoenvironmental signals derived from stable isotopes (Hopley et al., 2009; Martín-García et al., 2009; Zhang et al., 2014; Domínguez-Villar et al., 2017) and trace elements (Hopley et al., 2009; Martín-García et al., 2009; Domínguez-Villar et al., 2017). Nevertheless, the way in which the palaeoclimatic information is affected remains not fully studied and unclear (Fairchild et al., 2006; Zhang et al., 2014).

XRD mineralogical analyses indicate that ANDROMEDA is totally composed by calcite. Nevertheless, to discard the possibility of a primary aragonite composition different techniques were used to identify relics. A simple test for the presence of aragonite is epifluorescence; under this light aragonite has a blue color that contrasts with the dull orange of calcite (Ortega et al., 2005; Pickering et al., 2010).

The thin sections analyzed by this technique, covering the whole length of the speleothem, showed a homogeneous orange color, with no traces of aragonite. SEM images of freshly broken surfaces of Andromeda showed no aragonite-related textures (i.e. acicular, elongated columnar or whiskers (Frisia and Borsato, 2010) and the EDX analyses gave a composition of calcite in all the points and areas analyzed. Petrographically, according to Perrin et al., (2014), the transformation of aragonite into calcite strongly alter the lamination of the samples, and leads to an opening of the system provoking age anomalies (Borsato et al., 2003; Fairchild et al., 2006). None of these characteristic can be found in ANDROMEDA, which has well developed lamina and no age inversions or uncertainties. These results together with the behavior of the isotopes and trace metals, that is in concordance with the continental records, are indicators of the primary origin of the calcite.

6.16.1 Interpretation of the isotopes and trace metals

6.16.1.1. $\delta^{18}O$ profile

In the present-day, the oxygen isotopes of the calcite in this cave are controlled by the temperature effect. There are also an influence of the source of moisture and rainfall component, linked to the temperature. During summer, both effects are amplified by enhanced degassing of the drip waters prior to calcite precipitation (Pérez-Mejías et al., 2018). Likewise, in the past, there were some mechanisms that demonstrated influence in the $\delta^{18}O$ during short events, such as changes in the North Atlantic area due to a freshwater input in the ocean (Pérez-Mejías et al., 2017).

We hypothesize that the $\delta^{18}O$ profile of ANDROMEDA changed over the recorded time span influenced by several factors. To explore that possibility, we split the record into two parts, the first one spanning from 119 to 80 kyr, and the second part from 80 to 36 kyr, with a transition period between 80 and 68 kyr (Fig. 6.17). During MIS 5 $\delta^{18}O$ follows the precessional cycle of the boreal summer. At ~80 kyr, during a pronounced decrease in relative sea level (RSL) (Fig. 6.17c,d,j) both $\delta^{18}O$ and Northern Hemisphere summer insolation (NHSI) became decoupled. RSL is considered as a proxy of global sea level and ice volume, using the Red Sea level reconstruction (Grant et al., 2014) strongly correlated with Antarctic temperatures (Rohling et al., 2009) (Fig. 6.17j). Attending to the *temperature effect*, the increase in surface air temperature points to higher $\delta^{18}O$ in the stalagmite, whereas the *amount effect* leads to lower $\delta^{18}O$ with increased precipitation. In the case that both effects could exert influence at the same time would act in opposite direction (Pérez-Mejías et al., 2018). Hence, the precession-paced $\delta^{8}O$ of ANDROMEDA during MIS 5 suggest a prevalence of the amount effect.

On the contrary, the decoupling of the $\delta^{18}O$-NHSI leaded to a different dominant control of the $\delta^{18}O$ from 80 kyr on advance. That period was characterized by rapid abrupt changes in the climate and sea level drop until reaching minimal values (Fig. 6.17j). The results suggest a signal of wet and cold conditions during that time, pointing both effects in the same direction (low $\delta^{18}O$). That interpretation is in concordance with low Sea Surface Temperature (SST) in the North Atlantic during that time (Martrat et al., 2007; 2014), a regime of reinforced Asian Monsoon (AM) (Cheng et al., 2016) and an advance of the Iberian glaciers in northern Spain (Rodríguez-Rodríguez et al., 2016;

Sancho et al., 2018) (Fig. 6.17a,b). We propose that the strong similarities between the isotopes in our record and the intensity of the AM (Fig. 6.17b,c,e) were explained by a common response to abrupt changes in the North Atlantic realm, a tight relationship demonstrated previously during MIS 8 and 7 (Pérez-Mejías et al., 2017).

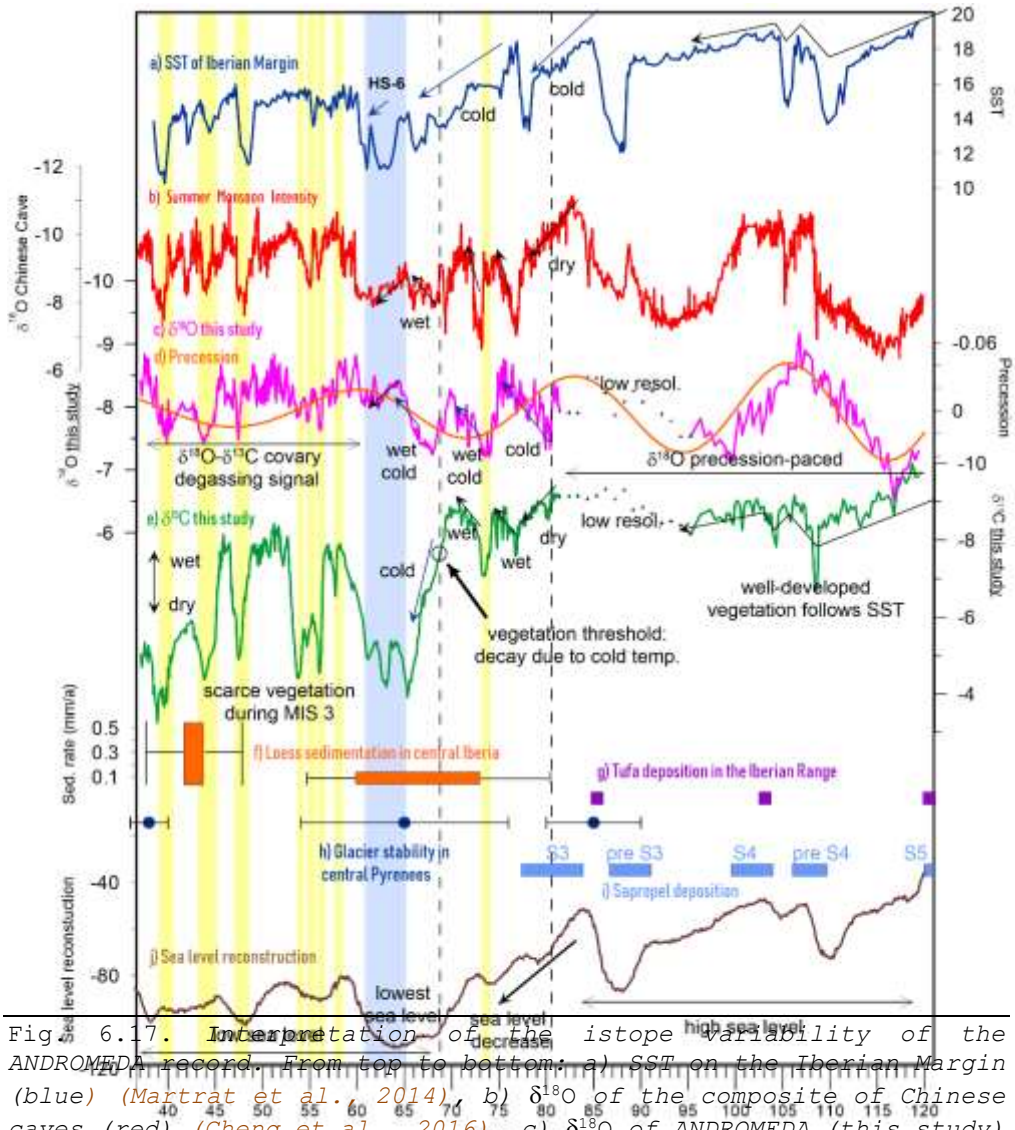

Fig. 6.17. *Interpretation of the istope variability of the ANDROMEDA record. From top to bottom: a) SST on the Iberian Margin (blue) (Martrat et al., 2014), b) $\delta^{18}O$ of the composite of Chinese caves (red) (Cheng et al., 2016), c) $\delta^{18}O$ of ANDROMEDA (this study) (pink) and d) the precessional cycle of boreal summer (orange), e) $\delta^{13}C$ of ANDROMEDA (this study) (green), f) sedimentation rate (mm/year) of loess in Central Iberia (orange) (Wolf et al., 2018), g) tufa deposits in the Iberian Range (violet) (Sancho et al., 2015), h) periods of glacier stability in the central Pyrenees (blue dots) (Lewis et al., 2009), i) sapropel deposits (blue*

squares) (Ziegler et al., 2010), and j) relative sea-level (brown) (Grant et al., 2014) (cont. on next page).

During MIS 5, that relationship was also seen in the rainfall in the East Mediterranean with wet periods in agreement with the sapropel deposits found in the Mediterranean basin (Ziegler et al., 2010) (Fig. 6.17i).

Once the lowest RSL is reached around ~65-61 kyr, coincident with Heinrich 6, there was a period of relative stability in the RSL that leaded to the D-O oscillations, in which the complex relationships between changes in the mode of the thermohaline circulation and the transference of heat from the atmosphere controled the climate (Broecker et al., 1985). This was a period in which the $\delta^{18}O$ and $\delta^{13}C$ covaried in ANDROMEDA (Fig. 6.17c,e) suggesting that both isotopes responded to the same process(es).

6.16.1.2. $\delta^{13}C$ and Mg/Ca

The $\delta^{13}C$ of ANDROMEDA during MIS 5 recorded a stable signal with the lowest values of the record and a small variability, in agreement with more vegetation productivity and microbial activity of a well-developed vegetation in the mild conditions of MIS 5. That epoch recorded an interglacial warmer than the Holocene (Pailler and Bard, 2002; Masson-Delmotte et al., 2010), sea level above present (Grant et al., 2014) and the maximum development of forest in all latitudes (Sánchez-Goñi et al., 2008). During MIS 5, the lower $\delta^{13}C$ values of ANDROMEDA ranged between −10 and −9‰ and the higher $\delta^{13}C$ between −9 to −8‰, both on the same range that the $\delta^{13}C$ from another stalagmite growing during mid-to-late Holocene in this cave (Moreno et al., 2017). During MIS 5, the $\delta^{13}C$ followed the SST and exhibited sensitivity to dry events as showed the comparison with the AM record (Fig. 6.17a,b,e).

This argumentation of sensitivity to both temperature and hydrology holds an interpretation of the $\delta^{13}C$ as a vegetation productivity proxy during MIS 5, with lower $\delta^{13}C$ controlled by the biogenic CO_2 of plant root respiration and microbial activity. This interpretation goes in the same line than a previous stalagmite from this cave growing during the MIS 8 - MIS 7 period (Pérez-Mejías et al., 2017). The higher diameter of ANDROMEDA in the base, when the $\delta^{18}O$ and $\delta^{13}C$ suggest the wettest period of the record, confirms the higher water availability that supported a well-developed vegetation.

Fig. 6.17. (cont). *The vertical yellow bars show the high values of both $\delta^{18}O$ and $\delta^{13}C$ in our record, a signal of cold-dry periods and the correspondence with other records. The vertical black dashed lines reflect two different stages and the transition*

between them, attending to the mechanisms controlling the climate. HS-6 is also marked with a blue bar. The arrows show the trends and similarities between records. The section with the lowest resolution in our isotope record is marked with dots.

The sensitivity to changes in hydrology is also supported by the high correlation between $\delta^{13}C$ and Mg/Ca, and the coincidence with high values of $\delta^{234}U$, a proxy of the water residence time in the epikarst (Hellstrom and McCulloch, 2000; Polyak et al., 2012), in spite of the limited resolution of the latter (Fig. 6.16d). Therefore, the high residence time in the epikarst and the enhanced degassing could explain the sensibility of the $\delta^{13}C$ to the changes in hydrology. Although a decay in the biogenic CO_2 during episodes of dryness in MIS 5 is not discarded, the high resilience of the Mediterranean vegetation (Aranbarri et al., 2014) could explain the scarce $\delta^{13}C$ variability and the fast return to low values in episodes of abrupt changes such as MIS 5c (Fig. 6.16b). This interpretation is on concordance with the behavior of the Mediterranean forest below the 40 °N of latitude, strongly imprinted by precession with short and episodic periods of contraction during C27 to C24 cold marine periods (Martrat et al., 2007; 2014) associated with the reduction in moisture availability as a response of changes in North Atlantic (Tzedakis, 2005; Fletcher and Sánchez Goñi, 2008; Sánchez-Goñi et al., 2008).

The drop of the temperatures from ~70 kyr onwards promoted a decay in the vegetation leading to higher values in $\delta^{13}C$. Despite the climate was getting wetter in 68 kyr, there was no turning back for the decay in the vegetation once the threshold is reached of an extremely cold climate conditions (Fig. 6.17e). Around ~60 kyr, the high variability in the $\delta^{13}C$ and the covariation with $\delta^{18}O$ suggested a domination of the degassing as a hydrologic control, that in the case of the $\delta^{13}C$ may amplify the effect of the input of biogenic CO_2. Therefore, higher $\delta^{13}C$ and $\delta^{18}O$ were recorded during the cold spells of Heinrich events associated with dryness, while lower $\delta^{13}C$ and $\delta^{18}O$ were recorded during warm interstadials with wet conditions in agreement with existent pollen data (Combourieu Nebout et al., 2002; Goñi et al., 2002).

A less input of biogenic CO_2 in the $\delta^{13}C$ of the stalagmite is expected during MIS 4-3, being explained by the extremely cold temperatures and the short length of the warm-wet periods, preventing the development of a well-stablished forest as in the MIS 5. The higher values of $\delta^{13}C$ during MIS 4-3 (−6.62‰) compared with MIS 5 (−8.59‰) and the prevalence of steppic taxa in this period (Combourieu Nebout et al., 2002; Vegas et al., 2010) supports this hypothesis.

6.16.2. From orbital-pacing to millennial-scale variability

Attending to temperature and rainfall, MIS 5 has been characterized in the North Hemisphere as a warm-wet period with stages of more humidity controlled by the two cycles of minima precession (Fig. 6.18e). The low precession peaks leaded to the major abrupt changes in ocean temperature, as evidenced by the increase of IRD discharges in North Atlantic and the abrupt changes in SST of the Iberian Margin (Fig. 6.18a,b), reflecting the balance between the southward expansion of subpolar waters and the northward displacement of subtropical water masses (de Abreu et al., 2003).

During the first (older) precession cycle, the $\delta^{18}O$ in ANDROMEDA followed closely the orbital signal (Fig. 6.18d,e), with lower precession (perihelion in boreal summer) evidenced by the high peak in NHSI enhancing seasonality that causes hotter-dry summers, and cooler-wetter winters (Fletcher and Sánchez Goñi, 2008). In that context, the increase of the evaporation in North Atlantic reinforced the storm tracks following the westerlies, and increased the rainfall over southwestern Europe (Stoll et al., 2015b), Near East (Bar-Matthews et al., 2003) and strengthen the AM (Cheng et al., 2016) (Fig. 6.18c,g,j).

The wet periods seen in ANDROMEDA, well-delimited in the $\delta^{18}O$ and $\delta^{13}C$, were in close agreement with the strong AM (Cheng et al., 2016) and coincident with maxima tufa deposition (Sancho et al., 2015) in the Iberian Range and sapropel deposits in East Mediterranean (Ziegler et al., 2010) (Fig. 6.17c,g,e,i), both proxies linked to minima precession and suggesting a continental pronounced hydric availability during this time. Our $\delta^{13}C$ exhibits great similarities with the SST of the Iberian Margin and the Alborán Sea (Martrat et al., 2014), and also with the temperature of continental records as Alps caves (Meyer et al., 2008; Boch et al., 2011) (Fig. 6.18b,l,n). The tight relationship between $\delta^{13}C$ and temperatures in this time would imply an inherent sensibility to temperature in the $\delta^{13}C$ signal that also responds to changes in hydrology (see previous point 6.16.1.2).

However, the orbital-pacing in the $\delta^{18}O$ of ANDROMEDA came to the end during the second cycle of precession (Fig. 6.18d,e). In this time, although the $\delta^{13}C$ exhibit low values during the peak of low precession that triggered the wet conditions, the $\delta^{18}O$ will exhibit onwards a saw-tooth signal suggesting a more complex climatic control on the $\delta^{18}O$ signal. The complete decoupling $\delta^{18}O$-NHSI is produced when the RSL was decreasing (Fig. 6.18j) and the precession forcing was especially weak

during MIS 4 and 3 (Sánchez-Goñi et al., 2008), in contrast to MIS 5 that showed stronger eccentricity and larger seasonal insolation changes (Capron et al., 2010). The end of the orbital-pacing will be common in all records during MIS 4 and 3 (see further).

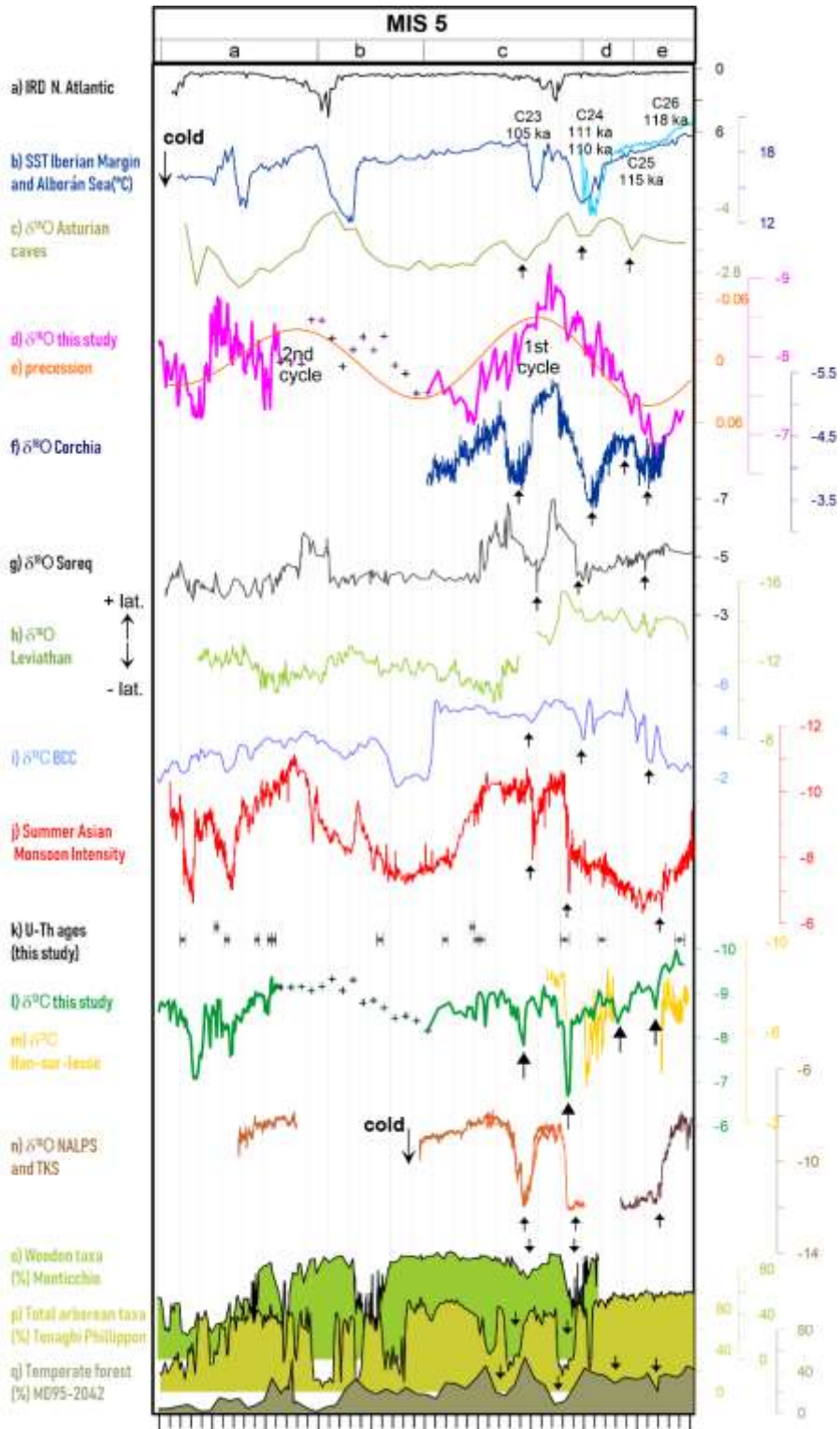

Hereafter, the saw-tooth signal with a slight variability characterized the $\delta^{18}O$ of ANDROMEDA, in contrast with the abrupt signal and high variability seen in the $\delta^{13}C$. However, both isotopes will exhibit onwards a common response to the millennial-scale variability seen during MIS 4 and MIS 3, and will be discussed further.

Fig. 6.18. *Comparison of records during MIS 5, including orbital forcing. From top to bottom: a) IRD discharge at U1308 (black) (Hodell et al., 2008), b) sea-surface temperature at MD95-2042 on the Iberian Margin (blue) and at ODP-976 in the Alboran Sea (sky blue) (Martrat et al., 2007), c)* $\delta^{18}O$ *of Asturias Caves (Stoll et al., 2015b), d)* $\delta^{18}O$ *of ANDROMEDA (pink) and e) precessional cycle of boreal summer (orange), f)* $\delta^{18}O$ *of Corchia Cave (navy blue) (Drysdale et al., 2007), g)* $\delta^{18}O$ *of Soreq Cave (black) (Bar-Matthews et al., 2003), h)* $\delta^{18}O$ *of Leviathan Cave (green) (Lachniet et al., 2014), i)* $\delta^{13}C$ *of BCC Cave (blue) (Springer et al., 2014), j)* $\delta^{18}O$ *of Chinese Caves (red) (Cheng et al., 2016), k) U-Th ages of ANDROMEDA, l)* $\delta^{13}C$ *of ANDROMEDA (green), m)* $\delta^{13}C$ *of Han-sur-lesse (yellow) (Vansteenberge et al., 2016), n)* $\delta^{18}O$ *of TKS cave (dark brown) (Meyer et al., 2008) and NALPS stalagmites, (light brown) (Boch et al., 2011), o) woody taxa (%) in Lago Grande di Monticchio (green) (Martin-Puertas et al., 2014), p) total arborean taxa (%) (Wulf et al., 2018) (yellow) in Tenaghi Philippon, q) temperate forest (%) of MD95-2042 (khaki) (Sánchez Goñi et al., 2017). Note that the isotope proxies of all stalagmite records are interpreted to reflect the amount of precipitation, with an exception of Leviathan (changes in moisture source), Han-sur-lesse (changes in vegetation type),* $\delta^{13}C$ *of ANDROMEDA (this study) and NALPS stalagmites (temperature effect). All vertical axes of the speleothem records are reversed, with the exception of NALPS.*

6.16.3. Abrupt centennial-scale pulses during the Last Interglacial and Glacial Inception

6.16.3.1. Abrupt dry-cold events

MIS 5 was a period of especial relevance, covering the end of the interglacial and the last glacial inception, represented an intermediate stage between full interglacial conditions of MIS 5e and the more glacial conditions during MIS 4-3 (Capron et al., 2010). The orbital-pacing during MIS 5 did not hinder the occurrence of abrupt centennial-scale dry-cold pulses, identified in worldwide records (Fig. 6.18) and associated with a declining in NHSI (Mokeddem et al., 2014).

We identified four marked pulses of aridity in ANDROMEDA with high $\delta^{13}C$ from 120 kyr to 95 kyr, two of less prominent decay in $\delta^{13}C$ (116.7 and 113.2 kyr) and two pulses of more intensity (108.6-108.3 and 104.3 kyr) (Fig. 6.18l). The four events recorded a decline of the temperate forest in a pollen record from the Iberian Margin (Sánchez-Goñi et al., 2008) (Fig. 6.18q), pointing to the sensibility of vegetation in Iberia to changes in North Atlantic (Gonzalez-Samperiz et al., 2008; Sánchez-Goñi et al., 2008). Those events were well defined in the marine record (C26 to C23) but generally only the two more intense (C24 and C23) was reflected in continental sequences, such as the pollen record from Lago Grande di Monticchio and Tenaghi Philippon (Martin-Puertas et al., 2014; Wulf et al., 2018) (Fig. 6.18o,p). Therefore, the signal of these events in ANDROMEDA stalagmite from NE Spain represents the first evidence of those changes in both temperature and humidity reflected in the $\delta^{13}C$ of a stalagmite from southwestern Europe, an area of special sensitivity to abrupt changes in the North Atlantic.

The two older events detected in ANDROMEDA could be contemporary to C26 and C25 marine events (Fig. 6.18b,l), barely evident in terms of SST in Alborán and Iberian Margin but evidencing that the interglacial was coming to an end after 115 kyr through the quantity of alkenones accumulated in the Alborán sediments (Martrat et al., 2014). In the monsoon record, there were evidences of weakness during 117 kyr, but not during 113 kyr, when the $\delta^{18}O$ pointed to a slow reinforcement of the AM after the minimum intensity reached during 115 kyr (Fig. 6.18j). The cold-dry excursion analog to C26 in ANDROMEDA is seen in all records worldwide, with a clear imprint in Europe through a slight drop of temperatures in Alps speleothems (Meyer et al., 2008), the drop in the $\delta^{13}C$ of Han-sur-lesse speleothem and in the drop in the $\delta^{18}O$ of Baradla Cave, Hungary (Demény et al., 2017) (Fig. 6.18m,n). Conversely, the C25 event do not recorded a global response and lacks in both North America (BCC and Leviathan cave) and Soreq cave, as well as the AM records (Cheng et al., 2016) (Fig. 6.18h,i,j), discarding the mechanism of the

disruption of the Atlantic Meridional Overturning Circulation (AMOC) at this time, hypothesis supported by the lack of changes in the RSL at that time (Fig. 6.17j). The small response in Corchia and Asturian caves (Drysdale et al., 2007; Stoll et al., 2015b) to C25 (Fig. 6.18c,f) suggests a common response in south-western Europe, although more data in other areas are needed to understand the C25 event.

The other two events (C24 and C23) recorded a strong response in all the records (Fig. 6.18). Around 111 kyr, the C24 event showed a drop from 18 °C to 13 °C in the Iberian Margin SST, pointing to the end of the LIG with a North Atlantic seasonally covered of ice and icebergs while the Mediterranean region exhibited arctic conditions (Martrat et al., 2007). In this state, the AMOC was expected to be subject to rapid instabilities leading to sub-millennial variability (Capron et al., 2010). The increased of the ice sheets, still small, makes them more vulnerable than the large ice sheet of MIS 4 and 3 to local radiative perturbations (Capron et al., 2010). In that basis, the strong NHSI and the changes in sea level and posterior discharge of meltwater from the IRDs could be of enough magnitude to produce a change in the state of the AMOC. Our record exhibited in this event the highest $\delta^{13}C$ values reached during MIS 5 and dated in 108.6 kyr that lasts until 108.3 kyr, strongly coincident in time with other absolute chronologies of the weakened AM and the end of the cold spell in NALPS (Fig. 6.18j,l,n).

Lastly, the C23 event was founded in all records, including Western America with a small hiatus but in a clear trend to a southward displacement of the moisture source (Fig. 6.18h), evidencing climatic teleconnections in a greater scale beyond the Atlantic Realm. In East North America, both C24 and C23 had a little impact, but the abrupt decay in the $\delta^{13}C$ was noticeable in BCC cave (Springer et al., 2014) later, around 96 kyr (Fig. 6.18i). In that time, the other records exhibited a weakness in the rainfall intensity such as the change to lower latitudes moisture sources in Leviathan (Lachniet et al., 2014), the cease of the growth in Alps stalagmites (Meyer et al., 2008; Boch et al., 2011), and the lower resolution in our record together with the decay in pollen records (Fig. 6.18l,o,p,q). Although there was a clear trend to cold conditions, the existence of an abrupt climate change during that time that would justify the abrupt response of some records is still unknown in the light of the present data.

6.16.3.2. The end of the Eemian

There was some controversy about the chronology of the end of the Eemian interglacial forest in Europe (Sánchez Goñi et al., 2005; Müller and Sánchez Goñi, 2007; Brewer et al., 2008) due to differences in the timing of the cold-dry events between areas and the different chronologies between records (Govin et al., 2015). However, there is a general agreement in time between records from similar latitude, whether if they have independent ages or if use tuned chronologies. In that line, the Eifel Maar record using proxies such as the increase in varve thickness, loess, charcoal and higher abundance of grass pollen (Sirocko et al., 2005) stablished a similar chronology for the end of the Eemian as a speleothem record from Belgium (Vansteenberge et al., 2016) with the age of 117.3 kyr, when the first hiatus was recorded in the speleothem record (Fig. 6.18m).

Likewise, the end of the Eemian in southern Germany was established later, around ~111 kyr (Müller and Sánchez Goñi, 2007), in the line of some independent chronologies from speleothems southwards, as south Iberia (~111 kyr) (Hodge et al., 2008), Mallorca (111.7±0.2 to 109.3±0.2 kyr) (Dumitru et al., 2018), Corchia (112.0±0.8 to 108±0.8 kyr) (Drysdale et al., 2007) and when a hiatus was recorded in a speleothem form northern Spain around ~112 kyr (Rossi et al., 2014).

Finally, a pollen record from the Iberian Margin used a tiepoint of peak abundance of nonarboreal within Melisey 1 period around ~107 kyr (Sánchez Goñi et al., 2005; Müller and Sánchez Goñi, 2007), in the same line that new independent chronologies from tephra of Lago Grande di Monticchio (40°57'N), with ages of 107.6-109.5 kyr (Allen and Huntley, 2009; Martin-Puertas et al., 2014), and the timing seen in Tenaghi Philippon (40°58'N) (Fig. 6.18o,p) that offered an age of 109.4±0.9 kyr (Wulf et al., 2018). Both pollen records, similar in latitude to Ejulve cave (40°45'N) was in agreement with our U-Th independent chronology of 108.6±0.3 to 108.3±0.3 kyr that is in the line of the Chinese speleothems (Cheng et al., 2016) (Fig. 6.18j,l).

Therefore, our results represent the first evidence of independent chronology from U-Th method for this late-ending of the Eemian from stalagmites of southwestern Europe.

6.16.4. Abrupt millennial-scale variability during MIS 4 to MIS 3

6.16.4.1. D-O variability

The end of MIS 5 was characterized by a great expansion of ice sheets involving widespread global impacts via changes in atmospheric circulation and temperature (Clark et al., 2009). In this context, the occurrence of D-O oscillations was the most notable expression of this abrupt millennial-scale variability. In the last decades, the identification of the terrestrial response to D-O in Villars cave (Genty et al., 2003; 2010) supposed a milestone to constrain the implications of those events in Europe.

It is known that the impact of D-O was not global, there are some examples of speleothems in mid-latitudes such as North America (e.g. BCC, Leviathan cave, Fig. 6.19g,h) (Springer et al., 2014; Lachniet et al., 2014) or low-latitudes such as Bahamas or Borneo (Arienzo et al., 2015; Carolin et al., 2016) that do not recorded any response to these events. Interestingly, the signal recorded during D-O highly differed in closely areas of Europe, great examples was in one side Sofular Cave that exhibited a great sensibility to D-O patterns (Fig. 6.19i) in close analogy to the ice record of Greenland (Svensson et al., 2008), on the other side the rainfall record of Soreq cave did not show a clear response to D-O oscillations (Fig. 6.19f).

Therefore, the sensitivity of the terrestrial records to D-O seems to be unique. On that basis, it is worth noting the significance of ANDROMEDA record, replicating the signal seen in Villars cave and covering previous hiatus during cold periods (Fig. 6.19n,o). The sensitivity of ANDROMEDA to the D-O oscillations enables the tentative identification through the $\delta^{13}C$ of the D-O cycles from the 19 (~70 kyr) until the 11 (~42 kyr), with the uncertainty of 13, that usually exhibited weak signal and short duration (Wainer et al., 2009).

6.16.4.2. Heinrich event variability

The Heinrich events were recorded markedly with high $\delta^{13}C$ in ANDROMEDA, although the magnitude differs between stadials. The Heinrich event and the reduction in SST is thought to be caused by the slowdown of the AMOC and the related reduction in

northward heat transport (McManus et al., 2004; de Vernal et al., 2006; Clement and Peterson, 2008; Wolff et al., 2010). In our record, HS-4 recorded the highest values of $\delta^{13}C$, a Heinrich event recognized as one of the most pronounced regarding IRD fluxes (Cortijo et al., 1997; Hemming, 2004), and more abrupt that HS-5 (López-García et al., 2013) with a probably nearly complete shutdown of the thermohaline circulation (Elliot et al., 2002; Roche et al., 2004).

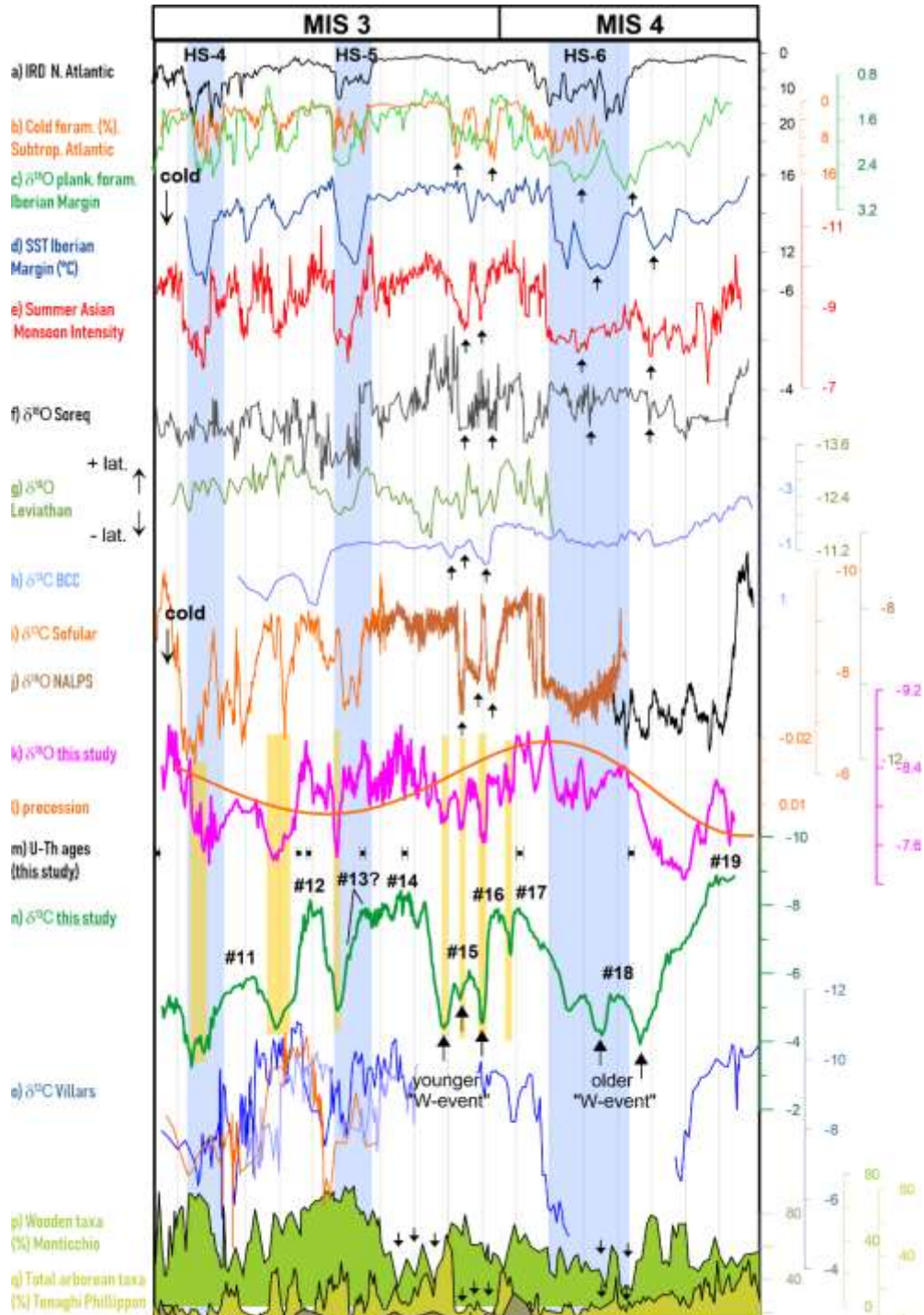

The dry conditions in Iberia during Heinrich events was inferred by the dust transported to the Alborán Sea (Moreno et al., 2002) and the reconstruction of the vegetation (Goñi et al., 2002) during HS-4, and more recently by a loess sequence from central Iberia (Wolf et al., 2018) that recorded higher loess sedimentation rate during HS-4 compared with HS-6 (Fig. 6.17f). While the first accumulation of pure aeolian loess of this record took place between 73.0±6.9 kyr and 59.7±4.7 kyr (matches with HS-6), the second took place between 41.3±4.0 kyr and 43±3.8 kyr, including HS-4 within dating uncertainties (Wolf et al., 2018).

The location of Ejulve cave in 40° N of latitude, on the path of the storm tracks when the Polar Front (PF) was displaced downwards during cold periods (Fig. 6.12), may explain the long record and the speleothem growth during Heinrich events, especially during HS-6. In that way, while in modern times the PF follows the coast of Greenland with a sinuous circulation (Eynaud et al., 2009), the reconstructions of the PF during the Heinrich Events established a general consensus with a position southern of the Ruddiman IRD belt (Fig. 6.12), that reached as far as 39° N (Voelker and Abreu, 2011) or 40° N (Eynaud et al., 2009 and references therein). Naughton et al (2009) proposed lower latitudes for the PF during the maximum discharge phase of IRD during the Heinrich events, reaching as far as 35 - 37° N. The southward migration of the PF and the meridional compression of the North Atlantic anticyclonic gyre, gave as a result an enhanced zonal atmospheric circulation (Pailler and Bard, 2002) (Fig. 6.12).

Fig. 6.19. *Comparison of records during MIS 4 and 3, including orbital forcing. From top to bottom: a) IRD discharge at core site U1308 (black) (Hodell et al., 2008), b) $\delta^{18}O$ of planktic foraminifera of MD01-2444 (Globigerina bulloides, Globigerinita glutinata) (green) (Vautravers and Shackleton, 2006) and c) cold foraminifera species (%) (Neogloboquadrina pachyderma, Turborotalia quinqueloba) in ODP 172-1060 (orange) (Vautravers et al., 2004), d) sea-surface temperature in MD95-2042 on the Iberian Margin (blue) (Martrat et al., 2014), e) $\delta^{18}O$ of Chinese speleothems (red) (Cheng et al., 2016), f) $\delta^{18}O$ of Soreq Cave (black) (Bar-Matthews et al., 2003), g) $\delta^{18}O$ of Leviathan Cave (green) (Lachniet et al., 2014), h) $\delta^{13}C$ of BCC Cave (blue) (Springer et al., 2014), i) $\delta^{13}C$ of Sofular Cave (blue) (Fleitmann et al., 2009), j) $\delta^{18}O$ of NALPS (brown) (Moseley et al., 2014), (black)* (R. Boch et al., 2011), *k) $\delta^{18}O$ of ANDROMEDA (pink) with a polynomial fit (black) and l) precessional cycle of boreal summer (orange), m) U-Th ages of ANDROMEDA, n) $\delta^{13}C$ of ANDROMEDA (green), o) $\delta^{13}C$ of Villars Cave (blue) (light blue) (orange) (Genty et al., 2010), p) woody taxa*

(%) of Monticchio (green) (Allen and Huntley, 2009), q) total arborean taxa (%) (Wulf et al., 2018) (yellow) in Tenaghi Philippon, temperate forest (%) of r) MD95-2042 (khaki) (Sánchez Goñi et al., 2017). The vertical axes of the speleothem records are reversed, with the exception of NALPS.

The suppression of the cyclogenesis, explained by the low SST in the Atlantic Ocean with low RSL and an extensive ice cover, promotes low evaporative flux ocean-atmosphere, leaded by a weakening of the AMOC (Genty et al., 2010; Rowe et al., 2012) that could explain the hiatuses found in some continental paleorecords of Europe (e.g. Villars cave, Han-Sur-Lesse, NALPS, Fig. 6.18m,n,o). Conversely, Ejulve cave would be on the path of the storm tracks, and the soil was able to produce enough CO_2 to generate $CaCO_3$ saturated dripwaters that promoted carbonate precipitation, despite the scarce vegetation existent during the cold periods. However, each cave system is unique and the latitudinal location below 40° N do not guarantee a continuous growth during these periods, as was seen in speleothems from Portugal and Mallorca (Denniston et al., 2017; Dumitru et al., 2018).

6.16.4.3. Heinrich intra-event variability

A prominent feature of the $\delta^{13}C$ of ANDROMEDA from 70 to 50 kyr was the existence of two events characterized by a "W-shape" (Fig. 6.19n), that we define as the response of the $\delta^{13}C$ to the weak D-O 15 and 18 respectively, that interrupted a long stadial characterized by a Heinrich event. The W-events exhibited a similar intensity attending to the drop in the $\delta^{13}C$ values, but a different timing, longer in the older event contemporary to HS-6. The structure of these events remains the one suggested previously in a marine record within HS-1 and HS-11 during the last two deglaciations (Martrat et al., 2014). In the marine record were known as "the double-ues", and recorded a sharp warming occurred halfway their progression that indicated the potential energy storage of the deep North Atlantic (Skinner and Elderfield, 2007), linked to the culmination of a large reduction in the AMOC, ice surge phases with moderate rise in sea level and possible sub-surface warming feedbacks (Flückiger et al., 2006).

In close analogy, the two "W-event" we propose in the terrestrial record of ANDROMEDA were characterized by an intense drop to higher $\delta^{13}C$ values, a brief excursion to lower values before reaching higher ones, and a final abrupt return to the similar low values reached at the onset of the event (Fig. 6.19n). They are associated with phases of decrease in the RSL (Fig. 6.17j) and an increase in the cold foraminifera taxa (Fig.

6.19b,c), however they were only present in few records (Fig. 6.19).

The older W-event (D-O 18), seen also in the marine record, was only identified somewhat distort in shape in the AM record (Fig. 6.19e). Likewise, neither Soreq Cave (Bar-Matthews et al., 2003) nor BCC Cave (Springer et al., 2014) recorded signal of this abrupt event (Fig. 6.19f,h). In this case, the scarce records growing during HS-6 turn out in a challenge to study the global signal of this event. The present data suggest a marine origin expressed in the low SST and the cold foraminifera taxa (Fig. 6.19b,c,d), probably far from the moisture source of the BCC Cave, that did not record any response to that event (Fig. 6.19h), but with repercussion in southern Europe and Asia (Fig. 6.19e,n). Our results of Mg/Ca ratio pointed to a markedly dry conditions in 65.5 kyr coincident with the older $\delta^{13}C$ peak of high values, but a more water availability during the second peak around 63 kyr within the HS-6 (Fig. 6.16c), an interpretation in agreement with the water availability interpreted from the $\delta^{18}O$ of ANDROMEDA.

Therefore, we propose a timing based in two-phases in this W-event, the first one characterized by a decrease in the RSL and a prevalence of dry-cold conditions until 63 kyr, and a second phase of wet-cold conditions with rising of RSL in agreement with the gradual recovering of the arboreal vegetation in Monticchio (Martin-Puertas et al., 2014) and a trend to lower $\delta^{13}C$ in ANDROMEDA. The model in two phases we propose for HS-6 has an opposite timing to that proposed by Naughton et al (2009) for HS-4, 3 and 1. In that work, the first phase was stablished with wet conditions in the IP and low IRD deposition, while the second phase had dry conditions and moderate to high IRD deposition. According to the present age models of HS-6 records, the increase in temperatures (Alps) and in precipitation (Monsoon) occurs abruptly around 59-60 kyr (Fig. 6.19j,e), in contraposition to the slow recovering seen in the $\delta^{13}C$ of ANDROMEDA (Fig. 6.19n).

The younger W-event (D-O 15) was clearly recognized in the speleothem records from China, NALPS (Fig. 6.19e,j) and barely present in BCC and Soreq (Fig. 6.19h,f). The decrease in temperatures and vegetation was clear throughout all the speleothem records cited above, and it is also confirmed by the pollen records of Tenaghi Philippon and Lago Grande di Monticchio (Fig. 6.19q,p). Our Mg/Ca replicated the signal of the $\delta^{13}C$ in this event (Fig. 6.16b,c), therefore the dry conditions we stablished coincided with the two peaks of higher $d^{13}C$ values.

Conversely to the clear terrestrial signal seen as a response of the intense cold-dry conditions during this W-event, it

presented complexities in the marine realm, that recorded only a brief reduction of the SST in the Iberian Margin in an isolated event during this time (Fig. 6.19d). The absence of great iceberg discharges in the North Atlantic, or a marked decrease in SST in the Iberian Margin around 55 kyr (Fig. 6.19a,d) was in contrast with the cold foraminifera data from the subtropical western Atlantic (Gulf Stream area) that points to cold conditions in two peaks, in close analogy to the W-shape of the event we proposed (Fig. 6.19b). These changes in the subtropical Atlantic triggered cold-dry anomalies in some records from America (BCC cave) (Springer et al., 2014) and Europe (NALPS, Ejulve cave) (Moseley et al., 2014) and Asia (Soreq) (Bar-Matthews et al., 2003) (Fig. 6.19h,j,n,f) that are sensitive to the changes in that source moisture area. The $\delta^{18}O$ of the planktonic foraminifera from the Iberian Margin (Fig. 6.19c), a proxy for upwelling intensity driven by trade winds (Vautravers and Shackleton, 2006) recorded an excursion to higher values on that time. The interpretation of a high influence of the NE trade winds off Portugal, associated with NAO+ conditions (Vautravers and Shackleton, 2006) is on agreement with the dry conditions seen on the continental european records during that time (Fig. 6.19). Some authors suggested the existence of HS-5a in this time, an additional Heinrich between HS-5 and HS-6 (e.g. (Rashid et al., 2003; Vautravers and Shackleton, 2006), in spite of the low IRD recorded (Fig. 6.19a). In that way, the coincidence of high $\delta^{13}C$ values of ANDROMEDA with the reinforcement of the northeasterly trade winds activity support the link between dry phases of Heinrich events and the positive phases of NAO suggested by some authors (Vautravers and Shackleton, 2006; Naughton et al., 2009).

The two W-events were seen also in the pollen records (Martin-Puertas et al., 2014; Sánchez Goñi et al., 2017; Wulf et al., 2018) with a pronounced decay in the wooden taxa (Fig. 6.19p,q,r) conforming the characteristic shape seen in Ejulve record. However, some differences exist in the chronology, while the older W-event seen in the pollen record was contemporary to ANDROMEDA, the younger one was displaced to younger ages as far as 3-4 kyr in Monticchio in comparison with the speleothem record.

We suggest a similar displacement to younger ages in Monticchio also in the D-O 14, that in the present chronology exhibit an increase of the wooden taxa during the HS-5. The tight relationship seen previously in the C24 event during MIS 5 between both pollen records and ANDROMEDA, suggested a common response to abrupt events that is now challenged by the offset seen in Monticchio during MIS 3. Previous findings pointed out the discrepancies in age of Monticchio during MIS 3, such as during the HS-4 with a poor varve preservation that probably enhanced by an imprecise attribution of the cold events to the

pollen record (Wulf et al., 2004) and the application of different methods to constructed the chronologies, namely varve counting versus radiometric dating or palynological tuning (Genty et al., 2010; Wulf et al., 2018). Therefore, the results presented here suggests that both events could be contemporary.

6.17. Conclusions

The present record of ANDROMEDA stalagmite from Ejulve cave exhibited a continuous growth from 118.9 to 36.9 kyr. Attending to the different controls on the isotope signal along the time series, we proposed two different stages: (1) during MIS 5 the $\delta^{18}O$ is controlled by orbital pacing, with low precession peaks leading wet conditions, and (2) MIS 4 and 3, where $\delta^{18}O$ and $\delta^{13}C$ covaried (ρ=0.53) after HS-6 and the variability of both isotopes could respond to an enhanced degassing of the drip waters during the dry periods.

During the first stage (MIS 5), the $\delta^{18}O$ is mainly controlled by amount of rainfall while the $\delta^{13}C$, highly correlated with Mg/Ca (ρ=0.75), exhibit the signal of the vegetation productivity and microbial activity, being sensitive to abrupt dry events. The dominant orbital pacing (precession) in the $\delta^{18}O$ is interrupted by some abrupt dry-cold periods. We have found four cold-dry events in our record in concordance with C27, C26, C25 and C24 cold events in the marine realm. The end of the Eemian period in this area is established in 108.6-108.3 kyr, in agreement with other records in South Europe and supporting the hypothesis of an early ending of this forest stage in higher latitudes around ~117 kyr, arriving until ~111 kyr southwards that lasts until ~108-107 kyr in the most southern records.

During the second stage (MIS 4 and 3), the $\delta^{18}O$ is decoupled from the precession, and the succession of D-O and Heinrich events characterize the abrupt changes in the $\delta^{13}C$ signal. The dry-cold periods are characterized by high values in both $\delta^{18}O$ and $\delta^{13}C$, explained by an enhanced degassing that in the case of the $\delta^{13}C$ amplifies the signal of the low biological CO_2, weakened during the cold period in agreement to the scarce vegetation present. The stalagmite experiences a decrease in the growth rate during MIS 4 and the cold stages of MIS 3 until 1.6-1.9 mm/kyr, but the arrival of the air masses and humidity is not interrupted during the displacement southwards of the PF, reaching 39-40° N of latitude during this time.

During 70-50 kyr, we propose two W-events characterized by an intense drop to higher $\delta^{13}C$ values in ANDROMEDA as a response to D-O 15 and 18 respectively, that interrupted a long stadial characterized by a Heinrich event. We stablished a two-phases structure in the older W-event, the first one characterized by a decrease in sea level and prevalence of dry-cold conditions until 63 kyr, and a second phase of increase in sea level and wet-cold conditions in the continent from 63 kyr onwards. The younger W-event is in concordance with a reinforcement of the northeasterly trade winds activity (NAO+ phase) that explain the dryness seen in the continental records.

“Rosetta, is that you?”

-Philae lander

Chapter

Epilogue

7.1. Conclusions

The conclusions of the present dissertation focused on Ejulve cave will be articulated attending to the three main points stablished in the sections of goals, results and discussion, as follows: speleogenesis, present-day speleothemic dynamics and paleoclimatic reconstruction. In each part, the conclusions are summarized as a list of points with the main findings, the more innovative results and significant repercussions.

a) Speleogenesis

- ✓ Some erosive morphologies from Ejulve cave including boxwork formations, tubes with rising ceiling cupolas, pendants and cups, spongeworks and micro-corrosion features are indicative of a hypogene-hydrothermal origin. The geometry

of cave passages and maze network also points to this origin, that in turn may be supported by the current regional low-temperature thermalism. Taking into account the stratigraphic and geomorphic local markers, the formation of the cave tentatively occurred during Upper Miocene-Pliocene.

- ✓ Some cave deposits have been analyzed (calcite botryoids, crusts, spar and aragonite fibers) and the stable isotope composition discards high temperatures during the carbonate formation under vadose conditions. The isotopic signal of these precipitates is similar to the vadose stalagmites, that precipitated at least during the last 650 kyr BP.
- ✓ We propose, consequentely, two stages in the speleogenesis of the cave: (1) former confined hypogenic setting during Upper Miocene-Pliocene, and (2) an unconfined epigenic phase before from 650 kyr BP to present.
- ✓ These results suppose the first evidences of hypogene speleogenesis in the Eastern Iberian Range.

b) Present-day speleothemic dynamics

- ✓ The $\delta^{18}O$ of the rainfall (mean = −7.86 ‰ V-SMOW), sampled during the period 2010-2015, exhibit a seasonal behavior with lower values during autumn through spring (autumn: −8.74, winter: −10.02, spring: −6.92) and higher during summer (−4.04), all in ‰ V-SMOW. The $\delta^{18}O$ is controlled by temperature (r^2 = 0.82, p-value < 0.001), linked to the rainfall component (air mass trajectory) and a minor control of the amount effect.
- ✓ The drip waters exhibited some degree of homogeneization, but the seasonality seen in the rainfall is still preserved in the $\delta^{18}O$ of the drip waters, albeit much more reduced (autumn: −9.24, winter: −9.66, spring: −9.59, summer: -9.47, all in ‰ V-SMOW).
- ✓ The discharge rate response of the cave to the external rainfall was faster than the response time to the isotopes, suggesting the existence of the 'piston effect'.
- ✓ Dripwaters from seepage and seasonal groups could reflect climatic signals at seasonal scale, with a bias to the wet season. The very low discharge points (< 0.01 ml min^{-1}) likely reflected inter-annual variability.
- ✓ The cave exhibited stable temperatures between 11.1 °C - 11.5 °C throughout the year. The cave air pCO_2 show the highest values from late summer to early fall (2160 ppm) and lower values in winter (461 ppm). The ventilation process is driven

by differences in air density during autumn through spring. The lowest cave pCO_2 and the highest calcite precipitation rates were recorded during that time. During winter and spring, the 31.8% and 37.9% respectively of the farmed calcite of the year is recorded. The growth rate of the farmed calcite was also controlled secondarily by dripwater chemistry and drip rate.

- ✓ The $\delta^{18}O$ values of the calcite are similar between seepage and seasonal sites (−8.19 and −8.25 ‰ PDB, respectively). The $\delta^{18}O$ values of the calcite suggest dependence of the $\delta^{18}O$ of the dripwater, with a weaker effect of drip rate. These data do not exhibit barely changes at a seasonal scale (total variability of 0.11 ‰), although some drips showed a seasonal signal due to the enhanced degassing kinetics during summer and autumn.
- ✓ The $\delta^{13}C$ record exhibited seasonality with a variability of 0.22 ‰, showing higher values during summer-autumn, and lower during winter-spring. Seepage sites exhibited higher $\delta^{13}C$ values compared to seasonal ones (−9.76 and −9.93 ‰ PDB, respectively). Longer time between drops promotes enhanced degassing and triggers high $\delta^{13}C$ values, with a variability up to 0.42 ‰. The low $\delta^{13}C$ values were recorded when the soil microbial activity is increased, with higher vegetation productivity and water availability.

c) Paleoclimatic reconstruction

- ✓ The ARTEMISA stalagmite (covering from 262.7 to 217.9 kyr, derived from 24 U/Th dates), recorded the climate changes related to the Termination III (end of Marine Isotope Stage 8), thus showing a great sensibility to glacial-interglacial changes. The variability in the $\delta^{13}C$ record during the timing of the Termination marked two events: S8.2, at 249-247.4 kyr, and S8.1, at 244.7-241 kyr. These events are related to Atlantic meridional overturning circulation (AMOC) slowdowns during MIS 8. The event S8.1 was additionally associated with the entrance of freshwater in the source of moisture (North Atlantic).
- ✓ Both S8.1 and S8.2 events exhibited similarities with Heinrich events 1 and 2, after a comparison of the succession of events during T-III, T-II and T-I. These similarities are supported by the *intense IRD discharges, the dominance of*

semidesert taxa and the *similar phasing of the benthic* $\delta^{18}O$. However, in terms of *sea level* and *insolation*, S8.1 event is more similar to the YD than HS-1.

- ✓ The ANDROMEDA stalagmite, covering from MIS 5 to MIS 3 (based on 21 U/Th dates), exhibited sensitivity in orbital-to-millennial-scale changes such as *D-O oscillations* and/or *Heinrich events*.
- ✓ During MIS 5, the $\delta^{18}O$ variability in ANDROMEDA is controlled by orbital pacing. The $\delta^{13}C$ exhibited a terrestrial response to C26-C25-C24-C23 marine cold events, with cold-dry conditions between 118 kyr and 105 kyr. In addition, interestingly, a late ending of the Eemian forest stage lasting until 108.6-108.3 kyr is proposed for this area.
- ✓ During MIS 4 and 3, the $\delta^{18}O$ and $\delta^{13}C$ oscillations in ANDROMEDA are controlled by enhanced degassing of drip waters during dry periods, in agreement with higher values of Mg/Ca. Likewise, the $\delta^{13}C$ values during the period from 70 to 50 kyr indicate that the response to weak D-O 18 and 15 are two "W-shaped" events with an intense drop to higher $\delta^{13}C$ values.
- ✓ Two stages in the older W-event (~67-60 kyr) can be differentiated in ANDROMEDA indicating dry-cold conditions until 63 kyr, and wet-cold conditions from 63 onwards. Likewise, the younger W-event (~57-53 kyr) is in concordance with a reinforcement of the northeasterly trade winds activity (NAO+ phase) explaining the dryness seen in the terrestrial records.

Conclusiones

Las conclusiones de la presente tesis están articuladas atendiendo a los tres puntos principales establecidos en el apartado de objetivos, resultados y discusión: espeleogénesis, dinámica espeleotémica actual y reconstrucción paleoclimática. En cada una de esas partes, las conclusiones están estructuradas en una serie de apartados con las principales aportaciones y los resultados más novedosos y de una mayor repercusión.

a) Speleogénesis

- ✓ Algunas morfologías erosivas de la cueva de Ejulve, entre las cuales se encuentran *boxwork*, tubos ascendentes con cúpulas, *pendants* y *cups*, *spongeworks* y rasgos de micro-corrosión, son indicativas de un origen hipogénico-hidrotermal. La geometría de algunas galerías y su aspecto laberíntico también sugieren este origen, que se ve reforzado asimismo por el termalismo regional existente de baja temperatura. Teniendo en cuenta los aspectos estratigráficos y geomorfológicos locales, la formación de la cueva se situaría durante el Mioceno Superior-Plioceno.
- ✓ Algunos precipitados han sido analizados (*botryoids*, *crusts*, *spar* y fibras de aragonito) y su análisis isotópico descartaría altas temperaturas durante la precipitación de dicho carbonato en condiciones vadosas. La señal isotópica en dichos precipitados es similar a la encontrada en las estalagmitas vadosas, y su crecimiento se sitúa, al menos, durante los últimos 650.000 años antes del presente (650 ka).
- ✓ Consecuentemente, se proponen dos fases en la espeleogénesis de la cueva: (1) acuífero confinado hipogénico durante el Mioceno Superior-Plioceno, y (2) condiciones no confinadas epigénicas antes de 650 ka.
- ✓ Estos resultados suponen la primera evidencia de espeleogénesis hipogéna en la Cordillera Ibérica oriental.

b) Dinámica espeleotémica actual

- ✓ Los valores de $\delta^{18}O$ de la lluvia (media = −7.86 ‰ V-SMOW), muestreados durante el período 2010-2015, muestran un comportamiento estacional con valores más bajos durante otoño a primavera (otoño: −8.74, invierno: −10.02, primavera: −6.92) y más altos durante verano (−4.04) ‰ V-SMOW. La variación del $\delta^{18}O$ de la lluvia está controlada por temperatura (r^2 = 0.82, p-value < 0.001), además del origen de la lluvia (trayectoria de la masa de aire) y en menor medida, de la cantidad de lluvia.

- ✓ El agua de goteo muestra cierto grado de homogeneización, pero la estacionalidad vista en el $\delta^{18}O$ de la lluvia aún se preserva en el $\delta^{18}O$ del agua de goteo, sensiblemente reducida (otoño: −9.24, invierno: −9.66, primavera: −9.59, verano: -9.47 ‰ V-SMOW).
- ✓ La respuesta de la cueva a la lluvia exterior en tasa de goteo es más rápida que en los isótopos del agua de goteo, sugiriendo la existencia de un efecto pistón.
- ✓ Tanto el agua de los goteos estacionales como la de los no estacionales puede reflejar la señal climática a escala estacional, con un sesgo hacia la estación húmeda. Los puntos de goteo más lentos (< 0.01 ml min^{-1}) pueden reflejar una variabilidad inter-anual.
- ✓ La cueva muestra temperatura estable entre 11.1 °C a 11.5 °C a lo largo de todo el año. El pCO_2 en la cueva muestra valores más altos de verano a otoño (2160 ppm), y más bajos en invierno (461 ppm). La ventilación está controlada por diferencias en la densidad del aire desde otoño a primavera. Los niveles más bajos de pCO_2 y la mayor cantidad de carbonato precipitado se registran durante ese momento. Durante invierno y primavera, se registra el 31.8% y 37.9% del total de carbonato precipitado durante todo el año. La tasa de crecimiento de carbonato está además controlada, en menor medida, por la hidroquímica del agua de goteo y por la tasa de goteo.
- ✓ Los resultados de $\delta^{18}O$ del carbonato precipitado son similares en los goteos estacionales y no estacionales (−8.19 y −8.25 ‰ PDB, respectivamente). El $\delta^{18}O$ del carbonato sugiere una dependencia del $\delta^{18}O$ del agua de goteo, con escasa influencia de la tasa de goteo. Estos resultados no muestran apenas cambios estacionales (con una variabilidad total del 0.11 ‰), aunque algunos goteos muestran una señal estacional propiciada por una mayor desgasificación del agua de goteo durante verano y otoño.
- ✓ Los resultados del $\delta^{13}C$ muestran estacionalidad, con una variabilidad total del 0.22 ‰ y exhibiendo valores más altos durante verano-otoño, y más bajos en invierno-primavera. El carbonato procedente de goteos no estacionales muestra valores más altos de $\delta^{13}C$ comparado con los estacionales (−9.76 y −9.93 ‰ PDB, respectivamente). Una tasa de goteo más lenta provoca mayor desgasificación y justifica los valores más altos de $\delta^{13}C$ en esos goteos, con una variabilidad que asciende hasta el 0.42 ‰. Los valores bajos de $\delta^{13}C$ se registran cuando hay mayor actividad microbiana en el suelo, mayor productividad vegetal y más disponibilidad hídrica.

c) Paleoclimatic reconstruction

- ✓ La estalagmita ARTEMISA (cubre el período desde 262.7 a 217.9 ka, como indican las 24 dataciones U/Th), registró los cambios climáticos producidos durante la Terminación III (final del Estadio Isotópico Marino 8), por lo tanto exhibiendo gran sensibilidad a los cambios glacial-interglacial. La variabilidad en el $\delta^{13}C$ durante el transcurso de la Terminación marca dos eventos caracterizados por valores especialmente negativos: S8.2, durante 249-247.4 ka, y S8.1, durante 244.7-241 ka. Esos eventos se explican por debilitamientos en la AMOC durante MIS 8. El evento S8.1 se encuentra asimismo asociado a la entrada de agua dulce en el área fuente de humedad situada en el Atlántico norte.
- ✓ Ambos eventos de ARTEMISA exhiben similitudes con los eventos Heinrich 1 y 2, tras una comparación de la sucesión de eventos entre la T-III, T-II y T-I. Esas similitudes se basan en la intensidad de descargas de IRD, la dominancia de taxones semidesérticos y los cambios en el $\delta^{18}O$ de los foraminíferos bentónicos marinos. No obstante, en términos de nivel del mar e insolación, el evento S8.1 es más parecido al YD que al HS-1.
- ✓ La estalagmita ANDROMEDA, que cubre el período desde MIS 5 hasta MIS 3 (basado en 21 dataciones U/Th), exhibe sensibilidad a los cambios tanto orbitales como a escala milenial, como por ejemplo las oscilaciones D-O y/o los eventos Heinrich.
- ✓ Durante MIS 5, la variabilidad del $\delta^{18}O$ en ANDROMEDA está controlada por parámetros orbitales. El $\delta^{13}C$ muestra asimismo una respuesta terrestre a los eventos marinos fríos C26-C25-C24-C23, exhibiendo condiciones frio-áridas desde 118 hasta 105 ka. Además, se propone un final tardío para el periodo interglacial Eemiense en esta área, que llegaría hasta los 108.6-108.3 ka.
- ✓ Durante MIS 4 y 3, la variabilidad en $\delta^{18}O$ y $\delta^{13}C$ de ANDROMEDA se encuentra controlada por una mayor desgasificación del agua de goteo durante los períodos áridos, en concordancia con valores más altos de Mg/Ca. Asimismo, los valores del $\delta^{13}C$ durante el período desde 70 a 50 ka, indican que la respuesta a los débiles D-O 18 y 15 son dos eventos con forma de W, debido a la intensa respuesta registrada con valores más altos en el $\delta^{13}C$.
- ✓ Dos períodos se pueden diferenciar en el evento W más antiguo (~67-60 ka) de ANDROMEDA indicando condiciones frío-áridas hasta hace 63 ka, para pasar a condiciones húmedo-frías a partir de 63 ka. Asimismo, el evento W más jóven (~57-53 ka)

está en concordancia con un reforzamiento en los vientos alisios del NE (fase NAO+) que explicaría la aridez vista en los registros terrestres.

7.2. Future perspectives

The speleothemic paleorecords from Ejulve cave presented here open new possibilities to further research. One outstanding example is ANDROMEDA stalagmite. The period covered by that stalagmite (MIS 5 – MIS 3) is of great interest for the paleoclimate community, and we think that this record could help to understand events and mechanisms poorly known and scarcely examined in the terrestrial record (e.g. Heinrich events). Additionally, the study of other sampled stalagmites from Ejulve cave could help to reconstruct the paleoclimate during Mid-Late Pleistocene and Holocene in Western Mediterranean. In that way, the future lines of research could be resumed on:

- ✓ The chronology of ANDROMEDA stalagmite will be improved. Hence, we would be able to offer for the first time, at continental scale, an independent chronology for such D-O oscillations and Heinrich events. The opportunity to offer new tie points to anchor non-independent chronologies would be of great interest for the paleoclimate community. The importance of such tie points lies in the impossibility to reach those chronologies in some other records because of the limitations of the ^{14}C dating method, and in the uncertainty of other chronologies (e.g. layer counting on ice cores beyond MIS 3-4) that restricts discussions about leads and lags of concrete events.

- ✓ The intra-Heinrich variability should be further explored with higher resolution in the trace elements of ANDROMEDA. Heinrich events are still poorly known, and only some marine proxies (e.g. foraminifera) have been used to unravel the timing of these events. Here, we have an outstanding opportunity to explore the repercussion of the Heinrich events in the terrestrial realm and characterize their timing.

- ✓ Some cataclysmic events during late Pleistocene has been altered the climate in a worldwide scale, such as the volcanic eruptions. One of the most dramatic during the Quaternary (Toba, ~84 kyr) and one of the most important in Europe during last glacial cycle (Campi Flegrei, ~39 kyr) happened during the growth of ANDROMEDA. The exploration of any signal of this volcanic activity in the stalagmite would be interesting for a better understanding of the consequences of these events on the climate of Western Europe.

- ✓ We have an outstanding opportunity to explore the terrestrial expression of the changes in the North Atlantic

in a territory such as the Iberian Peninsula, that is closer to the source area of the Atlantic than other records in Europe, and therefore are less prone to exhibit fractionation along the air mass trajectory.

✓ The past climatic teleconnections have been a field of study poorly studied in Eurasia. The present dissertation has shown the response to anomalies in the North Atlantic in different locations of Europe (especially the Iberian Peninsula) but also other locations of SE Europe and the repercussion in the Asian Monsoon, that controls the wet periods in such areas thousands of km far from our study area. The timing of some wet periods has not been explored yet in a transect W-E such as Iberian Peninsula, Middle East (e.g. through the sapropels) and the intensity of the Asian Monsoons. The analysis of the mechanisms involved, leads and lags, would be of great interest.

✓ New speleothems from Ejulve cave, with a known chronology as a result of the internships spent in the University of Minnesota, holds new secrets waiting to be discovered about other exciting periods.

✓ Despite the exhaustive chapter dedicated to the monitoring of Ejulve cave and the exhaustive dataset presented there, by no means it will represent the last contribution to the present-day speleothemic dynamics of the cave. More geochemical data of drip waters and the mineralogy of the farmed carbonate precipitates are pushing to see the light, and would be interesting features to working with in the future.

✓ There is life beyond Ejulve cave! In spite of the several research lines that this cave is offering us, we still think so! New data from other caves within the Iberian Range could replicate some periods existent in Ejulve or, on the contrary, would contribute to the characterization and comprehension of other new periods of palaeoclimatic interest (e.g. two rare speleothems has been identified covering the Last Glacial Maximum).

References

de Abreu L., Shackleton N. J., Schönfeld J., Hall M. A. and Chapman M. R. (2003) Millennial-scale oceanic climate variability off the Western Iberian margin during the last two glacial periods. *Mar. Geol.* **196**, 1–20.

Affolter S., Häuselmann A. D., Fleitmann D., Häuselmann P. and Leuenberger M. (2015) Triple isotope (δD, δ17O, δ18O) study on precipitation, drip water and speleothem fluid inclusions for a Western Central European cave (NW Switzerland). *Quat. Sci. Rev.* **127**, 73–89.

Allen J. R. M. and Huntley B. (2009) Last Interglacial palaeovegetation, palaeoenvironments and chronology: a new record from Lago Grande di Monticchio, southern Italy. *Quat. Sci. Rev.* **28**, 1521–1538.

Alley R. B. (2000) The Younger Dryas cold interval as viewed from central Greenland. *Quat. Sci. Rev.* **19**, 213–226.

Alley R. B., Finkel R. C., Nishiizumi K., Anandakrishnan S., Shuman C. A., Mershon G., Zielinski G. A. and Mayewski P. A. (1995) Changes in continental and sea-salt atmospheric loadings in central Greenland during the most recent deglaciation: model-based estimates. *J. Glaciol.* **41**, 503–514.

Alley R. B., Marotzke J., Nordhaus W. D., Overpeck J. T., Peteet D. M., Pielke R. A., Pierrehumbert R. T., Rhines P. B., Stocker T. F., Talley L. D. and Wallace J. M. (2003) Abrupt Climate Change. *Science* **299**, 2005–2010.

Alley R. B., Meese D. A., Shuman C. A., Gow A. J., Taylor K. C., Grootes P. M., White J. W. C., Ram M., Waddington E. D., Mayewski P. A. and Zielinski G. A. (1993) Abrupt increase in Greenland snow accumulation at the end of the Younger Dryas event. *Nature* **362**, 527–529.

Allmendinger R. W., Cardozo N. and Fisher D. (2012) *Structural Geology Algorithms: Vectors and Tensors*.,

Alonso A., Floquet M., Mas R. and Meléndez A. (1993) Late Cretaceous carbonate platform: origin and evolution. In *Cretaceous carbonate platforms* (eds. J. A. . Simó, R. . Scott, and J. . Masse). AAPG Mem.

Alonso-Zarza A. M. and Martín-Pérez A. (2008) Dolomite in caves: Recent dolomite formation in oxic, non-sulfate environments. Castañar Cave, Spain. *Sediment. Geol.* **205**, 160–164.

Alonso-Zarza A. M., Martín-Pérez A., Martín-García R., Gil-Peña I., Meléndez A., Martínez-Flores E., Hellstrom J. and Muñoz-Barco P. (2011) Structural and

host rock controls on the distribution, morphology and mineralogy of speleothems in the Castañar Cave (Spain). *Geol. Mag.* **148**, 211–225.

Álvaro M., Capote R. and Vegas R. (1979) Un modelo de evolución geotectónica para la Cadena Celtibérica. *Acta Geológica Hispánica*, 172–177.

Angosto M. C. and Latorre J. L. (2000) Cavidades naturales del término municipal de Ejulve (Somontano turolense): datos espeleométricos y bioespeleológicos. *Teruel* **1**, 75–108.

Araguás-Araguás L., Froehlich K. and Rozanski K. (2000) Deuterium and oxygen-18 isotope composition of precipitation and atmospheric moisture. *Hydrol. Process.* **14**, 1341–1355.

Aranbarri J., González-Sampériz P., Valero-Garcés B., Moreno A., Gil-Romera G., Sevilla-Callejo M., García-Prieto E., Di Rita F., Mata M. P., Morellón M., Magri D., Rodríguez-Lázaro J. and Carrión J. S. (2014) Rapid climatic changes and resilient vegetation during the Lateglacial and Holocene in a continental region of south-western Europe. *Glob. Planet. Change* **114**, 50–65.

Aranburu A., Arriolabengoa M., Iriarte E., Giralt S., Yusta I., Martínez-Pillado V., del Val M., Moreno J. and Jiménez-Sánchez M. (2015) Karst landscape evolution in the littoral area of the Bay of Biscay (north Iberian Peninsula). *Quat. Int.* **364**, 217–230.

Arienzo M. M., Swart P. K., Pourmand A., Broad K., Clement A. C., Murphy L. N., Vonhof H. B. and Kakuk B. (2015) Bahamian speleothem reveals temperature decrease associated with Heinrich stadials. *Earth Planet. Sci. Lett.* **430**, 377–386.

Asmerom Y., Polyak V. J. and Burns S. J. (2010) Variable winter moisture in the southwestern United States linked to rapid glacial climate shifts. *Nat. Geosci.* **3**, 114–117.

Atsawawaranunt K., Comas-Bru L., Amirnezhad Mozhdehi S., Deininger M., Harrison S. P., Baker A., Boyd M., Kaushal N., Ahmad S. M., Ait Brahim Y., Arienzo M., Bajo P., Braun K., Burstyn Y., Chawchai S., Duan W., Hatvani I. G., Hu J., Kern Z., Labuhn I., Lachniet M., Lechleitner F. A., Lorrey A., Pérez-Mejías C., Pickering R., Scroxton N. and SISAL Working Group Members (2018) The SISAL database: a global resource to document oxygen and carbon isotope records from speleothems. *Earth Syst. Sci. Data* **10**, 1687–1713.

Audra P., Bigot J.-Y. and Mocochain L. (2002) Hypogenic caves in Provence (France). Specific features and sediments. *Speleogenesis Evol. Karst Aquifers*.

Audra P., Mocochain L., Bigot J. and Novécourt J. . (2009) Morphological indicators of speleogenesis: hypogenic speleogenesis. In *Hypogene speleogenesis and karst hydrogeology of artesian basins* (eds. A. Klimchouk and D. Ford). Ukrainian Institute of Speleology and Karstology. pp. 23–32.

Aurell M., Bádenas B., Casas A. and Alberto S. (2001) La Geología del Parque Cultural del río Martín. *Asoc. Parq. Cult. Río Martín*, 171.

Ayalon A., Bar-Matthews M. and Sass E. (1998) Rainfall-recharge relationships within a karstic terrain in the Eastern Mediterranean semi-arid region, Israel: δ 18O and δD characteristics. *J. Hydrol.* **207**, 18–31.

Baeza J., Torreano R. and Cerezuela M. (2000) Estudio para caracterizar, evaluar y proteger las aguas minerales y termales de una comunidad: Aragón. In (eds. J. López Geta and J. Pinuaga). Panorama actual de las Aguas Minerales y Minero-medicinales en España. Instituto Tecnológico Geominero de España. pp. 283–303.

Bajo P., Hellstrom J., Frisia S., Drysdale R., Black J., Woodhead J., Borsato A., Zanchetta G., Wallace M. W., Regattieri E. and Haese R. (2016) "Cryptic" diagenesis and its implications for speleothem geochronologies. *Quat. Sci. Rev.* **148**, 17–28.

Bakalowicz M. J., Ford D. C., Miller T. E., Palmer A. N. and Palmer M. V. (1987) Thermal genesis of dissolution caves in the Black Hills, South Dakota. *Geol. Soc. Am. Bull.* **99**, 729.

Baker A., Barnes W. L. and Smart P. L. (1997) Variations in the discharge and organic matter content of stalagmite drip waters in Lower Cave, Bristol. *Hydrol. Process.* **11**, 1541–1555.

Baker A., Bradley C., Phipps S. J., Fischer M., Fairchild I. J., Fuller L., Spötl C. and Azcurra C. (2012) Millennial-length forward models and pseudoproxies of stalagmite δ^{18}O: an example from NW Scotland. *Clim. Past Discuss.* **8**, 869–907.

Baker A., Flemons I., Andersen M. S., Coleborn K. and Treble P. C. (2016) What determines the calcium concentration of speleothem-forming drip waters? *Glob. Planet. Change* **143**, 152–161.

Baker A., Genty D., Dreybrodt W., Barnes W. L., Mockler N. J. and Grapes J. (1998) Testing theoretically predicted stalagmite growth rate with recent annually laminated samples: Implications for past stalagmite deposition. *Geochim. Cosmochim. Acta* **62**, 393–404.

Baldini J. U. L., McDermott F. and Fairchild I. J. (2006) Spatial variability in cave drip water hydrochemistry: Implications for stalagmite paleoclimate records. *Chem. Geol.* **235**, 390–404.

Ballesteros D., Jiménez-Sánchez M., Giralt S., García-Sansegundo J. and Meléndez-Asensio M. (2015) A multi-method approach for speleogenetic research on alpine karst caves. Torca La Texa shaft, Picos de Europa (Spain). *Geomorphology* **247**, 35–54.

Banner J. L., Guilfoyle A., James E. W., Stern L. A. and Musgrove M. (2007) Seasonal Variations in Modern Speleothem Calcite Growth in Central Texas, U.S.A. *J. Sediment. Res.* **77**, 615–622.

Bar-Matthews M., Ayalon A., Gilmour M. A., Matthews A. and Hawkesworth C. J. (2003) Sea-land oxygen isotopic relationships from planktonic foraminifera and speleothems in the Eastern Mediterranean region and their implication for paleorainfall during interglacial intervals. *Geochim. Cosmochim. Acta* **67**, 3181–3199.

Bar-Matthews M., Ayalon A., Kaufman A. and Wasserburg G. J. (1999) The eastern Mediterranean paleoclimate as a reflection of regional events: Soreq cave, Israel. *Earth Planet. Sci. Lett.* **166**, 85–95.

Bar-Matthews M., Ayalon A., Matthews A., Sass E. and Halicz L. (1996) Carbon and oxygen isotope study of the active water-carbonate system in a karstic Mediterranean cave: Implications for paleoclimate research in semiarid regions. *Geochim. Cosmochim. Acta* **60**, 337–347.

Bartolomé M. (2016) La Cueva del Caserío de Seso (Pirineo Central): espeleogénesis, dinámica actual y reconstrucción paleoambiental de los últimos 13.000 años. Tesis doctoral, Universidad de Zaragoza.

Bartolomé M, Moreno A, Sancho C, Stoll H., Cacho I, Spötl C, Belmonte A., Edwards L., Cheng H and Hellstrom J. (2015) Hydrological change in Southern Europe responding to increasing North Atlantic overturning during Greenland Stadial 1. *Proc. Natl. Acad. Sci.* **112**, 6568–6572.

Bartolomé M., Sancho C., Moreno A., Oliva-Urcia B., Belmonte á., Bastida J., Cheng H. and Edwards R. L. (2015) Upper Pleistocene interstratal piping-cave speleogenesis: The Seso Cave System (Central Pyrenees, Northern Spain). *Geomorphology* **228**, 335–344.

Bazin L., Landais A., Lemieux-Dudon B., Toyé Mahamadou Kele H., Veres D., Parrenin F., Martinerie P., Ritz C., Capron E., Lipenkov V., Loutre M.-F., Raynaud D., Vinther B., Svensson A., Rasmussen S. O., Severi M., Blunier T., Leuenberger M., Fischer H., Masson-Delmotte V., Chappellaz J. and Wolff E. (2013) An optimized multi-proxy, multi-site Antarctic ice and gas orbital chronology (AICC2012). *Clim. Past* **9**, 1715–1731.

van Beynen P. and Febbroriello P. (2006) Seasonal isotopic variability of precipitation and cave drip water at Indian Oven Cave, New York. *Hydrol. Process.* **20**, 1793–1803.

Bintanja R., van de Wal R. S. W. and Oerlemans J. (2005) Modelled atmospheric temperatures and global sea levels over the past million years. *Nature* **437**, 125–128.

Birner B., Hodell D. A., Tzedakis P. C. and Skinner L. C. (2016) Similar millennial climate variability on the Iberian margin during two early Pleistocene glacials and MIS 3. *Paleoceanography* **31**, 203–217.

Boch R., Cheng H., Spötl C., Edwards R. L., Wang X. and Häuselmann P. (2011) NALPS: a precisely dated European climate record 120–60 ka. *Clim. Past Discuss.* **7**, 1049–1072.

Boch R, Spötl C. and Frisia S. (2011) Origin and palaeoenvironmental significance of lamination in stalagmites from Katerloch Cave, Austria: Origin of lamination in stalagmites. *Sedimentology* **58**, 508–531.

Boch R., Spötl C. and Kramers J. (2009) High-resolution isotope records of early Holocene rapid climate change from two coeval stalagmites of Katerloch Cave, Austria. *Quat. Sci. Rev.* **28**, 2527–2538.

Borsato A., Frisia S. and Miorandi R. (2015) Carbon dioxide concentration in temperate climate caves and parent soils over an altitudinal gradient and its influence on speleothem growth and fabrics: Carbon Dioxide Concentration in Temperate Climate Caves and Soils. *Earth Surf. Process. Landf.* **40**, 1158–1170.

Borsato A., Quinif Y., Bini A. and Dublyansky Y. (2003) Open-system alpine speleothems: implications for U-series dating and paleoclimate reconstructions. *Studi Trentini Sci. Nat. Acta Geol.* **80**, 71–83.

Brauer A., Haug G. H., Dulski P., Sigman D. M. and Negendank J. F. W. (2008) An abrupt wind shift in western Europe at the onset of the Younger Dryas cold period. *Nat. Geosci.* **1**, 520–523.

Breitenbach S. F. M., Adkins J. F., Meyer H., Marwan N., Kumar K. K. and Haug G. H. (2010) Strong influence of water vapor source dynamics on stable isotopes in precipitation observed in Southern Meghalaya, NE India. *Earth Planet. Sci. Lett.* **292**, 212–220.

Brewer S., Guiot J., Sánchez-Goñi M. F. and Klotz S. (2008) The climate in Europe during the Eemian: a multi-method approach using pollen data. *Quat. Sci. Rev.* **27**, 2303–2315.

Broecker W. S., Peteet D. and Rind D. (1985) Does the ocean-atmosphere system have more than one stable mode of operation? *Nature* **315**, 21–26.

Burns S., Fleitmann D., Matter A., Kramers J. and Al-Subbary A. A. (2003) Indian Ocean climate and an absolute chronology over Dansgaard/Oeschger events 9 to 13. *Science* **301**, 1365–1367.

Burns S. J. (2002) A 780-year annually resolved record of Indian Ocean monsoon precipitation from a speleothem from south Oman. *J. Geophys. Res.* **107**.

Caballero E., Jiménez De Cisneros C. and Reyes E. (1996) A stable isotope study of cave seepage waters. *Appl. Geochem.* **11**, 583–587.

Cacho I., Grimalt J. O., Pelejero C., Canals M., Sierro F. J., Flores J. A. and Shackleton N. J. (1999) Dansgaard-Oeschger and Heinrich event imprints in Alboran Sea temperatures. *Paleoceanography* **14**, 698–705.

Caddeo G. A., Railsback L. B., De Waele J. and Frau F. (2015) Stable isotope data as constraints on models for the origin of coralloid and massive speleothems: The interplay of substrate, water supply, degassing, and evaporation. *Sediment. Geol.* **318**, 130–141.

Cai Y., Fung I. Y., Edwards R. L., An Z., Cheng H., Lee J.-E., Tan L., Shen C.-C., Wang X., Day J. A., Zhou W., Kelly M. J. and Chiang J. C. H. (2015) Variability of stalagmite-inferred Indian monsoon precipitation over the past 252,000 y. *Proc. Natl. Acad. Sci.* **112**, 2954–2959.

Calaforra J. . and Berrocal J. A. (2008) *El Karst de Andalucía, Geoespeleología, Bioespeleología y Presencia Humana*. Consejería de Medio Ambiente de la Junta de Andalucía., Sevilla.

Camarero J. J., Gazol A., Tardif J. C. and Conciatori F. (2015) Attributing forest responses to global-change drivers: limited evidence of a CO_2 -fertilization effect in Iberian pine growth. *J. Biogeogr.* **42**, 2220–2233.

Canérot J. (1982) Ibérica central-Maestrazgo. In *El Cretácico de España* (ed. A. García). Universidad Complutense de Madrid. pp. 273–344.

Canérot J. (1974) Recherches géologiques aux confins des chaines Ibérique et Catalane. Tesis doctoral.

Capron E., Landais A., Chappellaz J., Schilt A., Buiron D., Dahl-Jensen D., Johnsen S. J., Jouzel J., Lemieux-Dudon B., Loulergue L., Leuenberger M., Masson-Delmotte V., Mayer H., Oerter H. and Stenni B. (2010) Millennial and sub-millennial scale climatic variations recorded in polar ice cores over the last glacial period. *Clim Past Discuss* **6**, 135–183.

Cardozo N. and Allmendinger R. (2013) Spherical projections with OSXStereonet. *Comput. Geosci.*, 193–205.

Carlson A. E. (2008) Why there was not a Younger Dryas-like event during the Penultimate Deglaciation. *Quat. Sci. Rev.* **27**, 882–887.

Carolin S. A., Cobb K. M., Lynch-Stieglitz J., Moerman J. W., Partin J. W., Lejau S., Malang J., Clark B., Tuen A. A. and Adkins J. F. (2016) Northern Borneo stalagmite records reveal West Pacific hydroclimate across MIS 5 and 6. *Earth Planet. Sci. Lett.* **439**, 182–193.

Castellano L., Fernández M., García F., Gil L., Gordillo J., Mallén D., Porcel E. and Royo J. (2015) *Cavidades de Teruel. 25 cuevas y simas de la provincia*., Centro de Estudios Espeleológicos Turolenses, Zaragoza.

Celle-Jeanton H., Travi Y. and Blavoux B. (2001) Isotopic typology of the precipitation in the Western Mediterranean Region at three different time scales. *Geophys. Res. Lett.* **28**, PP. 1215-1218.

Channell J. E. T., Hodell D. A., Romero O., Hillaire-Marcel C., de Vernal A., Stoner J. S., Mazaud A. and Röhl U. (2012) A 750-kyr detrital-layer stratigraphy for the North Atlantic (IODP Sites U1302–U1303, Orphan Knoll, Labrador Sea). *Earth Planet. Sci. Lett.* **317**–**318**, 218–230.

Chapman J. B., Ingraham N. L. and Hess J. W. (1992) Isotopic investigation of infiltration and unsaturated zone flow processes at Carlsbad Cavern, New Mexico. *J. Hydrol.* **133**, 343–363.

Charles C. D., Rind D., Jouzel J., Koster R. D. and Fairbanks R. G. (1994) Glacial-Interglacial Changes in Moisture Sources for Greenland: Influences on the Ice Core Record of Climate. *Science* **263**, 508–511.

Chen J. H., Lawrence Edwards R. and Wasserburg G. J. (1986) 238U,234U and232Th in seawater. *Earth Planet. Sci. Lett.* **80**, 241–251.

Cheng H., Edwards L. R., Hoff J., Gallup C. D., Richards D. A. and Asmerom Y. (2000) The half-lives of uranium-234 and thorium-230. *Chem. Geol.* **169**, 17–33.

Cheng H., Edwards R. L., Broecker W. S., Denton G. H., Kong X., Wang Y., Zhang R. and Wang X. (2009) Ice Age Terminations. *Science* **326**, 248–252.

Cheng H., Edwards R. L., Sinha A., Spötl C., Yi L., Chen S., Kelly M., Kathayat G., Wang X., Li X., Kong X., Wang Y., Ning Y. and Zhang H. (2016) The Asian monsoon over the past 640,000 years and ice age terminations. *Nature* **534**, 640–646.

Cheng H., Edwards R. L., Wang Y., Kong X., Ming Y., Kelly M. J., Wang X. and Gallup C. D. (2006) A penultimate glacial monsoon record from Hulu Cave and two-phase glacial terminations. *Geology* **34**, 217–220.

Cheng H., Lawrence Edwards R., Shen C.-C., Polyak V. J., Asmerom Y., Woodhead J., Hellstrom J., Wang Y., Kong X., Spötl C., Wang X. and Calvin Alexander E. (2013) Improvements in 230Th dating, 230Th and 234U half-life values, and U–Th isotopic measurements by multi-collector inductively coupled plasma mass spectrometry. *Earth Planet. Sci. Lett.* **371**–**372**, 82–91.

Clark and Fritz (1997) *Environmental Isotopes in Hydrogeology*., Lewis Publishers, New York.

Clark P. U., Dyke A. S., Shakun J. D., Carlson A. E., Clark J., Wohlfarth B., Mitrovica J. X., Hostetler S. W. and McCabe A. M. (2009) The Last Glacial Maximum. *Science* **325**, 710–714.

Clement A. C. and Peterson L. C. (2008) Mechanisms of abrupt climate change of the last glacial period. *Rev. Geophys.* **46**.

Cobb K. M., Adkins J. F., Partin J. W. and Clark B. (2007) Regional-scale climate influences on temporal variations of rainwater and cave dripwater oxygen isotopes in northern Borneo. *Earth Planet. Sci. Lett.* **263**, 207–220.

Coleman M. L., Shepherd T. J., Durham J. J., Rouse J. E. and Moore G. R. (1982) Reduction of water with zinc for hydrogen isotope analysis. *Anal. Chem.* **54**, 993–995.

Comas-Bru L. and McDermott F. (2015) Data-model comparison of soil–water δ18O at a temperate site in N. Spain with implications for interpreting speleothem δ18O. *J. Hydrol.* **530**, 216–224.

Combourieu Nebout N., Peyron O., Dormoy I., Desprat S., Beaudouin C., Kotthoff U. and Marret F. (2009) Rapid climatic variability in the west Mediterranean during the last 25 000 years from high resolution pollen data. *Clim. Past* **5**, 503–521.

Combourieu Nebout N., Turon J. L., Zahn R., Capotondi L., Londeix L. and Pahnke K. (2002) Enhanced aridity and atmospheric high-pressure stability over the western Mediterranean during the North Atlantic cold events of the past 50 k.y. *Geology* **30**, 863–866.

Coplen T. B. (2007) Calibration of the calcite–water oxygen-isotope geothermometer at Devils Hole, Nevada, a natural laboratory. *Geochim. Cosmochim. Acta* **71**, 3948–3957.

Coplen T. B., Kendall C. and Hopple J. (1983) Comparison of stable isotope reference samples. *Nature* **302**, 236–238.

Cortijo E., Labeyrie L., Vidal L., Vautravers M., Chapman M., Duplessy J.-C., Elliot M., Arnold M., Turon J.-L. and Auffret G. (1997) Changes in sea surface hydrology associated with Heinrich event 4 in the North Atlantic Ocean between 40° and 60°N. *Earth Planet. Sci. Lett.* **146**, 29–45.

Cowan B., Osborne M. and Banner J. (2013) Temporal Variability of Cave-Air CO2 in Central Texas. *J. Cave Karst Stud.*, 38–50.

Craig H. (1961) Isotopic Variations in Meteoric Waters. *Science* **133**, 1702–1703.

Cruz F. W., Burns S. J., Karmann I., Sharp W. D., Vuille M., Cardoso A. O., Ferrari J. A., Silva Dias P. L. and Viana O. (2005a) Insolation-driven changes in atmospheric circulation over the past 116,000 years in subtropical Brazil. *Nature* **434**, 63–66.

Cruz F. W., Burns S., Karmann I., Sharp W. D., Vuille M. and Ferrari J. A. (2006) A stalagmite record of changes in atmospheric circulation and soil processes in

the Brazilian subtropics during the Late Pleistocene. *Quat. Sci. Rev.* **25**, 2749–2761.

Cruz F. W., Karmann I., Viana O., Burns S. J., Ferrari J. A., Vuille M., Sial A. N. and Moreira M. Z. (2005b) Stable isotope study of cave percolation waters in subtropical Brazil: Implications for paleoclimate inferences from speleothems. *Chem. Geol.* **220**, 245–262.

Cruz F. W., Vuille M., Burns S. J., Wang X., Cheng H., Werner M., Lawrence Edwards R., Karmann I., Auler A. S. and Nguyen H. (2009) Orbitally driven east–west antiphasing of South American precipitation. *Nat. Geosci.* **2**, 210–214.

Cullen H., deMenocal P., Hemming S. R., Brown F. H., Guilderson T. P. and Sirocko F. (2000) Climate change and the collapse of the Akkadian empire: evidence from the deep sea. *Geology* **28**, 379–382.

Cuthbert M. O., Baker A., Jex C. N., Graham P. W., Treble P. C., Andersen M. S. and Ian Acworth R. (2014) Drip water isotopes in semi-arid karst: Implications for speleothem paleoclimatology. *Earth Planet. Sci. Lett.* **395**, 194–204.

Dansgaard W. (1964) Stable isotopes in precipitation. *Tellus* **16**, 436–468.

Dansgaard W. (1961) *The isotopic composition of natural waters*., Reitzel.

Darling W. G., Bath A. H., Gibson J. and Rozanski K. (2006) Isotopes in water. In *Isotopes in Paleaeoenvironmental Research* Developments in Paleoenvironmental Research. Springer. pp. 1–66.

Day C. C. and Henderson G. M. (2011) Oxygen isotopes in calcite grown under cave-analogue conditions. *Geochim. Cosmochim. Acta* **75**, 3956–3972.

Deaney E. L., Barker S. and van de Flierdt T. (2017) Timing and nature of AMOC recovery across Termination 2 and magnitude of deglacial CO2 change. *Nat. Commun.* **8**, 14595.

Demény A., Kern Z., Czuppon G., Németh A., Leél-Őssy S., Siklósy Z., Lin K., Hu H.-M., Shen C.-C., Vennemann T. W. and Haszpra L. (2017) Stable isotope compositions of speleothems from the last interglacial – Spatial patterns of climate fluctuations in Europe. *Quat. Sci. Rev.* **161**, 68–80.

Denniston R. F., González L. A., Asmerom Y., Baker R. G., Reagan M. K. and Bettis E. A. (1999) Evidence for increased cool season moisture during the middle Holocene. *Geology* **27**, 815.

Denniston R. F., Houts A. N., Asmerom Y., Wanamaker A. D., Haws J. A., Polyak V. J., Thatcher D. L., Altan-Ochir S., Borowske A. C., Breitenbach S. F. M., Ummenhofer C. C., Regala F. T., Benedetti M. M. and Bicho N. (2017) A Stalagmite Test of North Atlantic SST and Iberian Hydroclimate Linkages over the Last Two Glacial Cycles. *Clim. Past Discuss.*, 1–39.

Denton G. H., Alley R. B., Comer G. C. and Broecker W. S. (2005) The role of seasonality in abrupt climate change. *Quat. Sci. Rev.* **24**, 1159–1182.

Denton G. H., Anderson R. F., Toggweiler J. R., Edwards R. L., Schaefer J. M. and Putnam A. E. (2010) The Last Glacial Termination. *Science* **328**, 1652–1656.

Desprat S., Sanchez Goni M. F., Naughton F., Turon J. L., Duprat J., Malaize B., Cortijo E., Peypouquet J. P., Sirocko F., Claussen M., Goni M. F. S. and Litt T. (2007) Climate variability of the last five isotopic interglacials: Direct land-sea-ice correlation from the multiproxy analysis of North-Western Iberian margin deep-sea cores. In *Developments in Quaternary Science* Elsevier. pp. 375–386.

Desprat S., Sánchez Goñi M. F., Turon J.-L., Duprat J., Malaizé B. and Peypouquet J.-P. (2006) Climatic variability of Marine Isotope Stage 7: direct land–sea–ice correlation from a multiproxy analysis of a north-western Iberian margin deep-sea core. *Quat. Sci. Rev.* **25**, 1010–1026.

Diaz M. F., Perez F., Rodriguez J., Castano S. and Araguas-Araguas L. (2007) Factors controlling the stable isotopic composition of recent precipitation in Spain.

Dietzel M., Tang J., Leis A. and Köhler S. J. (2009) Oxygen isotopic fractionation during inorganic calcite precipitation — Effects of temperature, precipitation rate and pH. *Chem. Geol.* **268**, 107–115.

Dodero A., Bartolomé M., Sancho C., Moreno A., Oliva-Urcia B., Meléndez A., Sanz E. and Edwards L. (2015) Incisión fluvial a partir del conjunto multinivel de cuevas de La Galiana (Parque Natural del río Lobos, Soria). *Cuaternario Geomorfol.*, 4.

Domínguez-Villar D., Fairchild I. J., Baker A., Wang X., Edwards L. R. and Cheng H. (2009) Oxygen isotope precipitation anomaly in the North Atlantic region during the 8.2 ka event. *Geology* **37**, 1095–1098.

Domínguez-Villar D., Krklec K., Pelicon P., Fairchild I. J., Cheng H. and Edwards L. R. (2017) Geochemistry of speleothems affected by aragonite to calcite

recrystallization – Potential inheritance from the precursor mineral. *Geochim. Cosmochim. Acta* **200**, 310–329.

Domínguez-Villar D., Wang X., Cheng H., Martín-Chivelet J. and Edwards R. L. (2008) A high-resolution late Holocene speleothem record from Kaite Cave, northern Spain: δ18O variability and possible causes. *Quat. Int.* **187**, 40–51.

Dorale J. A., Edwards R. L., Ito E. and González L. A. (1998) Climate and vegetation history of the midcontinent from 75 to 25 ka: a speleothem record from Crevice Cave, Missouri, USA. *Science* **282**, 1871–1874.

Dorale J. A., Edwards R. L. and Onac B. P. (2002) Stable isotopes as environmental indicators in speleothems. In *Karst processes and the carbon cycle* (eds. Y. Daoxian and Z. Cheng). Geological Publishing House, Beijing, China. p. 107.120.

Dorale J. A., Gonzalez L. A., Reagan M. K., Pickett D. A., Murrell M. T. and Baker R. G. (1992) A High-Resolution Record of Holocene Climate Change in Speleothem Calcite from Cold Water Cave, Northeast Iowa. *Science* **258**, 1626–1630.

Dorale J. A. and Liu Z. (2009) Limitations of Hendy test criteria in judging the paleoclimatic suitability of speleothems and the need for replication. *J. Cave Karst Stud.* **71**, 73–80.

Dorale J. A., Onac B. P., Fornos J. J., Gines J., Gines A., Tuccimei P. and Peate D. W. (2010) Sea-Level Highstand 81,000 Years Ago in Mallorca. *Science* **327**, 860–863.

Dotsika E., Lykoudis S. and Poutoukis D. (2010) Spatial distribution of the isotopic composition of precipitation and spring water in Greece. *Glob. Planet. Change* **71**, 141–149.

Dreybrodt W. (1999) Chemical kinetics, speleothem growth and climate. *Boreas* **28**, 347–356.

Dreybrodt W. and Scholz D. (2011) Climatic dependence of stable carbon and oxygen isotope signals recorded in speleothems: From soil water to speleothem calcite. *Geochim. Cosmochim. Acta* **75**, 734–752.

Drysdale R. N., Hellstrom J. C., Zanchetta G., Fallick A. E., Sanchez Goni M. F., Couchoud I., McDonald J., Maas R., Lohmann G. and Isola I. (2009) Evidence for Obliquity Forcing of Glacial Termination II. *Science* **325**, 1527–1531.

Drysdale R. N., Zanchetta G., Hellstrom J. C., Fallick A. E., McDonald J. and Cartwright I. (2007) Stalagmite evidence for the precise timing of North Atlantic cold events during the early last glacial. *Geology* **35**, 77–80.

Duan W., Ruan J., Luo W., Li T., Tian L., Zeng G., Zhang D., Bai Y., Li J., Tao T., Zhang P., Baker A. and Tan M. (2016) The transfer of seasonal isotopic variability between precipitation and drip water at eight caves in the monsoon regions of China. *Geochim. Cosmochim. Acta* **183**, 250–266.

Dublyansky Y. (2012) *Hydrothermal Caves. Encyclopedia of caves*., Elsevier.

Dublyansky Y. (2013) Karstification of geothermal waters. In *Schroder, J., Frumkin, A., (Ed.). Treatise of geomorphology* Academic Press, San Diego, CA. pp. 57–71.

Dumitru O. A., Forray F. L., Fornós J. J., Ersek V. and Onac B. P. (2017) Water isotopic variability in Mallorca: a path to understanding past changes in hydroclimate: Stable Isotope Variability in Mallorcan Waters. *Hydrol. Process.* **31**, 104–116.

Dumitru O. A., Onac B. P., Polyak V. J., Wynn J. G., Asmerom Y. and Fornós J. J. (2018) Climate variability in the western Mediterranean between 121 and 67 ka derived from a Mallorcan speleothem record. *Palaeogeogr. Palaeoclimatol. Palaeoecol.* **506**, 128–138.

Durán J. (1996) Los sistemas kársticos de la provincia de Málaga y su evolución: contribución al conocimiento paleoclimático del Cuaternario en el Mediterráneo occidental. Universidad Complutense de Madrid.

Durán J. ., Grün R. and Ford D. . (1993) Dataciones geocronológicas absolutas (métodos ESR y Series de Uranio) en la Cueva de Nerja y su entorno. Implicaciones evolutivas, paleoclimáticas y neosismotectónicas. *Trab. Sobre Cueva Nerja* **3**, 233–248.

Durán J. J., López Martínez J., Dallai L., Bruschi G., Caballero E., Jiménez de Cisneros C. and Julià R. (1999) Palaeoenvironmental reconstruction based on a detailed stable isotope analysis and dating of a Holocene speleothem from Valporquero Cave, Northern Spain. *Geogaceta* **27**, 63–66.

Durán J. and López J. (1989) *El karst en España*., Sociedad Española de Geomorfología.

Edwards R., Gallup C. and Cheng H. (2003) Uranium-series Dating of Marine and Lacustrine Carbonates. In *Uranium-series geochemistry* Reviews in

mineralogy and geochemistry. Geochemical society and mineralogical society of America. pp. 363–405.

Edwards R. L., Chen J. H. and Wasserburg G. J. (1987) 238U-234U-230Th-232Th systematics and the precise measurements of time over the past 500.000 years. *Earth Planet. Sci. Lett.* **81**, 175–192.

Elliot M., Labeyrie L. and Duplessy J. C. (2002) Changes in North Atlantic deep-water formation associated with the Dansgaard-Oeschger temperature oscillations (10-60 ka). *Quat. Sci. Rev.* **21**, 1153–1165.

Even H., Carmi I., Magaritz M. and Gerson R. (1986) Timing the transport of water through the upper vadose zone in a Karstic system above a cave in Israel. *Earth Surf. Process. Landf.* **11**, 181–191.

Eynaud F., de Abreu L., Voelker A., Schönfeld J., Salgueiro E., Turon J.-L., Penaud A., Toucanne S., Naughton F., Sánchez Goñi M. F., Malaizé B. and Cacho I. (2009) Position of the Polar Front along the western Iberian margin during key cold episodes of the last 45 ka: tracking the PF along the Western Iberian Margin. *Geochem. Geophys. Geosystems* **10**, n/a-n/a.

Fairchild I. J. and Baker A. (2012) *Speleothem Science: From Process to Past Environments*., John Wiley & Sons.

Fairchild I. J., Borsato A., Tooth A. F., Frisia S., Hawkesworth C. J., Huang Y. M., McDermott F. and Spiro B. (2000) Controls on trace element (Sr-Mg) compositions of carbonate cave waters: implications for speleothem climatic records. *Chem. Geol.* **166**, 255–269.

Fairchild I, Smith C., Baker A, Fuller L, Spötl C, Mattey D and McDermott F (2006) Modification and preservation of environmental signals in speleothems. *Earth-Sci. Rev.* **75**, 105–153.

Fairchild I, Smith C., Baker A, Fuller L, Spötl C, Mattey D and McDermott F (2006) Modification and preservation of environmental signals in speleothems. *Earth-Sci. Rev.* **75**, 105–153.

Feng F., Li Z., Zhang M., Jin S. and Dong Z. (2013) Deuterium and oxygen 18 in precipitation and atmospheric moisture in the upper Urumqi River Basin, eastern Tianshan Mountains. *Environ. Earth Sci.* **68**, 1199–1209.

Feng W., Banner J. L., Guilfoyle A. L., Musgrove M. and James E. W. (2012) Oxygen isotopic fractionation between drip water and speleothem calcite: A 10-year monitoring study, central Texas, USA. *Chem. Geol.* **304**–**305**, 53–67.

Feng W., Casteel R. C., Banner J. L. and Heinze-Fry A. (2014) Oxygen isotope variations in rainfall, drip-water and speleothem calcite from a well-ventilated cave in Texas, USA: Assessing a new speleothem temperature proxy. *Geochim. Cosmochim. Acta* **127**, 233–250.

Fleitmann D., Burns S. J., Mangini A., Mudelsee M., Kramers J., Villa I., Neff U., Al-Subbary A. A., Buettner A., Hippler D. and Matter A. (2007) Holocene ITCZ and Indian monsoon dynamics recorded in stalagmites from Oman and Yemen (Socotra). *Quat. Sci. Rev.* **26**, 170–188.

Fleitmann D., Burns S., Mudelsee M., Neff U., Kramers J., Mangini A. and Matter A. (2003) Holocene forcing of the Indian Monsoon recorded in a stalagmite from Southern Oman. *Science* **300**, 1737–1739.

Fleitmann D., Cheng H., Badertscher S., Edwards L. R., Mudelsee M., Göktürk O. M., Fankhauser A., Pickering R., Raible C. C., Matter A., Kramers J. and Tüysüz O. (2009) Timing and climatic impact of Greenland interstadials recorded in stalagmites from northern Turkey. *Geophys Res Lett* **36**, 1–5.

Fletcher W. J. and Sánchez Goñi M. F. (2008) Orbital- and sub-orbital-scale climate impacts on vegetation of the western Mediterranean basin over the last 48,000 yr. *Quat. Res.* **70**, 451–464.

Fletcher W. J., Sánchez Goñi M. F., Allen J. R. M., Cheddadi R., Combourieu-Nebout N., Huntley B., Lawson I., Londeix L., Magri D., Margari V., Müller U. C., Naughton F., Novenko E., Roucoux K. and Tzedakis P. C. (2010) Millennial-scale variability during the last glacial in vegetation records from Europe. *Quat. Sci. Rev.* **29**, 2839–2864.

Flückiger J., Knutti R. and White J. W. C. (2006) Oceanic processes as potential trigger and amplifying mechanisms for Heinrich events: oceanic trigger for Heinrich events. *Paleoceanography* **21**. Available at: http://doi.wiley.com/10.1029/2005PA001204 [Accessed May 24, 2018].

Follieri M., Magri D. and Sadori L. (1988) 250 000-year pollen record from Valle di Castiglione (Roma). *Pollen Spores* **30**, 329–356.

Ford D. C. and Williams P. (2007) *Karst hydrogeology and geomorphology*., John Wiley & Sons.

Forti P., Galdenzi S. and Sarbu S. M. (2002) The hypogenic caves: a powerful tool for the study of seeps and their environmental effects. *Cont. Shelf Res.* **22**, 2373–2386.

Fricke H. C. and O'Neil J. R. (1999) The correlation between 18O/16O ratios of meteoric water and surface temperature: its use in investigating terrestrial climate change over geologic time. *Earth Planet. Sci. Lett.* **170**, 181–196.

Friedman I. and O'Neil J. R. (1977) *Compilation of stable isotope fractionation factors of geochemical interest*., U.S. G.P.O.

Friedman I., Smith G. I., Gleason J. D., Warden A. and Harris J. M. (1992) Stable isotope composition of waters in southeastern California 1. Modern precipitation. *J. Geophys. Res.* **97**, 5795.

Frigola J., Moreno A., Cacho I., Canals M., Sierro F. J., Flores J. A. and Grimalt J. O. (2008) Evidence of abrupt changes in Western Mediterranean Deep Water circulation during the last 50kyr: A high-resolution marine record from the Balearic Sea. *Quat. Int.* **181**, 88–104.

Frisia S. (2015) Microstratigraphic logging of calcite fabrics in speleothems as tool for palaeoclimate studies. *Int. J. Speleol.* **44**, 1.

Frisia, S. and Borsato, A. (2010) Karst. In *Carbonates in continental settings. Facies, environments and processes. Developments In Sedimentology 61.* (eds. Alonso-Zarza, A.M and Tanner, L.H.). Elsevier, Amsterdam. pp. 269–318.

Frisia S., Borsato A., Fairchild I. J. and McDermott F. (2000) Calcite Fabrics, Growth Mechanisms, and Environments of Formation in Speleothems from the Italian Alps and Southwestern Ireland. *J. Sediment. Res.* **70**, 1183–1196.

Frisia S., Borsato A., Fairchild I. J., McDermott F. and Selmo E. M. (2002) Aragonite-Calcite Relationships in Speleothems (Grotte De Clamouse, France): Environment, Fabrics, and Carbonate Geochemistry. *J. Sediment. Res.* **72**, 687–699.

Frisia S., Borsato A. and Hellstrom J. (2018) High spatial resolution investigation of nucleation, growth and early diagenesis in speleothems as exemplar for sedimentary carbonates. *Earth-Sci. Rev.* **178**, 68–91.

Frisia S., Fairchild I. J., Fohlmeister J., Miorandi R., Spötl C. and Borsato A. (2011) Carbon mass-balance modelling and carbon isotope exchange processes in dynamic caves. *Geochim. Cosmochim. Acta* **75**, 380–400.

Frohlich, Gibson, J.J and Aggarwal, P.K. (2002) Deuterium excess in precipitation and its climatological significance. In Proceedings of Study of Environmental Change using Isotope Techniques. IAEA, Vienna. pp. 54–66.

Fuller, Baker, A., Fairchild, J., Spotl, C. and Marca-Bell, A (2008) Isotope hydrology of dripwaters in a Scottish cave and implications for stalagmite palaeoclimate research. *Hydrol. Earth Syst. Sci. Discuss.* **5**, 547–577.

Gat J. R., Bowser C. J. and Kendall C. (1994) The contribution of evaporation from the Great Lakes to the continental atmosphere: estimate based on stable isotope data. *Geophys. Res. Lett.* **21**, 557–560.

Gázquez F., Calaforra J. M., Rodríguez-Estrella T., Ros A., Llamusí J. L. and Sánchez J. (2017) Evidence for Regional Hypogene Speleogenesis in Murcia (SE Spain). In *Hypogene Karst Regions and Caves of the World* (eds. A. Klimchouk, A. N. Palmer, J. De Waele, A. S. Auler, and P. Audra). Springer International Publishing, Cham. pp. 85–97.

Gázquez F., Calaforra J. M., Ros A., Llamusí J. . and Sánchez J. (2016) Hypogenic morphologies and speleothems in caves in the Murcia Region, southeastern Spain. In *Proceedings of deepkarst 2016: origins, resources, and management of hypogene karst* (eds. T. Chavez and P. Reehling). National cave and karst research institute, Carlsbad, NM. pp. 53–60.

Gázquez F., Calaforra J.-M., Forti P., De Waele J. and Sanna L. (2015) The role of condensation in the evolution of dissolutional forms in gypsum caves: Study case in the karst of Sorbas (SE Spain). *Geomorphology* **229**, 100–111.

Gázquez F., Columbu A., De Waele J., Breitenbach S., Huang C., Shen C., Lu Y., Vautravers M. and Hodell D. (2018) Quantification of paleo-aquifer changes using clumped isotopes in subaqueous carbonate speleothems. *Chem. Geol.*

Genty D., Baker A., Massault M., Proctor C., Gilmour M., Pons-Branchu E. and Hamelin B. (2001a) Dead carbon in stalagmites: carbonate bedrock paleodissolution vs. ageing of soil organic matter. Implications for 13C variations in speleothems. *Geochim. Cosmochim. Acta* **65**, 3443–3457.

Genty D., Baker A. and Vokal B. (2001b) Intra- and inter-annual growth rate of modern stalagmites. *Chem. Geol.* **176**, 191–212.

Genty D., Blamart D., Ghaleb B., Plagnes V., Causse C., Bakalowicz M., Zouari K., Chkir N., Hellstrom J. and Wainer K. (2006a) Timing and dynamics of the last deglaciation from European and North African δ13C stalagmite profiles—

comparison with Chinese and South Hemisphere stalagmites. *Quat. Sci. Rev.* **25**, 2118–2142.

Genty D., Blamart D., Ghaleb B., Plagnes V., Causse C., Bakalowicz M., Zouari K., Chkir N., Hellstrom J., Wainer K. and Bourges F. (2006b) Timing and dynamics of the last deglaciation from European and North African d13C stalagmite profiles - comparison with Chinese and South Hemisphere stalagmites. *Quat. Sci. Rev.* **25**, 2118–2142.

Genty D., Blamart D., Ouahdi R., Gilmour M. A., Baker A., Jouzel J. and Van-Exter S. (2003) Precise dating of Dansgaard-Oeschger climate oscillation in western Europe from stalagmite data. *Nature* **421**, 833–837.

Genty D., Combourieu-Nebout N., Peyron O., Blamart D., Wainer K., Mansuri F., Ghaleb B., Isabello L., Dormoy I., von Grafenstein U., Bonelli S., Landais A. and Brauer A. (2010) Isotopic characterization of rapid climatic events during OIS3 and OIS4 in Villars Cave stalagmites (SW-France) and correlation with Atlantic and Mediterranean pollen records. *Quat. Sci. Rev.* **29**, 2799–2820.

Genty, D., Deflandre, G., Quinif, Y. and Verheyden, S. (1997) Les lamines de croissance des spéléothèmes: origine et intérêt paleoclimatique. *Bull. Société Belge Géologie* **106**, 63–77.

Genty D., Labuhn I., Hoffmann G., Danis P. A., Mestre O., Bourges F., Wainer K., Massault M., Van Exter S., Régnier E., Orengo P., Falourd S. and Minster B. (2014) Rainfall and cave water isotopic relationships in two South-France sites. *Geochim. Cosmochim. Acta* **131**, 323–343.

Genty D. and Massault M. (1999) Carbon transfer dynamics from bomb 14C and d13C times series of a laminated stalagmite from SW France: modelling and comparison with other stalagmites. *Geochim. Cosmochim. Acta* **63**, 1537–1548.

Genty D., Massault M., Gilmour M., Baker A., Verheyden S. and Kepens E. (1999) Calculation of past dead carbon proportion and variability by the comparison of AMS 14C and TIMS U/Th ages on two Holocee stalagmites. *Radiocarbon* **41**, 251–270.

Giachetta E., Molin P., Scotti V. N. and Faccenna C. (2015) Plio-Quaternary uplift of the Iberian Chain (central–eastern Spain) from landscape evolution experiments and river profile modeling. *Geomorphology* **246**, 48–67.

Ginés J., Fornós J. J., Gràcia F., Merino A., Onac B. P. and Ginés A. (2017) Hypogene Imprints in Coastal Karst Caves from Mallorca Island (Western Mediterranean): Morphological Features and Speleogenetic Approach. In *Hypogene Karst Regions and Caves of the World* (eds. A. Klimchouk, A. N. Palmer, J. De Waele, A. S. Auler, and P. Audra). Springer International Publishing, Cham. pp. 99–112.

Gisbert M. and Carvajal S. (1993) *Cavidades de Aragón*., Federación Aragonesa de Espeleología, Zaragoza.

Giustini F., Brilli M. and Patera A. (2016) Mapping oxygen stable isotopes of precipitation in Italy. *J. Hydrol. Reg. Stud.* **8**, 162–181.

Goñi M. S., Eynaud F., Turon J. L. and Shackleton N. J. (1999) High resolution palynological record off the Iberian margin: direct land-sea correlation for the Last Interglacial complex. *Earth Planet. Sci. Lett.* **171**, 123–137.

Goñi M. S., I. C., J. T., J. Guiot, F. S., J. P., J. Grimalt and N. S. (2002) Synchroneity between marine and terrestrial responses to millennial scale climatic variability during the last glacial period in the Mediterranean region. *Clim. Dyn.* **19**, 95–105.

González-Sampériz P., Valero-Garcés B. L., Moreno A., Jalut G., García-Ruiz J. M., Martí-Bono C., Delgado-Huertas A., Navas A., Otto T. and Dedoubat J. J. (2006) Climate variability in the Spanish Pyrenees during the last 30,000 yr revealed by the El Portalet sequence. *Quat. Res.* **66**, 38–52.

Gonzalez-Samperiz P., Valero-Garces B. L., Moreno A., Morellon M., Navas A., Machin J. and Delgado-Huertas A. (2008) Vegetation changes and hydrological fluctuations in the Central Ebro Basin (NE Spain) since the Late Glacial period: Saline lake records. *Palaeogeogr. Palaeoclimatol. Palaeoecol.* **259**, 157–181.

Govin A., Capron E., Tzedakis P. C., Verheyden S., Ghaleb B., Hillaire-Marcel C., St-Onge G., Stoner J. S., Bassinot F., Bazin L., Blunier T., Combourieu-Nebout N., El Ouahabi A., Genty D., Gersonde R., Jimenez-Amat P., Landais A., Martrat B., Masson-Delmotte V., Parrenin F., Seidenkrantz M.-S., Veres D., Waelbroeck C. and Zahn R. (2015) Sequence of events from the onset to the demise of the Last Interglacial: Evaluating strengths and limitations of chronologies used in climatic archives. *Quat. Sci. Rev.* **129**, 1–36.

Gradziński M., Hercman H., Kicińska D., Pura D. and Urban J. (2011) Ascending speleogenesis of Sokola Hill: A step towards a speleogenetic model of the Polish Jura. *Acta Geol. Pol.* **61**, 341–365.

Grant K. M., Rohling E. J., Ramsey C. B., Cheng H., Edwards R. L., Florindo F., Heslop D., Marra F., Roberts A. P., Tamisiea M. E. and Williams F. (2014) Sea-level variability over five glacial cycles. *Nat. Commun.* **5**, 5076.

Guimerà J. (1988) Estudi structural de l'enllaç entre la Serralada Ibérica i la Serralada Costanera Catalana. Tesis doctoral, Universidad de Zaragoza.

Guo X., Jiang G., Gong X., Yin J. and Wu X. (2015) Recharge processes on typical karst slopes implied by isotopic and hydrochemical indexes in Xiaoyan Cave, Guilin, China. *J. Hydrol.* **530**, 612–622.

Gutiérrez F., Gutiérrez M., Gracia F. J., McCalpin J. P., Lucha P. and Guerrero J. (2008) Plio-Quaternary extensional seismotectonics and drainage network development in the central sector of the Iberian Chain (NE Spain). *Geomorphology* **102**, 21–42.

Gutiérrez M. and Peña J. L. (1994) Cordillera Ibérica. In *Gutiérrez, M. (ed). Geomorfología de España* Editorial Rueda. pp. 251–286.

Hellstrom J. . and McCulloch M. . (2000) Multi-proxy constraints on the climatic significance of trace element records from a New Zealand speleothem. *Earth Planet. Sci. Lett.* **179**, 287–297.

Hellstrom J., McCulloch M. and Stone J. (1998) A detailed 31,000-year record of climate and vegetation change, from the isotope geochemistry of two New Zealand speleothems. *Quat. Res.* **50**, 167–178.

Hemming S. R. (2004) Heinrich events: massive Late Pleistocene detritus layers of the North Atlantic and their global imprint. *Rev. Geophys.* **42**, doi: 10,1029/20003RG000128.

Hendy C. H. (1971) The isotopic geochemistry of speleothems--I. The calculation of the effects of different modes of formation on the isotopic composition of speleothems and their applicability as palaeoclimatic indicators. *Geochim. Cosmochim. Acta* **35**, 801–824.

Hodell D. A., Channell J. E. T., Curtis J. H., Romero O. E. and Röhl U. (2008) Onset of "Hudson Strait" Heinrich events in the eastern North Atlantic at the end of the middle Pleistocene transition (~640 ka)?: Pleistocene Heinrich events.

Paleoceanography **23**. Available at: http://doi.wiley.com/10.1029/2008PA001591 [Accessed August 23, 2017].

Hodge E. J, Richards D. A., Smart P. L., Andreo B., Hoffmann D. L., Mattey D. P. and González-Ramón A. (2008) Effective precipitation in southern Spain (266 to 46 kyr) based on a speleothem stable carbon isotope record. *Quat. Res.* **69**, 447–457.

Hodge E. J, Richards D. A., Smart P. L., Ginés A. and Mattey D. P. (2008) Sub-millennial climate shifts in the western Mediterranean during the last glacial period recorded in a speleothem from Mallorca, Spain. *J. Quat. Sci.* **23**, 713–718.

Hopley P. J., Marshall J. D. and Latham A. G. (2009) Speleothem preservation and diagenesis in South African hominin sites implications for paleoenvironments and geochronology. *Geoarchaeology* **24**, 519–547.

Huybers P. and Wunsch C. (2005) Obliquity pacing of the late Pleistocene glacial terminations. *Nature* **434**, 491–494.

IAEA/WMO (2015) *Global network of isotopes in precipitation.*,

James E. W., Banner J. L. and Hardt B. (2015) A global model for cave ventilation and seasonal bias in speleothem paleoclimate records: A global model for cave ventilation. *Geochem. Geophys. Geosystems* **16**, 1044–1051.

Jeelani G., Saravana Kumar U. and Kumar B. (2013) Variation of δ18O and δD in precipitation and stream waters across the Kashmir Himalaya (India) to distinguish and estimate the seasonal sources of stream flow. *J. Hydrol.* **481**, 157–165.

Jiménez de Cisneros C., Caballero E., Vera J. A., Durán J. J. and Juliá R. (2003) A record of Pleistocene climate from a stalactite, Nerja Cave, southern Spain. *Palaeogeogr. Palaeoclimatol. Palaeoecol.* **189**, 1–10.

Jiménez-Amat P. and Zahn R. (2015) Offset timing of climate oscillations during the last two glacial-interglacial transitions connected with large-scale freshwater perturbation. *Paleoceanography* **30**, 768–788.

Johnston V. E., Borsato A., Spötl C., Frisia S. and Miorandi R. (2013) Stable isotopes in caves over altitudinal gradients: fractionation behaviour and inferences for speleothem sensitivity to climate change. *Clim. Past* **9**, 99–118.

Jones B. (2010) The preferential association of dolomite with microbes in stalactites from Cayman Brac, British West Indies. *Sediment. Geol.* **226**, 94–109.

Jones I. C. and Banner J. L. (2003) Estimating recharge thresholds in tropical karst island aquifers: Barbados, Puerto Rico and Guam. *J. Hydrol.* **278**, 131–143.

Jouzel J., Masson-Delmotte V., Cattani O., Dreyfus G., Falourd S., Hoffmann G., Minster B., Nouet J., Barnola J. M., Chappellaz J., Fischer H., Gallet J. C., Johnsen S., Leuenberger M., Loulergue L., Luethi D., Oerter H., Parrenin F., Raisbeck G., Raynaud D., Schilt A., Schwander J., Selmo E., Souchez R., Spahni R., Stauffer B., Steffensen J. P., Stenni B., Stocker T. F., Tison J. L., Werner M. and Wolff E. W. (2007) Orbital and Millennial Antarctic Climate Variability over the Past 800,000 Years. *Science* **317**, 793–796.

Kaufman A., Wasserburg G. J., Porcelli D., Bar-Matthews M., Ayalon A. and Halicz L. (1998) U-Th isotope systematics from the Soreq cave, Israel and climatic correlations. *Earth Planet. Sci. Lett.* **156**, 141–155.

Kebede S. and Travi Y. (2012) Origin of the δ18O and δ2H composition of meteoric waters in Ethiopia. *Quat. Int.* **257**, 4–12.

Kim S.-T. and O'Neil J. R. (1997) Equilibrium and nonequilibrium oxygen isotope effects in synthetic carbonates. *Geochim. Cosmochim. Acta* **61**, 3461–3475.

Kim S.-T., O'Neil J. R., Hillaire-Marcel C. and Mucci A. (2007) Oxygen isotope fractionation between synthetic aragonite and water: Influence of temperature and Mg2+ concentration. *Geochim. Cosmochim. Acta* **71**, 4704–4715.

Klimchouk A. (2013) Hypogene Speleogenesis. In *Schroder, J., Frumkin, A. (Eds). Treatise on geomorphology* Academic Press, San Diego, CA. pp. 220–240.

Klimchouk A. (2009) Morphogenesis of hypogenic caves. *Geomorphology* **106**, 100–117.

Klimchouk A. (2017) Types and settings of hypogene karst. In *Klimchouk, A., Palmer, A.N., De Waele, J., Auler, A.S., Audra, Ph (eds). Hypogene karst regions and caves of the world* Springer. pp. 1–39.

Klimchouk A., Ford D., Palmer A. and Dreybrodt W. eds. (2000) *Speleogenesis. Evolution of karst aquifers*. National Speleological Society., Huntsville, Alabama.

Kluge T., Riechelmann D. F. C., Wieser M., Spötl C., Sültenfuß J., Schröder-Ritzrau A., Niggemann S. and Aeschbach-Hertig W. (2010) Dating cave drip water by tritium. *J. Hydrol.* **394**, 396–406.

Kobashi T., Severinghaus J. P., Brook E. J., Barnola J.-M. and Grachev A. M. (2007) Precise timing and characterization of abrupt climate change 8200 years ago from air trapped in polar ice. *Quat. Sci. Rev.* **26**, 1212–1222.

Koster R. D., Valpine D. P. de and Jouzel J. (1993) Continental water recycling and H218O concentrations. *Geophys. Res. Lett.* **20**, 2215–2218.

Kowalczk A. J. and Froelich P. N. (2010) Cave air ventilation and CO2 outgassing by radon-222 modeling: How fast do caves breathe? *Earth Planet. Sci. Lett.* **289**, 209–219.

Krklec K. and Domínguez-Villar D. (2014) Quantification of the impact of moisture source regions on the oxygen isotope composition of precipitation over Eagle Cave, central Spain. *Geochim. Cosmochim. Acta* **134**, 39–54.

Kutzbach J. E., Bonan G., Foley J. and Harrison S. P. (1996) Vegetation and soil feedbacks on the response of the African monsoon to orbital forcing in the early to middle Holocene. *Nature* **384**, 623–626.

Kwiecien O., Stockhecke M., Pickarski N., Heumann G., Litt T., Sturm M., Anselmetti F., Kipfer R. and Haug G. H. (2014) Dynamics of the last four glacial terminations recorded in Lake Van, Turkey. *Quat. Sci. Rev.* **104**, 42–52.

Lachniet M. S. (2004) A 1500-year El Niño/Southern Oscillation and rainfall history for the Isthmus of Panama from speleothem calcite. *J. Geophys. Res.* **109**.

Lachniet M. S. (2009) Climatic and environmental controls on speleothem oxygen-isotope values. *Quat. Sci. Rev.* **28**, 412–432.

Lachniet M. S., Bernal J. P., Asmerom Y. and Polyak V. (2012) Uranium loss and aragonite–calcite age discordance in a calcitized aragonite stalagmite. *Quat. Geochronol.* **14**, 26–37.

Lachniet M. S., Denniston R. F., Asmerom Y. and Polyak V. J. (2014) Orbital control of western North America atmospheric circulation and climate over two glacial cycles. *Nat. Commun.* **5**.

Lachniet M. S. and Patterson W. P. (2009) Oxygen isotope values of precipitation and surface waters in northern Central America (Belize and Guatemala) are dominated by temperature and amount effects. *Earth Planet. Sci. Lett.* **284**, 435–446.

Lambert J. and Aharon P. (2010) Oxygen and hydrogen isotopes of rainfall and dripwater at DeSoto Caverns (Alabama, USA): Key to understanding past

variability of moisture transport from the Gulf of Mexico. *Geochim. Cosmochim. Acta* **74**, 846–861.

Lang N. and Wolff E. W. (2011) Interglacial and glacial variability from the last 800 ka in marine, ice and terrestrial archives. *Clim. Past* **7**, 361–380.

Lauritzen S.-E. and Lundberg J. (1999) Speleothems and climate: a special issue of The Holocene. *The Holocene* **9**, 643–647.

Leél-Őssy S., Szanyi G. and Surányi G. (2011) Minerals and speleothems of the József-hegy Cave (Budapest, Hungary). *Int. J. Speleol.* **40**, 191–203.

LeGrande A. N. and Schmidt G. A. (2006) Global gridded data set of the oxygen isotopic composition in seawater. *Geophys. Res. Lett.* **33**.

LeGrande A. N., Schmidt G. A., Shindell D. T., Field C. V., Miller R. L., Koch D. M., Faluvegi G. and Hoffmann G. (2006) Consistent simulations of multiple proxy responses to an abrupt climate change event. *Proc. Natl. Acad. Sci.* **103**, 837–842.

Lewis C. J., McDonald E. V., Sancho C., Peña J. L. and Rhodes E. J. (2009) Climatic implications of correlated Upper Pleistocene glacial and fluvial deposits on the Cinca and Gállego Rivers (NE Spain) based on OSL dating and soil stratigraphy. *Glob. Planet. Change* **67**, 141–152.

Lewis C. J., Vergés J. and Marzo M. (2000) High mountains in a zone of extended crust: Insights into the Neogene-Quaternary topographic development of northeastern Iberia. *Tectonics* **19**, 86–102.

Liesa C. (1998) Estructura y cinemática del arco de cabalgamientos Portalrubio-Vandellós en el sector de Castellote (Teruel). *Grupo Estud. Masinos* **18**, 9–37.

López-García J. M., Blain H.-A., Bennàsar M., Sanz M. and Daura J. (2013) Heinrich Event 4 characterized by terrestrial proxies in southwestern Europe. *Clim. Past Discuss.* **9**, 647–681.

de Luis M., Brunetti M., Gonzalez-Hidalgo J. C., Longares L. A. and Martin-Vide J. (2010) Changes in seasonal precipitation in the Iberian Peninsula during 1946–2005. *Glob. Planet. Change* **74**, 27–33.

Luo W., Wang S. and Xie X. (2013) A comparative study on the stable isotopes from precipitation to speleothem in four caves of Guizhou, China. *Chem. Erde - Geochem.* **73**, 205–215.

Lüthi D., Le Floch M., Bereiter B., Blunier T., Barnola J.-M., Siegenthaler U., Raynaud D., Jouzel J., Fischer H., Kawamura K. and Stocker T. F. (2008) High-resolution carbon dioxide concentration record 650,000–800,000 years before present. *Nature* **453**, 379–382.

Ma J., Zhang P., Zhu G., Wang Y., Edmunds W. M., Ding Z. and He J. (2012) The composition and distribution of chemicals and isotopes in precipitation in the Shiyang River system, northwestern China. *J. Hydrol.* **436–437**, 92–101.

Macdonald A. M. (1998) The global ocean circulation: a hydrographic estimate and regional analysis. *Prog. Oceanogr.* **41**, 281–382.

Margari V., Skinner L. C., Hodell D. A., Martrat B., Toucanne S., Grimalt J. O., Gibbard P. L., Lunkka J. P. and Tzedakis P. C. (2014) Land-ocean changes on orbital and millennial time scales and the penultimate glaciation. *Geology* **42**, 183–186.

Marino G., Rohling E. J., Rodríguez-Sanz L., Grant K. M., Heslop D., Roberts A. P., Stanford J. D. and Yu J. (2015) Bipolar seesaw control on last interglacial sea level. *Nature* **522**, 197–201.

Martín-Chivelet J., Muñoz-García M. ., Domínguez-Villar D., Turrero M. J. and Ortega A. (2006) Comparative analysis of stalagmites from two caves of northern Spain. Implication for Holocene paleoclimate studies. *Geol. Belg.* **9**, 323–335.

Martín-Chivelet J., Turrero M., Sánchez L., Gómez P., Garralón A. and Ortega A. (2007) Geochemical evolution of drip-water and present-growing calcite at Kaite cave (N Spain). In *Water-Rock Interaction* (eds. Y. Wang and T. Bullen). Taylor & Francis.

Martín-García R., Alonso-Zarza A. M. and Martín-Pérez A. (2009) Loss of primary texture and geochemical signatures in speleothems due to diagenesis: Evidences from Castañar Cave, Spain. *Sediment. Geol.* **221**, 141–149.

Martin-Puertas C., Brauer A., Wulf S., Ott F., Lauterbach S. and Dulski P. (2014) Annual proxy data from Lago Grande di Monticchio (southern Italy) between 76 and 112 ka: new chronological constraints and insights on abrupt climatic oscillations. *Clim. Past* **10**, 2099–2114.

Martrat B., Grimalt J. O., Shackleton N., de Abreu L., Hutterli M. A. and Stocker T. F. (2007) Four climate cycles of recurring deep and surface water destabilizations on the Iberian Margin. *Science* **317**, 502–507.

Martrat B., Jimenez-Amat P., Zahn R. and Grimalt J. O. (2014) Similarities and dissimilarities between the last two deglaciations and interglaciations in the North Atlantic region. *Quat. Sci. Rev.* **99**, 122–134.

Masson-Delmotte V., Stenni B., Pol K., Braconnot P., Cattani O., Falourd S., Kageyama M., Jouzel J., Landais A., Minster B., Barnola J. M., Chappellaz J., Krinner G., Johnsen S., Röthlisberger R., Hansen J., Mikolajewicz U. and Otto-Bliesner B. (2010) EPICA Dome C record of glacial and interglacial intensities. *Quat. Sci. Rev.* **29**, 113–128.

Mattey D., Lowry D., Duffet J., Fisher R., Hodge E. and Frisia S. (2008) *Earth Planet. Sci. Lett.* **269**, 80–95.

Mattey D. P., Fairchild I. J., Atkinson T. C., Latin J.-P., Ainsworth M. and Durell R. (2010) Seasonal microclimate control of calcite fabrics, stable isotopes and trace elements in modern speleothem from St Michaels Cave, Gibraltar. *Geol. Soc. Lond. Spec. Publ.* **336**, 323–344.

McDermott F. (2004) Palaeo-climate reconstruction from stable isotope variations in speleothems: a review. *Quat. Sci. Rev.* **23**, 901–918.

McDermott F., Mattey D. P. and Hawkesworth C. J. (2001) Centennial-scale Holocene climate variability revealed by a high-resolution speleothem d18O record from SW Ireland. *Science* **294**, 1328–1331.

McDermott, Schwarcz, H. and Rowe, P.J. (2006) Isotopes in Speleothems. In *Isotopes in Palaeoenvironmental Research* Springer. pp. 185–226.

McManus J., Francois R., Gherardi J. M., Keigwin L. and Brown-Leger S. (2004) Collapse and rapid resumption of Atlantic meridional circulation linked to deglacial climate changes. *Nature* **428**, 834–837.

Medina-Elizalde M., Burns S. J., Lea D. W., Asmerom Y., von Gunten L., Polyak V., Vuille M. and Karmalkar A. (2010) High resolution stalagmite climate record from the Yucatán Peninsula spanning the Maya terminal classic period. *Earth Planet. Sci. Lett.* **298**, 255–262.

Medina-Elizalde M. and Rohling E. J. (2012) Collapse of Classic Maya Civilization Related to Modest Reduction in Precipitation. *Science* **335**, 956–959.

Meiliang Z., Xiaoyan Z., Xia W., Jianjun Y. and Moucheng P. (2015) δ18O characteristics of meteoric precipitation and its water vapor sources in the Guilin area of China. *Environ. Earth Sci.* **74**, 953–976.

Meyer K. W., Feng W., Breecker D. O., Banner J. L. and Guilfoyle A. (2014) Interpretation of speleothem calcite δ13C variations: Evidence from monitoring soil CO2, drip water, and modern speleothem calcite in central Texas. *Geochim. Cosmochim. Acta* **142**, 281–298.

Meyer M. C., Spötl C. and Mangini A. (2008) The demise of the Last Interglacial recorded in isotopically dated speleothems from the Alps. *Quat. Sci. Rev.* **27**, 476–496.

Michelsen N., Reshid M., Siebert C., Schulz S., Knöller K., Weise S. M., Rausch R., Al-Saud M. and Schüth C. (2015) Isotopic and chemical composition of precipitation in Riyadh, Saudi Arabia. *Chem. Geol.* **413**, 51–62.

Mickler P. J., Stern L. A. and Banner J. L. (2006) Large kinetic isotope effects in modern speleothems. *Geol. Soc. Am. Bull.* **118**, 65–81.

Miorandi R., Borsato A., Frisia S., Fairchild I. J. and Richter D. K. (2010) Epikarst hydrology and implications for stalagmite capture of climate changes at Grotta di Ernesto (NE Italy): results from long-term monitoring. *Hydrol. Process.* **24**, 3101–3114.

Mischel S. A., Scholz D. and Spötl C. (2015) δ18O values of cave drip water: a promising proxy for the reconstruction of the North Atlantic Oscillation? *Clim. Dyn.* **45**, 3035–3050.

Moerman J. W., Cobb K. M., Partin J. W., Meckler A. N., Carolin S. A., Adkins J. F., Lejau S., Malang J., Clark B. and Tuen A. A. (2014) Transformation of ENSO-related rainwater to dripwater δ^{18}O variability by vadose water mixing: ENSO variability in dripwater d18O. *Geophys. Res. Lett.* **41**, 7907–7915.

Mokeddem Z., McManus J. F. and Oppo D. W. (2014) Oceanographic dynamics and the end of the last interglacial in the subpolar North Atlantic. *Proc. Natl. Acad. Sci.* **111**, 11263–11268.

Moquet J. S., Cruz F. W., Novello V. F., Stríkis N. M., Deininger M., Karmann I., Santos R. V., Millo C., Apaestegui J., Guyot J.-L., Siffedine A., Vuille M., Cheng H., Edwards R. L. and Santini W. (2016) Calibration of speleothem δ 18 O records against hydroclimate instrumental records in Central Brazil. *Glob. Planet. Change* **139**, 151–164.

Morellón M., Valero-Garcés B., Vegas-Vilarrúbia T., González-Sampériz P., Romero Ó., Delgado-Huertas A., Mata P., Moreno A., Rico M. and Corella J. P. (2009)

Lateglacial and Holocene palaeohydrology in the western Mediterranean region: The Lake Estanya record (NE Spain). *Quat. Sci. Rev.* **28**, 2582–2599.

Moreno A., Cacho I., Canals M., Grimalt J. O., Sánchez-Goñi M. F., Shackleton N. J. and Sierro F. J. (2005) Links between marine and atmospheric processes oscillating at millennial time-scale. A multy-proxy study of the last 50,000 yr from the Alboran Sea (Western Mediterranean Sea). *Quat. Sci. Rev.* **24**, 1623–1636.

Moreno A., Cacho I., Canals M., Prins M. A., Sánchez-Goñi M. F., Grimalt J. O. and Weltje G. J. (2002) Saharan dust transport and high latitude glacial climatic variability: the Alboran Sea record. *Quat. Res.* **58**, 318–328.

Moreno A., Pérez-Mejías C., Bartolomé M., Sancho C., Cacho I., Stoll H., Delgado-Huertas A., Hellstrom J., Edwards R. L. and Cheng H. (2017) New speleothem data from Molinos and Ejulve caves reveal Holocene hydrological variability in northeast Iberia. *Quat. Res.*, 1–11.

Moreno A., Sancho C., Bartolomé M., Oliva-Urcia B., Delgado-Huertas A., Estrela M. J., Corell D., López-Moreno J. I. and Cacho I. (2014) Climate controls on rainfall isotopes and their effects on cave drip water and speleothem growth: the case of Molinos cave (Teruel, NE Spain). *Clim. Dyn.* **43**, 221–241.

Moreno A., Stoll H. M., Jiménez-Sánchez M., Cacho I., Valero-Garcés B., Ito E. and Edwards L. R. (2010) A speleothem record of rapid climatic shifts during last glacial period from Northern Iberian Peninsula. *Glob. Planet. Change* **71**, 218–231.

Moseley G. E., Spötl C., Cheng H., Boch R., Min A. and Edwards R. L. (2015) Termination-II interstadial/stadial climate change recorded in two stalagmites from the north European Alps. *Quat. Sci. Rev.* **127**, 229–239.

Moseley G. E., Spotl C., Svensson A., Cheng H., Brandstatter S. and Edwards R. L. (2014) Multi-speleothem record reveals tightly coupled climate between central Europe and Greenland during Marine Isotope Stage 3. *Geology* **42**, 1043–1046.

Mühlinghaus C., Scholz D. and Mangini A. (2009) Modelling fractionation of stable isotopes in stalagmites. *Geochim. Cosmochim. Acta* **73**, 7275–7289.

Mühlinghaus C., Scholz D. and Mangini A. (2007) Modelling stalagmite growth and δ13C as a function of drip interval and temperature. *Geochim. Cosmochim. Acta* **71**, 2780–2790.

Müller U. C. and Sánchez Goñi M. F. (2007) 19. Vegetation dynamics in southern Germany during marine isotope stage 5 (~ 130 to 70 kyr ago). In *Developments in Quaternary Sciences* Elsevier. pp. 277–287.

Muñoz A., Osácar M. C. and Sancho C. (2009) Estacionalidad de la laminación espeleotémica de las Cuevas de Ortigosa de Cameros (La Rioja): aproximación experimental. *Geogaceta*, 107–110.

Muñoz A. and Sancho C. (2008) Monitorización climática de las cuevas de Ortigosa de Cameros (La Rioja): aplicación a la interpretación del registro climático de los espeleotemas holocenos. *Zubía*, 21–36.

Muñoz Arsenio, Bartolomé M., Muñoz Alicia, Sancho C., Moreno A., Hellstrom J. C., Osácar M. C. and Cacho I. (2015) Solar influence and hydrological variability during the Holocene from a speleothem annual record (Molinos Cave, NE Spain). *Terra Nova* **27**, 300–311.

Muñoz-García M. ., Chivelet J. M., Rossi C., Ford D. C. and Schwarcz H. P. (2007) Chronology of Termination II and the Last Interglacial Period in North Spain based on stable isotope records of stalagmites from Cueva del Cobre (Palencia). *J. Iber. Geol.* **33**, 17–30.

Muñoz-García M. ., Martín-Chivelet J. and Rossi C. (2004) Implicaciones paleoclimáticas de la distribución geocronológica de espeleotemas en la Cueva del Cobre (Palencia). *Geogaceta* **35**, 179–182.

Musgrove M. and Banner J. L. (2004) Controls on the spatial and temporal variability of vadose dripwater geochemistry: Edwards aquifer, central Texas. *Geochim. Cosmochim. Acta* **68**, 1007–1020.

Mussi M., Leone G. and Nardi I. (1998) Isotopic geochemistry of natural waters from the Alpi Apuane-Garfagnana area, Northern Tuscany, Italy. *Mineral. Petrogr. Acta* **41**, 163–178.

National Research Council (2002) *Abrupt Climate Change: Inevitable Surprises*., Washington, DC: The National Academies Press.

Naughton F., Sánchez Goñi M. F., Kageyama M., Bard E., Duprat J., Cortijo E., Desprat S., Malaizé B., Joly C., Rostek F. and Turon J. L. (2009) Wet to dry climatic trend in north-western Iberia within Heinrich events. *Earth Planet. Sci. Lett.* **284**, 329–342.

Obrochta S. P., Crowley T. J., Channell J. E. T., Hodell D. A., Baker P. A., Seki A. and Yokoyama Y. (2014) Climate variability and ice-sheet dynamics during the last three glaciations. *Earth Planet. Sci. Lett.* **406**, 198–212.

Onac B. P., Pace-Graczyk K. and Atudirei V. (2008) Stable isotope study of precipitation and cave drip water in Florida (USA): implications for speleothem-based paleoclimate studies†. *Isotopes Environ. Health Stud.* **44**, 149–161.

Ortega A. I., Benito-Calvo A., Pérez-González A., Martín-Merino M. A., Pérez-Martínez R., Parés J. M., Aramburu A., Arsuaga J. L., Bermúdez de Castro J. M. and Carbonell E. (2013) Evolution of multilevel caves in the Sierra de Atapuerca (Burgos, Spain) and its relation to human occupation. *Geomorphology* **196**, 122–137.

Ortega R., Maire R., Devès G. and Quinif Y. (2005) High-resolution mapping of uranium and other trace elements in recrystallized aragonite–calcite speleothems from caves in the Pyrenees (France): Implication for U-series dating. *Earth Planet. Sci. Lett.* **237**, 911–923.

Orvošová M., Hurai V., Simon K. and Wiegerová V. (2004) Fluid inclusion and stable isotopic evidence for early hydrothermal karstification in vadose caves of the Nízke Tatry Mountains (Western Carpathians). *Geol. Carpathica* **55**, 421–429.

Osácar M. C., Sancho C., Muñoz A., Bartolomé M., Moreno A., Delgado-Huertas A. and Cacho I. (2014) Trazabilidad de la señal isotópica del oxígeno desde la lluvia a los espeleotemas en las cuevas de Ortigosa de Cameros (La Rioja, España). *Estud. Geológicos* **70**, 021.

Oster J. L., Montañez I. P. and Kelley N. P. (2012) Response of a modern cave system to large seasonal precipitation variability. *Geochim. Cosmochim. Acta* **91**, 92–108.

Pailhé P. (1984) La Chaîne Ibérique Orientale. Étude géomorphologique. Thèse de Doctorat d'Etat, Université Bordeaux III.

Pailler D. and Bard E. (2002) High frequency palaeoceanographic changes during the past 140,000 years recorded by the organic matter in sediments of the Iberian margin. *Palaeogeogr. Palaeoclimatol. Palaeoecol.* **181**, 431–452.

Palmer A. (1991) *Origin and morphology of limestone caves*. Bulletin 103., Geological Society of America.

Palmer A. N. (2011) Distinction between epigenic and hypogenic maze caves. *Geomorphology* **134**, 9–22.

Pape J. R., Banner J. L., Mack L. E., Musgrove M. and Guilfoyle A. (2010) Controls on oxygen isotope variability in precipitation and cave drip waters, central Texas, USA. *J. Hydrol.* **385**, 203–215.

Parkhurst D. L. and Appello C. A. . (2013) Description of input and examples for PHREEQC version 3--A computer program for speciation, batch- reaction, one-dimensional transport, and inverse geochemical calculations. In U.S. Geological Survey Techniques and Methods. p. 497.

Partin J. W., Cobb K. M., Adkins J. F., Clark B. and Fernandez D. P. (2007) Millennial-scale trends in west Pacific warm pool hydrology since the Last Glacial Maximum. *Nature* **449**, 452–455.

Past Interglacials Working Group of PAGES (2016) Interglacials of the last 800,000 years: Interglacials of the Last 800,000 Years. *Rev. Geophys.* **54**, 162–219.

Peña J. L., Gutiérre Elorza M., Jesus Ibáñez Marcellan M., Victoria Lozano Tena M., Vidal J., Sánchez Fabre M., Luis Simón Gomez J., Soriano M. and Miguel Yetano Ruiz L. (1984) *Geomorfología de la Provincia de Teruel*.,

Pena L. D., Francés G., Diz P., Esparza M., Grimalt J. O., Nombela M. A. and Alejo I. (2010) Climate fluctuations during the Holocene in NW Iberia: High and low latitude linkages. *Cont. Shelf Res.* **30**, 1487–1496.

Pérez-Mejías C., Moreno A., Sancho C., Bartolomé M., Stoll H., Cacho I., Cheng H. and Edwards R. L. (2017) Abrupt climate changes during Termination III in Southern Europe. *Proc. Natl. Acad. Sci.* **114**, 10047–10052.

Pérez-Mejías C., Moreno A., Sancho C., Bartolomé M., Stoll H., Osácar M. C., Cacho I. and Delgado-Huertas A. (2018) Transference of isotopic signal from rainfall to dripwaters and farmed calcite in Mediterranean semi-arid karst. *Geochim. Cosmochim. Acta* **243**, 66–98.

Pérez-Mejías C., Moreno A., Sancho C., Martín-García R., Spötl C., Cacho I., Cheng H. and Edwards R. L. Orbital-to-millennial scale climate variability since last glacial inception recorded in a stalagmite from Southern Europe.

Pérez-Mejías C., Moreno Caballud A. and Sancho Marcén C. (2013) La cueva de El Recuenco (Ejulve, Teruel): Espeleogénesis y registro de cambios climáticos rápidos durante el Holoceno. *Zaragoza*.

Perrin C., Prestimonaco L., Servelle G., Tilhac R., Maury M. and Cabrol P. (2014) Aragonite-Calcite Speleothems: Identifying Original and Diagenetic Features. *J. Sediment. Res.* **84**, 245–269.

Perrin J., Jeannin P.-Y. and Zwahlen F. (2003) Epikarst storage in a karst aquifer: a conceptual model based on isotopic data, Milandre test site, Switzerland. *J. Hydrol.* **279**, 106–124.

Pickering R., Kramers J. D., Partridge T., Kodolanyi J. and Pettke T. (2010) U–Pb dating of calcite–aragonite layers in speleothems from hominin sites in South Africa by MC-ICP-MS. *Quat. Geochronol.* **5**, 544–558.

Polyak V. J. and Asmerom Y. (2001) Late Holocene Climate and Cultural Changes in the Southwestern United States. *Science* **294**, 148–151.

Polyak V. J., Asmerom Y., Burns S. J. and Lachniet M. S. (2012) Climatic backdrop to the terminal Pleistocene extinction of North American mammals. *Geology* **40**, 1023–1026.

Pu J., Wang A., Shen L., Yin J., Yuan D. and Zhao H. (2016) Factors controlling the growth rate, carbon and oxygen isotope variation in modern calcite precipitation in a subtropical cave, Southwest China. *J. Asian Earth Sci.* **119**, 167–178.

Rai S. P., Purushothaman P., Kumar B., Jacob N. and Rawat Y. S. (2014) Stable isotopic composition of precipitation in the River Bhagirathi Basin and identification of source vapour. *Environ. Earth Sci.* **71**, 4835–4847.

Ramsey C. B. (2008) Deposition models for chronological records. *Quat. Sci. Rev.* **27**, 42–60.

Rashid H., Hesse R. and Piper D. J. W. (2003) Evidence for an additional Heinrich event between H5 and H6 in the Labrador Sea: Heinrich event 5A in the Labrador Sea. *Paleoceanography* **18**. Available at: http://doi.wiley.com/10.1029/2003PA000913 [Accessed May 24, 2018].

Rasmussen S. O., Bigler M., Blockley S. P., Blunier T., Buchardt S. L., Clausen H. B., Cvijanovic I., Dahl-Jensen D., Johnsen S. J., Fischer H., Gkinis V., Guillevic M., Hoek W. Z., Lowe J. J., Pedro J. B., Popp T., Seierstad I. K., Steffensen J. P., Svensson A. M., Vallelonga P., Vinther B. M., Walker M. J. C., Wheatley J. J. and Winstrup M. (2014) A stratigraphic framework for abrupt climatic changes during the Last Glacial period based on three synchronized Greenland ice-core records: refining and extending the INTIMATE event

stratigraphy. *Dating Synth. Interpret. Palaeoclim. Rec. Model-Data Integr. Adv. Intim. Proj. Ice Core Mar. Terr. Rec. COST Action ES0907* **106**, 14–28.

Rasmussen T. L., Thomsen E. and Moros M. (2016) North Atlantic warming during Dansgaard-Oeschger events synchronous with Antarctic warming and out-of-phase with Greenland climate. *Sci. Rep.* **6**.

Ren W., Yao T., Xie S. and He Y. (2017) Controls on the stable isotopes in precipitation and surface waters across the southeastern Tibetan Plateau. *J. Hydrol.* **545**, 276–287.

Renssen H., Mairesse A., Goosse H., Mathiot P., Heiri O., Roche D. M., Nisancioglu K. H. and Valdes P. J. (2015) Multiple causes of the Younger Dryas cold period. *Nat. Geosci.* **8**, 946–949.

Resmi T. R., Sudharma K. V. and Hameed A. S. (2016) Stable isotope characteristics of precipitation of Pamba River basin, Kerala, India. *J. Earth Syst. Sci.* **125**, 1481–1493.

Riechelmann D. F. C., Deininger M., Scholz D., Riechelmann S., Schröder-Ritzrau A., Spötl C., Richter D. K., Mangini A. and Immenhauser A. (2013) Disequilibrium carbon and oxygen isotope fractionation in recent cave calcite: Comparison of cave precipitates and model data. *Geochim. Cosmochim. Acta* **103**, 232–244.

Riechelmann S., Schröder-Ritzrau A., Spötl C., Riechelmann D. F. C., Richter D. K., Mangini A., Frank N., Breitenbach S. F. M. and Immenhauser A. (2017) Sensitivity of Bunker Cave to climatic forcings highlighted through multi-annual monitoring of rain-, soil-, and dripwaters. *Chem. Geol.* **449**, 194–205.

Risi C., Bony S. and Vimeux F. (2008) Influence of convective processes on the isotopic composition (δ^{18}O and δD) of precipitation and water vapor in the tropics: 2. Physical interpretation of the amount effect. *J. Geophys. Res.* **113**.

Roberts M. S., Smart P. L. and Baker A. (1998) Annual trace element variations in a Holocene speleothem. *Earth Planet. Sci. Lett.* **154**, 237–246.

Roche D., Paillard D. and Cortijo E. (2004) Constraints on the duration and freshwater release of Heinrich event 4 through isotope modelling. *Nature* **432**, 379–382.

Rodríguez-Rodríguez L., Jiménez-Sánchez M., Domínguez-Cuesta M. J., Rinterknecht V., Pallàs R. and Bourlès D. (2016) Chronology of glaciations in the Cantabrian

Mountains (NW Iberia) during the Last Glacial Cycle based on in situ-produced 10Be. *Quat. Sci. Rev.* **138**, 31–48.

Rohling E. J., Grant K., Bolshaw M., Roberts A. P., Siddall M., Hemleben C. and Kucera M. (2009) Antarctic temperature and global sea level closely coupled over the past five glacial cycles. *Nat. Geosci.* **2**, 500–504.

Romanov D., Kaufmann G. and Dreybrodt W. (2008) Modeling stalagmite growth by first principles of chemistry and physics of calcite precipitation. *Geochim. Cosmochim. Acta* **72**, 423–437.

Rossi C., Bajo P., P Lozano R. and Hellstrom J. (2018) Younger Dryas to Early Holocene paleoclimate in Cantabria (N Spain): Constraints from speleothem Mg, annual fluorescence banding and stable isotope records. *Quat. Sci. Rev.* **192**.

Rossi C., Mertz-Kraus R. and Osete M.-L. (2014) Paleoclimate variability during the Blake geomagnetic excursion (MIS 5d) deduced from a speleothem record. *Quat. Sci. Rev.* **102**, 166–180.

Rowe P. J., Mason J. E., Andrews J. E., Marca A. D., Thomas L., van Calsteren P., Jex C. N., Vonhof H. B. and Al-Omari S. (2012) Speleothem isotopic evidence of winter rainfall variability in northeast Turkey between 77 and 6 ka. *Quat. Sci. Rev.* **45**, 60–72.

Rozanski K., Araguás-Araguás L. and Gonfiantini R. (1993) Isotopic patterns in modern global precipitation. *Geophys. Monogr. Ser.* **78**, PP. 1-36.

Salomons W. and Mook W. G. (1986) Isotope geochemistry of carbonates in the weathering zone. In *The Terrestrial Environment, B* Elsevier. pp. 239–269.

Sánchez Goñi M. F., Desprat S., Daniau A.-L., Bassinot F. C., Polanco-Martínez J. M., Harrison S. P., Allen J. R. M., Anderson R. S., Behling H., Bonnefille R., Burjachs F., Carrión J. S., Cheddadi R., Clark J. S., Combourieu-Nebout N., Courtney-Mustaphi C. J., Debusk G. H., Dupont L. M., Finch J. M., Fletcher W. J., Giardini M., González C., Gosling W. D., Grigg L. D., Grimm E. C., Hayashi R., Helmens K., Heusser L. E., Hill T., Hope G., Huntley B., Igarashi Y., Irino T., Jacobs B., Jiménez-Moreno G., Kawai S., Kershaw P., Kumon F., Lawson I. T., Ledru M.-P., Lézine A.-M., Liew P. M., Magri D., Marchant R., Margari V., Mayle F. E., McKenzie M., Moss P., Müller S., Müller U. C., Naughton F., Newnham R. M., Oba T., Pérez-Obiol R., Pini R., Ravazzi C., Roucoux K. H., Rucina S. M., Scott L., Takahara H., Tzedakis P. C., Urrego D. H., van Geel B., Valencia B. G., Vandergoes M. J., Vincens A., Whitlock C. L., Willard D. A. and Yamamoto M. (2017) The ACER pollen and charcoal database: a global

resource to document vegetation and fire response to abrupt climate changes during the last glacial period. *Earth Syst. Sci. Data Discuss.*, 1–33.

Sánchez Goñi M. F., Loutre M. F., Crucifix M., Peyron O., Santos L., Duprat J., Malaizé B., Turon J.-L. and Peypouquet J.-P. (2005) Increasing vegetation and climate gradient in Western Europe over the Last Glacial Inception (122–110 ka): data-model comparison. *Earth Planet. Sci. Lett.* **231**, 111–130.

Sánchez J. Á., Coloma López P. and Perez-Garcia A. (2004) Evaluation of geothermal flow at the springs in Aragón (Spain), and its relation to geologic structure. *Hydrogeol. J.* **12**, 601–609.

Sánchez-Goñi M. F., Landais A., Fletcher W. J., Naughton F., Desprat S. and Duprat J. (2008) Contrasting impacts of Dansgaard-Oeschger events over a western European latitudinal transect modulated by orbital parameters. *Quat. Sci. Rev.* **27**, 1136–1151.

Sancho C., Arenas C., Pardo G., Peña-Monné J. L., Rhodes E. J., Bartolomé M., García-Ruiz J. M. and Martí-Bono C. (2018) Glaciolacustrine deposits formed in an ice-dammed tributary valley in the south-central Pyrenees: New evidence for late Pleistocene climate. *Sediment. Geol.* **366**, 47–66.

Sancho C., Arenas C., Vázquez-Urbez M., Pardo G., Lozano M. V., Peña-Monné J. L., Hellstrom J., Ortiz J. E., Osácar M. C., Auqué L. and Torres T. (2015) Climatic implications of the Quaternary fluvial tufa record in the NE Iberian Peninsula over the last 500ka. *Quat. Res.* **84**, 398–414.

Scholz D., Frisia S., Borsato A., Spötl C., Fohlmeister J., Mudelsee M., Miorandi R. and Mangini A. (2012) Holocene climate variability in north-eastern Italy: potential influence of the NAO and solar activity recorded by speleothem data. *Clim. Past* **8**, 1367–1383.

Scholz D. and Hoffmann D. L. (2011) StalAge - An algorithm designed for construction of speleothem age models. *Quat. Geochronol.* **6**, 369–382.

Scholz D., Tolzmann J., Hoffmann D. L., Jochum K. P., Spötl C. and Riechelmann D. F. C. (2014) Diagenesis of speleothems and its effect on the accuracy of 230Th/U-ages. *Chem. Geol.* **387**, 74–86.

Schwarz K., Barth J. a. C., Grathwohl P. and Postigo-Rebello C. (2008) Storage and transport in cave seepage- and groundwater in a South German karst system. *Hydrol. Earth Syst. Sci. Discuss.* **5**, 1267–1287.

Scotti V. N., Molin P., Faccenna C., Soligo M. and Casas-Sainz A. (2014) The influence of surface and tectonic processes on landscape evolution of the Iberian Chain (Spain): Quantitative geomorphological analysis and geochronology. *Geomorphology* **206**, 37–57.

Shackleton N. J. (1987) Oxygen isotopes, ice volume and sea level. *Quat. Sci. Rev.* **6**, 183–190.

Sharp (2007) *Principles of Stable Isotope Geochemistry*., Pearson Prentice Hall, Upper Saddle River, NJ.

Sierra P. (2016) Superficies de erosión y evolución morfotectónica de un sector de la Cordillera Ibérica oriental. Trabajo Fin de Grado, Universidad de Zaragoza.

Sierro F. J., Hodell D. A., Curtis J. H., Flores J. A., Reguera I., Colmenero-Hidalgo E., Bárcena M. A., Grimalt J. O., Cacho I., Frigola J. and Canals M. (2005) Impact of iceberg melting on Mediterranean thermohaline circulation during Heinrich events. *Paleoceanography* **20**.

Simón J. L. (1984) Compresión y distensión alpinas en la Cadena Ibérica oriental. *Inst. Estud. Turol.*, 269.

Simón J. L., Liesa C. L. and Arlegui L. E. (2002) Alpine tectonics I. The Iberian Ranges. In *The Geology of Spain* (eds. W. Gibbons and M. T. Moreno). Geological Society, London. pp. 385–397.

Sirocko F., Seelos K., Schaber K., Rein B., Dreher F., Diehl M., Lehne R., Jäger K., Krbetschek M. and Degering D. (2005) A late Eemian aridity pulse in central Europe during the last glacial inception. *Nature* **436**, 833–836.

Skinner L. C. and Elderfield H. (2007) Rapid fluctuations in the deep North Atlantic heat budget during the last glacial period: rapid deepwater temperature change. *Paleoceanography* **22**. Available at: http://doi.wiley.com/10.1029/2006PA001338 [Accessed May 24, 2018].

Skinner L. and Shackleton N. (2004) Rapid transient changes in northeast Atlantic deep water ventilation age across Termination 1. *Paleoceanography* **19**.

Smart P. L. and Friedrich M. (1987) Water movement and storage in the unsaturated zone of a maturely karstified carbonate aquifer, Mendip Hills, England. *Proc. Environ. Probl. Karst Terranes Their Solut. Conf.*, 57–87.

Soil Science Division Staff (2017) Examination and Description of Soils. In *Soil Survey Manual* (eds. C. Ditzler, K. Scheffe, and H. . Monger). USDA Handbook 18, Washington, D. C.

Sopeña, A. (2004) Cordilleras Ibérica y Costero Catalana. In *Geología de España* (ed. J. A. Vera). Madrid. pp. 467–470.

Soria A. R. (1997) La sedimentación en las cuencas marginales del surco Ibérico durante el Cretácico inferior y su control tectónico. Tesis doctoral, Universidad de Zaragoza.

Spötl C. (2011) Long-term performance of the Gasbench isotope ratio mass spectrometry system for the stable isotope analysis of carbonate microsamples. *Rapid Commun. Mass Spectrom.* **25**, 1683–1685.

Spötl C., Dublyansky Y., Meyer M. and Mangini A. (2009) Identifying low-temperature hydrothermal karst and palaeowaters using stable isotopes: a case study from an alpine cave, Entrische Kirche, Austria. *Int. J. Earth Sci.* **98**, 665–676.

Spötl C., Fairchild I. J. and Tooth A. F. (2005) Cave air control on dripwater geochemistry, Obir Caves (Austria): Implications for speleothem deposition in dynamically ventilated caves. *Geochim. Cosmochim. Acta* **69**, 2451–2468.

Spötl C., Fohlmeister J., Cheng H. and Boch R. (2016) Modern aragonite formation at near-freezing conditions in an alpine cave, Carnic Alps, Austria. *Chem. Geol.* **435**, 60–70.

Spötl C. and Mangini A. (2002) Stalagmite from the Austrian Alps reveals Dansgaard-Oeschger events during isotope stage 3: implications for the absolute chronology of Greenland ice cores. *Earth Planet. Sci. Lett.* **203**, 507–518.

Spötl C., Mangini A. and Richards D. A. (2006) Chronology and paleoenvironment of Marine Isotope Stage 3 from two high-elevation speleothems, Austrian Alps. *Quat. Sci. Rev.* **25**, 1127–1136.

Spotl C., Scholz D. and Mangini A. (2008) A terrestrial U/Th-dated stable isotope record of the Penultimate Interglacial. *Earth Planet. Sci. Lett.* **276**, 283–292.

Spratt R. M. and Lisiecki L. E. (2016) A Late Pleistocene sea level stack. *Clim. Past* **12**, 1079–1092.

Springer G. S., Rowe H. D., Hardt B., Cheng H. and Edwards R. L. (2014) East central North America climates during marine isotope stages 3-5: East-Central North America climates. *Geophys. Res. Lett.* **41**, 3233–3237.

Stocker T. F. and Marchal O. (2000) Abrupt climate change in the computer: Is it real? *Proc. Natl. Acad. Sci.* **97**, 1362–1365.

Stoll H. M., Moreno A., Mendez-Vicente A., Gonzalez-Lemos S., Jimenez-Sanchez M., Dominguez-Cuesta M. J., Edwards R. L., Cheng H. and Wang X. (2013) Paleoclimate and growth rates of speleothems in the northwestern Iberian Peninsula over the last two glacial cycles. *Quat. Res.*

Stoll H. M., Müller W. and Prieto M. (2012) I-STAL, a model for interpretation of Mg/Ca, Sr/Ca and Ba/Ca variations in speleothems and its forward and inverse application on seasonal to millennial scales. *Geochem. Geophys. Geosystems* **13**. Available at: http://www.agu.org/pubs/crossref/pip/2012GC004183.shtml [Accessed July 2, 2013].

Stoll H., Mendez-Vicente A., Gonzalez-Lemos S., Moreno A., Cacho I., Cheng H. and Edwards R. L. (2015a) Interpretation of orbital scale variability in mid-latitude speleothem δ18O: Significance of growth rate controlled kinetic fractionation effects. *Quat. Sci. Rev.* **127**, 215–228.

Stoll H., Mendez-Vicente A., Gonzalez-Lemos S., Moreno A., Cacho I., Cheng H. and Edwards R. L. (2015b) Interpretation of orbital scale variability in mid-latitude speleothem δ18O: Significance of growth rate controlled kinetic fractionation effects. *Quat. Sci. Rev.* **127**, 215–228.

Stoll H., Pérez-Mejías C., Cacho I., Moreno A., Iglesias M., Edwards R. L. and Cheng H. (2018) Chronology for deglaciation during Termination II from stalagmites in NW Spain. In *18654* EGU 2018.

Stumpp C., Klaus J. and Stichler W. (2014) Analysis of long-term stable isotopic composition in German precipitation. *J. Hydrol.* **517**, 351–361.

Svensson A., Andersen K. K., Bigler M., Clausen H. B., Dahl-Jensen D., Davies S. M., Johnsen S. J., Muscheler R., Parrenin F., Rasmussen S. O. and others (2008) A 60 000 year Greenland stratigraphic ice core chronology. *Clim. Past* **4**, 47–57.

Taylor K. C. (1997) The Holocene-Younger Dryas Transition Recorded at Summit, Greenland. *Science* **278**, 825–827.

Thornthwaite C. W. (1948) An Approach toward a Rational Classification of Climate. *Geogr. Rev.* **38**, 55–94.

Tinner W. and Lotter A. F. (2001) Central European vegetation response to abrupt climate change at 8.2 ka. *Geology* **29**, 551–554.

Tooth A. F. and Fairchild I. J. (2003) Soil and karst aquifer hydrological controls on the geochemical evolution of speleothem-forming drip waters, Crag Cave, southwest Ireland. *J. Hydrol.* **273**, 51–68.

Treble P. C., Bradley C., Wood A., Baker A., Jex C. N., Fairchild I. J., Gagan M. K., Cowley J. and Azcurra C. (2013) An isotopic and modelling study of flow paths and storage in Quaternary calcarenite, SW Australia: implications for speleothem paleoclimate records. *Quat. Sci. Rev.* **64**, 90–103.

Tremaine D. M., Froelich P. N. and Wang Y. (2011) Speleothem calcite farmed in situ: Modern calibration of δ18O and δ13C paleoclimate proxies in a continuously-monitored natural cave system. *Geochim. Cosmochim. Acta* **75**, 4929–4950.

Tyler J. J., Jones M., Arrowsmith C., Allott T. and Leng M. J. (2016) Spatial patterns in the oxygen isotope composition of daily rainfall in the British Isles. *Clim. Dyn.* **47**, 1971–1987.

Tzedakis C. (2005) Towards an understanding of the response of southern European vegetation to orbital and suborbital climate variability. *Quat. Sci. Rev.* **24**, 1585–1599.

Tzedakis C., McManus J., Hooghiemstra H., Oppo D. W. and Wijmstra T. A. (2003) Comparison of changes in vegetation in northeast Greece with records of climate variability on orbital and suborbital frequencies over the last 450000 years. *Earth Planet. Sci. Lett.* **212**, 197–212.

Tzedakis P. C. (2004) The Duration of Forest Stages in Southern Europe and Interglacial Climate Variability. *Science* **306**, 2231–2235.

Tzedakis P. C., Andrieu V., de Beaulieu J.-L., Crowhurst S., Follieri M., Hooghiemstra H., Magri D., Reille M., Sadori L., Shackleton N. J. and Wijmstra T. A. (1997) Comparison of terrestrial and marine records of changing climate of the last 500,000 years. *Earth Planet. Sci. Lett.* **150**, 171–176.

Tzedakis P. C., McManus J. F., Hooghiemstra H., Oppo D. W. and Wijmstra T. A. (2003) Comparison of changes in vegetation in northeast Greece with records of climate variability on orbital and suborbital frequencies over the last 450 000 years. *Earth Planet. Sci. Lett.* **212**, 197–212.

Valero-Garcés B. (1999) Sedimentary facies analyses as paleohydrological proxies for saline lakes, Central Ebro Basin, Spain. In *Correlations of Late Weichselian and Holocene palaeoenvironment proxy data. 4th Workshop of the European Lake Drilling Programme (ELDP)* (ed. E. S. Foundation). Terra Nostra, Lund, Sweden.

Van Rampelbergh M., Verheyden S., Allan M., Quinif Y., Keppens E. and Claeys P. (2014) Monitoring of a fast-growing speleothem site from the Han-sur-Lesse cave, Belgium, indicates equilibrium deposition of the seasonal d18O and d13C signals in the calcite. *Clim. Past* **10**, 1871–1885.

Vandenschrick G., van Wesemael B., Frot E., Pulido-Bosch A., Molina L., Stievenard M. and Souchez R. (2002) Using stable isotope analysis (δD–δ18O) to characterise the regional hydrology of the Sierra de Gador, south east Spain. *J. Hydrol.* **265**, 43–55.

Vanghi V., Frisia S. and Borsato A. (2017) Genesis and microstratigraphy of calcite coralloids analysed by high resolution imaging and petrography. *Sediment. Geol.* **359**, 16–28.

Vansteenberge S., Verheyden S., Cheng H., Edwards L. R., Keppens E. and Claeys P. (2016) Paleoclimate in continental northwestern Europe during the Eemian and Early-Weichselian (125–97 ka): insights from a Belgian speleothem. *Clim. Past Discuss.*, 1–22.

Vautravers M. J. and Shackleton N. J. (2006) Centennial-scale surface hydrology off Portugal during marine isotope stage 3: Insights from planktonic foraminiferal fauna variability: off Portugal during MIS 3. *Paleoceanography* **21**.

Vautravers M. J., Shackleton N. J., Lopez-Martinez C. and Grimalt J. O. (2004) Gulf Stream variability during marine isotope stage 3: Gulf Stream variability. *Paleoceanography* **19**. Available at: http://doi.wiley.com/10.1029/2003PA000966 [Accessed July 22, 2018].

Vegas J., Ruiz-Zapata B., Ortiz J. E., Galán L., Torres T., García-Cortés Á., Gil-García M. J., Pérez-González A. and Gallardo-Millán J. L. (2010) Identification of arid phases during the last 50 cal. ka BP from the Fuentillejo maar-lacustrine record (Campo de Calatrava Volcanic Field, Spain). *J. Quat. Sci.* **25**, 1051–1062.

de Vernal A., Rosell-Melé A., Kucera M., Hillaire-Marcel C., Eynaud F., Weinelt M., Dokken T. and Kageyama M. (2006) Comparing proxies for the

reconstruction of LGM sea-surface conditions in the northern North Atlantic. *Quat. Sci. Rev.* **25**, 2820–2834.

Vesica P. L., Tuccimei P., Turi B., Fornós J. J., Ginés A. and Ginés J. (2000) Late Pleistocene paleoclimates and sea-level change in the Mediterranean as inferred from stable isotope and U-series studies of overgrowths on speleothems, Mallorca, Spain. *Quat. Sci. Rev.* **19**, 865–879.

Vodila G., Palcsu L., Futó I. and Szántó Z. (2011) A 9-year record of stable isotope ratios of precipitation in Eastern Hungary: Implications on isotope hydrology and regional palaeoclimatology. *J. Hydrol.* **400**, 144–153.

Voelker A. H. L. and Abreu L. (2011) A review of abrupt climate change events in the northeastern 631 Atlantic Ocean (Iberian Margin): Latitudinal, Longitudinal, and Vertical Gradients. In *Abrupt Climate Change: Mechanisms, Patterns, and Impacts* (eds. H. Rashid, L. Polyak, and E. Mosley-Thompson). Geophysical Monograph Series.

Wackerbarth A., Langebroek P. M., Werner M., Lohmann G., Riechelmann S., Borsato A. and Mangini A. (2012) Simulated oxygen isotopes in cave drip water and speleothem calcite in European caves. *Clim Past* **8**, 1781–1799.

Wackerbarth A., Scholz D., Fohlmeister J. and Mangini A. (2010) Modelling the δ18O value of cave drip water and speleothem calcite. *Earth Planet. Sci. Lett.* **299**, 387–397.

Wainer K., Genty D., Blamart D., Hoffmann D. and Couchoud I. (2009) A new stage 3 millennial climatic variability record from a SW France speleothem. *Palaeogeogr. Palaeoclimatol. Palaeoecol.* **271**, 130–139.

Wang X., Li Z., Tayier R. and Wang S. (2015) Characteristics of atmospheric precipitation isotopes and isotopic evidence for the moisture origin in Yushugou River basin, Eastern Tianshan Mountains, China. *Quat. Int.* **380–381**, 106–115.

Weiss H., Courty M.-A., Wetterstrom W., Guichard F., Senior L., Meadow R. and Curnow A. (1993) The Genesis and Collapse of Third Millennium North Mesopotamian Civilization. *Science* **261**, 995–1004.

Wiedner E., Scholz D., Mangini A., Polag D., Mühlinghaus C. and Segl M. (2008) Investigation of the stable isotope fractionation in speleothems with laboratory experiments. *Quat. Int.* **187**, 15–24.

Williams and Fowler (2002) Relationship between oxygen isotopes in rainfall, cave percolation watersand speleothem calcite at Waitomo - New Zealand. *N. Z. J. Hydrol.* **41**, 53–70.

Wirmvem M. J., Ohba T., Fantong W. Y., Ayonghe S. N., Suila J. Y., Asaah A. N. E., Asai K., Tanyileke G. and Hell J. V. (2014) Monthly δ18O, δD and Cl− characteristics of precipitation in the Ndop plain, Northwest Cameroon: Baseline data. *Quat. Int.* **338**, 35–41.

Wolf D., Kolb T., Alcaraz-Castaño M., Heinrich S., Baumgart P., Calvo R., Sánchez J., Ryborz K., Schäfer I., Bliedtner M., Zech R., Zöller L. and Faust D. (2018) Climate deteriorations and Neanderthal demise in interior Iberia. *Sci. Rep.* **8**.

Wolff E. W., Chappellaz J., Blunier T., Rasmussen S. O. and Svensson A. (2010) Millennial-scale variability during the last glacial: The ice core record. *Quat. Sci. Rev.* **29**, 2828–2838.

Woodhead J. and Pickering R. (2012) Beyond 500ka: Progress and prospects in the UPb chronology of speleothems, and their application to studies in palaeoclimate, human evolution, biodiversity and tectonics. *Chem. Geol.* **322**–**323**, 290–299.

World Reference Base for Soil Resources (2014) *International soil classificaiton system for naming soils and creating legends for soil maps*., FAO, Rome.

Wulf S., Brauer A., Kraml M., Keller J. and Negendank J. F. W. (2004) Tephrochronology of the 100 ka lacustrine sediment record of Lago Grande di Monticchio (southern Italy). *Quat. Int.* **122**, 7–30.

Wulf S., Hardiman M. J., Staff R. A., Koutsodendris A., Appelt O., Blockley S. P. E., Lowe J. J., Manning C. J., Ottolini L., Schmitt A. K., Smith V. C., Tomlinson E. L., Vakhrameeva P., Knipping M., Kotthoff U., Milner A. M., Müller U. C., Christanis K., Kalaitzidis S., Tzedakis P. C., Schmiedl G. and Pross J. (2018) The marine isotope stage 1–5 cryptotephra record of Tenaghi Philippon, Greece: Towards a detailed tephrostratigraphic framework for the Eastern Mediterranean region. *Quat. Sci. Rev.* **186**, 236–262.

Yonge C. J., Ford D. C., Gray J. and Schwarcz H. P. (1985) Stable isotope studies of cave seepage water. *Chem. Geol. Isot. Geosci. Sect.* **58**, 97–105.

Yuan D., Cheng H., Edwards R. L., Dykoski C. A., Kelly M. J., Zhang M., Qing J., Lin Y., Wang Y., Wu J., Dorale J. A., An Z. and Cai Y. (2004) Timing, Duration, and Transitions of the Last Interglacial Asian Monsoon. *Science* **304**, 575–578.

Zhan L., Chen J., Zhang S., Li L., Huang D. and Wang T. (2016) Isotopic signatures of precipitation, surface water, and groundwater interactions, Poyang Lake Basin, China. *Environ. Earth Sci.* **75**.

Zhang H., Cai Y., Tan L., Qin S. and An Z. (2014) Stable isotope composition alteration produced by the aragonite-to-calcite transformation in speleothems and implications for paleoclimate reconstructions. *Sediment. Geol.* **309**, 1–14.

Ziegler M., Tuenter E. and Lourens L. J. (2010) The precession phase of the boreal summer monsoon as viewed from the eastern Mediterranean (ODP Site 968). *Quat. Sci. Rev.* **29**, 1481–1490.